MICROBIAL PROCESSES AND ELEMENT CYCLING FROM MICRO- TO MESO-SCALE:

From single cells and aggregates to the whole water column perspective.

Dissertation

Zur Erlangung des akademischen Grades eines Doktors der Naturwissenschaften

-Dr. rer. nat.-

Vorgelegt von

Andreas Rogge

Bremen, Februar 2019

Alfred-Wegener-Institut

Helmholtz-Zentrum für Polar- und

Meeresforschung

Universität Bremen

Fachbereich II

Biologie / Chemie

Die vorliegende Arbeit wurde von Februar 2015 bis Februar 2019 an der Universität Bremen durchgeführt. Die Untersuchungen fanden am Alfred-Wegener-Institut Helmholtz-Zentrum für Polar- und Meeresforschung in Bremerhaven statt.

1. Gutachter: Prof. Dr. Anya M. Waite
2. Gutachter: Dr. Morten H. Iversen

Tag des Promotionskolloquiums:

01.04.2019

ACKNOWLEDGEMENTS

Bremen, February 2019

Andreas Rogge

TABLE OF CONTENTS

LIST OF PAPERS

This thesis is based on the papers listed below:

Paper I: Rogge, A.; Vogts, A.; Voss, M.; Jürgens, K.; Jost, G.; Labrenz, M. (2017): Success of chemolithoautotrophic SUP05 and *Sulfurimonas* GD17 cells in pelagic Baltic Sea redox zones is facilitated by their lifestyles as K- and r-strategists. Environ. Microbiol. 19: 2495-2506.

Content: In this paper, I investigated the substrate uptake behavior of the two spatially overlapping prokaryotic key-players in pelagic Baltic Sea redox zones, the gammaproteobacterial SUP05 cluster and the epsilonproteobacterial *Sulfurimonas* subgroup GD17. To elucidate their ecological niche separation, non-stimulating stable isotope incubations of environmental samples were performed and the uptake analyzed on a single-cell level using fluorescent *in situ* hybridization (FISH) and nano-scale secondary ion mass spectrometry (NanoSIMS). Significant organism specific differences in cell size were taken into account and isotope enrichments corrected by individual biovolumes.

Conclusions: *Sulfurimonas* GD17 cells seem to outcompete SUP05 by faster substrate uptake, even in the upper suboxic zone, where SUP05 is usually more abundant. Together with earlier described features of GD17 and SUP05, such as genome size, motility, and metabolic versatility, I concluded that the spatially overlapping association is caused by different lifestyles. Whereas SUP05 cells are streamlined, non-motile K-strategists, which are adapted to low substrate concentrations, cells of *Sulfurimonas* GD17 are motile r-strategists adapted to high and fluctuating substrate conditions.

Paper II: Flintrop, C.; Rogge, A.; Miksch, S.; Waite, A. M.; Iversen, M. H. (2018): Embedding and slicing of intact *in situ* collected marine snow. Limnol. Oceanogr. Methods 16: 339-355.

Content: In this paper, we developed a non-disturbing embedding approach for sampling, sectioning and staining of fragile marine particles and i.e. aggregates. The cryogel-based method enabled precise structural investigations using a wide variety of structural stains, such as Alcian Blue for TEP, Coomassie Blue for CSP, but also detailed phylogenetic investigations using several fluorescent *in situ* hybridization

(FISH) protocols, such as monoFISH, CARDFISH, or MiL-FISH. The adjustable slice thickness from 5 to 100 µm enabled high resolution porosity investigations and the compatibility with sediment or drifting traps allowed direct *in situ* sampling in the field.

Conclusions: The method offers new possibilities to study the microstructure of fragile particles and aggregates and will deliver realistic porosity measurements for hydrodynamical models of particle settling. Moreover, it enables detailed investigations of the microbial ecology within particles, such as colonization and communitization strategies of different organisms. To sum up, this approach will help to increase our knowledge of small-scale physical and biological processes associated with the biological carbon pump.

Paper III: Rogge, A.; Flintrop, C.; Iversen, M. H.; Salter, I.; Fong, A. A.; Vogts, A.; Waite, A. M. (2018): Hard and soft plastic resin embedding for single-cell element uptake investigations of marine-snow-associated microorganisms using nano-scale secondary ion mass spectrometry. Limnol. Oceanogr. Methods 16: 484-503.

Content: In this paper, we developed a plastic resin-based approach for the embedding, sectioning and staining of fragile marine particles and aggregates. The resulting slices were resistant to ultra-high vacuum conditions, which allowed investigations of isotope and element distributions using NanoSIMS with reduced shrinking, outgassing or ablation effects.

Conclusions: The approach enables single-cell element uptake measurements of organisms within the particle structure. This allows for the first time the investigation of elemental transfer in microbial consortia within particles or even the detection of anaerobic metabolism, such as sulfate reduction. The application of this method might change our view of element cycling within particle associated microenvironments and their biogeochemical implications.

Paper IV: Eduard Fadeev, Morten H. Iversen, Claudia Wekerle, Ian Salter, Christina Bienhold, Andreas Rogge, Anya M. Waite, Laura Hehemann, Antje Boetius (in prep.): Arctic sea ice enhances vertical connectivity of microbial communities through sinking particles.

Content: In this paper, we investigated the vertical connectivity of the microbial community attached to sinking particles based on 16S rRNA gene sequencing, particle sinking trajectories, and microbial source tracking in Fram Strait.

Conclusions: We could show that the microbial community in the Arctic shows a much stronger vertical connectivity between surface and bathypelagic microbial communities in sea ice-covered regions. We concluded that further loss of sea ice-coverage in the Arctic may affect microbial connectivity and alters biogeochemical cycling.

Paper V: Rogge, A.; Karstensen, J.; Prondzinsky, A. P.; Iversen, M. H.; Waite, A. M. (in prep.): Sub-mesoscale driven deep particle export in a cyclonic eddy of the South Atlantic.

Content: In this paper, I investigated the spatial particle and zooplankton distribution within a cyclonic eddy of the South Atlantic. Using Underwater Vision Profiler, ADCP, and CTD data, as well as nutrient measurements, we were able to explain the particle distribution within this eddy.

Conclusions: We could show that the particles were distributed in a pronounced V-shape down to a depth of > 3000 m. Vertical inertial wave energy propagation at the eddy perimeter caused an 'inertial chimney' effect which increased production. Produced particles were repackaged and fragmented by copepods and converged towards the eddy center with depth while following the vorticity field. Additional low degradation below the eddy core led to further reduced flux attenuation and a threefold increased carbon flux towards the Deep Sea. We concluded that cyclonic eddies cause regularly occurring rapid deep export events in the otherwise oligotrophic southeast Atlantic Ocean.

ZUSAMMENFASSUNG

Mikroorganismen sind eine wichtige Triebkraft der Kohlenstoff-, Stickstoff- und Schwefelkreisläufe auf der Erde. Sie können sich an verschiedenste Substrate anpassen und somit ökologische Nischen in, für höhere Lebewesen, zu extremen Umgebungen besetzen. Zu diesen gehören sub- und anoxische, oder sogar sulfidische Wassermassen. Dabei verfolgen sie unterschiedlichste ökologische Strategien mit verschiedenen Graden der Spezialisierung an ihre Umwelt.

In der intensiv stratifizierten Wassersäule der Ostsee führen starke Respirationsprozesse, in Verbindung mit geringer Ventilation, zu der Bildung von anoxischen Zonen. Dadurch bedingt wird organisches Material anaerob abgebaut was wiederum eine erhöhte Produktion von Schwefelwasserstoff zur Folge hat. Diese Verbindung stellt eine hochtoxische Chemikalie für höhere Lebewesen, insbesondere für Mehrzeller, dar. Die Übergangszone zwischen sulfidischen und suboxischen Wassermassen, die Redoxzone, ist von zwei chemolithoautotrophen Schlüsselorganismen besetzt, die beide in der Lage sind Schwefelwasserstoff mittels Nitrat zu oxidieren und somit zu detoxifizieren. Interessanterweise zeigen beide Organismen eine überlappende Abundanz. Während Vertreter der *Gammaproteobakteria*, die sogenannte SUP05-Klade, insbesondere den suboxischen Bereich besetzen, dominieren Vertreter der *Sulfurimonas* GD17 Untergruppe, welche zu den *Epsilonproteobakteria* zählen, die sulfidische Zone. Dies führte zu der Frage wie beide Organismen innerhalb desselben Habitats überleben können, obwohl sie dieselben Substratanforderungen aufweisen. In **Abhandlung I** dieser Dissertation kombinierte ich phylogenetische Identifizierungen mit Einzelzellaufnahmeanalysen von *Sulfurimonas* GD17- und SUP05-Organismen. Diese stammten aus Umweltproben der Redoxzone des Gotlandtiefs, welche mit stabilen-isotopenmarkierten Substraten inkubiert wurden. Zusammen mit Ergebnissen früher Studien konnte ich eine Nischenseparation aufgrund unterschiedlicher Substratnutzungsstrategien identifizieren. Es stellte sich heraus, dass Organismen der SUP05-Klade als rationalisierte, nicht freibewegliche und langsam verwertende K-Strategen angesehen werden können, die an geringe Substratkonzentrationen angepasst sind und in den meisten Sauerstoffminimumzonen der Welt omnipräsent sind. Organismen der *Sulfurimonas* GD17 Untergruppe, auf der anderen Seite, können als schnellverwertende r-Strategen angesehen werden, welche hochspezialisiert auf hohe und fluktuierende Substratkonzentration sind und dabei ihr chemotaktisches Verhalten nutzen um in Regionen mit favorisierten Substratbedingungen zu gelangen. Zusammen treiben beide

Organismengruppen eine hocheffektive Detoxifizierungsmaschinerie in der Redoxzone der Ostsee an. Weitere bemerkenswerte mikrobielle Strategien, die Stoffflüsse beeinflussen, können auch in anderen pelagischen Milieus aufgefunden werden.

Sinkende Partikel werden aufgrund ihrer Substratreichhaltigkeit, ihrer strukturellen Homogenität, sowie ihrer globalen Omnipräsenz in den Weltmeeren als wichtiges Habitat für pelagische Mikroorganismen angesehen. Allerdings stellen sie immer noch eine große Unbekannte in der mikrobiellen Ökologie dar, was durch ihre fragile Natur bedingt ist, die sie unzugänglich für detaillierte mikroskalige Untersuchungen macht. Zu diesem Zweck präsentiere ich in **Abhandlung II** einen Kryogel-basierten Einbettungs- und Segmentierungsansatz, der detaillierte mikroskopische Analysen der mikrobiellen Gesellschaft innerhalb der intakten Partikelstruktur erlaubt. Die Methode ist kompatibel mit den meisten strukturellen und phylogenetischen Färbungsprotokollen, beispielsweise für verschiedene extrazelluläre Exopolymere, sowie für mikrobielle Identifizierungen mittels verschiedener Fluoreszenz-*in-situ*-Hybridisierungs-Protokolle (FISH). Darüber hinaus kann die dreidimensionale Struktur von Partikeln mittels struktureller Färbungen rekonstruiert und die Porosität exakt berechnet werden. Die Anwendbarkeit in Sinkstofffallen erlaubt es zudem Partikel unbeeinträchtigt *in situ* zu beproben und zu analysieren.

Wie **Abhandlung I** deutlich veranschaulicht, ist die zelluläre Abundanz allerdings nicht immer das wichtigste Merkmal um die ökologische Rolle eines Organismus zu beschreiben. In **Abhandlung III** präsentiere ich deshalb eine optimierte Einbettungs- und Segmentierungsmethode, basierend auf weichen und harten Plastikharzen, die Einzelzellaufnahmemesungen mittels nanoskaliger Sekundärionenmassenspektrometrie auch in sinkenden Partikeln ermöglicht. Die resultierenden Präparate zeichneten sich durch geringe Ausgasungs- und Ablösungseigenschaften in der Ultrahochvakuumkammer, aber eine hohe Sekundärionenausbeute aus. Darüber hinaus gelang es zum ersten Mal die potenzielle Nutzung von alternativen Elektronenakzeptoren durch Mikroorganismen in Partikeln zu identifizieren, welche als ^{34}S- und ^{15}N-Anreicherungen von stabilen-isotopenmarkierten Nitrat und Sulfat in Einzelzellen erkennbar war. Zusätzlich ermöglichen ähnliche Färbeeigenschaften der Präparate wie in **Abhandlung II** auch mit dieser Methode dreidimensionale Rekonstruktionen und Porositätsberechnungen. Die Kombination beider Ansätze aus **Abhandlung II** und **Abhandlung III** eröffnet neue Möglichkeiten, die mikrobielle Ökologie und ihre Wechselwirkung mit der Partikelstruktur, in Bezug auf Phylogenie und Aktivität detailliert zu untersuchen.

Der Einfluss der partikelassoziierten Mikrobengesellschaft auf den Materialumsatz auf höheren Skalen ist von der Partikelabundanz in der Wassersäule abhängig. Dies macht es nötig fragile Partikel mit hoher vertikaler Auflösung ohne physikalische Störung zu detektieren. In **Abhandlung IV** präsentiere ich eine kombinierte Untersuchung optischer Partikelquantifizierungen, physischer Partikelcharakterisierungen, sowie molekularer Sequenzierungen in der Region der Framstraße. Die berechneten Partikelsinkkurven und die Rückverfolgung des genetischen Mikrobenursprungs ergaben eine starke vertikale Konnektivität der beobachteten Mikrobengemeinschaften. Diese war am stärksten in meereisbedeckten Gebieten ausgeprägt, in denen annähernd die Hälfte der partikelassoziierten Gemeinschaften der Tiefsee mit der Gemeinschaft an der Oberfläche verbunden waren. Infolgedessen konnte angenommen werden, dass ein weiterer Rückgang der Meereisbedeckung im Arktischen Ozean die mikrobielle Konnektivität beeinflusst und möglicherweise die biogeochemischen Kreisläufe insgesamt verändert. Diese Studie veranschaulicht, welches Potenzial die Kopplung optischer Partikelquantifizierungen mit mikrobiellen oder molekularen Techniken für Untersuchungen von Partikeln auf multiplen Skalen hat.

Die Abundanz und das Sinkverhalten von Partikeln wird in hohem Maße von biologischen Prozessen, beispielsweise mikrobieller Degradation oder Remineralisierung, aber auch durch Fraßdruck und Umverpackung durch Zooplankton bestimmt. Allerdings gestalten auch submeso- und mesoskalige physikalische Einflüsse die Partikelverteilung in der Wassersäule. In **Abhandlung V** präsentiere ich eine Untersuchung, welche optische Partikelquantifizierung und -identifizierung mit Ultraschall-Doppler-Profil-Strömungsmessungen eines zyklonischen Wirbels des Südatlantiks kombiniert. Dabei zeigte sich, dass die vertikale Propagation der Energie der möglicherweise winderzeugten internen Trägheitswellen dem Vortizitätsfeld im Bereich der Wirbelperipherie folgt. Dieser sogenannte „Kamineffekt" für interne Trägheitswellen führte zu einer Zone erhöhter horizontaler Schärung in den oberen 1500 m des Wirbelperimeters und bewirkte einen vertikalen Nährstofffluss, sowie erhöhte Primärproduktion und Partikelformation. Weiterhin konnte ich zeigen, dass Partikel > 0.5 mm im allgemeinen auch dem Vortizitätsfeld folgten, was zu einer charakteristischen V-Form der Partikelverteilung führte. Weitere Umverpackung und Fragmentierung durch Ruderfußkrebse, in Verbindung mit geringer kohlenstoffspezifischer Degradation, hatte einen dreifach erhöhten Kohlenstofffluss in die Tiefsee zur Folge. Aus diesen Ergebnissen schlussfolgerte ich, dass zyklonische Wirbel regelmäßig intensive und

tiefe Kohlenstoffexportereignisse im andererseits oligotrophen Südatlantischen Ozeanwirbel auslösen.

Globale Stoffkreisläufe als auch pelagische Nahrungsnetze werden durch die mikrobielle Ökologie und Aktivität innerhalb sinkender Partikeln beeinflusst. Letztere wiederum werden durch verschiedenste physikalische und biologische Prozesse von der Mikro- bis zur Mesoskala gestaltet. Somit repräsentieren sinkende Partikel und die mit ihnen assoziierte Mikrobengemeinschaft ein biogeochemisches Bindeglied zwischen klein- und großskaligen Prozessen. Meine Arbeit unterstreicht, dass der globale Einfluss partikelassoziierter Mikrobengemeinschaften nur durch Anwendung interdisziplinärer Ansätze auf multiplen Skalen verstanden werden kann. In meiner Dissertation nutzte ich aktuelle Methoden um mikrobielle Prozesse auf der Mikroskala zu untersuchen und entwickelte Strategien um diese Prozesse in das größere Verständnis der mikrobiellen Dynamik auf ozeanographischen Skalen mit globaler Relevanz einfließen zu lassen.

SUMMARY

Microorganisms are important drivers of the carbon, nitrogen, and sulfur cycles on earth. They can adapt to various substrates and, thus, inhabit ecological niches too extreme for higher lifeforms, such as sub- and anoxic or even sulfidic waters. They follow a wide range of ecological strategies with variable levels of specialization to their environment.

In the highly stratified water column of the Baltic Sea, respiration of organic matter in combination with sluggish ventilation causes the formation of anoxic zones. Here, organic material is decomposed anaerobically, which leads to the increased production of hydrogen sulfide – a highly toxic compound for higher lifeforms (e.g. multicellular organisms). The transition zone between sulfidic and suboxic conditions, the redox zone, is inhabited by two chemolithoautotrophic key organisms, both with the same ability to detoxify hydrogen sulfide via oxidation with nitrate. Interestingly, both organisms show an overlapping abundance. While the gammaproteobacterial SUP05 clade is most abundant in the suboxic zone, the epsilonproteobacterial *Sulfurimonas* GD17 subgroup dominates the sulfidic zone. This led to the question of how these two organisms can survive within the same habitat although they exhibit the same substrate requirements. In **Paper I**, I coupled phylogenetic identification with single-cell uptake measurements of SUP05 and *Sulfurimonas* GD17 in environmental samples from the Gotland Deep redox zone. I was able to identify niche separation due to different substrate utilization strategies: SUP05 is streamlined, non-motile, and slowly utilizing; essentially a K-strategist, adapted to low substrate conditions and omnipresent in most of the oxygen minimum zones worldwide. In contrast, *Sulfurimonas* GD17 is a fast utilizing r-strategist, specialized for high and fluctuating substrate conditions, which uses chemotactic behavior to move into regions of favorable substrate conditions. Together they drive a highly efficient detoxification machinery in the Baltic Sea redox zone. Remarkable microbial strategies which influence matter cycling can be found in other pelagic environments as well.

Sinking particles are considered an important potential habitat for pelagic microorganisms due to their substrate richness and structural heterogeneity, as well as their omnipresence in the world oceans. Within individual porous particles, it is theorized that innumerable redox gradients should exist at the microscale, whose attributes in aggregate would drive and control significant elemental fluxes globally. However, marine particles still represent a major black box in microbial ecology due to their fragile nature, which makes them inaccessible for detailed micro-scale observations. Therefore, I present in **Paper II** a

cryogel-based embedding and slicing approach, which enables detailed microscopic investigations of the microbial community within the intact particle structure. The approach is compatible with most structural and phylogenetic staining protocols, such as for different extracellular exopolymers and microbial identification using various fluorescent *in situ* hybridization (FISH) protocols. It also allows the three-dimensional reconstruction of whole aggregates as well as precise porosity calculations and is, moreover, applicable to sediment traps for undisturbed *in situ* samplings.

As **Paper I** clearly illustrates, cellular abundance and species distribution must be accompanied by cellular activity measurements to fully describe an organism's ecological role. In **Paper III**, I therefore present an optimized embedding and slicing method based on soft and hard plastic resins, which enables single-cell uptake measurements using modern nano-scale secondary ion mass spectrometer (NanoSIMS) measurements across the complex microzone structures of marine particles. Embedded specimens were characterized by low outgassing and ablation properties within the ultra-high vacuum chamber (i.e. good conditions for NanoSIMS), but high secondary ion yields. Moreover, critical aspects of cellular biogeochemistry, such as the potential use of alternative electron acceptors by microorganisms, could be identified within particles for the first time, visible as ^{34}S and ^{15}N enrichments from stable isotope labelled sulfate and nitrate in single cells. Staining properties for structural compounds similar to those in **Paper II**, enabled three-dimensional reconstruction and porosity calculations as well. The combination of both methods presented in **Paper II** and **Paper III** opens up new ways to investigate the microbial ecology and their interaction with the particle structure in terms of phylogeny and activity.

The influence of the particle-associated microbial community on matter cycling at larger scales depends both on particle structure (above) and on particle abundance and distribution in the water column. To scale up results measured by the methods developed above, we need to identify and measure the distributions of fragile particles at high vertical resolution, without physical distortion. In **Paper IV**, I present a coupled study of optical particle quantification, physical particle characterization, as well as molecular sequencing in the region of Fram Strait. Calculated particle sinking trajectories and microbial genetic source tracking revealed a strong vertical connectivity between the observed microbial communities. This connectivity was most pronounced in areas with sea ice coverage, where almost half of the particle-associated communities in the deep sea were linked to surface-derived microbes. In turn, it could be concluded that further sea ice decline in the Arctic Ocean may reduce vertical

microbial connectivity, which possibly alters current biogeochemical cycling. This study exemplifies the huge potential of optical quantification coupled to microbiological and molecular methods for multiscale particle investigations.

The abundance and sinking behavior of particles are highly influenced by biological processes, including microbial degradation and remineralization, as well as grazing and repackaging by zooplankton. However, physical forcing, particularly on the sub-meso and mesoscale, critically shape particle distributions in the water column. In **Paper V**, I present a combined investigation of optical particle counting and classification as well as Acoustic Doppler Current Profiler (ADCP) based current velocity measurements in a cyclonic eddy of the South Atlantic. I observed vertical propagation of presumably wind-driven inertial wave energy following the vorticity field at the eddy perimeter, a process known as 'inertial chimney' effect. The resulting zone of increased horizontal shear in the upper 1500 m caused increased upward vertical nutrient flux, supporting enhanced primary production and intensified particle formation in surface eddy. I could show that particles > 0.5 mm in diameter generally followed the relative vorticity field, leading to a sub-surface V-shape of the particle distribution that has not previously been observed. Repackaging and fragmentation by copepods in combination with low carbon-specific degradation led to a threefold increased carbon flux to the deep sea in the center of the eddy. I concluded that cyclonic eddies must regularly cause increased deep carbon export events, in the oligotrophic South Atlantic gyre, and globally.

Global matter cycles, including entire pelagic food webs, are affected by the microbial dynamics of sinking particles. These, in turn, are shaped by a wide variety of physical and biological processes ranging from the microscale to mesoscale. Sinking particles and their complex communities thus represent a biogeochemical link between small- and large-scale processes. My work highlights how the global impacts of particle-associated microbial communities can only be understood through investigations using interdisciplinary approaches at multiple scales. In my thesis, I used cutting-edge methodologies to investigate microbial processes at the micro-scale, and built strategies to integrate these processes into a broader understanding of microbial dynamics at oceanographic scales of relevance to the global ocean.

1   INTRODUCTION

1.1   Redox gradients and their influence on life in the pelagic zone of the oceans

Life as we know it has been described as a thermodynamically open system, which makes use of gradients in its surroundings to create imperfect copies of itself (Prigogine *et al.* 1972; Lammer *et al.* 2009). The majority of gradients mentioned in this definition are redox gradients. Organisms use reduced and oxidized compounds for energy transformation processes based on redox reactions, to run cellular metabolism. Their preferred oxidant and reductant depends on the redox potential, and hence the amount of energy gained from the reaction (Standard Gibbs free energy (ΔG^0; Lam and Kuypers 2011). Since the great oxygenation event ~2.3 billion years ago, most likely caused by the emergence of photosynthetic bacteria, oxygen is broadly available on earth (Holland 2002; Planavsky *et al.* 2014). Because oxygen is one of the most efficient electron acceptors, the oxic mode of life gradually became the most common. However, there are increasingly large environments in the world oceans, where oxygen concentrations permanently drop far below 90 µmol L^{-1} – conditions where most metazoans cannot exist (Karstensen *et al.* 2008; Keeling *et al.* 2010). Those oxygen minimum zones are usually a result of intense oxygen consumption combined with low resupply caused by sluggish ocean ventilation. Below ~4.5 µmol L^{-1}, residual microorganisms have to utilize alternative electron acceptors, usually the ones with the next highest electrode potential. After oxygen, the next most effective electron acceptor is nitrate, but manganese(IV) dioxide, iron(III) oxide-hydroxide or even sulfate are also usable electron acceptors for many marine microbes (Lam and Kuypers 2011; Fig.1).

		E^0 [mV]	ΔG^0 [kJ mol-1]
Oxic	**Aerobic respiration** $[CH_2O] + O_2 \rightarrow CO_2 + H_2O$	816	-479
Anoxic / Suboxic	**Denitrification** $5[CH_2O] + 4NO_3^- \rightarrow 2N_2 + 4HCO_3^- + CO_2 + 3H_2O$	520	-453
	Manganese reduction $[CH_2O] + 3CO_2 + H_2O + 2MnO_2 \rightarrow 2Mn^{2+} + 4HCO_3^-$	748	-349
	Iron reduction $[CH_2O] + 7CO_2 + 4Fe(OH)_3 \rightarrow 4Fe^{2+} + 8HCO_3^- + 3H_2O$	-50	-114
Sulfidic	**Sulfate reduction** $2[CH_2O] + SO_4^{2-} \rightarrow H_2S + 2HCO_3^-$	-234	-77
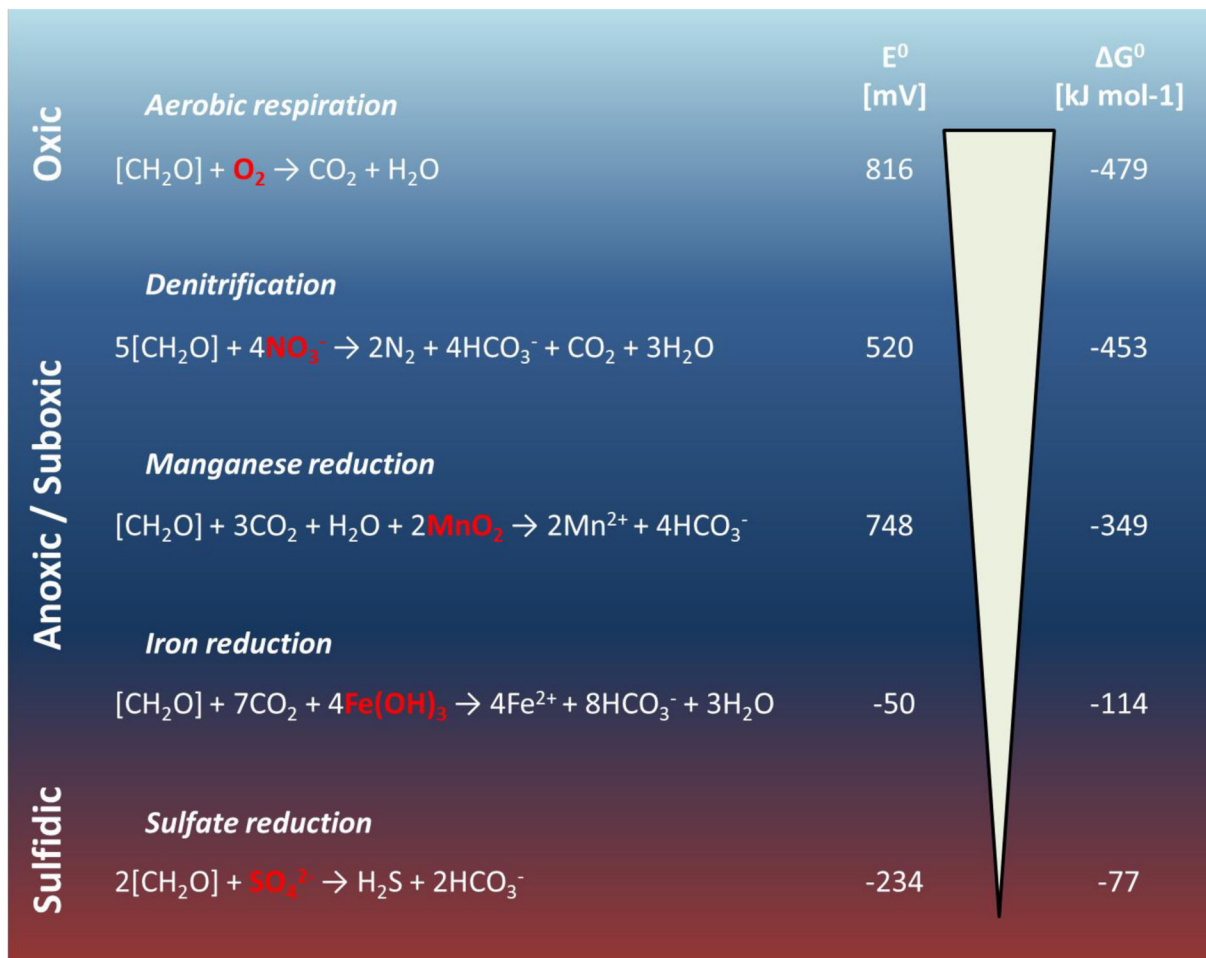
Figure 1: Stoichiometries of selected metabolic pathways of organic matter oxidation in different redox regimes. $[CH_2O]$ symbolizes organic matter of unspecified composition. Respective electron acceptors are marked in red and the respective redox potential (E^0) shown for conditions at pH 7 and 25 °C. Resulting Gibbs free standard energy (ΔG^0) is shown per mole of organic carbon. Note that other reduced compounds, such as elemental sulfur or hydrogen sulfide, can be used as electron donors by many microorganisms as well. (The figure was created according to Jørgensen 2006, Lam and Kuypers 2011, and Seager *et al.* 2012)

Fluctuating redox and substrate conditions caused by turbulence, for example, represent a challenging environment for microorganisms (Stocker 2012). The ability to avoid suboptimal substrate conditions is restricted by the small size of microbes, which limits their mobility range (Purcell 1977). In consequence, the level of specialization to optimize cell metabolism for a given redox regime competes with the organism's need for versatility in the utilization of different substrates and mobility (Stocker 2012; Giovannoni *et al.* 2014). Using single-cell analyses of element uptake, I show in this thesis that this species-specific strategy in the utilization of alternative electron acceptors can cause niche-separation among microbes, influencing both microbial community composition and their ecology (Paper I). This effect

was exemplified on two bacterial key players of the pelagic Gotland Deep redox zone in the Baltic Sea, but similar processes are likely to shape the microbial ecology in many other pelagic redox zones.

1.2 Sinking particles and their impact on the global carbon cycle

The amount of biologically available energy also determines an organism´s capacity to catalyze biomass transformation, in other words, rates of carbon assimilation and dissimilation. Carbon assimilation is linked to the fixation of gaseous CO_2 into more complex molecules, whereas carbon dissimilation ultimately produces CO_2 from more complex molecules. Thus, the efficiency of metabolic microbial processes is always intimately linked to climate relevant processes.

In the open ocean, almost all carbon assimilation takes place in the sunlit euphotic zone, where phytoplankton fix CO_2 into organic matter photosynthetically (Zhang *et al.* 2018). Their settling velocity depends on the type of marine particles with which they become associated: Growing and reproducing cells aggregate, which increases sinking velocity and leads to vertical export of phytoplankton aggregates (Fig. 2). Some of the largest particles are known as marine snow (porous aggregates > 500 µm) which can have very high sinking rates (~500 – 1000 m d^{-1}; Alldredge and Silver 1988). In its entirety, this process, known as the biological carbon pump (BCP), transports carbon into the deeper ocean and feeds the pelagic and benthic food web of the deep sea. The BCP also has a critical influence on the global carbon budget: heterotrophic activity of organisms attached to sinking aggregates lead to a net loss of carbon in the form of release of CO_2 from organic matter in deeper waters (Barker *et al.* 2003). The depth at which CO_2 is produced determines in turn the residence time of carbon in the water column, and deeper release makes it less likely to reach the ocean surface, with the potential to contribute to atmospheric processes, such as the greenhouse effect. When significant amounts of carbon get sequestered in deep sea sediments and thereby are removed from the atmosphere system for geological time scales, the BCP effectively buffers the effect of global warming (Dunne *et al.* 2007; Zhang *et al.* 2018).
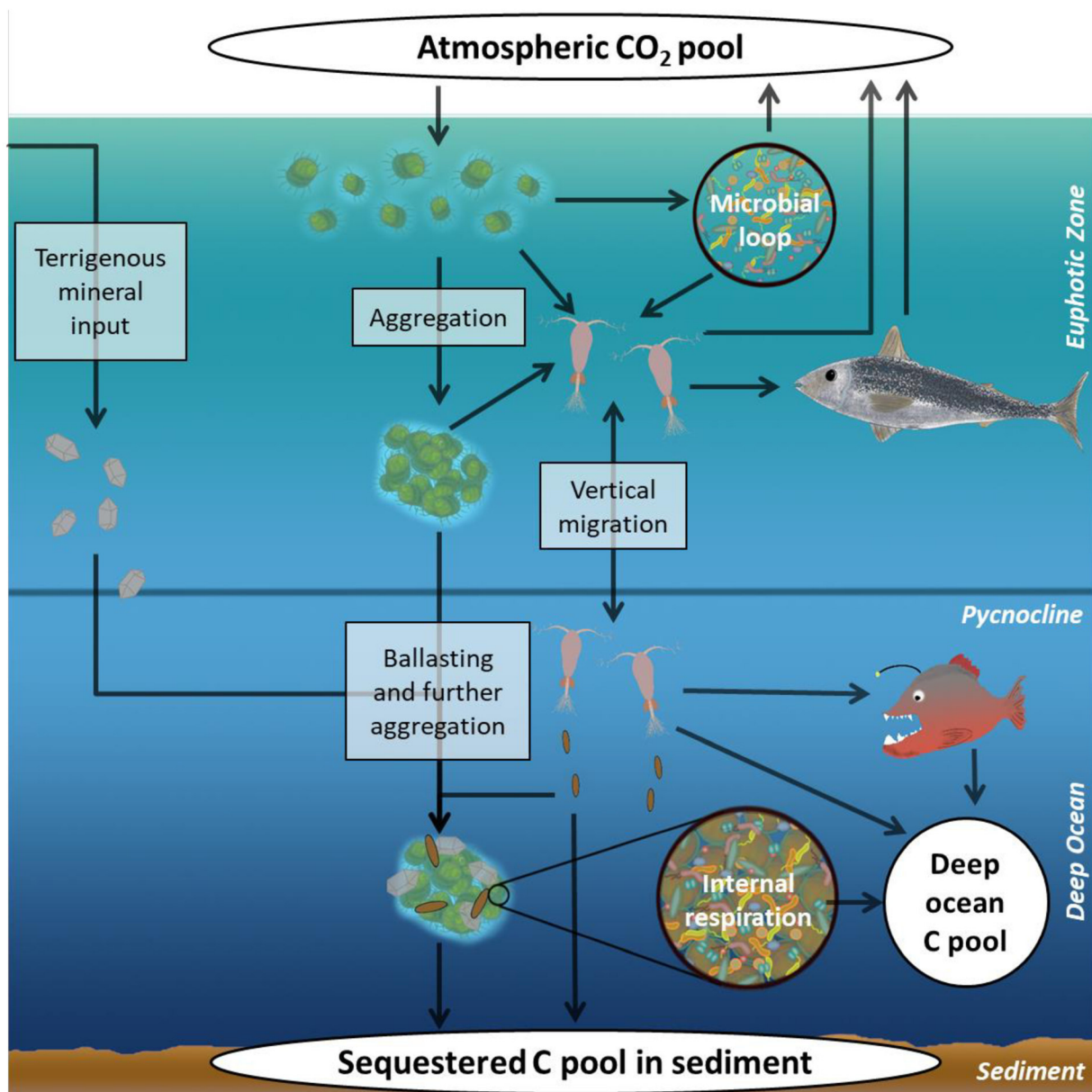
Figure 2: Schematic view of the biological carbon pump. Gas exchange physically transports atmospheric CO_2 into the euphotic zone, where it is fixed photosynthetically by phytoplankton. Aggregation leads to passive export of fixed carbon due to sinking, which is intensified by ballasting and densification. Zooplankton (e.g. copepods) actively transports incorporated carbon via vertical migration, an adaptation to avoid predation (e.g. by fish). Respiration by microbes, zooplankton, and higher trophic levels in shallow waters leads to a release of carbon ultimately back into the atmospheric pool, whereas deep respiration removes carbon from the atmosphere for up to several thousand years. Sequestration in deep sea sediments removes carbon from the atmosphere on geological time scales (up to millions of years; The figure was created according to Kiørboe 2001; Buesseler *et al.* 2007; Turner 2015).

Martin *et al.* (1987) provided the first description of the general attenuation of the vertical particle flux. It is characterized by an exponential decrease in particulate organic matter flux with depth, caused by respiration and degradation. However, the intensity of the attenuation is very heterogeneous regionally and depends on a whole orchestra of biological, physical, and geological processes on several scales: Geologically, terrigenous ballast minerals, such as Sahara dust, transported by global weather phenomena, can increase bloom intensity via iron and phosphorus supply and increase the sinking velocity of aggregates through ballast effects (Iversen and Ploug 2010; van der Jagt *et al.* 2018). On the other hand, the aggregation efficiency is influenced by the biologically-controlled stickiness of phytoplankton cells, which is again influenced by the species composition and the quantity of sticky exudates, such as proteins and polysaccharides, produced by the respective species (Passow 2002; Cisternas-Novoa *et al.* 2015). An attenuation of the sinking speed, caused by physical oceanographic phenomena, such as strong density gradients (Franks 1992) leads in turn to changes in the rate of respiratory carbon loss (Ploug *et al.* 2008a). Grazing by salps or copepods causes carbon loss as well (Everett *et al.* 2011; Laurenceau-Cornec *et al.* 2015). The repackaging of the excreted organic matter by those organisms into denser fecal pellets, however, results in a higher sinking velocity and may increase net export efficiency (Ploug *et al.* 2008a).

1.3 Small-scale redox zones as diverse microenvironments in sinking particles

It is thought that microbial respiration and remineralization alters the redox state within denser regions of aggregates and especially fecal pellets (Bristow 2018). This potentially leads to the development of innumerable strong redox gradients similar to those in pelagic redox zones but on the micro-scale. The overall impact of these micro-environments within individual aggregates may be enormous globally due to the omnipresence of aggregates in the oceans (Bianchi *et al.* 2018). Consumption of alternative electron acceptors associated with particles that could only have been related to sub- or anoxic conditions, such as nitrate respiration (Wolgast *et al.* 1998), provided first indications for sub- or anoxic metabolism. However, it has hitherto been impossible to verify these ideas because of our lack of ability to handle and investigate within-particle redox structures, undisturbed, at relevant scales.

I present in this thesis two complementary embedding and sectioning methods, which enable detailed investigations of microbial strategies and matter cycling within sinking particles: A cryogel-based approach enables microbial identification using phylogenetic staining as well as structural staining with a high vertical resolution (Paper II). A plastic resin approach enables single-cell activity measurements using secondary ion mass spectrometry, as well as structural and potentially phylogenetic staining (Paper III). The two methods will allow the first glimpses inside intact settling particles and will help to gain new understandings of their spatial structure and the colonization strategies of microbes. Moreover, they will help to shed new light on community succession processes, microbial activity and the establishment of microenvironments of reduced oxidation state within marine snow. This will consequently help to understand the role of microbial activity for the BCP.

1.4 Sinking particles as vehicles for microbes in the water column

Due to their sinking behavior through different water masses of the whole water column, particles also play an important role as a vehicle for microbes associated with them (Thiele *et al.* 2015). Individual gravitational settling velocities of phytoplankton aggregates are mainly influenced by the density of the composite parts they consist of. Here, the composition of the phytoplankton species they are formed of, in particular the ballasting material related with them, such as frustules or coccoliths, are of special importance (Iversen and Ploug 2010). Lower settling velocities of aggregates increase their residence time in the upper water column, leading to increased remineralization of those aggregates in shallower waters and, hence, decreased export towards the deep sea (Ploug *et al.* 2008a; Ploug *et al.* 2008b; Iversen and Ploug 2010). This raises the question of how a shift in particle composition and distribution affects the microbial community and its vertical connectivity.

The acquisition of the particle distribution, however, is as challenging as the microscopic investigation of particles. Whereas net tows are destructive and not useful for fragile aggregates, sediment traps only describe the particle distribution with a limited vertical resolution (Buesseler *et al.* 2007). Modern optical imaging profilers enable us to simultaneously quantify the size-distribution of fragile particles with a high vertical resolution *in situ* – an opportunity that is not feasible with nets or sediment traps alone (Picheral *et al.* 2010). In Paper IV, we used the latest version of an Underwater Vision Profiler (v5 HD) to calculate sinking trajectories based on acquired particle distributions in Fram Strait. We

combined those results with microbial source tracking calculations based on extensive 16S rRNA gene sequencing of particle-associated and free-living microorganisms, to resolve the vertical connectivity of the microbial community attached to particles. A strong vertical connectivity between sea ice-covered surface waters and the deep sea suggested that a further decline in sea ice coverage might influence biogeochemical cycling in the Arctic deep sea in the future.

1.5   The impact of meso-scale oceanography on sinking particles

Extensive investigations on the particle distribution in the water column by applying high-resolution optical profilers with an appropriate vertical resolution would further allow us to quantify the workings of the biological carbon pump at the submeso- to meso-scale. This scale represents the range of scales where most regional oceanographic phenomena occur, which shape the transport and transformation of organic matter through the water column (Dickey 2003; Fig. 3).
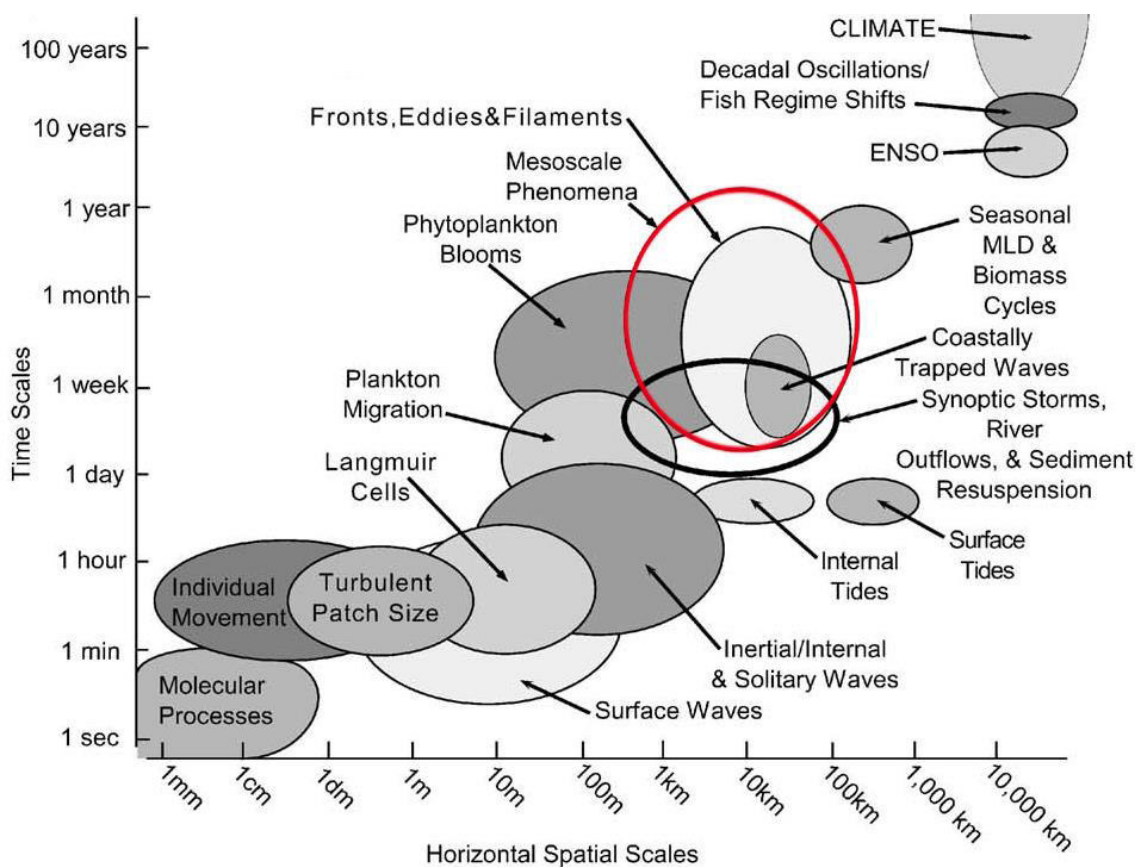
Figure 3: Time-horizontal space scale diagram for selected physical and biological processes influencing the ocean (The figure was modified from Dickey 2003).

Fronts and strong density gradients, for instance, can separate two different water masses vertically or horizontally, respectively, and slow down particle transport in between (Franks 1992). Anticyclonic eddies, on the other hand, have been found to concentrate particles physically across hundreds of kilometers, leading to an enrichment of aggregates within the central warm core of the eddy (Waite *et al.* 2016). This is due to net inward velocity in the eddy center, which moves particles radially inward as they are sinking. As the retention time of particles in the water column decreases, however, the intensity of grazing and disaggregation by zooplankton as well as microbial remineralization also decrease. This ultimately increases the amount of sequestered carbon and hence the efficiency of the BCP (Ploug *et al.* 2008a). The effect of sub-mesoscale physical features of mesoscale cyclonic eddies on the particle distribution, however, is still unclear.

In Paper V, I show the impact of a cyclonic eddy on the particle and zooplankton distribution in the South Atlantic. These investigations were performed using an optical Underwater Vision Profiler attached to a water sampler rosette including conductivity, temperature and density sensor (CTD) with parallel shipboard and lowered acoustic Doppler Current Profiler measurements (sADCP/lADCP; Paper V). I show, that a combination of physical and biological processes cause regular deep export events in the otherwise oligotrophic South Atlantic gyre.

Our understanding of the earth system, especially in the context of global change, requires a broad and interdisciplinary view of all involved processes on all spatial and temporal scales. This thesis uses cutting-edge methodologies to investigate microbial processes at the micro-scale and aims to build strategies to integrate these small-scale microbial processes into large-scale ocean dynamics.

1.6 Questions to be answered

The main research questions in my thesis are listed below.

1. *What ecological strategies are followed by the key microbial players in pelagic redox zones of the Baltic Sea?*
   Hypothesis: The overlapping occurrence of the investigated organisms can be explained by niche separation due to different substrate utilization strategies, which is a result of adaptation to different substrate conditions in the suboxic and sulfidic zone.

2. *How can the spatial microbial distribution and diversity, as well as the structural composition be visualized in sinking particles?*
   Objective: Create a method, which enables microscopic investigations within particles, preserves the three-dimensional particle structure, and is compatible with common structural and phylogenetic staining protocols.

3. *How can single-cell uptake measurements be applied to sinking particles?*
   Objective: Create a method, which enables NanoSIMS measurements of single-cell element uptake within particles, preserves the three-dimensional particle structure, is compatible with common structural staining protocols, and characterized by low nitrogen and sulfur label dilution effects.

4. *How can anoxic micro-zones be identified within sinking particles?*
   Objective: Illustrate possible approaches to identify anoxic micro-zones within particles utilizing the method described in Paper III.

5. *How does sea ice coverage affect the vertical connectivity of the microbial community in the Arctic?*
   Hypothesis: Diatom-dominated phytoplankton communities associated with sea ice form fast sinking aggregates, which sink deeper compared to aggregates formed in ice-free regions and, thus, increase the microbial connectivity between surface and deep sea in ice-covered regions.

6. *How does a cyclonic eddy influence the particle-driven BCP and what are the main drivers?*

   Hypothesis: Cyclonic eddies promote primary production and particle formation due to deep water advection and mixing, and shape the particle distribution by current velocity and vorticity patterns, which increases carbon export.

1.7 Definitions

I define the terms used for the different types of particles in this thesis as follows: **particle**: one single entity of particulate matter, including fecal pellets and aggregates but also living organisms; **detritus**: material consisting of dead particulate matter of various origin; **phytodetritus**: material consisting of dead algae cells and algae cell compounds, **zoodetritus**: material consisting of dead animal cells and animal cell compounds; **aggregate**: a particle formed by aggregation of smaller particles; **fecal pellet**: faeces surrounded by a peritrophic membrane; **phytodetritus aggregate**: aggregate consisting mainly of dead phytoplankton cells; **zoodetritus aggregate**: aggregate consisting mainly of dead animal cells; **mixed aggregate**: aggregates consisting of a mixture of phytodetritus, zoodetritus and fecal pellets; **marine snow**: aggregates larger than 0.5 mm in diameter.

2   RESULTS AND DISCUSSION

Investigations of microbial ecology and biogeochemistry are very often limited to one single scale, such as of whole microbial assemblages. Most common approaches use bottle experiments to investigate nutrient cycling of billions of organisms at the same time. However, considering that most bacteria are smaller than 1 µm³, already 1 mL or a cube with an edge length of 1cm represents a huge volume. Imagining a bacteria being of the size of a human two meters in height; the distance for a bacteria to cross 1 cm would equal ~ 20 km for a human. This very clearly illustrates the scale of the so-called single-cell level with respect to the present scale of "black box" measurements in the research of intercellular interactions. I show in this thesis how secondary ion mass spectrometry sheds new light on microbial ecology. Moreover, I show how the development of two methods will make single-cell investigations applicable for organisms within fragile marine snow and discuss a possible approach to investigate microenvironments within aggregates. I demonstrate how molecular sequencing, combined with particle characterization and quantification can explain the vertical microbial connectivity in the Arctic, and I show how physical-processes on the mesoscale can shape the particle distribution in the water column. Table 1 provides an overview of the presented publications and manuscripts.

Table 1: Overview about the presented papers and manuscripts.

	Experiment parameters	Objectives and questions	Methods applied	Main results	Conclusions

Paper I	• Investigated chemolithoautotrophic bacterial groups: gammaproteobacterial SUP05 clade, epsilonproteobacterial *Sulfurimonas* GD17 subgroup
	• Non stimulating incubations with stable isotope labelled nutrients (^{13}C-HCO_3, ^{15}N-NO_3, ^{34}S-S_8) of water samples from suboxic zone, oxic-anoxic interface, and sulfidic zone of the Gotland Deep redox zone
		• Can niche-partitioning explain the overlapping occurrence of both sulfur-oxidizing denitrifiers?
		• Investigation of uptake behavior:
		  ○ ^{13}C uptake: autotrophic CO_2 fixation
		  ○ ^{15}N uptake: proxy for denitrification
		  ○ ^{34}S uptake: proxy for sulfur oxidation
			• Stable isotope incubations of environmental samples
			• Flowcytometric total cell counting
			• Phylogenetic identification of SUP05 and GD17 (FISH and CARDFISH) and microscopic counting of hybridized cells
			• Marking of fields of interest using Laser Microdissection Microscopy (LMD)
			• NanoSIMS measurements of ^{12}C, ^{13}C, ^{14}N, ^{15}N, ^{32}S, ^{34}S, and secondary electrons in FOIs
			• Calculation of individual biovolume-corrected isotope enrichments
				• SUP05 and GD17 most prominent C, N, and S incorporating organisms in Gotland Deep redox zone
				• SUP05: slow substrate uptake, non-motile, adapted to low sulfide concentrations, small genome, small cells
				• GD17: fast substrate uptake, chemotactic movement, adapted to high sulfide concentrations, large genome, large cells, active oxygen scavenging
					• SUP05 and GD17 drive an efficient detoxification machinery in the sulfidic basins of the Baltic Sea
					• Niche separation caused by different ecological strategies explains overlapping occurrence
					• SUP05 streamlined K-strategist
					• GD17 highly specialized r-stategist

	Experiment parameters	Objectives and questions	Methods applied	Main results	Conclusions

Paper II	• Sampling of aggregates using marine snow catcher and drifting sediment traps
	• Embedding in alcohol-based cryogel
	• Cryotome sectioning
	• Varios structural and phylogenetic staining approaches
	• Microscopy (including Confocal Laser Scanning microscopy
	• 3D reconstruction and porosity calculation
		Create a method for particle embedding and slicing with following features:
		
		• Possibilty for *in situ* sampling
		• Reduction of material loss
		• Possibility for structural staining with reduced sample loss and dye precipitation
		• Preservation of the three-dimensional structure
		• High vertical resolution
			• Cryogel embedding *in situ* using drifting sediment traps
			• Cryotome slicing
			• Staining of structural compounds
			  o Alcian Blue
			  o Coomassie Blue
			  o DAPI
			  o FITC-/Alexa647-ConA
			  o Ruthenium Red
			• Phylogenetic staining
			  o monoFISH
			  o CARDFISH
			  o MiLFISH
			• Microscopy
			• 3D reconstruction and porosity calculation
				• Successful *in situ* sampling demonstrated
				• Structural preservation and reduced sample loss shown
				• Applicability of structural and phylogenetic staining exemplified
				• High vertical resolution (5 – 100 µm) enabled precise 3D reconstruction and porosity calculation
					• Easy-to-use method for sampling in the field, including *in situ* sampling
					• Enables studies on microbiological ecology in aggregates including co-localization of microbial groups with each other and with specific exopolymeric compounds
					• Enables detailed porosity investigations

	Experiment parameters	Objectives and questions	Methods applied	Main results	Conclusions

Paper III	• Incubations of laboratory generated aggregates with stable isotope labelled nutrients (^{13}C-HCO$_3$, ^{15}N-NO$_3$, ^{34}S-SO$_4$)
	• Embedding in methyl-methacrylate and Araldite 502
	• Sectioning using semi-microtome and polishing technology
	• Various structural staining approaches and microscopic analyses
	• 3D reconstruction and porosity calculation
	• Measurement of vacuum behavior, secondary ion yield, elemental composition and isotopic abundances in cells and of the ambient resin using NanoSIMS
		Create a method for particle embedding and slicing with following features:
		
		• Reduction of material loss during preservation and handling
		• Possibility for structural staining with reduced sample loss and dye precipitation
		• Preservation of the three-dimensional structure
		• Suitability for NanoSIMS measurements, including minimal enrichment dilution
		• Suitability for field experiments, i.e. simple and stable storage conditions
			• Pre-embedding in agarose
			• Embedding in methyl-methacrylate and Araldite 502
			• Semi-microtome sectioning or polishing
			• Staining of structural compounds
			  o Alcian Blue
			  o Coomassie Blue
			  o DAPI
			  o Eosin
			• Microscopy
			• Laser microdissection marking of fields of interest
			• 3D reconstruction
			• Porosity calculation
			• NanoSIMS analyses
				• Structural preservation and stable storage conditions in agarose demonstrated
				• 3D reconstruction and porosity calculation successful
				• Methyl-methacrylate:
				  o various structural staining possibilities demonstrated
				  o high vertical resolution could be achieved
				  o low N and S content proven
				  o plain surface, low outgassing, and low ablation effects, but high secondary electron yields in NanoSIMS shown
				• Araldite 502:
				  o Sectioning of aggregates including hard compounds demonstrated
				  o Water and ethanol based staining was not possible
				  o Applicability for NanoSIMS proven in literature
				• First N and S enriched organisms within undisturbed aggregates localized
					• Agarose pre-embedding easy-to-use in the field
					• Methacrylate embedding compatible with structural staining approaches and NanoSIMS
					• Elemental uptake measurements of single cells within the aggregate pore and exopolymer distribution enables investigations of matter cycling within micro-environments

	Experiment parameters	Objectives and questions	Methods applied	Main results	Conclusions
Paper IV	• Particle composition, size distribution and sinking velocities • Microbial source tracking in ice-covered and ice-free regions in Fram Strait • Particle distribution • Particle Sinking trajectories	• How does sea ice coverage influence the particle composition and characteristics in the Arctic? • How does this difference influence the vertical connectivity of microbial communities?	• Particle sampling using traditional water samplers and marine snow catchers • Characterization of particle composition as well as size and sinking velocity measurements in flow chamber • Underwater Vision Profiling • 16S rRNA gene sequencing • Calculation of particle sinking trajectories and microbial source tracking	• Sustained export of mainly small and slowly sinking *Phaeocystis spp.* aggregates down to 1000 m in ice-free waters • Lower export in ice-free regions, but regularly occurring, rapid deep export of large, fast sinking *Melosira arctica* aggregates in ice-covered waters • Low lateral transport of particles between both regions • Microbial community associated with particles much more connected throughout the water column in ice-covered regions	• Decline in sea ice coverage causes shift of phytoplankton communities from *Melosira arctica* dominated to *Phaecystis spp.* dominated assemblages • This shift leads to increased but shallower export of particles in ice-free regions due to decreased particle size and sinking velocity • Further decline in sea ice coverage, caused by global warming, will decrease deep particle export and vertical connectivity of the microbial communities in the future

	Experiment parameters	Objectives and questions	Methods applied	Main results	Conclusions
Paper V	• Current velocity, vorticity, and horizontal shear • Water mass properties (e.g. potential density) • Particle size distribution • Sorted particle distribution into classes (e.g. zooplankton, intact fecal pellets, aggregates etc.) • Carbon flux and carbon-specific degradation • Nutrient measurements	• How do sub-mesoscale physical processes affect productivity and particle dynamics in a cyclonic eddy? • What is the influence of grazers on the particle distribution?	• Acquisition of main oceanographic parameters using conductivity, temperature, and density sensor (CTD), including fluorometer • Acquisition of lowered and shipboard Acoustic Doppler current Profiler measurements (lADCP, sADCP), and vorticity and horizontal shear calculations • Acquisition of particle distributions using Underwater Vision Profiler and software assisted image analyses • Nutrient sampling and analyses	• Deep water advection in the eddy center up to 100 m • Vertical propagation of inertial wave energy (also 'Inertial chimney effect') increased vertical nutrient flux at the eddy perimeters and enhanced primary and particle production at ~50 m • Shift from aggregate and fecal pellets dominated particle distribution towards fecal pellet fragment dominated distribution co-located with abundance maximum of grazers, i.e. copepods at 150m • Particles followed vorticity field in a V-shape • Reduced carbon-specific degradation below 1500 m • Threefold increased carbon export down to 3500 m	• Sub-mesoscale physical features of cyclonic eddies of the South Atlantic produce, in combination with biological properties, regularly occurring deep export events in oligotrophic waters • Corprohexy by copepods in combination with low carbon-specific degradation at depth potentially promoted deep export

2.1 Strategies among free-living microbial communities

The different species-specific needs for alternative electron acceptors and donors critically distinguish the microbial ecology in redox gradients. In intensely stratified coastal sediments, for example, a clear succession is already visible by eye: oxygenated surface sediments form a thin bright layer above a brown manganese and iron-rich layer, followed by iron sulfide containing black regions in deeper sediments (Giere 1993). The microbial community in each of those sediment depth horizons is unique and characterized by a high microbial abundance (e.g. Gao *et al.* 2011).

In the water column, oxygen depleted zones can be found worldwide (Fuchs *et al.* 2005; Lavik *et al.* 2009; Walsh *et al.* 2009; Zaikova *et al.* 2010) and are currently expanding due to higher water temperatures induced by global warming (Stramma *et al.* 2008; Stramma *et al.* 2011). The strongest pelagic redox gradients can be found in highly isolated and stratified water bodies, such as the Black Sea (Jørgensen *et al.* 1991), the Cariaco Basin (Taylor *et al.* 2001), and the Baltic Sea (Brettar and Rheinheimer 1991). Here, an intense stratification leads not only to oxygen depletion and anoxic metabolism, but even to the production of sulfide due to anaerobic decomposition of organic matter (Brüchert *et al.* 2003; Stewart 2011). In consequence of its highly toxic effect on most eukaryotes, but also many prokaryotes, the appearance of sulfide changes the microbial composition drastically (Gilly *et al.* 2013). The conditions in sulfidic waters are so reduced, that electron acceptors are lacking, preventing a detoxification of sulfide into more oxidized forms, such as elemental sulfur or sulfate. Only the upper region of sulfidic zones, known as the interface area, contains nitrate at significant concentrations (Lam and Kuypers 2011). Further community complexity is driven by micro-turbulences and other mixing events leading to intrusions of oxygen into this zone (e.g. Axell 1998), where oxygen itself is toxic to many anaerobic prokaryotes specialized in sulfidic zone survival (Cypionka *et al.* 1985). In the pelagic Baltic Sea redox zone, *Epsilonproteobacteria* of the *Sulfurimonas* subgroup GD17 are very abundant in the upper sulfidic zone, including the interface (Labrenz *et al.* 2004; Brettar *et al.* 2006; Grote *et al.* 2007), whereas *Gammaproteobacteria* of the SUP05 clade show highest abundances in the suboxic zone and the interface (Labrenz *et al.* 2007; Glaubitz *et al.* 2013). Both organisms are capable of oxidizing sulfide with nitrate to gain energy, while they assimilate inorganic carbon for biomass production, a process called chemoautotrophic denitrification coupled to sulfide oxidation (Brettar *et al.* 2006; Grote *et al.* 2007; Glaubitz *et al.* 2013). From an ecological perspective, it is very uncommon that two organisms share the same habitat with overlapping

occurrence and similar substrate utilization. Thus, I hypothesized that the organisms must have special ecological strategies, which causes niche separation most likely due to discriminable substrate uptake behavior, allowing their coexistence.

In Paper I, I present a study based on stable isotope-incubated samples from all three zones of the Gotland Deep redox zone. Samples were analyzed using a coupled approach of fluorescence *in situ* hybridization (FISH) identification and secondary ion mass spectrometry. Together with results from the literature, we were able to gain a detailed understanding of the substrate uptake strategies of SUP05 and *Sulfurimonas* GD17.

PAPER I

Success of chemolithoautotrophic SUP05 and *Sulfurimonas* GD17 cells in pelagic Baltic Sea redox zones is facilitated by their lifestyles as *K-* and *r*-strategists

Andreas Rogge,[†] Angela Vogts, Maren Voss, Klaus Jürgens, Günter Jost and Matthias Labrenz*

Leibniz Institute for Baltic Sea Research Warnemünde (IOW), Rostock-Warnemünde, Germany.

Summary

Chemolithoautotrophic sulfur-oxidizing and denitrifying *Gamma*- (particularly the SUP05 cluster) and *Epsilonproteobacteria* (predominantly *Sulfurimonas* subgroup GD17) are assumed to compete for substrates (electron donors and acceptors) in marine pelagic redox gradients. To elucidate their ecological niche separation we performed $^{34}S^0$, $^{15}NO_3^-$ and $H^{13}CO_3^-$ stable-isotope incubations with water samples from Baltic Sea suboxic, chemocline and sulfidic zones followed by combined phylogenetic staining and high-resolution secondary ion mass spectrometry of single cells. SUP05 cells were small-sized (0.06–0.09 μm^3) and most abundant in low-sulfidic to suboxic zones, whereas *Sulfurimonas* GD17 cells were significantly larger (0.26–0.61 μm^3) and most abundant at the chemocline and below. Together, SUP05 and GD17 cells accumulated up to 48% of the labelled substrates but calculation of cell volume-specific rates revealed that GD17 cells incorporated labelled substrates significantly faster throughout the redox zone, thereby potentially outcompeting SUP05 especially at high substrate concentrations. Thus, in synopsis with earlier described features of SUP05/GD17 we conclude that their spatially overlapping association in stratified sulfidic zones is facilitated by their different lifestyles: whereas SUP05 cells are streamlined, non-motile *K*-strategists adapted to low substrate concentrations, GD17 cells are motile *r*-strategists well adapted to fluctuating substrate and redox conditions.

Introduction

Pelagic oxygen depleted zones can be found nearly world-wide in brackish or marine systems as in African shelf waters (Lavik *et al.*, 2009), the Arabian Sea (Fuchs *et al.*, 2005), the eastern tropical South Pacific and in seasonally anoxic fjords like Saanich Inlet (Walsh *et al.*, 2009; Zaikova *et al.*, 2010). Due to the higher water temperatures and enhanced stratification of the water column induced by global warming, these oxygen minimum zones (OMZs) are currently expanding (Stramma *et al.*, 2008). In addition to the already existing oxygen depletion, reduced sulfur compounds, especially hydrogen sulfide, can be produced by the anaerobic microbial decomposition of organic matter (Brüchert *et al.*, 2003; Canfield *et al.*, 2010; Stewart, 2011) and may have serious ecological and economic consequences (Stramma *et al.*, 2011; Gilly *et al.*, 2013). These euxinic zones, such as those of the Black Sea (Jørgensen *et al.*, 1991), the Cariaco Basin (Taylor *et al.*, 2001) and the Baltic Sea (Brettar and Rheinheimer, 1991; Conley *et al.*, 2009; Carstensen *et al.*, 2014), are less numerous but still comprise important areas within diverse marine systems.

The characteristic transition zone between reduced and oxidized water bodies, the redox zone, is characterized by a high microbial abundance and activity, including the catalysis of biogeochemical transformation of major elements like N and S (Lam and Kuypers, 2011). In the Baltic Sea, three clusters of prokaryotes predominate within this zone. Phylogenetically, they are members of: (i) *Thaumarchaeota*, including cluster GD2, which is closely related to *Candidatus* Nitrosopumilus maritimus and whose cell counts are highest in the suboxic zone (Labrenz *et al.*, 2010), (ii) *Gammaproteobacteria*, including SUP05 as a member of the gammaproteobacterial sulfur-oxidizing cluster (GSO) most prominent at the suboxic zone or

Table 1. Chemical parameters and cell counts of the Gotland Deep redox zone sampled, showing characteristic chemical gradients and cellular compositions.

Zone	Depth [m]	O_2 [µM]	NO_2 [µM]	NO_3 [µM]	H_2S [µM]	Total cell counts [ml^{-1}]	SUP05 cell counts [ml^{-1}]	GD17 cell counts [ml^{-1}]
Suboxic	80.3	41.4	0.3	1.0	bdl	4.0×10^5 ($\pm 5.1 \times 10^4$)	9.0×10^4 ($\pm 1.0 \times 10^4$)	6.3×10^3 ($\pm 6.8 \times 10^2$)
Chemocline	90.5	0.6	0.7	bdl	1.3	1.3×10^6 ($\pm 7.5 \times 10^4$)	1.4×10^5 ($\pm 2.3 \times 10^4$)	2.1×10^5 ($\pm 5.0 \times 10^4$)
Sulfidic	95.3	nd	0.4	bdl	3.2	1.3×10^6 ($\pm 1.0 \times 10^5$)	4.6×10^4 ($\pm 2.2 \times 10^4$)	3.5×10^5 ($\pm 8.1 \times 10^4$)

Total cell counts were determined flow cytometrically, SUP05 cell counts using CARD-FISH, *Sulfurimonas* subgroup GD17 cell counts using FISH.
bdl, Below detection limit; nd, not determined.

chemocline (Labrenz *et al.*, 2007; Glaubitz *et al.*, 2013) and (iii) the *Epsilonproteobacteria*, represented by the *Sulfurimonas* subgroup GD17, whose cell counts are highest below the chemocline, at the first appearance of sulfide (Labrenz *et al.*, 2004; Brettar *et al.*, 2006; Grote *et al.*, 2007). Meanwhile, the successful isolation of a representative of the GD17 subgroup, *Sulfurimonas gotlandica* strain GD1^T (Grote *et al.*, 2012; Labrenz *et al.*, 2013), and of one pelagic representative of the SUP05 cluster [with 99% 16S rRNA sequence similarity to the abundant Baltic Sea SUP05 clone OTU GD3 (Labrenz *et al.*, 2007; Glaubitz *et al.*, 2013)], Candidatus Thioglobus autotrophicus EF1 (Shah and Morris, 2015; Shah *et al.*, 2017), provided further insights into their physiological flexibility. Both taxonomic groups are chemolithoautotrophic sulfur-oxidizing and nitrate-reducing organisms (Brettar *et al.*, 2006; Grote *et al.*, 2007; Glaubitz *et al.*, 2013), with EF1 reducing nitrate only to nitrite (Shah *et al.*, 2017), but their individual contribution to the C-, N- and S-cycles on single cell level *in situ* has not been demonstrated yet.

Given the overlapping occurrence of the two sulfur-oxidizing key players in Baltic redox zones, a redox-driven niche partitioning can be assumed in which cells of the SUP05 cluster are most active in the suboxic zone and oxic/anoxic interface and the GD17 subgroup slightly below the chemocline. The implication is that GD17 is exposed to higher sulfide (but lower nitrate) concentrations and SUP05 vice versa. However, local mixing events or lateral intrusions can occur in the central Baltic Sea (Axell, 1998), potentially regularly introducing nitrate- or oxygen-containing water masses in sulfidic zones. This should promote autotrophic denitrification by both proteobacterial groups, which in turn suggest that their ecological and biogeochemical roles are more complex than simply sulfide oxidation at different redox potentials. Our main hypothesis was that niche partitioned organisms with overlapping occurrences must have discriminable substrate utilization behaviour to survive in the same habitat, the redox zone.

To identify discriminable substrate uptake behavior and thus lifestyles of SUP05 and *Sulfurimonas* GD17 in Baltic pelagic redox zones, we performed stable isotope labelling experiments followed by high-resolution secondary ion mass spectrometry (NanoSIMS) on a single-cell level. It has to be noticed that, in contrast to CO_2 fixation, denitrification and sulfide oxidation can only be detected in traces using the NanoSIMS technology, because those substrates are incorporated into cells to a lesser extent than carbon. We used ^{13}C-labeled bicarbonate to investigate autotrophic CO_2 fixation, ^{15}N labelled nitrate to detect nitrogen uptake as a proxy for nitrate reduction and ^{34}S labelled elemental sulfur to determine cellular sulfur uptake as a proxy for sulfide consumption or sulfide oxidation respectively.

Results

Environmental parameters of the pelagic redox zone and incubation biases

The pelagic Gotland Deep redox zone was located at a depth of 80–95 m, where oxygen decreased and sulfide increased with increasing depth (Table 1). Within this zone, nitrate levels were below the detection limit of 0.05 µM in the chemocline and sulfidic layer whereas nitrite concentrations of <1 µM occurred throughout the redox zone. Total prokaryotic cell counts (TCC) were highest at the chemocline and the sulfidic zone, with approximately 1.3×10^6 cells ml^{-1} (Table 1, Supporting Information Fig. 1). Highest cell counts of the SUP05 cluster have been determined at the chemocline (1.4×10^5 cells ml^{-1}, 23% relative abundance) and of the *Sulfurimonas* subgroup GD17 at the sulfidic zone (3.5×10^5 cells ml^{-1}, 25% relative abundance). However, GD17 also had considerable cell counts at the chemocline (2.1×10^5 cells ml^{-1}, 16% relative abundance).

During the incubation time cell growth was usually not stimulated by labelling addition, with the exception of cells of the GD17 subgroup in the suboxic zone where the accordant cell counts increased significantly by approximately 400% during an incubation time of 24 h (Supporting Information Fig. S1).

^{13}C-, ^{15}N- and ^{34}S-enrichments in SUP05 and GD17

In the labelling experiments, a total of 1704 cells were examined by NanoSIMS, with two to three independent
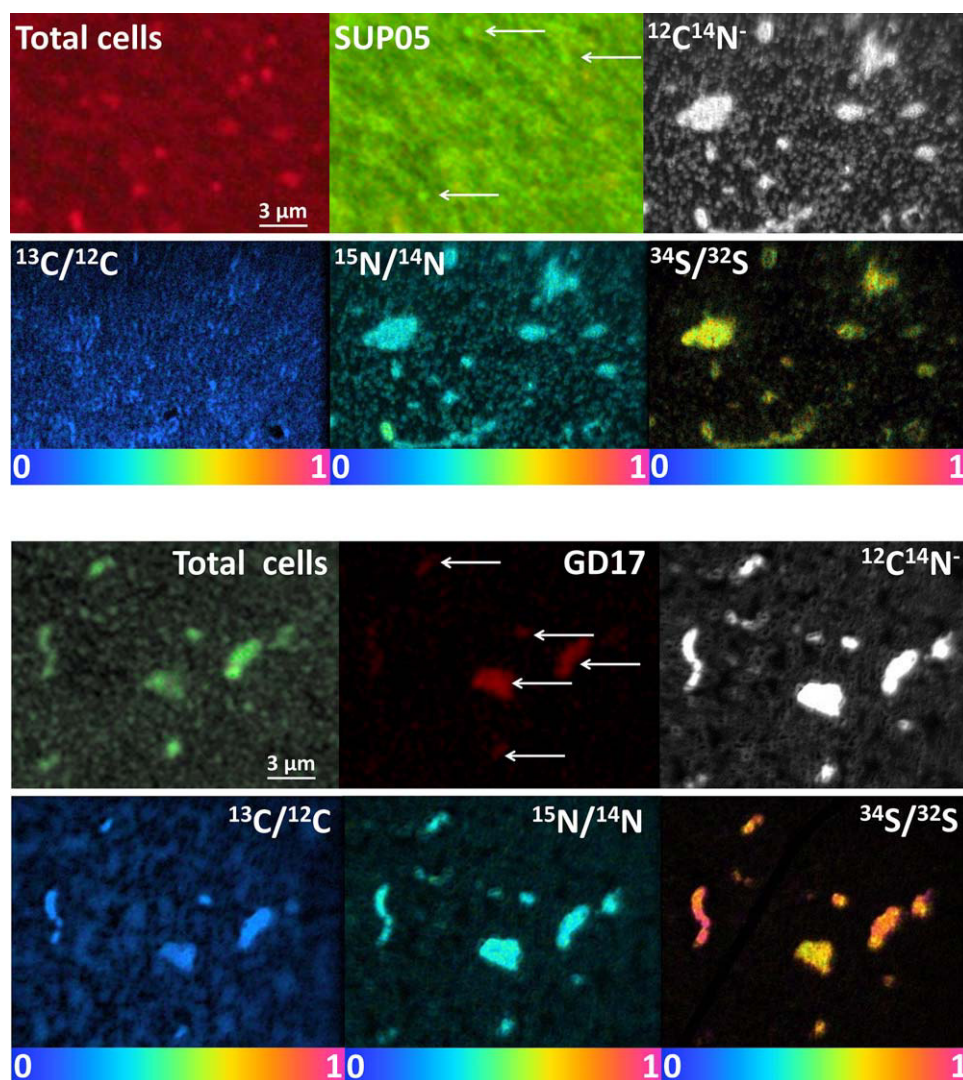
Fig. 1. Identification of SUP05 cells within samples of the suboxic zone, GD17 cells within samples of the sulfidic zone, and determination of cellular isotope enrichments. Upper panel: Total cells stained with propidium iodide and SUP05 hybridized using CARD-FISH protocols, $^{12}C^{14}N^-$ shown as grey scale image and isotope images as hue saturation and intensity (HSI) images of the respective isotope ratio. Lower panel: Total cells stained with SybrGreen and GD17 hybridized using FISH protocols, $^{12}C^{14}N^-$ counts (in general used for cell volume analyses) shown as gray scale image and isotope images as hue saturation and intensity (HSI) images of the respective isotope ratio. Arrows indicate SUP05 or GD17 cells.

replicates analysed for each depth and cell type. 51 of the analysed cells belonged to the SUP05 cluster and 159 to the GD17 subgroup (Supporting Information Table S1). The remainder of the cells was unidentified. As control, 366 cells from incubations with unlabelled substrates were also analysed and, based on the calculation of their average isotopic composition, used for the calibration of our labelling approach (Supporting Information Table S2).

Heavy carbon, nitrogen and sulfur isotopes added to environmental samples were enriched in cells from all three redox zones (Fig. 1). Compared with the controls, 59% ($\pm$22%) and 73% ($\pm$27%) of the identified and analysed SUP05 and *Sulfurimonas* cells, respectively, were characterized by increased ^{13}C-, ^{15}N- or ^{34}S-ratios. Highest proportions of isotope enriched cells with at least 67% for both taxonomic groups were found in the sulfidic zone or chemocline (^{13}C), as well as the suboxic zone (^{15}N or ^{34}S). Lowest concentration of enriched cells was

determined for ^{34}S at the chemocline, where only 13% of the *Sulfurimonas* cells incorporated this isotope.

Different cell volumes of SUP05 and GD17

We used NanoSIMS measurements based on the $^{12}C^{14}N^-$ ion signal for calculation of individual cell volumes. The similarity to epifluorescence microscope based calculations was already confirmed by Musat *et al.* (2008). For the cells investigated, the cell volumes of the SUP05 cluster were significantly different from those of the GD17 subgroup ($\alpha = < 0.01$). These differences were most pronounced in the suboxic zone where the volume of GD17 cells was approximately nine times larger than that of SUP05 cells (0.61 $\mu m^3 \pm 0.47$ μm^3 versus 0.07 $\mu m^3 \pm 0.09$ μm^3; Supporting Information Table S3). The difference in cell size between both groups does not only affect a difference between cellular and biovolume percentages in the environment (Fig. 2 versus Supporting Information
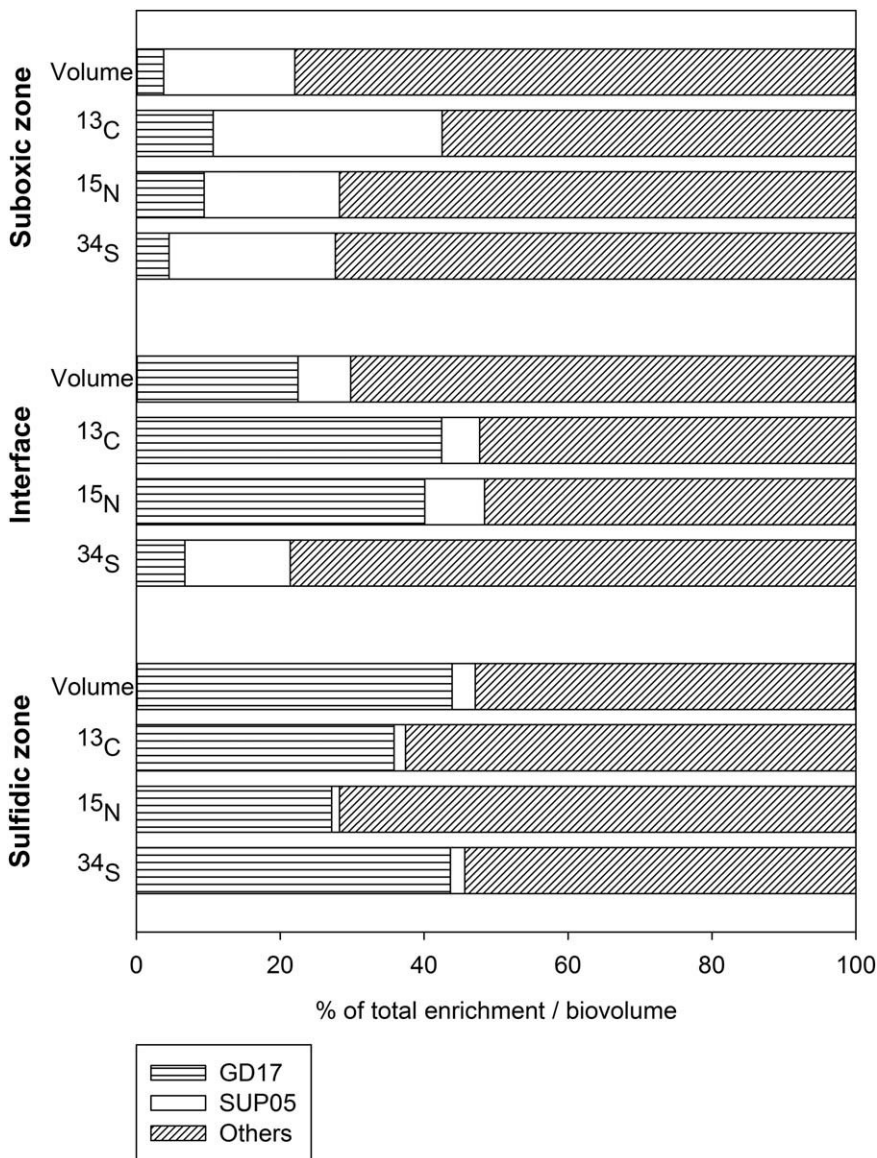
Fig. 2. Cell volume adjusted biovolumes and stable isotope enrichment percentages within the three different redox zones. Volume bar shows average ratios of the GD17 subgroup, SUP05 cluster and unidentified cells (others) on the total biovolume; ^{13}C-, ^{15}N- and ^{34}S-bar shows enrichment ratios (cell volume corrected) of the GD17 subgroup, SUP05 cluster and other cells on the total isotope enrichments.

Fig. S3), it is also attended by crucial implications for stable isotope enrichment interpretations: Larger cells must assimilate higher amounts of labelled substrate to reach cellular isotope ratios similar to those of smaller ones. To include the parameter cell size, cellular isotope enrichments were cell volume-corrected (see *Experimental procedures*; results in Supporting Information Fig. S2).

Contributions of SUP05 and Sulfurimonas *GD17 to ^{13}C-, ^{15}N- and ^{34}S-enrichments in redox zones*

SUP05 and *Sulfurimonas* GD17 significantly contributed to cellular ^{13}C-, ^{15}N- and ^{34}S-enrichments in the different redox zones. Based on cell volume adjusted isotope enrichment calculations, the two groups together accounted for up to 48% of the total cellular isotope enrichments, with, compared with their biovolume, SUP05 being proportionally more active in the suboxic zone, enriching 19–32% of the labelled substrates, and GD17 dominating at the chemocline and sulfidic zone, often in the range of 40% of the labelled substrates (Fig. 2). In the suboxic zone and at the chemocline, the enrichment ratios of SUP05 and GD17 often exceeded their relative total biovolume ratios, whereas this was never the case in the sulfidic zone. In the sulfidic zone, SUP05 was practically inactive while at the chemocline its contribution to ^{13}C- and ^{15}N-enrichments was only 10–20% of that of GD17. The exception to this trend was the contribution of SUP05 to ^{34}S-enrichment at the chemocline (Fig. 2). Calculations of isotope incorporation ratios using the cellular isotope enrichment dataset without cell volume normalization revealed very similar but

less pronounced trends in enrichment activities (see Supporting Information Fig. S3).

The cellular isotope enrichment characteristics of SUP05 and GD17 differed in that high isotope enrichments ratios were determined for GD17 cells in all redox zones, even in suboxic samples, where the biovolumetric percentages of these cells were five times lower than those of SUP05 (Fig. 2). Stable isotope enrichments of GD17 and SUP05 cannot be compared directly because of unknown, and potentially divergent, isotope dilution factors due to the FISH/CARD-FISH procedures used (Musat *et al.*, 2014). However, stable isotope enrichments of SUP05 versus non-SUP05 cells (others, including GD17) as well as GD17 versus non-GD17 cells (others, including SUP05) can be calculated within their respective gene probe treatments. This enables a relative comparison of SUP05 and GD17 isotope enrichment capabilities without different dilution effects. Doing this for cell volume normalized enrichments, specific *Sulfurimonas* GD17 ^{13}C-, ^{15}N- and ^{34}S-isotope enrichments were, altogether, in median 3.1 times higher than those of non-GD17 cells in the FISH approach after 12 or 24 h of incubation. In contrast, the accordant median incorporation ratio of SUP05 cells versus non-SUP05 cells in the CARD-FISH approach was below 1 (0.76) after 12 or 24 h of incubation (Fig. 3). Due to the potential isotope dilution effects of the different gene probes and hybridization methods, both ratios probably represent the lowest possible value.

Discussion

Chemolithoautotrophic cells of the GSO cluster and *Sulfurimonas* GD17 subgroup occupy, as far as we can conclude from existing information on their distribution and genomic features, similar niches and utilize similar substrates in euxinic systems. To better understand the contribution of these bacteria to substrate cycling on a cellular level, we focused on a Baltic pelagic redox zone where both groups are abundant and constantly present.

The results of stable-isotope *in situ* experiments that included NanoSIMS measurements further validated cells of the SUP05 cluster (Glaubitz *et al.*, 2013) and *Sulfurimonas* GD17 subgroup (Brettar *et al.*, 2006; Grote *et al.* 2012) as key players within the C-, N- and S-cycles of pelagic central Baltic Sea redox zones. Together, the two groups accounted for up to 48% of total cellular stable isotope enrichment, with SUP05 most relevant in the suboxic zone and GD17 at the chemocline and in the sulfidic zone (Fig. 2). We conclude that the success of SUP05 and GD17 cells is based on their roles as chemolithoautotrophic *K*- and *r*-strategists respectively. In some cases the terms *K*- and *r*-strategist have been used interchangeably with copiotroph
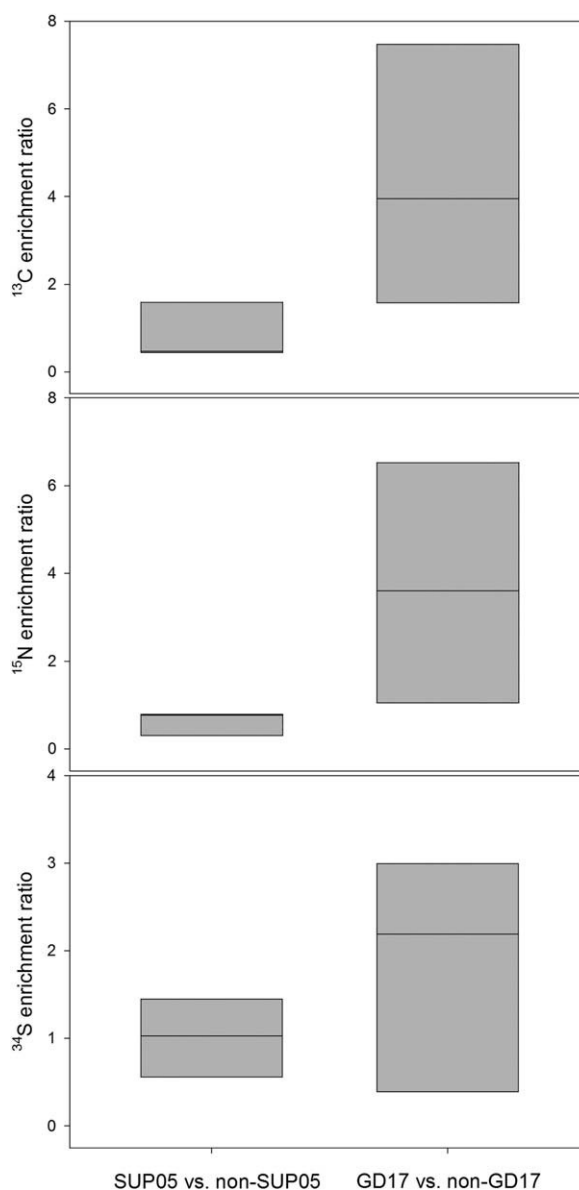
Fig. 3. ^{13}C-, ^{15}N-, ^{34}S-stable isotope enrichment ratios of all investigated zones of SUP05 versus non-SUP05 (others, including GD17) as well as GD17 versus non-GD17 (others, including SUP05) cells after 12 or 24 h of incubation. Used isotope enrichments were cell volume corrected.

and oligotroph (Giovannoni *et al.*, 2014), and especially for oligotrophic bacteria a confusing variety of definitions exist (Schut *et al.*, 1997). We define the lifestyles of SUP05 and *Sulfurimonas* GD17 as being a *K*- and r-strategist, respectively, which is based on the assumption of Andrews and Harris (1986) that *K*-strategists require low substrate concentrations to support slower growth rates whereas *r*-strategists depend on comparably higher substrate concentrations to support rapid growth rates.

Table 2. Features characterizing cells of the SUP05 cluster and *Sulfurimonas* subgroup GD17/GD1[T] as streamlined *K*-strategist or fast reacting *r*-strategist respectively.

	Feature	SUP05	*Sulfurimonas* GD17
I	Sulfide concentration [µM][a]	Up to 15[b], median: 5	Up to 35, median: 17
II	Cell size [µm³]	0.32–0.96[c,1]	0.36–1.04 (mean: 0.64)[c,2]
		0.06–0.09[d]	0.26–0.61[d]
		0.04 (±0.02)[e]	
		0.01–0.033	
III	Motility feature	Not described	Mono- or bipolar flagella2
IV	Genome size [Mb]	1.164	2.956
		1.265	
		1.53	
V	Substrate uptake[d]	Slow	Fast

a. References for preferred H_2S concentrations of SUP05 and *Sulfurimonas* GD17 are shown in Supporting Information Tables S4 and S5 respectively.
b. Only at Saanich Inlet SUP05 is very abundant (Hawley *et al.*, 2014) while members of the *Epsilonproteobacteria* are practically absent or present only in very low concentrations (Zaikova *et al.*, 2010) in waters with relatively high concentrations (15 µM) of sulfide. This is the only such case documented worldwide and requires further examination.
c. Cell volume was calculated according to the cell volume calculation model of this study using the cell areas and the length–width ratios (SUP05) or the cell lengths and widths (GD17) as determined in the respective investigation.
d. Results of this study.
e. Data based on Glaubitz *et al.* (2013).
[1]Sunamura *et al.* (2004); [2]Labrenz *et al.* (2013); [3]Shah *et al.* (2017); [4]Walsh *et al.* (2009); [5]Anantharaman *et al.* (2013); [6]Grote *et al.* (2012).

K-strategist SUP05 versus r*-strategist* Sulfurimonas

The streamlining theory defines successful oligotrophic (oligocarbophilic) cells in substrate-limiting environments as being compact in size, non-motile, and exhibiting a small genome (Stocker, 2012; Giovannoni *et al.*, 2014). According to this definition, chemolithoautotrophic SUP05 cells should analogously be considered as streamlined for several reasons (Table 2): (i) They are adapted to low sulfide concentrations (Table 2; literature overview provided in Supporting Information Table S4) and in this study were most active at lowest sulfide concentrations (Fig. 2). Moreover, Shah *et al.* (2017) described only very recently that also the biogenic nitrogen requirement of strain EF1 is low and only around ∼0.22 µM of nitrogen for biosynthesis in cultures. (ii) They are immobile, given that thus far neither flagella nor the corresponding genes have been detected. (iii) They are smaller than average prokaryotic cells (Table 2, Supporting Information Table S3) which have a mean volume of ∼0.1 µm³ (Schulz and Jørgensen, 2001). To our knowledge, larger environmental SUP05 cells have been reported in only one study but these were cells from a hydrothermal vent system (Sunamura *et al.*, 2004), where detection by fluorescence could have biased cell size. (iv) Their genome is small, with a maximal size of 1.5 Mb determined for strain EF1 (Shah and Morris, 2015) (Table 2).

According to these physiological and morphological features, SUP05 cells should be considered to be streamlined chemolithoautotrophic *K*-strategists. Moreover, they have been detected in all as yet investigated marine areas where sulfide concentrations are moderate to undetectable (Fuchs *et al.*, 2005; Stevens and Ulloa, 2008; Lavik *et al.*,

2009). The omnipresence of this cluster suggests that it could represent a chemolithoautotrophic counterpart of *Pelagibacter ubique* (Canfield *et al.*, 2010; Carini *et al.*, 2012; Giovannoni *et al.*, 2014) in the ocean, with both being streamlined organisms adapted to low inorganic or organic substrate concentrations respectively.

The characteristic features of the *Sulfurimonas* subgroup GD17, including their representative isolate *S. gotlandica* GD1[T] (Labrenz *et al.*, 2013) are different from those of SUP05: (i) GD17 is able to adapt to permanently or seasonally sulfidic waters with higher sulfide concentrations (Table 2; literature overview provided in Supporting Information Table S5). In addition, our NanoSIMS analyses revealed that the cells are able to enrich substrates significantly faster than SUP05 cells during 12–24 h of incubation (Fig. 3). (ii) The cells are motile and able to identify favourable ecological niches, as the bacterium responds chemotactically to nitrate (Grote *et al.*, 2012). *S. gotlandica* GD1[T] also clearly modifies conditions in the water by scavenging oxygen to establish anoxic conditions and is thus able to withstand oxygen intrusions, promoting denitrification (Frey *et al.*, 2014). (iii) Their cell size is above average (Schulz and Jørgensen, 2001) (Table 2; Supporting Information Table S3). (iv) GD1[T] has one of the largest epsilonproteobacterial genomes sequenced thus far (2.95 Mb), which suggests a potentially enhanced metabolic versatility (Grote *et al.*, 2012). Together, these data depict *Sulfurimonas* GD17/GD1[T] as fast-reacting, able to sense chemical gradients and to move into regions of optimal growth conditions. These traits are consistent with the conclusion reached by Campbell *et al.* (2006) that members of

the *Epsilonproteobacteria* respond quickly to changing substrate conditions and serve as primary colonizers in ecosystems where *Sulfurimonas* subgroup GD17 cells thrive as chemolithoautotrophic *r*-strategists.

SUP05 and Sulfurimonas *as key players in sulfur, carbon and nitrogen modification*

In vitro and *in situ* studies of Bruckner *et al.* (2013) already showed that the *Sulfurimonas* subgroup is highly efficient in removing hydrogen sulfide and nitrate from pelagic Baltic Sea redox gradients. However, our samples contained a high percentage of stable-isotope-enriched but phylogenetically unidentified cells (Fig. 2), indicating that other prokaryotes are also significant drivers of the C-, N- and S-cycles. In the suboxic zone *Thaumarchaea* should be responsible for a substantial ^{13}C incorporation proportion by CO_2 fixation as reported recently (Berg *et al.*, 2015). Individual cell counts of species involved in other metabolic pathways should be much less than those of SUP05 and *Sulfurimonas* GD17, which is usually in a range from 10% to 20% of the total cell counts (Grote *et al.*, 2007; Labrenz *et al.*, 2007; Glaubitz *et al.*, 2013), but pathways as dissimilatory nitrate reduction to ammonium, anaplerotic CO_2 fixation (Roslev *et al.*, 2004), or aerobic sulfide oxidation (Friedrich *et al.*, 2005) maybe of importance and remain to be discovered in Baltic Sea redox zones.

Methodical biases within our experimental design have to be considered which, in a sum, could have led to an underestimation of the role of SUP05 and GD17 cells in biochemical cycling. For example, we cannot exclude the transfer of stable isotope signals from SUP05 or GD17 to other prokaryotes, for instance due to cell lysis, which would have led to an overestimation of other organisms. An underestimation of the impact of GD17 or SUP05 on substrate enrichment was also possible through a potential dilution of the ^{13}C or ^{15}N signal by the FISH or CARD-FISH procedures (accordant ^{34}S data do not exist yet), as demonstrated by Musat *et al.* (2014). Concerning sulfur, labelling is also likely to be repressed by the dilution of the ^{34}S signal due to the uptake of other reduced sulfur species in the sulfidic zone. Particularly hydrogen sulfide (H_2S) and thiosulfate ($S_2O_3^{2-}$) are known as alternative substrates for both groups (Labrenz *et al.*, 2013; Shah *et al.*, 2017). Analogously, a dilution of the ^{15}N signal can be assumed for samples originating from the area of higher nitrate concentrations occurring in the suboxic zone or by the uptake of ammonia in the interface or sulfidic zone (Labrenz *et al.*, 2010) because it is used as N-source by both investigated groups (Shah *et al.*, 2017). We chose ^{15}N labelled nitrate for our investigation, since autotrophic denitrifiers are of special interest for nitrogen cycling in marine redox zones. However, it is astonishing and may be the basis of future investigations that, despite the fact that

denitrification and sulfide oxidation can only be detected in traces by NanoSIMS, measured cellular N- and S-enrichments are on a similar level as C-enrichment due to CO_2 fixation (Supporting Information Fig. S2). Intracellular storage of S- and N-compounds could be one reasonable explanation for this phenomenon, but this aspect needs further investigation.

It is hard to estimate the value of potential biases because comparable cellular sulfur or nitrogen incorporation data are not available for Baltic Sea redox zones yet. Though, these data exist with regard to CO_2 incorporation. In their $^{14}CO_2$ incorporation experiments coupled to CARD-FISH combined with microautoradiography (micro-CARD-FISH), Grote *et al.* (2008) estimated that, for a comparable sulfidic zone of the Baltic Sea and depending on depth, 55–73% of all CO_2-fixing prokaryotic cells were related to *Sulfurimonas* GD17. Based on our NanoSIMS analyses, these values are smaller, with 36–42% on a biovolume basis (Fig. 2) and 28–35% on a cellular basis (Supporting Information Fig. S3). However, they are still significant and within the expected range, taking in account the fact that the data were generated by different methods and based on samplings temporally separated by 5 years.

We decided to correct individual isotope abundances by the respective cell volumes because the two investigated groups showed significant differences in size which hinders a direct comparison. The principal has already be used elsewhere (Musat *et al.*, 2008; Thompson *et al.*, 2012; Foster *et al.*, 2013); however, never in pelagic redox zones with that high variation of organisms. Hence, the implementation of a complete quantitative calculation based on the Redfield ratio could not be realized in this study because exact information about every group was missing. However, the calculation applied in this study leads to more realistic enrichment differences than without correction and hence more pronounced results. Nonetheless, the two highest abundant proteobacterial groups in the Baltic Sea redox zone often exhibited much higher stable isotope accumulation than would be expected based on their relative biovolume percentages (Fig. 2). Thus, in Baltic Sea redox zones an efficient sulfide detoxification system is enabled due to the association of the sulfide oxidizers SUP05 and *Sulfurimonas* GD17.

Taken together, we conclude that SUP05 and *Sulfurimonas* GD17 cells are the most prominent bicarbonate-, nitrate- and sulfur-incorporating organisms in pelagic central Baltic Sea pelagic redox zones, but they exhibit distinct cellular characteristics: Whereas SUP05 cells are streamlined, non-motile *K*-strategists adapted to low electron donor (sulfide) concentrations and omnipresent worldwide, GD17 cells are motile *r*-strategists well adapted to fluctuating redox conditions and higher substrate concentrations. The different lifestyles of SUP05 and GD17 cells result in a spatially overlapping association of these organisms in

stratified sulfidic zones and an efficient sulfide detoxification machinery for oxygenated surface areas. Further analyses should discover in more detail the potential niche partitioning of SUP05 and GD17 concerning alternative electron donors (as sulfur of different oxidation states), as it has been proposed for the primarily conversion of free S at the seafloor surface by members of the of *Sulfurimonas/ Sulfurovum* group (Pjevac *et al.*, 2014), or alternative electron acceptors.

Experimental procedures

Sampling

Sampling was performed during a cruise with the *R/V Meteor* (M87/3) in the pelagic Gotland Deep redox zone (57° 19.1906′ N, 20° 2.9969′ E) in June 2012. Samples were collected from suboxic (80.3 m), chemocline (90.5 m) and sulfidic (95.3 m) water masses (Supporting Information Fig. S4) using free-flow bottles and a conductivity, temperature and depth device (CTD). For each zone, three independent replicates were taken. Exetainers (12 ml) were rigorously flushed with at least three volumes of sample water after which the samples were bottled directly at the CTD and then incubated in the dark as described below.

Environmental physicochemical parameters

Oxygen, hydrogen sulfide, nitrite and nitrate concentrations were measured in discrete water samples according to standard protocols (Grasshoff *et al.*, 1999).

Choice of label

Stable-isotope-labelled elemental sulfur (S^0) was used for the determination of cellular sulfur incorporation. The presence of S^0 has been confirmed in pelagic redox zones of the Baltic Sea (Jost *et al.*, 2008) and the Black Sea (Jørgensen *et al.*, 1991). S^0 particles are formed during the direct biotic or abiotic oxidation of H_2S or as a product of the reaction of FeS, via polysulfides and the detachment of an electron from nitrate ions (Schippers and Jørgensen, 2002). Direct information about the oxidation abilities of cyclooctasulfur by SUP05 and *Sulfurimonas* GD17 is missing so far. Only for *Sulfurimonas denitrificans* this pathway could already be shown (Pjevac *et al.*, 2014). However, both the SUP05 clade and the *Sulfurimonas* GD17 cluster are generally able to oxidize S^0 to SO_4^{2-}. In SUP05, this occurs via an incomplete *Sox* pathway (Walsh *et al.*, 2009; Marshall and Morris, 2013) and in GD17 via the *Sox* multienzyme complex and the *Sox*-independent intermediate adenosine-5′-phosphosulfate (Grote *et al.*, 2012). Thus, next to NO_3^- and HCO_3^- for nitrogen and carbon uptake, also S^0 is as an appropriate tracer for active sulfur enrichment by these organisms.

Evaluation of incubation times

Optimal incubation times for isotope incorporation analyses were determined in a preliminary culture experiment with the recently isolated model organism of the *Sulfurimonas* GD17 cluster, *S. gotlandica* strain GD1^T (Labrenz *et al.*, 2013). Cultures were grown in artificial brackish water medium (ABW) as described previously (Grote *et al.*, 2012; Labrenz *et al.*, 2013), supplemented with 200 μM $NaNO_3$ and 200 μM $NaHCO_3$ in which ^{15}N and ^{13}C abundances were 50%. S^0 was weighed directly into the glass tubes to obtain final concentrations ranging from 8.9 to 16.2 μM and ^{34}S abundances between 25% and 44%. The samples were incubated at 10°C in the dark for 12 and 24 h. NanoSIMS analyses (described in detail below) showed that the difference between 12 h and 24 h of incubation did not affect further saturation of the accordant isotope enrichments in GD1 cells (Supporting Information Fig. S5). Therefore, exetainers used in the environmental stable isotope experiments were sacrificed after 12 or 24 h of incubation.

Environmental stable isotope experiments

To mimic natural conditions in our experimental approach, substrate additions were kept to a minimum. Two different labelled substrate concentrations were used for the environmental experiments: (i) 0.1 μM nitrate, 0.1 μM S^0 and 20 μM bicarbonate and (ii) 0.33 μM nitrate, 0.33 μM S^0 and 67 μM bicarbonate. For further analyses, only those incubations were selected in which stable-isotope-enriched cells were detectable but their growth was either only slightly or not stimulated.

In addition, unlabelled controls and negative controls without substrate addition were analysed. Unlabelled controls were incubated for 48 h with 0.33 μM NO_3, 0.33 μM S_8 and 67 μM HCO_3 after which 11 ml of each sample was fixed for 2 h with 500 μl of formaldehyde (final concentration 4.3%). The fixed samples were then filtered through gold-sputtered or unsputtered 0.2 μm polycarbonate filters and kept at −80°C until processing. Unsputtered filters were gold-coated after identification and laser marking (see below) using a Cressington 108 auto-sputter coater. For total cell counting by flow cytometry, 4 ml of each sample was fixed with 400 μl of paraformaldehyde:glutaraldehyde (final concentrations 1% and 0.05% respectively (Jost *et al.*, 2008)) and kept at −80°C until processing.

Flow cytometric cell counting

Samples were stained with SYBR Green I or SYBR Gold dye according to standard protocols (Marie *et al.*, 1997; Gasol *et al.*, 1999; Gasol and Del Giorgio, 2000; Zubkov *et al.*, 2006) and then counted in a FACSCalibur flow cytometer (Becton & Dickinson).

Selection of incubation times and substrate concentrations

To prevent changes in the community composition and thus to get representative results for the redox zone community, samples consisting of non-growing but actively substrate-enriching cells were selected on the basis of test measurements prior to the NanoSIMS analyses. Eventually, the graphical user interface of the Software Look@NanoSIMS (Polerecky *et al.*, 2012) was used for statistical comparison of regions of interest classes via ANOVA. By comparing the different incubation

times and substrate concentrations, the following configurations were chosen for further analysis:

Suboxic: 0.33 μM $^{15}NO_3$, 0.33 μM $^{34}S_8$ and 67 μM $H^{13}CO_3$; 24 h incubation

Chemocline: 0.33 μM $^{15}NO_3$, 0.33 μM $^{34}S_8$ and 67 μM $H^{13}CO_3$; 12 h incubation

Sulfidic: 0.1 μM $^{15}NO_3$, 0.1 μM $^{34}S_8$ and 20 μM $H^{13}CO_3$; 24 h incubation

Whole-cell hybridization and laser microdissection microscopy

Round sections compatible with the NanoSIMS sample holder were stamped out of the polycarbonate filters without touching the filter surface intended for analysis. rRNA-targeted probe hybridizations were then performed according to standard protocols. SUP05 was identified using the specific gene probe GSO1032 together with the respective competitor (Glaubitz *et al.*, 2013). Because the fluorescence *in situ* hybridization (FISH) signals were too low, FISH was carried out using horseradish-peroxidase-labeled oligonucleotide probes and tyramide signal amplification, as described elsewhere (Pernthaler *et al.*, 2004), followed by counterstaining with propidium iodide. *Sulfurimonas* subgroup GD17 was identified using the specific FISH gene probe SUL90-Cy3 (Grote *et al.*, 2007). The formamide concentration of the hybridization buffer was 35%. Hybridization was performed at 46°C overnight, and counterstaining with SYBR Green I, propidium iodide or 4′,6-diamidin-2-phenylindol (DAPI).

Using the nonsense NonEUB probe, controls for non-specific hybridization were performed for the SUP05 CARD-FISH protocol as well as for the GD17 FISH protocol on samples from the cell count maxima in the suboxic and sulfidic zone respectively. Non-specific hybridizations were, with 0.32% of total cell counts using the SUP05 CARD-FISH protocol and 0.22% using the GD17-FISH protocol, negligible. The mean signal to noise ratio was 7.8, embedded in a range between 4.5 and 16.4.

SUP05 and GD17 total cell counts and laser marking of spots of interest were determined using a Leica LMD7000 microscope. Images of the marked spots as well as overview images of the whole filter were taken. If needed, the filters were stored at −20°C until NanoSIMS processing.

NanoSIMS measurements of single cells, image acquisition and data processing

SIMS imaging was performed using a NanoSIMS 50L instrument (Cameca, France) at the Leibniz-Institute for Baltic Sea Research Warnemünde (IOW). A $^{133}Cs^+$ primary ion beam was used to erode and ionize atoms of the sample. Among the received secondary ions, images of $^{12}C^-$, $^{13}C^-$, $^{12}C^{14}N^-$, $^{12}C^{15}N^-$, $^{32}S^-$ and $^{34}S^-$ were recorded simultaneously for cells inside the laser microdissectional (LMD)-marked regions using six mass detectors equipped with electron multipliers (Hamamatsu). The average mass resolving power (according to CAMECA definition) was 6110 which is sufficient to suppress interferences at all masses allowing, e.g. the separation of $^{12}C^{15}N^-$ from interfering ions such as $^{13}C^{14}N^-$. Prior to the analysis, sample areas of 50 × 50 μm were sputtered for 1 min with 600 pA to reach the steady state of secondary ion formation. The primary ion beam current during the analysis was 2–3 pA; the scanning parameters were 512 × 512 pixels for areas of 20–30 μm, with a dwell time of 250 μs per pixel. Up to 120 planes were accumulated.

The scans of each mass were accumulated and shift-corrected using the software Look@NanoSIMS (Polerecky *et al.*, 2012). The cells were defined as regions of interest (ROI) using the interactive threshold tool of the same software. To avoid artefacts or the misinterpretation of sulfur particles, a cell was defined based on a strong $^{12}C^{14}N$ signal, a lower ^{32}S signal and a cell-typical shape. Overlapping cells were avoided during the definition process to ensure only single-cell measurements. Isotope abundances for ^{13}C, ^{15}N and ^{34}S, as well as length–width ratios and top-view areas were calculated and exported for each cell. NanoSIMS images of the different isotope ratios were prepared as hue, saturation and intensity (HSI) images using the software ImageJ and the plug-in Open MIMS (Poczatek *et al.*, 2012).

Images of the marked spots taken with LMD were aligned and then correlated with the NanoSIMS images (aperture, rotation, mirroring), using the software GIMP2. Catalysed reporter deposition (CARD)-FISH-identified SUP05 were defined as SUP05 and the other cells as unidentified cells in SUP05 hybridizations (others, non-SUP05). FISH-identified *Sulfurimonas* subgroup GD17 cells and the other cells were similarly defined as GD17 and others (non-GD17) respectively.

Standard isotope abundances from each cell class and each zone were calculated based on unlabelled control parallels. Due to inadequate sample numbers, the individual ratios of SUP05 and non-SUP05 in the sulfidic zone and of GD17 and non-GD17 in the suboxic zone were averaged. Isotope enrichments of ^{13}C, ^{15}N and ^{34}S were calculated by subtracting the standard abundances from the individual cellular isotope abundances in the labelling experiment, resulting in percentage increases compared with the standard values (% of standard abundance).

Stable-isotope dilution effects during the FISH and CARD-FISH procedures (Musat *et al.*, 2014) could lead to underestimations of the impact of gene-probe-labeled bacteria on isotope enrichment, with a more pronounced dilution effect associated with the CARD-FISH procedure. In consequence, comparisons of cellular isotope enrichments generated after FISH or CARD-FISH procedures could only be performed for each of these procedures specifically. Thus, cellular SUP05 ^{13}C, ^{15}N and ^{34}S enrichments in comparison with the non-SUP05 cells were only generated from CARD-FISH analyses and, accordingly, *Sulfurimonas* GD17 in comparison with the non-GD17 from FISH analyses.

Cell volume calculation and correction of isotope abundances

Volumes were calculated for each cell on the basis of the NanoSIMS-exported top-view areas and the length–width ratios of the individual cells of the $^{12}C^{14}N$ signal. It was assumed that the cells were straight-sided rods with hemispherical ends or, in the case of a length–width ratio of 1, spheres. Because significant differences between cell

volumes of SUP05 and GD17 cells were detected in this study, measured cellular stable isotope ratios were not directly comparable anymore because larger cells need to enrich more of a labelled substrate to reach similar cellular mean isotope ratios than smaller cells. To take this effect into account, cellular isotope enrichments were multiplied by the individual cell volumes, resulting in a linear relationship of enrichments directly proportional to cell size. Similar but not identical approaches to the precise characterization of isotope enrichments have been described in other studies (Musat *et al.*, 2008; Thompson *et al.*, 2012; Foster *et al.*, 2013).

Calculation of the proportions of cellular isotope enrichment in the environment

Cellular isotope enrichment characteristics were calculated as follows: (1) Averaged cell volume adjusted isotope enrichments of SUP05 and GD17 cells were multiplied by the accordant cell number in the environment. (2) The ratio of the group-specific SUP05 or GD17-isotope enrichment was determined in comparison with the total cellular enrichments. (3) The enrichment proportion of the other unidentified cells was determined by subtracting the percentage of SUP05 from non-GD17 and that of GD17 from non-SUP05 ratios.

Statistical analyses

Significant differences between cell counts before and after the incubations as well as between cell volumes of the different cell classes were determined using the Kruskal–Wallis test included in the software IBM SPSS Statistics 20. Significant differences in the saturations of isotope abundances between enrichments incubated for 12 or 24 h in the preliminary culture experiments were determined using SigmaPlot 12.5 and the Mann–Whitney rank sum test.

Acknowledgements

References

Anantharaman, K., Breier, J.A., Sheik, C.S., and Dick, G.J. (2013) Evidence for hydrogen oxidation and metabolic plasticity in widespread deep-sea sulfur-oxidizing bacteria. *Proc Natl Acad Sci USA* **110:** 330–335.

Andrews, J.H., and Harris, R.F. (1986) *r*- and *K*-selection in microbial ecology. *Adv Microb Ecol* **9:** 99–147.

Axell, L.B. (1998) On the variability of Baltic Sea deepwater mixing. *J Geophys Res* **103:** 21667–21682.

Berg, C., Vandieken, V., Thamdrup, B., and Jürgens, K. (2015) Significance of archaeal nitrification in hypoxic waters of the Baltic Sea. *ISME J* **8:** 1319–1332.

Brettar, I., Labrenz, M., Flavier, S., Bötel, J., Kuosa, H., Christen, R., and Höfle, M.G. (2006) Identification of a *Thiomicrospira denitrificans*-like epsilonproteobacterium as a catalyst for autotrophic denitrification in the central Baltic Sea. *Appl Environ Microbiol* **72:** 1364–1372.

Brettar, I., and Rheinheimer, G. (1991) Denitrification in the central Baltic: evidence for H₂S-oxidation as motor of denitrification at the oxic-anoxic interface. *Microbial Ecol* **77:** 157–169.

Brüchert, V., Jørgensen, B.B., Neumann, K., Riechmann, D., Schlösser, M., and Schulz, H. (2003) Regulation of bacterial sulfate reduction and hydrogen sulfide fluxes in the central Namibian coastal upwelling zone. *Geochim Cosmochim Acta* **67:** 4505–4518.

Bruckner, C.G., Mammitzsch, K., Jost, G., Wendt, J., Labrenz, M., and Jürgens, K. (2013) Chemolithoautotrophic denitrification of epsilonproteobacteria in marine pelagic redox gradients. *Environ Microbiol* **15:** 1505–1513.

Campbell, B.J., Engel, A.S., Porter, M.L., and Takai, K. (2006) The versatile ε-proteobacteria: key players in sulphidic habitats. *Nat Rev Microbiol* **4:** 458–468.

Canfield, D.E., Stewart, F.J., Thamdrup, B., Brabandere, L., de, Dalsgaard, T., DeLong, E.F., *et al.* (2010) A cryptic sulfur cycle in oxygen-minimum-zone waters off the Chilean coast. *Science* **330:** 1375–1378.

Carini, P., Steindler, L., Beszteri, S., and Giovannoni, S.J. (2012) Nutrient requirements for growth of the extreme oligotroph 'Candidatus Pelagibacter ubique' HTCC1062 on a defined medium. *ISME J* **7:** 592–602.

Carstensen, J., Andersen, J.H., Gustafsson, B.G., and Conley, D.J. (2014) Deoxygenation of the Baltic Sea during the last century. *Proc Natl Acad Sci USA* **111:** 5628–5633.

Conley, D.J., Björck, S., Bonsdorff, E., Carstensen, J., Destouni, G., Gustafsson, B.G., *et al.* (2009) Hypoxia-related processes in the Baltic Sea. *Environ Sci Technol* **43:** 3412–3420.

Foster, R.A., Sztejrenszus, S., Kuypers, M.M.M., and Raven, J. (2013) Measuring carbon and N₂ fixation in field populations of colonial and free-living unicellular cyanobacteria using nanometer-scale secondary ion mass spectrometry. *J Phycol* **49:** 502–516.

Frey, C., Hietanen, S., Jürgens, K., Labrenz, M., and Voss, M. (2014) N and O isotope fractionation in nitrate during chemolithoautotrophic denitrification by *Sulfurimonas gotlandica*. *Environ Sci Technol* **48:** 13229–13237.

Friedrich, C.G., Bardischewsky, F., Rother, D., Quentmeier, A., and Fischer, J. (2005) Prokaryotic sulfur oxidation. *Curr Opin Microbiol* **8:** 253–259.

Fuchs, B.M., Woebken, D., Zubkov, M.V., Burkill, P.H., and Amann, R. (2005) Molecular identification of picoplankton populations in contrasting waters of the Arabian Sea. *Aquat Microb Ecol* **39:** 145–157.

Gasol, J.M., and Del Giorgio, P.A. (2000) Using flow cytometry for counting natural planktonic bacteria and understanding the structure of planktonic bacterial communities. *Sci Mar* **64:** 197–224.

Gasol, J.M., Zweifel, U.L., Peters, F., Fuhrman, J.A., and Hagström, Å. (1999) Significance of size and nucleic acid content heterogeneity as measured by flow cytometry in

natural planktonic bacteria. *Appl Environ Microbiol* **65:** 4475–4483.

Gilly, W.F., Beman, J.M., Litvin, S.Y., and Robison, B.H. (2013) Oceanographic and biological effects of shoaling of the oxygen minimum zone. *Annu Rev Mar Sci* **5:** 393–420.

Giovannoni, S.J., Cameron Thrash, J., and Temperton, B. (2014) Implications of streamlining theory for microbial ecology. *ISME J* **8:** 1553–1565.

Glaubitz, S., Kießlich, K., Meeske, C., Labrenz, M., and Jürgens, K. (2013) SUP05 dominates the gammaproteobacterial sulfur oxidizer assemblages in pelagic redoxclines of the central Baltic and Black Seas. *Appl Environ Microbiol* **79:** 2767–2776.

Grasshoff, K., Kremling, K., and Ehrhardt, M. (1999) *Methods of Seawater Analysis*. Weinheim, Germany: Wiley-VCH Verlag GmbH.

Grote, J., Jost, G., Labrenz, M., Herndl, G.J., and Jürgens, K. (2008) Epsilonproteobacteria represent the major portion of chemoautotrophic bacteria in sulfidic waters of pelagic redoxclines of the Baltic and Black Seas. *Appl Environ Microbiol* **74:** 7546–7551.

Grote, J., Labrenz, M., Pfeiffer, B., Jost, G., and Jürgens, K. (2007) Quantitative distributions of *Epsilonproteobacteria* and a *Sulfurimonas* subgroup in pelagic redoxclines of the central Baltic Sea. *Appl Environ Microbiol* **73:** 7155–7161.

Grote, J., Schott, T., Bruckner, C.G., Glöckner, F.O., Jost, G., Teeling, H., *et al.* (2012) Genome and physiology of a model *Epsilonproteobacterium* responsible for sulfide detoxification in marine oxygen depletion zones. *Proc Natl Acad Sci USA* **109:** 506–510.

Hawley, A.K., Brewer, H.M., Norbeck, A.D., Paša-Tolić, L., and Hallam, S.J. (2014) Metaproteomics reveals differential modes of metabolic coupling among ubiquitous oxygen minimum zone microbes. *Proc Natl Acad Sci USA* **111:** 11395–11400.

Jørgensen, B.B., Fossing, H., Wirsen, C.O., and Jannasch, H.W. (1991) Sulfide oxidation in the anoxic Black Sea chemocline. *Deep Sea Res A* **38:** S1083–S1103.

Jost, G., Zubkov, M.V., Yakushev, E., Labrenz, M., and Jürgens, K. (2008) High abundance and dark CO_2 fixation of chemolithoautotrophic prokaryotes in anoxic waters of the Baltic Sea. *Limnol Oceanogr* **53:** 14–22.

Labrenz, M., Brettar, I., Christen, R., Flavier, S., Botel, J., and Höfle, M.G. (2004) Development and application of a real-time PCR approach for quantification of uncultured bacteria in the central Baltic Sea. *Appl Environ Microbiol* **70:** 4971–4979.

Labrenz, M., Grote, J., Mammitzsch, K., Boschker, H.T.S., Laue, M., Jost, G., *et al.* (2013) *Sulfurimonas gotlandica* sp. nov., a chemoautotrophic and psychrotolerant *Epsilonproteobacterium* isolated from a pelagic redoxcline, and an emended description of the genus *Sulfurimonas*. *Int J Syst Evol Microbiol* **63:** 4141–4148.

Labrenz, M., Jost, G., and Jürgens, K. (2007) Distribution of abundant prokaryotic organisms in the water column of the central Baltic Sea with an oxic–anoxic interface. *Aquat Microb Ecol* **46:** 177–190.

Labrenz, M., Sintes, E., Toetzke, F., Zumsteg, A., Herndl, G.J., Seidler, M., and Jürgens, K. (2010) Relevance of a crenarchaeotal subcluster related to *Candidatus* Nitrosopumilus maritimus to ammonia oxidation in the suboxic zone of the central Baltic Sea. *ISME J* **4:** 1496–1508.

Lam, P., and Kuypers, M.M.M. (2011) Microbial nitrogen cycling processes in oxygen minimum zones. *Ann Rev Mar Sci* **3:** 317–345.

Lavik, G., Stührmann, T., Brüchert, V., van der Plas, A., Mohrholz, V., Lam, P., *et al.* (2009) Detoxification of sulphidic African shelf waters by blooming chemolithotrophs. *Nature* **457:** 581–584.

Marie, D., Partensky, F., Jacquet, S., and Vaulot, D. (1997) Enumeration and cell cycle analysis of natural populations of marine picoplankton by flow cytometry using the nucleic acid stain SYBR Green I. *Appl Environ Microbiol* **63:** 186–193.

Marshall, K.T., and Morris, R.M. (2013) Isolation of an aerobic sulfur oxidizer from the SUP05/Arctic96BD-19 clade. *ISME J* **7:** 452–455.

Musat, N., Halm, H., Winterholler, B., Hoppe, P., Peduzzi, S., Hillion, F., *et al.* (2008) A single-cell view on the ecophysiology of anaerobic phototrophic bacteria. *Proc Natl Acad Sci USA* **105:** 17861–17866.

Musat, N., Stryhanyuk, H., Bombach, P., Adrian, L., Audinot, J.-N., and Richnow, H.H. (2014) The effect of FISH and CARD-FISH on the isotopic composition of ^{13}C- and ^{15}N-labeled *Pseudomonas putida* cells measured by nanoSIMS. *Syst Appl Microbiol* **37:** 267–276.

Pernthaler, A., Pernthaler, J., and Amann, R. (2004) Section 3 update: sensitive multi-color fluorescence *in situ* hybridization for the identification of environmental microorganisms. In *Molecular Microbial Ecology Manual*. Kowalchuk, G.A., de Bruijn, F.J., Head, I.M., Akkermans, A.D.L., and van Elsas, J. D. (eds). Dordrecht [u.a.]: Kluwer Acad., pp. 2613–2627.

Pjevac, P., Kamyshny, A., Jr, Dyksma, S., and Mussmann, M. (2014) Microbial consumption of zero-valence sulfur in marine benthic habitats. *Environ Microbiol* **16:** 3416–3430.

Poczatek, C., Kaufman, Z., and Lechene, C. (2012) Open-MIMS ImageJ Plugin Guide. NRIMS: 1–18. http://nrims.harvard.edu/files/nrims/files/openmims-manual.pdf.

Polerecky, L., Adam, B., Milucka, J., Musat, N., Vagner, T., and Kuypers, M.M.M. (2012) Look@NanoSIMS – a tool for the analysis of nanoSIMS data in environmental microbiology. *Environ Microbiol* **14:** 1009–1023.

Roslev, P., Larsen, M.B., Jørgensen, D., and Hesselsoe, M. (2004) Use of heterotrophic CO_2 assimilation as a measure of metabolic activity in planktonic and sessile bacteria. *J Microbiol Methods* **59:** 381–393.

Schippers, A., and Jørgensen, B.B. (2002) Biogeochemistry of pyrite and iron sulfide oxidation in marine sediments. *Geochim Cosmochim Acta* **66:** 85–92.

Schmale, O., Blumenberg, M., Kießlich, K., Jakobs, G., Berndmeyer, C., Labrenz, M., Thiel, V. and Rehder, G. (2012) Aerobic methanotrophy within the pelagic redoxzone of the Gotland Deep (central Baltic Sea). *Biogeosciences* **9:** 4969–4977.

Schulz, H.N., and Jørgensen, B.B. (2001) Big bacteria. *Ann Rev Microbiol* **55:** 105–137.

Schut, F., Prins, R.A., and Gottschal, J.C. (1997) Oligotrophy and pelagic marine bacteria: facts and fiction. *Aquat Microb Ecol* **12:** 177–202.

Shah, V., Chang, B.X., and Morris, R.M. (2017) Cultivation of a chemoautotroph from the SUP05 clade of marine bacteria that produces nitrite and consumes ammonium. *ISME J* **11:** 263–271.

Shah, V., and Morris, R.M. (2015) Genome sequence of "Candidatus Thioglobus autotrophica" strain EF1, a chemoautotroph from the SUP05 clade of marine gammaproteobacteria. *Genome Announc* **3:** e01156–15.

Stevens, H., and Ulloa, O. (2008) Bacterial diversity in the oxygen minimum zone of the eastern tropical South Pacific. *Environ Microbiol* **10:** 1244–1259.

Stewart, F.J. (2011) Dissimilatory sulfur cycling in oxygen minimum zones: an emerging metagenomics perspective. *Biochem Soc Trans* **39:** 1859–1863.

Stocker, R. (2012) Marine microbes see a sea of gradients. *Science* **338:** 628–633.

Stramma, L., Johnson, G.C., Sprintall, J., and Mohrholz, V. (2008) Expanding oxygen-minimum zones in the tropical oceans. *Science* **320:** 655–658.

Stramma, L., Prince, E.D., Schmidtko, S., Luo, J., Hoolihan, J.P., Visbeck, M., *et al.* (2011) Expansion of oxygen minimum zones may reduce available habitat for tropical pelagic fishes. *Nat Clim Chang* **2:** 33–37.

Sunamura, M., Higashi, Y., Miyako, C., Ishibashi, J.-I., and Maruyama, A. (2004) Two bacteria phylotypes are predominant in the Suiyo seamount hydrothermal plume. *Appl Environ Microbiol* **70:** 1190–1198.

Taylor, G.T., Iabichella, M., Ho, T.-Y., Scranton, M.I., Thunell, R.C., Muller-Karger, F.E., and Varela, R. (2001) Chemoautotrophy in the redox transition zone of the Cariaco Basin: a significant mid-water source of organic carbon production. *Limnol Oceanogr* **46:** 148–163.

Thompson, A.W., Foster, R.A., Krupke, A., Carter, B.J., Musat, N., Vaulot, D., *et al.* (2012) Unicellular cyanobacterium symbiotic with a single-celled eukaryotic alga. *Science* **337:** 1546–1550.

Walsh, D.A., Zaikova, E., Howes, C.G., Song, Y.C., Wright, J.J., Tringe, S.G., *et al.* (2009) Metagenome of a versatile chemolithoautotroph from expanding oceanic dead zones. *Science* **326:** 578–582.

Zaikova, E., Walsh, D.A., Stilwell, C.P., Mohn, W.W., Tortell, P.D., and Hallam, S.J. (2010) Microbial community dynamics in a seasonally anoxic fjord: Saanich Inlet, British Columbia. *Environ Microbiol* **12:** 172–191.

Zubkov, M.V., Tarran, G.A., and Burkill, P.H. (2006) Bacterioplankton of low and high DNA content in the suboxic waters of the Arabian Sea and the Gulf of Oman: abundance and amino acid uptake. *Aquat Microb Ecol* **43:** 23–32.

Supporting information

Additional Supporting Information may be found in the online version of this article at the publisher's web-site:

Fig. S1. Cell numbers within the Gotland Deep redox zone and after stable isotope labeled substrate incubation. Cell numbers in the environment show typical overlapping abundance gradients of SUP05 and GD17. Total cell numbers were determined by flowcytometrical cell counting and the proportions of SUP05 by CARD-FISH and of GD17 by FISH, whereas unidentified cells (others) were calculated by subtracting the average cell numbers of SUP05 and GD17 from the average total cell number. Error bars indicate the standard deviation.
Cell numbers after individual incubation times and substrate concentrations show low stimulated conditions. Determination of cell numbers after incubations occurred analogously to the environmental samples. Error bars indicate the standard deviation of three independent replicates.

Fig. S2. Individual cell volume adjusted ^{13}C, ^{15}N and ^{34}S enrichment (%) of SUP05 and *Sulfurimonas* GD17 cells with a higher isotope ratio than the unlabeled controls. Percentage drawings show proportion of cells of the particular group with a positive enrichment.

Fig. S3. Average percentages of GD17, SUP05 and unidentified cells (others) on total cells (Cells bar) and on cellular ^{13}C, ^{15}N and ^{34}S enrichment on total isotope enriched cells (^{13}C-, ^{15}N- and ^{34}S-bar shows). Visible is a high activity of SUP05 in the suboxic zone and a high activity of GD17 in the sulfidic zone and the chemocline, except for ^{34}S enrichment.

Fig. S4. Position of the sampling station within the Eastern Gotland Deep of the Baltic Sea. Lines indicate deep basins of the Baltic Sea as depth contours. Modified after Schmale *et al.*, (2012)

Fig. S5. ^{13}C, ^{15}N and ^{34}S abundances in cells of *Sulfurimonas gotlandica* strain GD1^{T} after 12 and 24 hours of incubation with ^{13}C bicarbonate, ^{15}N nitrate and ^{34}S elemental sulfur. The incubation time had no effect on the saturation of the ^{13}C and ^{34}S abundance ($\alpha = 0.426$; $\alpha = 0.668$) and the ^{15}N abundance showed significant differences between the two incubation times ($\alpha = 0.003$) but no further saturation.

Table S1. Number of measured parallels, spots, and cells of the stable isotope labelled substrate experiments. Others, unidentified cells.

Table S2. Number of measured parallels, spots, and cells of the unlabelled stable isotope substrate experiments. Others, unidentified cells.

Table S3. NanoSIMS based cell volumes and Length-Width ratios of single cells of SUP05 and GD17 in the particular zones indicate higher average biovolumes of GD17 than SUP05 in all zones. A: suboxic zone; B: chemocline; C: sulfidic zone.

Table S4. Overview of the sulfidic conditions in the global distributed environments of SUP05.

Table S5. Overview of the sulfidic conditions in the global distributed environments of *Sulfurimonas* subgroup GD17 and *Sulfurimonas gotlandica* strain GD1^{T}.

2.1.1 What ecological strategies are followed by the key microbial players in pelagic redox zones of the Baltic Sea?

Based on a definition by Andrews and Harris (1986), K-strategists require low substrate concentrations to support slower growth rates, whereas r-strategists are depending on comparably higher substrate concentrations to support rapid growth rates. In addition, the streamlining theory defines successful oligotrophic (or here oligocarbophilic) cells in substrate-limiting environments as compact in size, non-motile, and exhibiting a small genome (Stocker 2012; Giovannoni *et al.* 2014).

To investigate the uptake behavior of *Sulfurimonas* GD17 and SUP05, we performed a non-stimulating incubation experiment of environmental samples from three zones of the Gotland Deep redox zone using stable isotope labelled substrates (Paper I). ^{13}C-labelled bicarbonate was used for direct carbon assimilation measurements, whereas ^{15}N-labelled nitrate and ^{34}S-labelled elemental sulfur served as proxies for nitrate reduction and sulfur oxidation. We identified *Sulfurimonas* GD17 via fluorescent *in situ* hybridization (FISH) and SUP05 via catalyzed reporter deposition FISH (CARDFISH) and determined total cell counts flowcytometrically. Laser microdissection microscopy (LMD) was used for cell identification and marking, which was followed by NanoSIMS analyses of labelled samples and unlabelled controls, and the calculation of biovolume corrected ^{13}C, ^{15}N, and ^{34}S abundances. The latter was of special importance due to significant cell volume differences of both investigated organisms and the qualitative nature of SIMS measurements. Detailed methods including references and all calculations are presented in Paper I.

Together with studies on the recently isolated representative of GD17 (*Sulfurimonas gotlandica* strain GD1^{T}; (Labrenz *et al.* 2013)), and the literature, I drew a picture of ecological niche separation with SUP05 representing a streamlined K-strategist and *Sulfurimonas* GD17 being a specialized r-strategist: Streamlined SUP05 organisms were characterized by a small cell and genome size and were omnipresent in oxygen minimum zones worldwide. The organism was adapted to low electron donor concentrations, and uptake of the substrate occurred relatively slowly when both redox compounds were available. If one compound was not available, non-motile SUP05 had the genomic potential to switch to other metabolic pathways. SUP05 followed the same ecological strategy in global oxygen minimum zones as *Pelagibacter ubique* in the oxygenated ocean (Carini *et al.* 2012), the K-strategy. The r-strategic *Sulfurimonas* subgroup GD17, on the other hand, was able to adapt to permanently or seasonally sulfidic waters with higher sulfide concentrations and enriched

substrates significantly faster than SUP05. The cells were motile and able to identify favorable ecological niches chemotactically (Grote *et al.* 2012). Moreover, they actively modified conditions in their surroundings by scavenging oxygen to establish anoxic conditions and were thus able to withstand oxygen intrusions (Frey *et al.* 2014). Their cell size was above average (Schulz and Jørgensen 2001) and they had one of the largest epsilonproteobacterial genomes discovered so far (2.95 Mb), which suggested a potentially enhanced metabolic versatility (Grote *et al.* 2012). Thus, *Sulfurimonas* GD17 could be characterized as fast reacting, able to sense chemical gradients and as a mobile organism in Baltic Sea redox zones. Together, both organisms drove an efficient detoxification machinery on top of the pelagic sulfidic zone of the Baltic Sea.

Possible methodical biases within the experimental design of Paper I were element transfers to other cells, due to cell lysis, and enrichment dilution effects caused by sample treatment (i.e. FISH and CARDFISH), which could have led to underestimations of isotope enrichments by *Sulfurimonas* GD17 and SUP05. Moreover, a dilution of the ^{15}N signal by the uptake of ammonia in the interface or sulfidic zone by both investigated groups could be assumed (Labrenz *et al.* 2010; Shah *et al.* 2017).

SUP05 and *Sulfurimonas* GD17 cells were the most prominent bicarbonate-, nitrate- and sulfur-incorporating organisms in this study, but a high percentage of stable-isotope-enrichment was incorporated by phylogenetically unidentified cells. I postulated, that other organsims, such as *Thaumarchaea* could have been responsible for a substantial ^{13}C incorporation proportion in the suboxic zone (Berg *et al.* 2015). Also alternative pathways, such as dissimilatory nitrate reduction to ammonium, anaplerotic CO_2 fixation (Roslev *et al.* 2004), or aerobic sulfide oxidation (Friedrich *et al.* 2005) could be of importance and remained to be discovered in Baltic Sea redox zones. Furthermore, the observation, that measured cellular N- and S- enrichments were on a similar level as C-enrichment due to CO_2 fixation suggested intracellular storage of S- and N-compounds, and might have been an interesting topic for further investigations.

A subsequent study on the recently isolated representative of the *Sulfurimonas* GD17 subgroup, *Sulfurimonas gotlandica* strain GD1^T, completed the picture of a highly specialized r-strategist (Paper A1). Scanning transmission electron microscopy coupled to electron dispersive X-ray analyses (STEM-EDX) and growth experiments within redox gradients demonstrated energy storage behavior of this organism: In case of low nitrate concentration, *Sulfurimonas* GD17 chemotactically moved towards nitrate-richer environments using its

flagellum fueled by intra-cellular polyphosphate reserves. When *Sulfurimonas* GD17 reached adequate substrate conditions, it gained energy and replenished polyphosphate storage for future deficiency scenarios (Fig. 4).
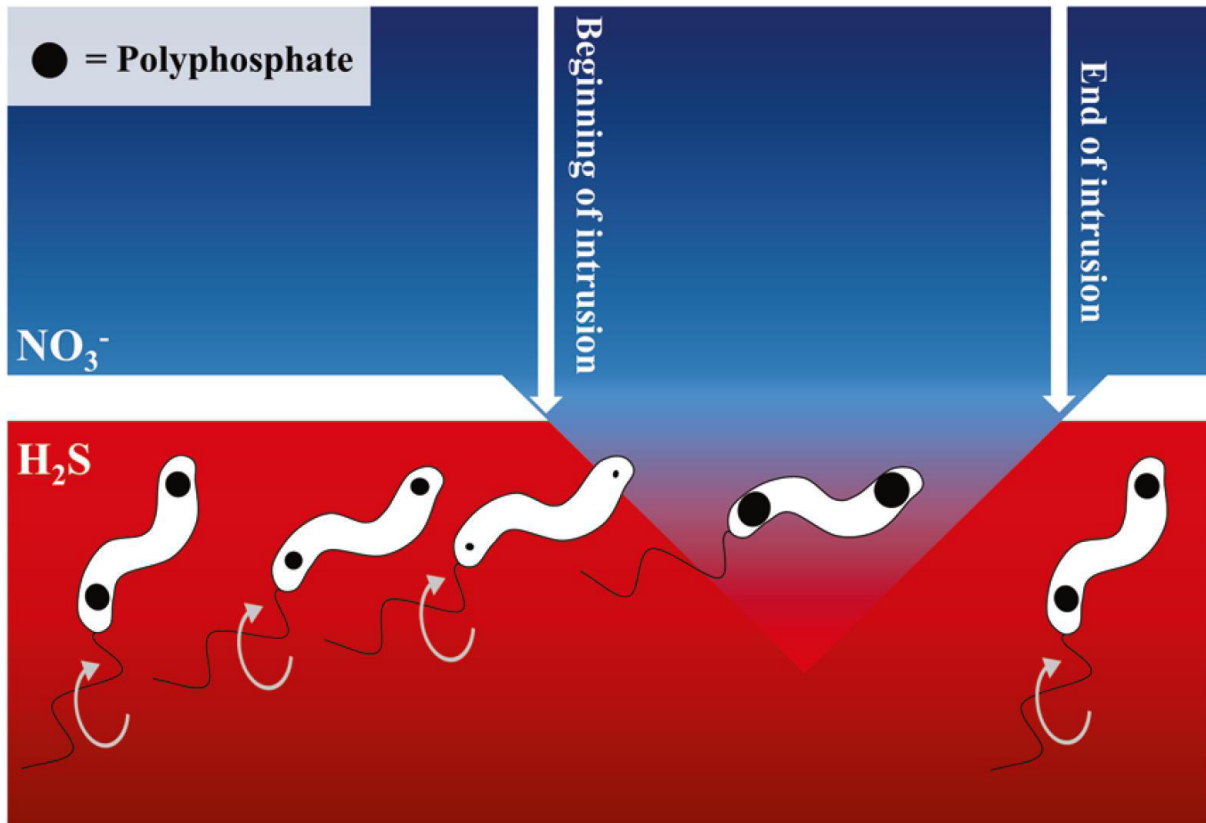
Figure 4: Behavior of *Sulfurimonas* GD17 in redox zones exemplified by the isolated representative *Sulfurimonas gotlandica* strain GD1[T]. Mixing events, such as micro-scale intrusions, create zones where suitable electron acceptors (NO_3) and electron donors (H_2S) co-localize. Under these optimal conditions, cells accumulate polyphosphate, using it as an energy source to sustain cellular integrity and to enable motility to new favorable zones (The figure was modified from Paper AI).

How such highly specialized organisms once colonized the pelagic Baltic Sea redox zone in an otherwise oxygenated ocean remains unclear. However, there is evidence that crustaceans may act as vectors for anaerobic microorganisms. Their gut can be seen as a mobile anoxic microenvironment for obligatory anaerobic bacteria, which are unviable in the oxygenated water column (e.g. Tang *et al.* 2011; Proctor 1997). With the excretion of rapidly sinking fecal pellets, those microbes could be distributed until they reach adequate conditions for the colonization of a new habitat. Microbial detachment from particles into the sulfidic waters could be promoted by particle retention at density interfaces (Prairie *et al.* 2015), such

as those associated with redox zones (e.g. Jakobs *et al.* 2013). It is therefore possible that microbes attached to settling fecal pellets act as a seeding community for pelagic sub- and anoxic environments. However, we still know little about the structures of such particle micro-zones, or the frequency of interactions between free-living and aggregate-associated microbial communities.

2.2 Towards a better understanding of aggregate-associated microbial assemblages

Strong redox gradients are not necessarily limited to oxygen depleted water columns or sediments. They may also occur at the micro-scale everywhere in the ocean within complex porous organic particles such as fecal pellets or marine snow (Bianchi *et al.* 2018; Bristow 2018). The presence of sub- or anoxic microenvironments in particles has been postulated in several early studies (Gowing and Silver 1983; Paerl and Pinckney 1996), but extensive investigations of such micro-zones within structurally undisturbed particles are currently lacking. The results of Paper I and Paper AI clearly demonstrate the tremendous opportunities provided by small-scale within-particle investigations for gaining new knowledge about fundamental processes in microbial ecology and element cycling. Phylogenetic identification approaches, such as FISH, in combination with single-cell element analyses, such as nano-scale secondary ion mass spectrometry (NanoSIMS) or electron dispersive X-ray (EDX) analyses, combine diversity and activity investigations and have been applied to free-living organisms in various studies (e.g. Milucka *et al.* 2012; Musat *et al.* 2012; Krupke *et al.* 2013). The special physical properties of sinking particles, i.e. their fragile nature, will lead to sample loss and the destruction of the three-dimensional structure without specialized handling techniques, which prevented such analyses so far. Here I present two methods, developed in close collaboration with Clara Flintrop, which enable detailed investigations on the internal microbial ecology and activity within particles.

2.2.1 Enabling small-scale investigations within sinking particles

Exopolymeric substances, such as polysaccharides or proteins, and other structural compounds make up the matrix of aggregates and play a central role for microbial activity. Alcian Blue stainable polysaccharides (transparent exopolymeric particles; TEP) and Coomassie Blue stainable proteins (Coomassie Blue stainable particles; CSP) provide nutrients for microorganisms (Busch *et al.* 2017), which results in increased respiration rates (Iversen and Ploug 2010). Moreover, those compounds can prevent advection so that mass transport into some denser areas is driven by slower diffusion (Ploug and Passow 2007). This combination of impacts may result in decreased oxygen concentrations within particles and the need for alternative electron acceptors, and hence anaerobic metabolism in some micro-zones of a particle as postulated by e.g. Gowing and Silver (1983).

More recent molecular investigations found, indeed, evidence for particle-associated anammox bacteria (Woebken *et al.* 2007) and nitrogen reducers (Ganesh *et al.* 2013; Smith *et al.* 2013) in oxygenated and suboxic waters. Moreover, nitrogen based respiration could be measured outside anoxic waters (Michotey and Bonin 1997; Wolgast *et al.* 1998; Kalvelage *et al.* 2011), and there is also evidence for sulfur based metabolism in nitrate rich waters (Canfield *et al.* 2010; Carolan and Beman 2015) or even in vast oxygenated regions (Swan *et al.* 2011). Where these organisms originate and how they colonize aggregates, as well as their potential association strategy, is still unknown. Some investigations on the spatial distribution of microorganisms, i.e. based on confocal microscopy, have been performed before (e.g. Waite *et al.* 2000). However, the fragile nature of aggregates has prevented precise microscopic investigations within intact aggregates, including structural staining, as well as modern single-cell identification approaches, such as FISH. The utilization of the latter would allow new insights into the spatial distribution of specific microbes within aggregates, but also about the colonization strategies and microbial associations, analogously to benthic consortia as documented by McGlynn *et al.* (2015).

To overcome this analytical limitation, we developed an optimized method for the embedding and slicing of particles in cryogel. Cryogel is a vinyl alcohol based embedding matrix, which is in liquid state at room temperature and freezes without forming crystals or changing volume at temperatures below 0 °C. It preserves the collected aggregates without altering their physical structure and allows various structural and phylogenetic staining approaches and the utilization in sediment traps *in situ* (Paper II).

PAPER II

Embedding and slicing of intact in situ collected marine snow

Clara M. Flintrop [iD],[1,2]* Andreas Rogge [iD],[1] Sebastian Miksch,[3] Stefan Thiele,[4] Anya M. Waite [iD],[1,5]
Morten H. Iversen [iD][1,2]*

[1]Alfred Wegener Institute for Polar and Marine Research, Bremerhaven, Germany
[2]MARUM and University of Bremen, Bremen, Germany
[3]Max-Planck-Institute for Marine Microbiology, Bremen, Germany
[4]Institute for Inorganic and Analytical Chemistry, Friedrich Schiller University, Jena, Germany
[5]FB2 Chemistry/Biology, University of Bremen, Bremen, Germany

Abstract

The biological carbon pump is largely driven by the formation and sinking of marine snow. Because of their high organic matter content, marine snow aggregates are hotspots for microbial activity, and microbial organic matter degradation plays an important role in the attenuation of carbon fluxes to the deep sea. Our inability to examine and characterize microscale distributions of compounds making up the aggregate matrix, and of possible niches inside marine snow, has hindered our understanding of the basic processes governing marine carbon export and sequestration. To address this issue, we have adapted soft-embedding and sectioning to study the spatial structure and components of marine aggregates at high resolution. Soft-embedding enables rapid quantitative sampling of undisturbed marine aggregates from the water column and from sediment traps, followed by spatially resolved staining and characterization of substrates of the aggregate matrix and the microorganisms attached to it. Particular strengths of the method include in situ embedding in sediment traps and successful fluorescence in situ hybridization (FISH)-probe labeling, supporting studies of microbial diversity and ecology. The high spatial resolution achieved by thin-sectioning of soft-embedded aggregates offers the possibility for improved understanding of the composition and structure of marine snow, which directly influence settling velocity, microbial colonization and diversity, degradation rates, and carbon content. Our method will help to elucidate the small-scale processes underlying large-scale carbon cycling in the marine environment, which is especially relevant in the context of rising anthropogenic CO_2 emissions and global change.

The world's oceans play a key role in the global carbon cycle because of their capacity to act as active carbon sinks (Passow and Carlson 2012; Ciais et al. 2014). There is an annual flux of 80 Pg C from the atmosphere to the ocean, of which 0.1 Pg C are exported to the deep sea where carbon is sequestered over timescales of $\geq 10^3$ yr (IPCC 2013). A central mechanism modulating marine carbon sequestration is the large-scale export of organic matter to the dark ocean via the Biological Carbon Pump: phytoplankton fix dissolved inorganic carbon through photosynthesis and, upon sinking, remove carbon from the euphotic zone in the form of particulate organic carbon (POC). Vertical carbon flux is dominated by zooplankton fecal pellets and aggregated organic matter, which together result in an estimated flux of $\sim$ 0.04 Pmol C yr^{-1} (Honjo et al. 2008). Once aggregates are larger than 500 μm in diameter they are collectively called "marine snow" (Alldredge and Silver 1988). Zooplankton grazing and microbial degradation of marine snow are largely responsible for the attenuation of carbon flux to the deep sea, respiring and consuming $\geq$ 97% of carbon fixed in the surface ocean (Turner 2015).

Despite the important role of marine snow in the marine carbon cycle, the in situ processes and mechanisms underlying colonization and degradation by heterotrophic microorganisms on a sub-aggregate level are relatively unexplored. There are two main reasons for this: (1) the difficulty of sampling undisturbed particles in situ, particularly at depths in the water column where aggregate collection by scuba diving is not possible, and (2) their intricate three-dimensional (3D) structure and composition, which create a heterogeneous habitat with several micro-niches. As a result, microbial colonization and degradation vary in space and intensity both

*Correspondence: clara.flintrop@awi.de; morten.iversen@awi.de

Table 1. Oligonucleotide probes used in this study with specified target organism, oligonucleotide sequence, formamide (FA) concentration in hybridization buffer, and FISH method(s) the probe was used with (mono-FISH, CARD-FISH and/or Mil-FISH).

Probe	Target	Sequence (5′–3′)	FA (%)	FISH method
EUB338	Most bacteria	GCTGCCTCCCGTAGGAGT	35	mono, CARD, MiL
EUB II	Planctomycetes	GCAGCCACCCGTAGGTGT	35	mono, CARD, MiL
EUB III	Verrucomicrobiales	GCTGCCACCCGTAGGTGT	35	mono, CARD, MiL
CF319a	Bacteroidetes	TGGTCCGTGTCTCAGTAC	35	CARD
ALT1413	Alteromonas/Colwellia	TTTGCATCCCACTCCCAT	40	CARD
SYN405	Synechococcus	AGAGGCCTTCATCCCTCA	30	CARD
NON338	Control	ACTCCTACGGGAGGCAGC	35	mono, CARD, MiL

between and within aggregates, and information about biogeochemical processes and microbial interactions is lost without the means to study marine snow at sub-aggregate resolution. Solid, dense material regularly makes up less than 1% of the aggregate volume (Ploug et al. 2008) and consists of a variety of organic and inorganic matter including phytoplankton, fecal pellets, phyto- and zoo-detritus, and ballasting minerals like airborne dust, biominerals, and silt from glaciers (Alldredge and Silver 1988; Ransom et al. 1998; Van der Jagt et al. 2018). How tightly these solids are packed affects the porosity of marine snow, which in turn affects settling behavior and carbon remineralization (Ploug et al. 2008; Iversen and Ploug 2010). In addition to the solid fraction, marine aggregates contain high amounts of extracellular polymeric substances (EPS) including transparent exopolymer particles (TEP). TEP are defined as discrete particles that consist predominantly of surface-active acidic polysaccharides and are stained by Alcian Blue (Alldredge et al. 1993). They can exert significant control over carbon export due to their sticky nature and molecular composition, which influence aggregation dynamics and aggregate buoyancy (Mari et al. 2017). TEP have also been proposed to render aggregates impermeable due to clogging of aggregate pore space (Ploug and Passow 2007). While there is a widely used method to quantify TEP spectrophotometrically (Passow and Alldredge 1995), no method currently exists to assess the spatial distribution and extent of pore space reduction and clogging caused by different fractions of EPS.

Organic matter distribution and quality are tightly interlinked with microbial colonization of aggregates. Bacterial abundance, diversity, enzymatic activity, and carbon respiration per volume aggregate are higher than in the surrounding water column due to increased substrate availability (Alldredge and Gotschalk 1990; DeLong et al. 1993; Smith et al. 1992; Ploug and Grossart 2000; D'Ambrosio et al. 2014). Krupke et al. (2016) showed how quorum sensing can regulate enzymatic activity and POC degradation in sinking aggregates, suggesting that the positioning and connectivity of microbial clusters within aggregates is an important determinant of microbial activity. This further corroborates the importance of studying the spatial distribution of solid

material and EPS/TEP, especially in relation to the localization of heterotrophic microorganisms, to better understand the microbial ecology and small-scale degradation dynamics of marine snow. Advances in the in situ collection of marine snow, e.g., by using a Marine Snow Catcher (MSC; Riley et al. 2012) or sediment traps containing gel-filled collection cups (first proposed by Lundsgaard 1995), have made it possible to non-destructively sample individual aggregates, but the spatial distribution of matter and cells inside aggregates remains obscure without the means to preserve their 3D structure during staining and microscopy.

Published works exploring aggregates that were structurally preserved include studies of the structure and colonization of resin-embedded, microtome-sectioned marine aggregates using Transmission Electron Microscopy (Heissenberger et al. 1996; Leppard et al. 1996), confocal laser scanning microscopy (CLSM) of whole marine aggregates (Holloway and Cowen 1997; Waite et al. 2000), riverine aggregates (Neu 2000; Böckelmann et al. 2002) and microtome-sectioned sludge aggregates (Chu et al. 2004), and cryosectioning of riverine aggregates (Luef et al. 2009a,2009b). To study the 3D structure of marine snow with special regard to the localization of matrix components and microbial colonizers, we have developed cryosectioning of gel-embedded, in situ collected marine snow. This approach is suited for rapid subsampling of aggregates collected in situ using sediment trap gels, and for probing of aggregates with bioactive markers such as FISH. We present a modular workflow that enables spatially resolved visualization of individual aggregates and their components, and will advance the study of small-scale processes governing microbial assemblages in marine snow and their connection to carbon cycling in the marine environment.

Materials and procedures

The workflow is divided into (1) aggregate collection, (2) aggregate embedding and sectioning, (3) visualization and imaging of the aggregate matrix, including staining of EPS, 3D-reconstruction, and assessment of aggregate porosity, and (4) visualization of aggregate colonizers, including nucleic
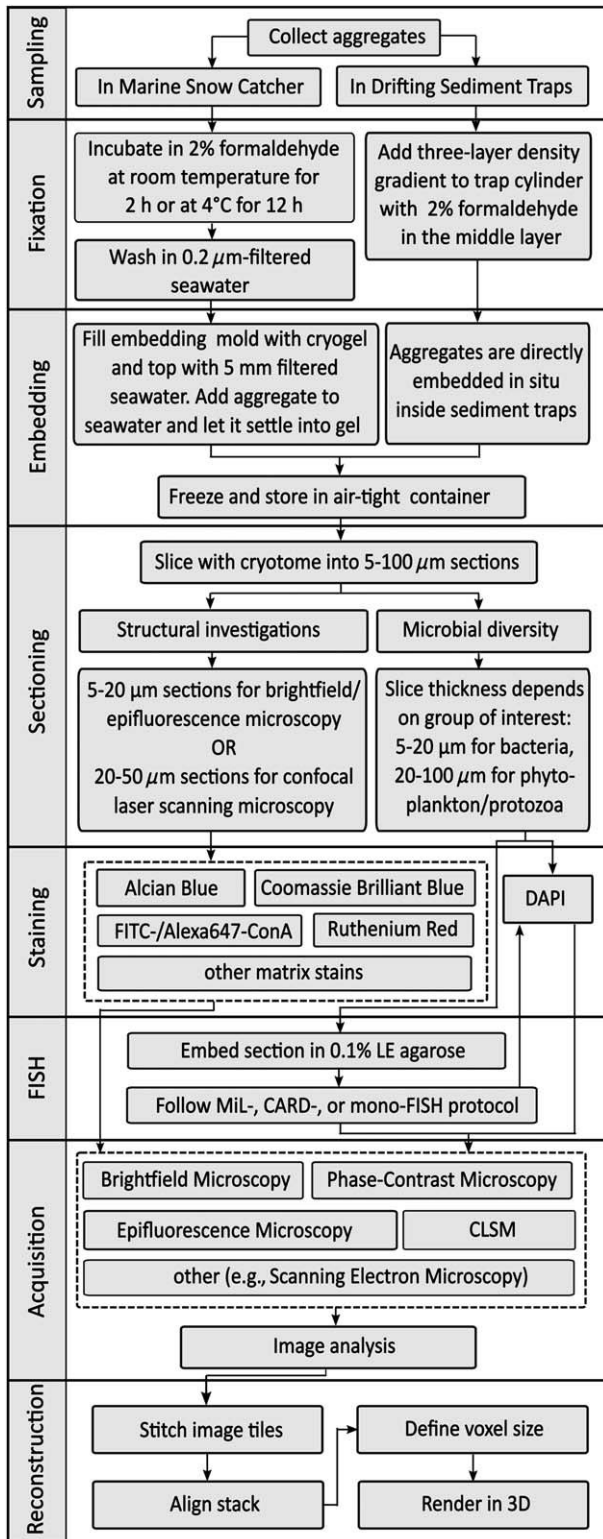
Fig. 1. Work flow of soft-embedding method. Boxes framed by dashed lines denote a "mix-and-match" process depending on the targeted substrate and the required imaging technique. The order in which staining and FISH are carried out depends on the FISH method used. Please refer to "Materials and procedures" section for details.

acid (DAPI) staining and probing of selected bacterial clades using FISH. Please refer to the accompanying flow chart (Fig. 1) for a step-by-step breakdown of the procedures involved.

Sample collection

Samples were collected during the research cruises POS495 and POS508 (RV *Poseidon*) to Cape Blanc, Mauretania in 2016/2017, and DY050 (RRS Discovery) to the Porcupine Abyssal Plain observatory in 2016, using a Marine Snow Catcher and free-drifting sediment traps containing gel-filled collection cups. The MSC was lowered to a chosen depth and closed using a drop weight. Back on deck, aggregates contained in the 100 L volume of seawater were left to settle for any desired amount of time (≤ 2 h for fast-settling particles, longer for a broader range of particles). Hereafter, the water in the top part of the MSC was gently drained and the base of the MSC containing the sedimented aggregates was removed.

For passive handling and to collect samples over depth and time, drifting sediment traps containing gel-filled collection cups were deployed (Fig. 2a). Prior to deployment, one 1 m-long trap cylinder per depth was fitted with a collection cup containing 200 ml of frozen Tissue-Tek® O.C.T.™ Compound (Sakura FineTek; from here on referred to as "Tissue-Tek" or "cryogel") (Wiedmann et al. 2014; Thiele et al. 2015). Tissue-Tek is a viscous transparent cryogel and was selected as the embedding medium to allow a slow diffusive exchange of pore water with the cryogel during settling. To allow for analysis of the microbial community with FISH, a three-layer salinity gradient containing 2% v/v formaldehyde solution (diluted from 37% formaldehyde solution with filtered seawater) in the middle layer was added to each tube by dissolving different concentrations of sodium chloride (2‰, 4‰, or 6‰) in GF/F filtered seawater (*see* Thiele et al. 2015 for a detailed description of the in situ fixation method). The cylinders were suspended gyroscopically at depths of 100 m, 200 m, and 400 m, and any aggregates settling directly into the trap cylinders were first fixed with 2% formaldehyde, then washed in the lower and densest water layer before they settled into the gel, where they were recovered after 24 h (Fig. 2b). Prior to removing the gel cup, aggregates contained in the trap cylinder were left to settle for 6–12 h (depending on the height of the trap tube) to ensure that slow-settling particles would also be embedded in the gel. Gel cups were photographed at high magnification (Fig. 2c,d) and stored at −20°C until further processing.

Embedding and slicing

Aggregates picked from the detached base of the MSC were transferred to a disposable embedding mold (22 × 22 × 20 mm) containing Tissue-Tek with a wide-bore pipette. To maximize structural preservation, aggregates were not added directly to the gel, but to an approximately 5 mm thick layer of filtered seawater added on top, and left to settle into the
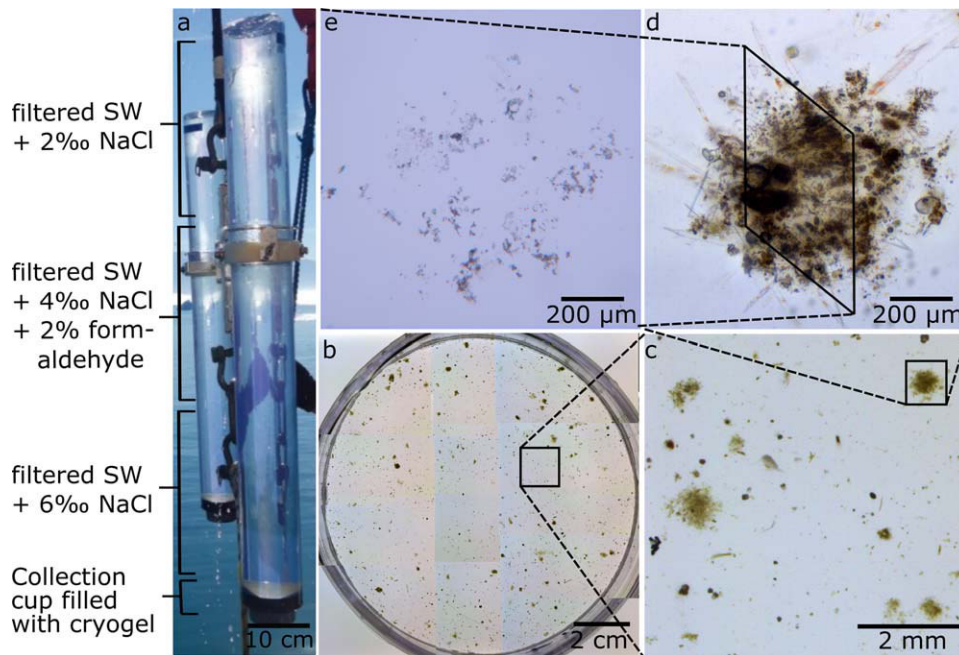
Fig. 2. Collecting and embedding marine snow in situ (counter-clockwise). (**a**) annotated sediment trap cylinder (SW = seawater; NaCl = sodium chloride); (**b**) top view of gel collection cup with in situ embedded aggregates; (**c**) close-up of the gel cup; (**d**) microscopic image of gel-embedded aggregate; (**e**) 10 μm thin-section of in situ embedded aggregate.

gel. Prior to freezing, the position of the aggregate was marked to facilitate the localization of the sample when mounted on the cryotome.

Aggregates embedded in situ in the drifting traps were cut out directly from the frozen collection cup using a small corer. The frozen embedded samples were mounted on a CM-3050S cryostat (Leica Biosystems). Knowing the position of the embedded aggregate, the block containing the sample was cut to size with a razor blade for better handling. Using an object temperature of $-30°C$ and a chamber temperature of $-35°C$, samples were cut into sections ranging from 5 μm to 100 μm (Fig. 2e). Immediately after cutting, sections were mounted on Superfrost^{TM} Plus slides (ThermoFisher Scientific) and stored at 4°C for short-term processing (within weeks) or at $-20°C$ for longer-term storage (months to years). For microscopic examination, sections were embedded in mounting medium made up of 80% (v/v) Citifluor AF1 (Electron Microscopy Sciences) and 20% (v/v) Vectashield (Vector Laboratories) and covered with a cover slip (ThermoFisher Scientific). The cover slip was sealed with nail polish to avoid smearing the underlying sample.

Visualization and imaging of the aggregate matrix
Staining of EPS
To visualize the EPS matrix, we stained aggregate sections with dyes commonly used for marine snow such as Alcian Blue and Coomassie Brilliant Blue and tested dyes targeting different EPS fractions, including Ruthenium Red, Periodic Acid Schiff-base stain, and the fluorophore-conjugated lectin stain

Concanavalin A. Acidic polysaccharides were stained with 0.2 μm-filtered 0.02% Alcian Blue (Sigma-Aldrich) dissolved in 0.06% (v/v) acetic acid (pH 2.5) for 5 s and washed with ultrapure water (UPW; Passow and Alldredge 1995; Long and Azam 1996). A-mannopyranosyl- and α-glucopyranosyl residues of other EPS fractions were targeted with Concanavalin A conjugated with FITC (FITC-ConA; Sigma-Aldrich) or Alexa647 (Alexa647-ConA; Life Technologies) dissolved in 0.3% NaCl was tested at concentrations ranging from 100 μg/mL to 1000 μg/mL (after Uthicke et al. 2009). Proteinaceous particles were stained with Coomassie Brilliant Blue (Sigma-Aldrich). Proteins were stained with 0.2 μm-filtered 0.04% (w/v) Coomassie Brilliant Blue G-250 dissolved in UPW (pH 7.4) for 30 s and washed with UPW (Passow and Alldredge 1995; Long and Azam 1996). Glycosaminoglycans were stained with 0.05% (w/v) Ruthenium Red (Sigma-Aldrich) dissolved in UPW for 10 min followed by washing with UPW (Tiessen and Stewart 1988), and with a Periodic Acid-Schiff kit (Sigma-Aldrich) following the protocol enclosed. Briefly, sections were stained with Periodic Acid Solution for 5 min, with Schiff's reagent for 15 min and counterstained with Hematoxylin Solution, Gill No. 3, for 90 s including intermediate washing steps with UPW.

All stains were applied to untreated sections as well as to sections embedded in 25 μL 0.1% LE agarose prior to staining to test if agarose-embedding can minimize sample loss, as reported for filtered samples. (N.B. in this study, "agarose-embedding" refers to applying a drop of agarose to the sample, and must not to be confused with embedding of intact whole aggregates in agarose).

Aggregate porosity

For a direct, optical measure of porosity (from here on referred to as "optical porosity"), thin-sections were photographed at 200X magnification with phase-contrast microscopy. In addition to in situ collected marine snow, we also examined the optical porosity of marine snow formed in the laboratory from cultures of the diatom *Skeletonema marinoi* to compare porosity between structurally complex, in situ collected aggregates and homogeneous aggregates formed from a monoculture (*see* Iversen and Ploug 2013 for a detailed protocol of diatom culturing and marine snow formation). To assess the reduction of pore space caused by EPS, aggregates were stained with combinations of Alcian Blue, Ruthenium Red, and FITC-ConA/Alexa647-ConA (please refer to "Staining of EPS" for a detailed staining protocol). Alcian Blue and Ruthenium Red-stained sections were photographed at 200X magnification using a light microscope. FITC-ConA/Alexa647-ConA stained sections were imaged at 200X magnification with an epifluorescence microscope (FITC Ex/Em 490 nm/525 nm; Alexa647 Ex/Em 590 nm/617 nm).

All images where processed with the image processing software package FIJI/ImageJ (Schindelin et al. 2012, 2015; Schneider et al. 2012). Images of partial sections ("tiles") were stitched with the FIJI TrakEM2 plug-in (Saalfeld et al. 2010, 2012; Cardona et al. 2012). For processing, images were converted to 8-bit and a threshold value was chosen to separate the aggregate from the background. To measure optical porosity, the area of the solid or stained fraction was measured using the "Analyze Particles" function in ImageJ, divided by the total area of the section and the quotient subtracted from 1. Optical porosity was then compared (1) to the most commonly used method of calculating porosity, where porosity is indirectly inferred from aggregate volume, solid hydrated density, and dry weight (Alldredge and Gotschalk 1988); (2) between and across sections of the same aggregate to assess the distribution of pore space within individual aggregates; (3) between sections of stained and unstained aggregates to assess the respective contributions of selected EPS fractions to changes in porosity.

3D-reconstruction

Two fully sectioned aggregates were selected for 3D reconstruction: one Alcian Blue-stained aggregate sectioned into 50 slices of 10 μm thickness, of which 46 were successfully recovered for alignment; and one unstained aggregate that had been incubated with fluorescently labeled bacteria and was sectioned into 38 sections of 10 μm thickness, of which 35 were successfully recovered. Recovered sections were photographed at 200X magnification using light or epifluorescence microscopy. Image tiles were stitched using the FIJI TrakEM2 plug-in followed by alignment of stitched tiles of consecutive sections in the z-direction using the same plug-in. Sections were aligned based on the positioning of Alcian Blue-stained or green fluorescent material. The aligned sections were exported and rendered in 3D using the 3D viewer plug-in in ImageJ (Schmid et al. 2010).

Visualization of aggregate colonizers

DAPI staining

To visualize microbial cells, cryosections were stained with 1 μg/mL 4′,6-diamidino-2-phenylindole (DAPI) for 10 min at room temperature in the dark. After careful rinsing with UPW, sections were air-dried and embedded in mounting medium for microscopic identification. Alternatively, 1% (v/v) DAPI solution (100 μg/mL) was added directly to the embedding medium. DAPI-stained cells were imaged with epifluorescence or confocal laser scanning microscopy (DAPI Ex/Em 358 nm/461 nm).

Fluorescence in situ hybridization (FISH)

For a more targeted identification of different bacterial groups, we used existing protocols for mono-labeled fluorescence in situ hybridization (mono-FISH), catalyzed reporter deposition fluorescence in situ hybridization (CARD-FISH; Amann et al. 1990; Pernthaler et al. 2002) and multi-labeled fluorescence in situ hybridization (MiL-FISH; Schimak et al. 2015) for staining aggregate thin-sections on glass slides (see Table 1 for a list of organisms targeted in this study and their corresponding oligonucleotide probes). Prior to staining, sections were circled with a hydrophobic PAP pen (Sigma-Aldrich) to retain buffer solutions. Sections were embedded in 25 μL 0.1% low-melting point agarose to maximize structural preservation. For mono- and multi-labeled FISH, hybridization buffer (5M NaCl, 1M TrisHCl, 20% SDS, formamide) with 50 ng/μL probe at a ratio of 15 : 1 was applied followed by hybridization at 46°C for 2 h and subsequent washing at 48°C for 15 min with the adjusted washing buffer (5M NaCl, 1M Tris/HCl, 20% SDS, 0.5M EDTA). For CARD-FISH, thin-sections were treated with lysozyme (50 mg lysozyme dissolved in 500 μL 0.5M EDTA + 500 μL 1M Tris/HCl + 4 mL UPW) for 30–60 min at 37°C for cell wall permeabilization. Hybridization buffer (900 mM NaCl, 20 mM Tris-HCl (pH 7.5), 0.02% sodium dodecyl sulphate (SDS), 10% dextran sulphate (w/v) and 1% (w/v) Blocking Reagent) was mixed with the probe at a buffer : probe ratio of 300 : 1 and applied to the sample. Hybridization at 46°C for 3 h was followed by a subsequent 10 min wash step at 48°C with the adjusted washing buffer (14–900 mM NaCl, 20 mM Tris/HCl, pH 8, 5 mM EDTA, pH 8 and 0.01% SDS). Amplification buffer ($\times$1 PBS [pH 7.3], 0.0015% [v/v] H_2O_2, 1% Alexa Fluor 488 or 594 dye ThermoFisher Scientific, Waltham, Massachusetts, U.S.A.) was prepared and slides incubated for 1 h at 46°C in a humid chamber until a final wash for 10 min in $\times$1 PBS. After washing, sections were incubated with a 1 μg/mL DAPI solution for 5–10 min at room temperature in the dark, washed with UPW, air-dried and embedded with 4 : 1 Citifluor/Vectashield mounting medium. Mounted samples were imaged with an epifluorescence microscope

(Ex/Em 490 nm/525 nm for FITC-labeled probes or tyra-mides, Ex/Em 358 nm/461 nm for CY3-labeled probes or tyramides).

Assessment

Embedding and slicing

We assessed the feasibility of aggregate embedding and thin-sectioning based on criteria relating to the direct ease of the procedure, the cost and time involved, and the quality of the sections obtained. Embedding of marine snow in Tissue-Tek was a fast and simple process. All aggregates collected from the MSC for this study were ballasted enough to sink into the cryogel within less than 1 h. Moreover, aggregates embedded in situ were spread evenly across the collection cup, enabling clear differentiation between aggregate types before slicing (Fig. 2b,c). Close examination showed very good structural preservation of gel-embedded aggregates with intact pigments and clearly identifiable components, e.g., diatoms protruding from the center of the aggregate (Fig. 2c,d). To avoid gradual dehydration of the Tissue-Tek during frozen storage, we recommend leaving a layer of 0.2 μm-filtered seawater on top of the gel and placing the frozen embedded samples in air-tight bags. During thawing, the relatively higher density of the cryogel prevents mixing with the water layer, which can be removed gently before the gel is re-frozen, mounted, and sectioned.

Tissue-Tek embedded marine snow was successfully sectioned with a mounting efficiency of 90% ($\pm$ 10%). The material properties of Tissue-Tek permitted cutting sections between 5 μm and 100 μm in thickness, which enabled spatially resolved examination of organisms and structures spanning two orders of magnitude. Sections below 5 μm were prone to rupturing, probably because the supporting embedding matrix was not rigid enough to allow structurally preserved slicing of ultra-thin sections. Sections thicker than 100 μm on the other hand were prone to breaking during sectioning because of the rigidity of frozen cryogel. Thick sections (> 50 μm) yielded optimal results when studying the distribution of larger organisms such as phytoplankton cells or flagellates within an aggregate, or in conjunction with CLSM, where optical sectioning of nano- to micrometer-thick slices can be combined with cryotome-sectioning to reduce physical disturbance. However, Tissue-Tek is liquid (albeit highly viscous) at room temperature and in sections thicker than 50 μm the gel was observed to spill over the original boundaries of the section after thawing, resulting in flattening and possible distortion of the 3D structure. Therefore, we recommend a section thickness of 50–100 μm when studying larger organisms, and a section thickness of 5–50 μm for porosity measurements and reconstruction of the aggregate matrix.

Other possible artifacts introduced through slicing include smearing of the sample due to high amounts of silica and lithogenic material found in marine snow which can break along fault lines or be dragged across the section, resulting in the displacement and rupture of material. While this is a potentially strong contraindication against soft-embedding, we did not observe smearing in sections thicker than 5 μm and successfully reconstructed entire aggregates in three dimensions from thin-sections (*see* "3D-reconstruction" section). Optionally, cutting relatively thick sections (> 30 μm) combined with optical sectioning using CLSM can be used to obtain high depth resolution while avoiding smearing. The freezing process during soft-embedding has also been reported to cause damage, mainly through tissue rupturing due to ice crystal formation (Tokuyasu 1973). Ice crystal formation can be minimized through freezing at −80°C or snap-freezing in liquid nitrogen, although no freezing artifacts were observed in cryosections of marine snow frozen at −20°C, possibly due to loose connectivity of the solid fraction and thorough infiltration of pore space by the cryogel.

Soft-embedding and cryosectioning required low-cost consumables, and costs could be reduced further by using non-coated glass slides, applying a coating, or only mounting every n^{th} section of the aggregate, depending on the purpose of sectioning. We conclude that due to easy manipulation and mounting of frozen embedded samples and high recovery efficiency of sections, soft-embedding is a feasible tool for users with little to no previous experience with thin-sectioning.

Visualization and imaging of the aggregate matrix

Staining of the aggregate matrix was assessed based on the coverage and visibility of the stain, the compatibility with cell stains, the compatibility with soft-embedding, and the comparison to whole-aggregate staining. Generally, any stain applicable to aggregates filtered as a whole could also be used on aggregate sections. Concerning the brightness and visibility of any stain, the issue of strong autofluorescence of aggregate components applied here as much as it has been noted to be a problem for whole aggregate examination (Fig. 3; Woebken et al. 2007; Thiele et al. 2015).

When using fluorescent stains, we found that examining sections prior to staining helped with selecting a suitable stain with little overlap in the spectrum of autofluorescent material. We observed the highest amount of autofluorescence to be emitted in the green spectrum, while autofluorescence was weakest in the blue, red and deep red spectra. However, this may change according to aggregate composition and is highly dependent on organic matter quality, as e.g., chlorophyll *a* emits red fluorescence and was observed to have high fluorescent intensities in laboratory-formed aggregates containing healthy, active diatom cells, but not in in situ collected marine snow.

Staining of EPS

Alcian Blue successfully stained TEP of the aggregate matrix (Fig. 4a–c), as previously reported for whole, filtered
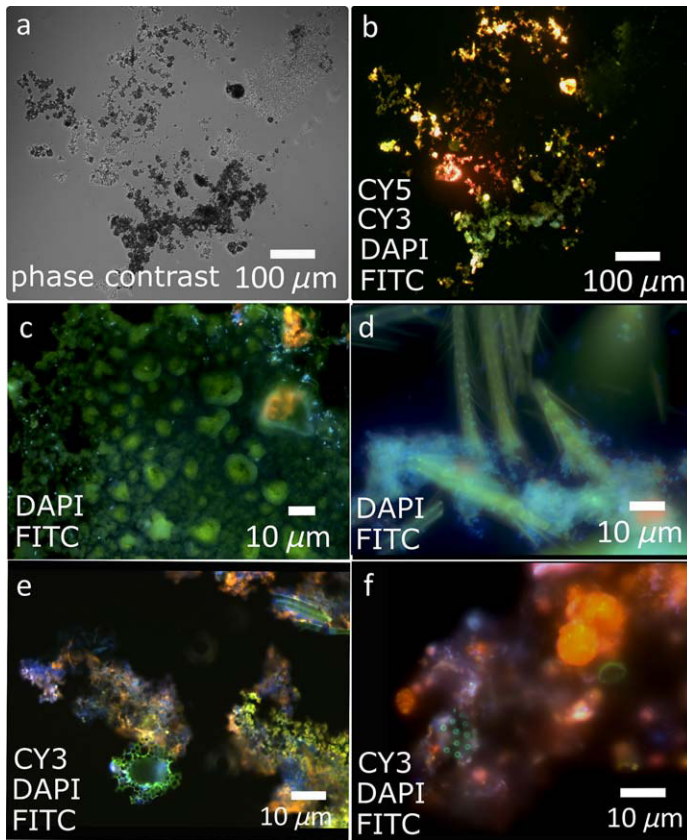
Fig. 3. Autofluorescent matrix components of unstained aggregate sections. (**a**) phase-contrast image of 10 μm-thick section; (**b**) the same section imaged with fluorescence microscopy; (**c**) unidentified structure with sparse bacterial attachment (DAPI-stained cells in blue); (**d**) heavy colonization of copepodide legs by DAPI-stained bacteria (blue); (**e, f**) unidentified structures.

marine snow (Passow and Alldredge 1995; Cisternas-Novoa et al. 2015). Coomassie Brilliant Blue staining yielded visible but weak signals of CSP and we observed CSP to be considerably less abundant than TEP, if not completely absent, which could be explained by the higher solubilization of proteins compared to polysaccharides in marine snow (Smith et al. 1992). FITC-ConA and Alexa647-ConA also successfully stained the aggregate matrix at concentrations as low as 100 μg/mL (Figs. 4d, 7), which was expected as lectin stains have been explored in considerable depth for staining EPS in biofilms (Neu et al. 2001; Strathmann et al. 2002), river snow (Neu 2000; Böckelmann et al. 2002), and sludge aggregates (McSwain et al. 2005; Weissbrodt et al. 2013). Compared to Alcian Blue, FITC-ConA/Alexa647-ConA covered similar areas of the aggregate matrix but stained slightly distinctive features. A similar observation was made for Ruthenium Red (Fig. 4). All three stains partially overlapped in their specificity for certain polysaccharides, but also bound to substrates not targeted by any of the other tested stains, highlighting the necessity to further explore polysaccharide diversity and their

respective effects on particle aggregation (their "stickiness"), pore space reduction and degradation dynamics.

Special attention must be paid to avoid sample loss during rigorous staining or washing because of the solubility of cryogel in water. The SuperFrost Plus™ coating of the glass slides used in this study is designed to confer maximum samples adherence, but there is a risk of material being washed off, especially of thicker sections where material is not in direct contact with the adhesive coating of the slide. Decreased adhesion was seen in sections that had been stored for > 1 yr, meaning that swift processing of sections is advisable. We found that carefully applying the staining or washing solution with a pipette, removing the liquid with a pipette and lint-free wipes, and letting the sample dry face up (not tilted) caused negligible displacement or washing off of material, resulting in well preserved, distinctly stained sections. However, there was a limit of staining and washing steps before sample loss became difficult to avoid. For example, PAS staining successfully stained matrix components (Fig. 4g–i) but the intense staining and washing protocol led to visible disruption of section integrity (Fig. 4g). For staining procedures involving multiple staining and washing steps, agarose-embedding of sections added structural stability and improved section integrity and preservation. However, agarose-embedding is limited by non-specific binding to agarose by lectins (as observed in our study and reported by Bennke et al. 2013). Staining prior to embedding in cryogel may be considered to sidestep this problem, but limits the possibility of combining incompatible stains across consecutive slices and excludes aggregates embedded in situ.

Aggregate porosity

Optical porosity vs. calculated porosity Optical porosity of aggregate thin-sections ranged from 0.8 to 0.97 (void volume/total volume), and was found to be about 5–10% lower than calculated porosity (Alldredge and Gotschalk 1988). A possible cause was the integration of multiple layers of matter across the thickness of the section, leading to the omission of pore space and therefore underestimation of porosity. To minimize pore space omission, sections for measuring optical porosity should be cut as thinly as possible, i.e., 5–10 μm using our soft-embedding technique. Combining cryosectioning with optical sectioning (i.e., CLSM) improved resolution across depth, but was dependent on autofluorescence of solids or fluorescently stained substrates. Boundaries of aggregate thin-sections proved to be hard to determine due to loose connectivity and heterogeneous distribution of the solid fraction. We found that optical porosity varied by up to 50% depending on how the aggregate boundary was determined. This strongly suggested that a consistent approach for defining the section boundary was necessary. We compared various shapes for approximating the outer boundary of the sectioned aggregate (convex hull fittings, various ellipsoid fittings, polygons), and observed that the most robust approach for determining the outer boundary, and consequently to estimate the total area
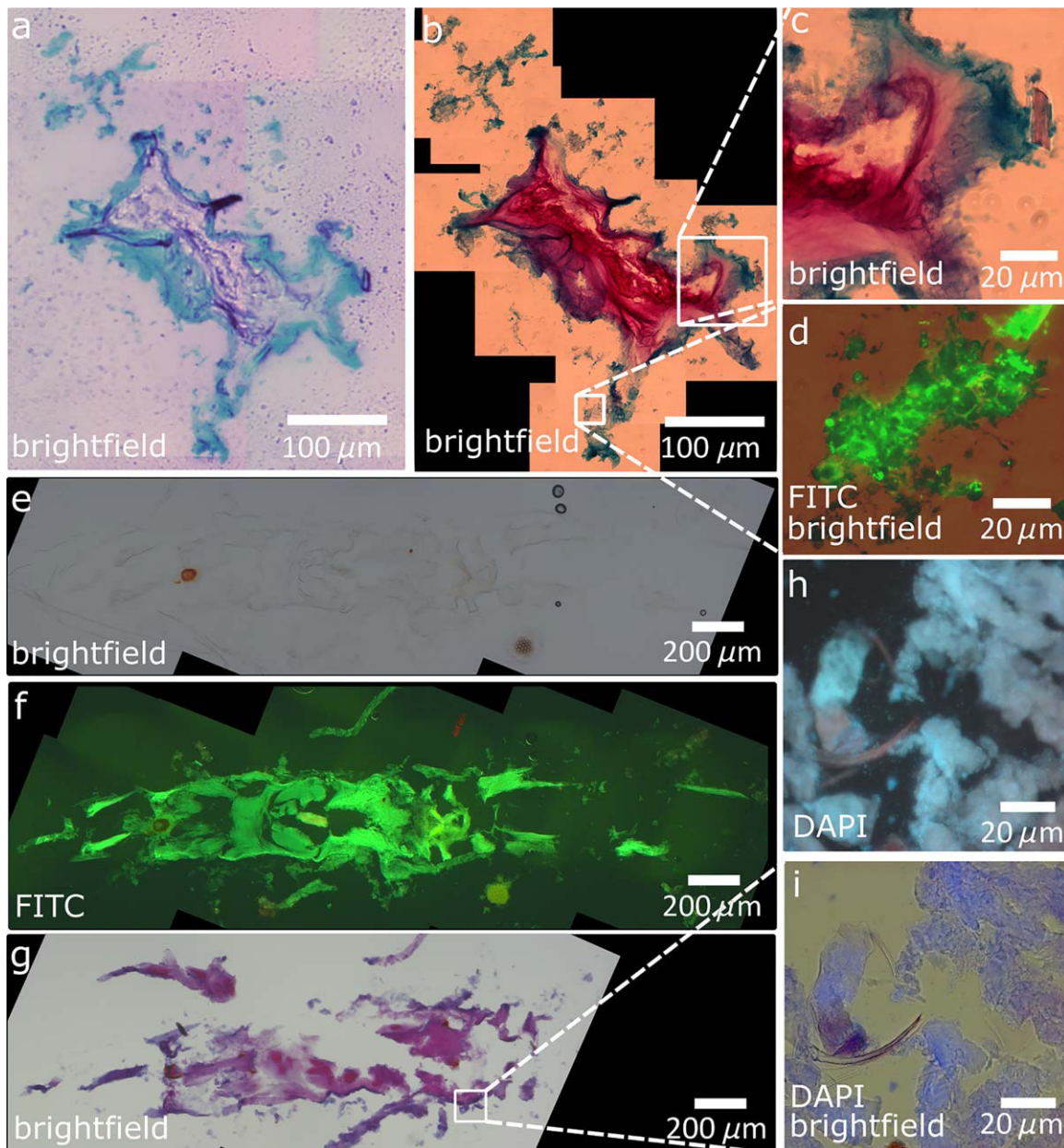
Fig. 4. Overview of matrix components in two separate thin-sections stained with selected dyes (section I **a–d**, section II **e–i**). (**a**) 10 μm-thick section I stained with Alcian Blue; (**b**) section I stained with Alcian Blue and Ruthenium Red; (**c**) close-up of section I stained with Alcian Blue and Ruthenium Red; (**d**) close-up of section I stained with Alcian Blue and FITC-ConA; (**e**) unstained 20 μm-thick section II imaged with brightfield microscopy; (**f**) section II imaged with fluorescence microscopy; (**g**) section II stained with PAS; (**h**) close-up of section II imaged with fluorescence microscopy; (**i**) close-up of section II imaged with fluorescence and brightfield microscopy.

of the section, was to fit an ellipse to the maximum aggregate width and height (Fig. 5). The same approach is used for measuring aggregate volume for porosity calculations (Alldredge and Gotschalk 1988) which is why this fitting resulted in the closest match to calculated porosity.

Pore size distribution between and across aggregate sections   Op-

Optical porosity values were relatively constant across stacked aggregates sections, with mean values of 0.975

(SD $\pm$ 0.013) measured for the unstained aggregate. Porosity and pore size was much more variable across single sections where we generally observed regions with high porosity interspersed by regions of low porosity, with pore space being distributed more heterogeneously in aggregates collected in situ (Fig. 5a,b,d–f,h) compared with aggregates formed from diatom monocultures in the laboratory (Fig. 5c,g). Further, we observed large reductions in porosity down to 0.8454 (SD $\pm$ 0.040) in sections stained with Alcian Blue (Fig. 5g,h). Direct

assessment of thin-sections not only enabled the determination of porosity defined as the fraction of solid components to overall aggregate volume, but also of the effective porosity, i.e., porosity defined as the fraction of "non-void" components, including the EPS matrix, to aggregate volume. While Alcian Blue-staining reduced porosity by approximately 10%, we observed that Ruthenium Red reduced optical porosity by another 5–10%, but these observations can be expected to vary greatly depending on aggregate type and source. Thus, a combination of stains covering a broad range of polymers found in the marine snow matrix could potentially help to obtain more accurate estimates of effective aggregate porosity.

3D-reconstruction

3D reconstruction from cryosections highlighted the porous nature and heterogeneity of marine snow because of the possibility to examine aggregates from any chosen angle. The decrease in effective pore size by TEP became especially obvious when comparing the unstained with the Alcian Blue-stained reconstructed aggregate (Fig. 6). However, the patchy distribution of visible substrates and large amount of pore space complicated alignment of sections along the *z*-axis and stains with higher coverage (e.g., Alcian Blue) facilitated more precise alignment because of better cross-referencing between consecutive sections. To enable alignment independent of staining, we suggest introducing an external reference into the embedding matrix, which we so far have not achieved.

Visualization of aggregate colonizers

In addition to staining the aggregate matrix, we tested methods of staining bacteria in aggregate sections. Nucleic acid (DAPI) staining clearly visualized bacterial cells and their localization relative to autofluorescent and ConA-stained substrate, showing close bacteria-substrate associations (Figs. 3c,d, 7, 8).

Of the three FISH methods tested (mono-labeled FISH, multi-labeled FISH, and CARD-FISH), we determined multi-labeled FISH to be the most versatile method for staining selected clades of bacteria or archaea in soft-embedded sections: mono-labeled FISH (Fig. 8d) resulted in low fluorescent signal intensity and labeling success, possibly due to high autofluorescence of the samples (Fig. 3). CARD-FISH (Fig. 8c, e–g) yielded distinctive signals, but CARD-chemistry necessitates additional permeabilization and washing steps that can destabilize the integrity of the section and thus requires agarose-embedding of sections prior to CARD-FISH. Multi-labeled FISH combines the high signal intensity of CARD-FISH with the low amount of washing and sample handling of mono-labeled FISH (Fig. 8a,b). An additional advantage of multi-labeled FISH is the option of multiplexing several probes on the same section without the horseradish peroxidase inactivation necessary for CARD-FISH.

Following the FISH protocol without prior embedding of sections in 0.1% LE agarose led to some sections being lost in the process. Although not all sections were washed off, we observed that soft-embedding cannot provide sufficient structural support during FISH to guarantee sustained integrity of the sections, and recommend agarose-embedding before FISH.

Agarose-embedding has been found to limit the use of lectins in conjunction with CARD-FISH, as unspecific binding to agarose prohibits staining after CARD-FISH, but staining prior to embedding and CARD-FISH leads to severely reduced fluorescent signal intensity of the lectin stain. However, we did not observe any impact on the quality of the lectin stain following the mono- or multi-labeled FISH protocols. We attributed this to the lower number of washing steps compared to CARD-FISH which reduces loss of the label ligand as well as to the absence of protein-denaturing buffer solutions that are part of the CARD-FISH protocol. This endorses the use of multi-labeled FISH to be used in conjunction with EPS staining, as a protective agarose coating can be applied to the section after lectin staining but prior to multi-labeled FISH. Combining multi-labeled FISH and lectin staining in structurally preserved sections, we could see the accumulation of bacteria inside small channels in the polysaccharide matrix (Fig. 8a).

Discussion

In this study, we showed how combining soft-embedding with thin-sectioning of in situ collected aggregates provides insight into their physical structure and the distribution and diversity of microbial colonizers. A particular strength of this method lies in the minimal amount of active handling, particularly of aggregates embedded in situ in gel-filled collection cups. Without the possibility to analyze the composition and 3D structure of intact, non-embedded macro-aggregates, the degree of structural preservation during embedding and slicing cannot be assessed quantitatively. However, the consistent agreement of our findings regarding stainability, porosity, and composition to existing literature (as discussed in the "Assessment" section) strongly suggest minimal disturbance of aggregates during embedding and slicing. Good structural preservation during embedding is further supported by observations of natural aggregates collected with gel traps in previous studies (Ebersbach and Trull 2008; Laurenceau-Cornec et al. 2015; Wiedmann et al. 2016). Although some disturbance during sectioning and staining cannot be ruled out we have provided recommendations on how potential disturbances can be minimized (*see* "Assessment" for details). This is further supported by good alignment of consecutive sections enabling 3D reconstruction. The relative ease, lack of hazardous chemicals or specialized equipment, and low time expenditure for the embedding process make this method especially suited for ship- or field-based sampling. The compatibility with existing FISH protocols offers a previously unattainable spatial resolution of the distribution of microbial groups
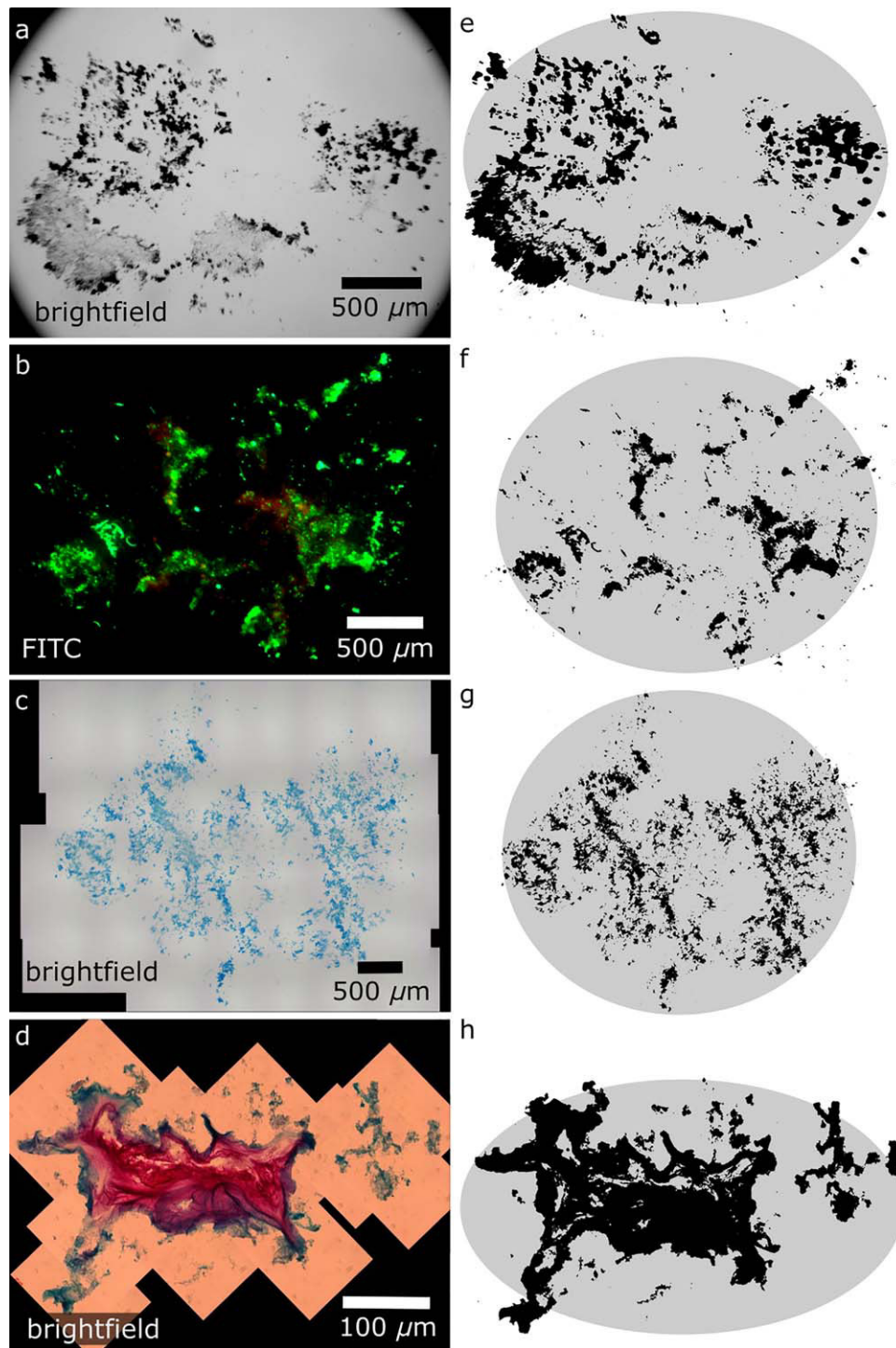
Fig. 5. Sections used to test optical porosity measurements. (**a**, **b**) Unstained 10 μm section of in situ collected aggregates; (**c**) Alcian Blue-stained 10 μm section of laboratory-formed *S. marinoi* aggregate; (**d**) Alcian Blue and Ruthenium Red-stained 10 μm section of in situ collected aggregate; (**e–h**) corresponding thresholded images used for measuring the area of solid or stained fractions (black) and ellipses fitted using the maximum width and height of the section to measure the total area of the section (overlay in gray).

within individual aggregates, with the added possibility of studying their co-localization with selected substrates of the aggregate matrix.

Preserving aggregate structure throughout staining and microscopy can shed light on attributes of marine snow that could so far not be examined because of disaggregation and

Fig. 6. 3D reconstruction of two 10 μm-sectioned aggregates based on (**a**) green autofluorescence and (**b**) Alcian Blue staining. Aggregates are pictured from three different angles, with a gradual change in color representing an increase in *z*-depth (frontback). Rotating video clips of both aggregates are available as Supporting Information.

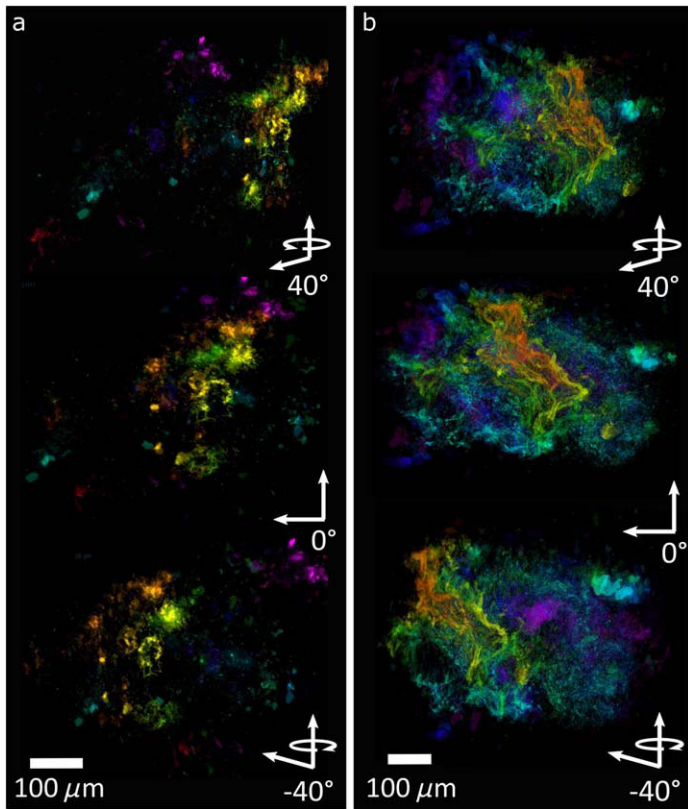Böckelmann et al. 2002). Compared to optical sectioning, embedding followed by physical sectioning can introduce sectioning artifacts (*see* "Assessment" section). However, optical sectioning also produces artifacts such as effects of self-shadowing, reduced fluorescent signal intensity with increasing scanning depth, bleaching of fluorescent signals, and limited working distance for larger samples (Dixon et al. 1991). Marine snow regularly reaches sizes of several millimeters, thereby limiting the resolution at which aggregates can be studied using Confocal Laser Scanning Microscopy alone. Embedding enables structurally preserved storage of samples, whereas optical sectioning requires immediate analysis as samples lack a supporting embedding matrix to retain structural integrity. Perhaps most importantly, we showed how physical sectioning offers the possibility of applying different stains to consecutive sections of the same aggregate to study the distribution of different matrix components across the aggregate (a form of pseudo-multiplexing), thus reducing limits imposed by overlapping color spectra of stains, fluorescent quenching, and stain incompatibility or interference. We do not consider optical section to be a feasible stand-alone method for analyzing in situ collected marine snow, but as we demonstrated in this study it can be a valuable complement to physical sectioning by increasing resolution across section depth, which is especially useful with respect to porosity measurements.

An alternative to the soft-embedding method presented here is embedding aggregates in hard resin (Leppard et al. 1996; Chu et al. 2004). Hard-embedding matrices support sectioning of ultra-thin slices (< 1 μm), which can be particularly useful for the investigation of sub-cellular structures and compartments (Heissenberger et al. 1996). Moreover, the resin matrix cannot be re-dissolved after polymerization, effecting high structural cohesion during washing and staining. Transport and long-term storage of hard-embedded samples is also more convenient, as it is not dependent on maintaining sub-zero temperatures. However, it is impossible

structural disturbance during filtering. Several studies have explored the use of confocal laser scanning microscopy for the examination of structurally intact marine, riverine, and sludge aggregates (Thill et al. 1998; Neu 2000; Waite et al. 2000;
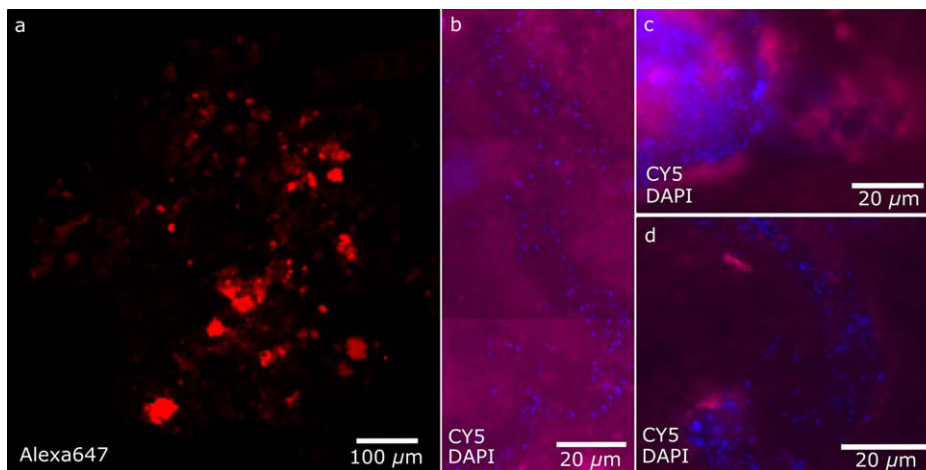
Fig. 7. (**a**) Section stained with Alexa647-ConA; (**b**–**d**) details showing ConA matrix (purple) with DAPI-stained bacteria embedded (blue).
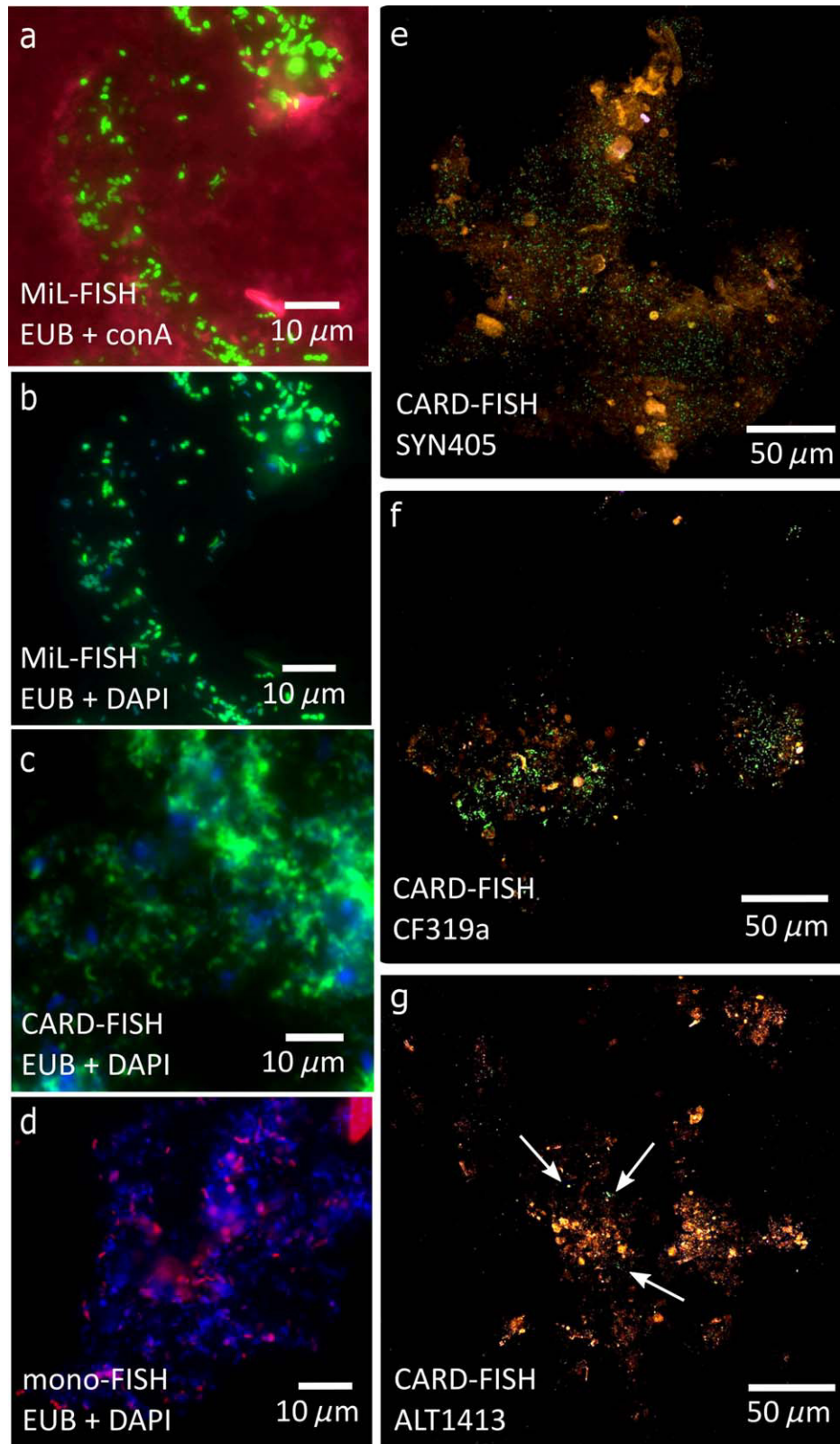
Fig. 8. FISH-probing of marine snow thin-sections. (**a**) EUB-labeled bacteria (green) embedded in channels inside the aggregate EPS matrix stained by conA (purple); (**b–d**) comparison of EUB labeling efficiency and fluorescent signal intensity for the three FISH methods used in this study: (**b**) MiL-FISH (green-fluorescent fluorophores); (**c**) CARD-FISH (green-fluorescent tyramides); (**d**) mono-FISH (red-fluorescent fluorophores); (**e–g**) thin-section from one in situ collected aggregate (phytoplankton autofluorescence shown in red) stained with probes for selected bacterial clades (green) using CARD-FISH: (**e**) *Synechococcus* spp.-specific probe; (**f**) *Bacteroidetes*-specific probe; (**g**) *Alteromonadales*-specific probe (arrows indicate localization of hardly visible FISH-stained bacteria). Rotating video clips of aggregate sections (**e–g**) are available as Supporting Information.

to equip sediment traps with hard resins to embed aggregates in situ. We consider direct fixation, washing, and embedding in situ to be one of the most substantial features of soft-embedding, as the absence of active handling prevents any risks of handling artifacts. The handling steps for soft-embedding of aggregates collected with a Marine Snow Catcher exclude the heating and complete dehydration that are needed for hard-embedding. The compatibility with FISH protocols furthermore enables taxonomic analysis of aggregate colonizers.

Practical applications of soft-embedding

Aggregate structure and porosity

By successfully staining the matrix of soft-embedded aggregate thin-sections using established staining protocols, we could visualize the spatial distribution of TEP and other EPS. By aligning consecutive sections along the *z*-axis we succeeded in rendering a 3D reconstruction of entire aggregates based on solid and Alcian Blue-stained fractions of the matrix. Aside from an increased appreciation of the aggregate-scale distribution of selected matrix fractions, 3D rendering enables clearer determination of aggregate boundaries in any direction than can be achieved by analyzing single sections. The current standard of quantifying TEP (and by extension EPS) developed by Passow and Alldredge (1995) involves filtering of organic material onto polycarbonate filters followed by staining and subsequent dissolution in sulfuric acid for spectrophotometric analysis, meaning no inferences can be made about the spatial distribution of TEP in aggregates.

In combination with spectrophotometric Alcian Blue assays (or lectin quantification assays as developed by Uthicke et al. 2009), and/or incubation experiments, examining the distribution and patchiness of EPS on a sub-aggregate level can advance our knowledge of what determines "stickiness" of aggregates and their components both during formation and disaggregation, and of the contribution by different EPS fractions to effective pore-space reduction. We also showed how applying several stains to cover a range of EPS could be used as a measure for "non-void," i.e., effective porosity, which can be used to approximate aggregate permeability. A separation into total and effective porosity can be useful to better understand mass transport of particulate and dissolved matter between aggregates and ambient water, as solid matter is restricted to being transported via actual pores, whereas fluids and gases can diffuse into and out of the aggregate matrix, which is of significance for colonization, nutrient release, oxygen supply, settling velocities, and mass fluxes.

Measuring the area of the solid or stainable fraction relative to the total area of thin-sections enabled us to estimate the optical porosity of sectioned aggregates and to give a spatially resolved structural description of intact marine snow. We do not suggest that the "optical porosity method" introduced here is superior to calculated porosity, as the inherent challenges (definition of the aggregate boundary, integration of

matter across section depth) require further revision of this method. However, we regard it as a valuable complement to existing methods of calculating porosity, as direct visualization of matrix fractions and pore space can address questions that could so far not be resolved, including the effect of different solid and EPS fractions on porosity and pore distribution, and the variability of pore space across single sections. Furthermore, optical porosity can be estimated from singles aggregates, whereas calculating porosity according to Alldredge and Gotschalk (1988) requires averaging of values obtained from multiple aggregates due to methodological constraints. Analysis of pore distribution-connectivity across single sections together with alignment of consecutive sections and 3D reconstruction as demonstrated in this study, can enable detection of any channels through the aggregate matrix that could permit advective flow (i.e., channels that are connected to the outside of the aggregate and have a diameter greater than the Kolmogorov length scale of 5 μm, below which advection is drastically limited by viscosity). Exploring the presence and extent of advective flow remains a key goal, as advection has the potential to influence metabolic processes inside marine snow through influx of oxygenated water that reduces the occurrence or increases the patchiness of processes other than aerobic respiration (e.g., denitrification).

Microbial colonization and taxonomic diversity

Because of the preserved structure of embedded aggregates, we could spatially resolve the distribution of microbial colonizers inside individual aggregates. We consider this an important step toward exploring microbial colonization of marine snow in situ which can help resolve many outstanding questions about the colonization and succession dynamics on settling aggregates. Chemotactic, pelagic bacteria have been shown to be highly successful at seeking out small-scale nutrient patches like diatom cells or chains (Stocker et al. 2008; Smriga et al. 2016) and settling particles, which were newly colonized on scales of minutes to hours (Kiørboe et al. 2002, 2003; Grossart et al. 2003, 2006). Because of the dynamic aggregation and disaggregation of marine aggregates it is particularly hard to study in situ bacterial colonization and succession patterns. Often, such studies have been restricted to laboratory model systems (Datta et al. 2016) or inferences made from comparing community composition of free-living and particle-attached bacteria using filtered size-fractions (e.g., Mestre et al. 2017). Unfortunately, taxonomic composition of filter fractions has been shown to deviate notably from that of non-fractionated samples (Craig 1986; Padilla et al. 2015). In situ gel-embedding of marine aggregates sidesteps this issue as aggregates can be picked selectively from the gel to analyze their microbial composition, e.g., using FISH (Thiele et al. 2015). Thin-sectioning of embedded aggregates further allows high resolution studies of microbial colonization processes and dynamics in relation to small-scale aggregate structure and composition.

With preserved spatial structure, we showed the accumulation of bacteria inside small channels in the polysaccharide matrix. These channels could be formed through hydrolysis of the substrate by colonizing bacteria, or during aggregation and direct advective and diffusive flow of water carrying microorganisms through the aggregate matrix. Analyzing the localization of microbial groups or clusters inside aggregates over water depth and/or time could provide a way to study the respective importance or dominance of the bacterial community originally present during aggregate formation with that of bacteria attaching to (or being scavenged by) the aggregates during settling. Imaging of bacterial clades co-localized with substrates or degradation products also presents a way to directly visualize microbe–substrate interactions and complement current techniques used to infer microbial activity such as tracer addition to incubation experiments, transcriptomics, or single-cell uptake measurements.

Marine carbon fluxes and closing statement

Collecting and embedding aggregates in situ using drifting sediment traps not only minimizes active handling but presents a new and exciting possibility to study the micro-scale structure, composition and diversity of the aggregate matrix and aggregate colonizers in combination with particle characteristics, biogeochemical fluxes, and molecular methods applied to sediment trap material (e.g., DNA/RNA extraction). We consider this an important step toward understanding the ecology and connectivity of the pelagic zone with strong potential to open up new possibilities to research the microbial processes controlling the biological carbon pump and recycling of organic matter in the water column.

References

Alldredge, A. L., and C. Gotschalk. 1988. In situ settling behavior of marine snow. Limnol. Oceanogr. **33**: 339–351. doi:10.4319/lo.1988.33.3.0339

Alldredge, A. L., and M. W. Silver. 1988. Characteristics, dynamics and significance of marine snow. Prog. Oceanogr. **20**: 41–82. doi:10.1016/0079-6611(88)90053-5

Alldredge, A. L., and C. C. Gotschalk. 1990. The relative contribution of marine snow of different origins to biological processes in coastal waters. Cont. Shelf Res. **10**: 41–58. doi:10.1016/0278-4343(90)90034-J

Alldredge, A. L., U. Passow, and B. E. Logan. 1993. The abundance and significance of a class of large, transparent organic particles in the ocean. Deep-Sea Res. Part I **40**: 1131–1140. doi:10.1016/0967-0637(93)90129-Q

Amann, R. I., B. J. Binder, R. J. Olson, S. W. Chisholm, R. Devereux, and D. A. Stahl. 1990. Combination of 16S RRNA-targeted oligonucleotide probes with flow cytometry for analyzing mixed microbial populations. Appl. Environ. Microbiol. **56**: 1919–1925.

Bennke, C. M., T. R. Neu, B. M. Fuchs, and R. Amann. 2013. Mapping glycoconjugate-mediated interactions of marine bacteroidetes with diatoms. Syst. Appl. Microbiol. **36**: 417–425. doi:10.1016/j.syapm.2013.05.002

Böckelmann, U., W. Manz, T. R. Neu, and U. Szewzyk. 2002. Investigation of lotic microbial aggregates by a combined technique of fluorescent in situ hybridization and lectin-binding-analysis. J. Microbiol. Methods **49**: 75–87. doi:10.1016/S0167-7012(01)00354-2

Cardona, A., and others. 2012. TrakEM2 software for neural circuit reconstruction. PLoS One **7**: e38011. doi:10.1371/journal.pone.0038011

Chu, C. P., D. J. Lee, and X. F. Peng. 2004. Structure of conditioned sludge flocs. Water Res. **38**: 2125–2134. doi:10.1016/j.watres.2004.02.003

Ciais, P., and others. 2014. Current systematic carbon-cycle observations and the need for implementing a policy-relevant carbon observing system. Biogeosciences **11**: 3547–3602. doi:10.5194/bg-11-3547-2014

Cisternas-Novoa, C., C. Lee, and A. Engel. 2015. Transparent exopolymer particles (TEP) and Coomassie stainable particles (CSP): Differences between their origin and vertical distributions in the ocean. Mar. Chem. **175**: 56–71. doi:10.1016/j.marchem.2015.03.009 doi:10.1016/j.marchem.2015.03.009

D'Ambrosio, L., K. Ziervogel, B. MacGregor, A. Teske, and C. Arnosti. 2014. Composition and enzymatic function of particle-associated and free-living bacteria: A coastal/offshore comparison. ISME J. **8**: 2167–2179. doi:10.1038/ismej.2014.67

Datta, M. S., E. Sliwerska, J. Gore, M. F. Polz, and O. X. Cordero. 2016. Microbial interactions lead to rapid microscale successions on model marine particles. Nat. Commun. **7**: 11965. doi:10.1038/ncomms11965

DeLong, E. F., D. G. Franks, and A. L. Alldredge. 1993. Phylogenetic diversity of aggregate-attached vs. free-living marine bacterial assemblages. Limnol. Oceanogr. **38**: 924–934. doi:10.4319/lo.1993.38.5.0924

Dixon, A. E., S. Damaskinos, and M. R. Atkinson. 1991. A scanning confocal microscope for transmission and reflection imaging. Nature **351**: 551–553. doi:10.1038/351551a0

Ebersbach, F., and T. W. Trull. 2008. Sinking particle properties from polyacrylamide gels during the Kerguelen Ocean and Plateau compared Study (KEOPS): Zooplankton control of carbon export in an area of persistent natural iron inputs in the Southern Ocean. Limnol. Oceanogr. **53**: 212–224. doi:10.4319/lo.2008.53.1.0212

Grossart, H. P., T. Kiørboe, K. Tang, and H. Ploug. 2003. Bacterial colonization of particles: Growth and interactions. Appl. Environ. Microbiol. **69**: 3500–3509. doi:10.1128/AEM.69.6.3500-3509.2003

Grossart, H. P., T. Kirboe, K. W. Tang, M. Allgaier, E. M. Yam, and H. Ploug. 2006. Interactions between marine snow and heterotrophic bacteria: Aggregate formation and microbial dynamics. Aquat. Microb. Ecol. **42**: 19–26. doi:10.3354/ame042019

Heissenberger, A., G. G. Leppard, and G. J. Herndl. 1996. Ultrastructure of marine snow. II. Microbiological considerations. Mar. Ecol. Prog. Ser. **135**: 299–308. doi:10.3354/meps135299

Holloway, C. F., and J. P. Cowen. 1997. Development of a scanning confocal laser microscopic technique to examine the structure and composition of marine snow. Limnol. Oceanogr. **42**: 1340–1352. doi:10.4319/lo.1997.42.6.1340

Honjo, S., S. J. Manganini, R. A. Krishfield, and R. Francois. 2008. Particulate organic carbon fluxes to the ocean interior and factors controlling the biological pump: A synthesis of global sediment trap programs since 1983. Prog. Oceanogr. **76**: 217–285. doi:10.1016/j.pocean.2007.11.003

IPCC. 2013. Climate change 2013: The Physical Science Basis. 1535 pp. *In* T. F. Stocker, D. Qin, G.-K. Plattner, and others [eds.], Contribution of Working Group I to the Fifth Assessment Report of the Intergovernmental Panel on Climate Change. Cambridge University Press, Cambridge, United Kingdom and New York, NY, USA, doi:10.1017/CB09781107415324

Iversen, M. H., and H. Ploug. 2010. Ballast minerals and the sinking carbon flux in the ocean: Carbon-specific respiration rates and sinking velocity of marine snow aggregates. Biogeosciences **7**: 2613–2624. doi:10.5194/bg-7-2613-2010

Iversen, M. H., and H. Ploug. 2013. Temperature effects on carbon-specific respiration rate and sinking velocity of diatom aggregates – potential implications for deep ocean export processes. Biogeosciences **10**: 4073–4085. doi:10.5194/bg-10-4073-2013 doi:10.5194/bg-10-4073-2013

Kiørboe, T., H. P. Grossart, H. Ploug, and K. Tang. 2002. Mechanisms and rates of bacterial colonization of sinking aggregates. Appl. Environ. Microbiol. **68**: 3996–4006. doi:10.1128/AEM.68.8.3996-4006.2002

Kiørboe, T., K. W. Tang, H. P. Grossart, and H. Ploug. 2003. Dynamics of microbial communities on marine snow aggregates: Colonization, growth, detachment, and grazing mortality of attached bacteria. Appl. Environ. Microbiol. **69**: 3036–3047. doi:10.1128/AEM.69.6.3036-3047.2003

Krupke, A., L. R. Hmelo, J. E. Ossolinski, T. J. Mincer, and B. A. S. Van Mooy. 2016. Quorum sensing plays a complex role in regulating the enzyme hydrolysis activity of microbes associated with sinking particles in the ocean. Front. Mar. Sci. **3**: 55. doi:10.3389/fmars.2016.00055

Laurenceau-Cornec, E. C., and others. 2015. The relative importance of phytoplankton aggregates and zooplankton fecal pellets to carbon export: Insights from free-drifting sediment trap deployments in naturally iron-fertilised waters near the Kerguelen Plateau. Biogeosciences **12**: 1007–1027. doi:10.5194/bg-12-1007-2015

Leppard, G. G., A. Heissenberger, and G. J. Herndl. 1996. Ultrastructure of marine snow. I. Transmission electron microscopy methodology. Mar. Ecol. Prog. Ser. **135**: 289–298. doi:10.3354/meps135289

Long, R., and F. Azam. 1996. Abundant protein-containing particles in the sea. Aquat. Microb. Ecol. **10** (June): 213–221. doi:10.3354/ame010213

Luef, B., T. R. Neu, and P. Peduzzi. 2009a. Imaging and quantifying virus fluorescence signals on aquatic aggregates: A new method and its implication for aquatic microbial ecology. FEMS Microbiol. Ecol. **68**: 372–380. doi:10.1111/j.1574-6941.2009.00675.x

Luef, B., T. R. Neu, I. Zweimüller, and P. Peduzzi. 2009b. Structure and composition of aggregates in two large European rivers, based on confocal laser scanning microscopy and image and statistical analyses. Appl. Environ. Microbiol. **75**: 5952–5962. doi:10.1128/AEM.00186-09

Lundsgaard, C. 1995. Use of a high viscosity medium in studies of aggregates, p. 141–152. *In* S. Floderus, A.-S. Heisakanen, M. Oleson, and P. Wassman [eds.], Sediment trap studies in the Nordic countries 3. Proceedings of the Symposium on Seasonal Dynamics of Planktonic Ecosystems and Sedimentation in Coastal Nordic Waters.

Mari, X., U. Passow, C. Migon, A. B. Burd, and L. Legendre. 2017. Transparent exopolymer particles: Effects on carbon cycling in the ocean. Prog. Oceanogr. **151** (February): 13–37. doi:10.1016/j.pocean.2016.11.002

McSwain, B. S., R. L. Irvine, M. Hausner, and P. A. Wilderer. 2005. Composition and distribution of extracellular polymeric substances in aerobic flocs and granular sludge. Appl. Environ. Microbiol. **71**: 1051–1057. doi:10.1128/AEM.71.2.1051-1057.2005

Mestre, M., E. Borrull, M. Montserrat Sala, and J. M. Gasol. 2017. Patterns of bacterial diversity in the marine planktonic particulate matter continuum. ISME J. **11**: 999–1010. doi:10.1038/ismej.2016.166

Neu, T. R. 2000. In situ cell and glycoconjugate distribution in river snow studied by confocal laser scanning microscopy. Aquat. Microb. Ecol. **21**: 85–95. doi:10.3354/ame021085

Neu, T., G. D. Swerhone, and J. R. Lawrence. 2001. Assessment of lectin-binding analysis for in situ detection of glycoconjugates in biofilm systems. Microbiology **147** (Pt 2): 299–313. doi:10.1099/00221287-147-2-299

Padilla, C. C., S. Ganesh, S. Gantt, A. Huhman, D. J. Parris, N. Sarode, and F. J. Stewart. 2015. Standard filtration practices may significantly distort planktonic microbial diversity estimates. Front. Microbiol. **6**: 547. doi:10.3389/fmicb.2015.00547

Passow, U., and A. L. Alldredge. 1995. A dye-binding assay for the spectrophotometric measurement of transparent exopolymer particles (TEP). Limnol. Oceanogr. **40**: 1326–1335. doi:10.4319/lo.1995.40.7.1326

Passow, U., and C. A. Carlson. 2012. The biological carbon pump in a high CO2 world. Mar. Ecol. Prog. Ser. **470**: 249–271. doi:10.3354/meps09985

Pernthaler, A., J. Pernthaler, and R. Amann. 2002. Fluorescence in situ hybridization and catalyzed reporter

deposition for the identification of marine bacteria. Appl. Environ. Microbiol. **68**: 3094–3101. doi:10.1128/AEM.68.6.3094-3101.2002

Ploug, H., and H.-P. Grossart. 2000. Bacterial growth and grazing on diatom aggregates: Respiratory carbon turnover as a function of aggregate size and sinking velocity. Limnol. Oceanogr. **45**: 1467–1475. doi:10.4319/lo.2000.45.7.1467

Ploug, H., M. H. Iversen, and G. Fischer. 2008. Ballast, sinking velocity, and apparent diffusivity within marine snow and zooplankton fecal pellets: Implications for substrate turnover by attached bacteria. Limnol. Oceanogr. **53**: 1878–1886. doi:10.4319/lo.2008.53.5.1878

Ploug, H., and U. Passow. 2007. Direct measurement of diffusivity within diatom aggregates containing transparent exopolymer particles. Limnol. Oceanogr. **52**: 1–6. doi:10.4319/lo.2007.52.1.0001

Ransom, B., K. F. Shea, P. J. Burkett, R. H. Bennett, and R. Baerwald. 1998. Comparison of pelagic and nepheloid layer marine snow: Implications for carbon cycling. Mar. Geol. **150**: 39–50. doi:10.1016/S0025-3227(98)00052-8

Riley, J. S., R. Sanders, C. Marsay, F. A. C. Le Moigne, E. P. Achterberg, and A. J. Poulton. 2012. The relative contribution of fast and slow sinking particles to ocean carbon export. Global Biogeochem. Cycles **26**: GB1026. doi:10.1029/2011GB004085

Saalfeld, S., A. Cardona, V. Hartenstein, and P. Tomančák. 2010. As-rigid-as-possible mosaicing and serial section registration of large ssTEM datasets. Bioinformatics **26**: i57–i63. doi:10.1093/bioinformatics/btq219

Saalfeld, S., R. Fetter, A. Cardona, and P. Tomancak. 2012. Elastic volume reconstruction from series of ultra-thin microscopy sections. Nat. Methods **9**: 717–720. doi:10.1038/nmeth.2072

Schimak, M. P., M. Kleiner, S. Wetzel, M. Liebeke, N. Dubilier, and B. M. Fuchs. 2015. MiL-FISH: Multi-labelled oligonucleotides for fluorescence in situ hybridisation improve visualization of bacterial cells. Appl. Environ. Microbiol. **82**:62–70. doi:10.1128/AEM.02776-15

Schindelin, J., and others. 2012. Fiji: An open-source platform for biological-image analysis. Nat. Methods **9**: 676–682. doi:10.1038/nmeth.2019

Schindelin, J., C. T. Rueden, M. C. Hiner, and K. W. Eliceiri. 2015. The ImageJ ecosystem: An open platform for biomedical image analysis. Mol. Reprod. Dev. **82**: 518–529. doi:10.1002/mrd.22489

Schmid, B., J. Schindelin, A. Cardona, M. Longair, and M. Heisenberg. 2010. A high-level 3D visualization API for Java and ImageJ. BMC Bioinf. **11**: 274. doi:10.1186/1471-2105-11-274

Schneider, C. A., W. S. Rasband, and K. W. Eliceiri. 2012. NIH Image to ImageJ: 25 years of image analysis. Nat. Methods **9**: 671–675. doi:10.1038/nmeth.2089

Smith, D. C., M. Simon, A. L. Alldredge, and F. Azam. 1992. Intense hydrolytic enzyme activity on marine aggregates

and implications for rapid particle dissolution. Nature **359**: 139–142. doi:10.1038/359139a0

Smriga, S., V. I. Fernandez, J. G. Mitchell, and R. Stocker. 2016. Chemotaxis toward phytoplankton drives organic matter partitioning among marine bacteria. Proc. Natl. Acad. Sci. USA **113**: 1576–1581. doi:10.1073/pnas.1512307113

Stocker, R., J. R. Seymour, A. Samadani, D. E. Hunt, and M. F. Polz. 2008. Rapid chemotactic response enables marine bacteria to exploit ephemeral microscale nutrient patches. Proc. Natl. Acad. Sci. USA **105**: 4209–4214. doi:10.1073/pnas.0709765105

Strathmann, M., J. Wingender, and H.-C. Flemming. 2002. Application of fluorescently labelled lectins for the visualization and biochemical characterization of polysaccharides in biofilms of Pseudomonas aeruginosa. J. Microbiol. Methods **50**: 237–248. doi:10.1016/S0167-7012(02)00032-5

Thiele, S., B. M. Fuchs, R. Amann, and M. H. Iversen. 2015. Colonization in the photic zone and subsequent changes during sinking determines bacterial community composition in marine snow. Appl. Environ. Microbiol. **81**: 1463–1471. doi:10.1128/AEM.02570-14

Thill, A., S. Veerapaneni, B. Simon, M. Wiesner, J. Y. Bottero, and D. Snidaro. 1998. Determination of structure of aggregates by confocal scanning laser microscopy. J. Colloid Interface Sci. **204**: 357–362. doi:10.1006/jcis.1998.5570

Tiessen, H., and J. W. B. Stewart. 1988. Light and electron microscopy of stained microaggregates: The role of organic matter and microbes in soil aggregation. Biogeochemistry **5**: 312–322. doi:10.1007/BF02180070

Tokuyasu, K. T. 1973. A technique for ultracryotomy of cell suspensions and tissues. J. Cell Biol. **57**: 551–565. doi:10.1083/jcb.57.2.551

Turner, J. T. 2015. Zooplankton fecal pellets, marine snow, phytodetritus and the ocean's biological pump. Prog. Oceanogr. **130**: 205–248. doi:10.1016/j.pocean.2014.08.005

Uthicke, S., L. Llewellyn, and F. Eder. 2009. Fluorescent lectin assay to quantify particulate marine polysaccharides on 96-well filtration plates. Limnol. Oceanogr.: Methods **7**: 449–458. doi:10.4319/lom.2009.7.449

Van der Jagt, H., C. Friese, J.-B. W. Stuut, G. Fischer, and M. H. Iversen. 2018. The ballasting effect of Saharan dust deposition on aggregate dynamics and carbon export: Aggregation, settling, and scavenging potential of marine snow. Limnol. Oceanogr. 9. doi:10.1002/lno.10779

Waite, A. M., R. J. Olson, H. G. Dam, and U. Passow. 1995. Sugar-containing compounds on the cell surfaces of marine diatoms measured using concanavalin a and flow cytometry. J. Phycol. **31**: 925–933. doi:10.1111/j.0022-3646.1995.00925.x

Waite, A. M., K. A. Safi, J. A. Hall, and S. D. Nodder. 2000. Mass sedimentation of picoplankton embedded in organic aggregates. Limnol. Oceanogr. **45**: 87–97. doi:10.4319/lo.2000.45.1.0087

Weissbrodt, D. G., T. R. Neu, U. Kuhlicke, Y. Rappaz, and C. Holliger. 2013. Assessment of bacterial and structural dynamics in aerobic granular biofilms. Front. Microbiol. **4**: 175. doi:10.3389/fmicb.2013.00175

Wiedmann, I., M. Reigstad, M. Marquardt, A. Vader, and T. M. Gabrielsen. 2016. Seasonality of vertical flux and sinking particle characteristics in an ice-free high arctic fjord—Different from subarctic fjords? J. Mar. Syst. **154(B)**: 192–205. doi:10.1016/j.jmarsys.2015.10.003

Wiedmann, I., M. Reigstad, A. Sundfjord, and S. Basedow. 2014. Potential drivers of sinking particle's size spectra and vertical flux of particulate organic carbon (POC): Turbulence, phytoplankton, and zooplankton. J. Geophys. Res. Oceans **119**: 6900–6917. doi:10.1002/2013JC009754

Woebken, D., B. M. Fuchs, M. M. M. Kuypers, and R. Amann. 2007. Potential interactions of particle-associated anammox bacteria with bacterial and archaeal partners in the Namibian upwelling system. Appl. Environ. Microbiol. **73**: 4648–4657. doi:10.1128/AEM.02774-06

Acknowledgments

Conflict of Interest

None declared.

To enable detailed microscopic analyses of the physical structure, as well as the microbial distribution and diversity within structurally undisturbed particles, we developed a cryogel-based embedding approach, which enabled structural and phylogenetic staining of aggregate slices (Paper II). A detailed description of benefits and limitations, as well as possible applications of the method is presented in Paper II. In the following paragraphs, I will focus on the most important points.

The method enabled a variety of specific and non-specific stainings, such as for TEP, CSP, and nucleic acids, but also allowed the application of rRNA gene probes for the identification of individual microbial types. Moreover, we could confirm the applicability of the cryogel deployed in drifting sediment traps as recently reported by Thiele *et al.* (2015), and performed *in situ* sampling and preservation of settling aggregates. The high vertical resolution of 5-100 µm slicing allowed three-dimensional reconstruction of whole aggregates, which in turn enabled the calculation of porosity values.

Three-dimensional aggregate reconstruction, based on opaque compounds, as well as Alcian Blue stained TEP, revealed an adequate alignment of the respective sections, suggesting low sample loss and deformation during the slicing and staining process. Moreover, structural preservation could be confirmed by comparisons with observations of natural aggregates from sediment trap gels (Ebersbach and Trull 2008; Laurenceau-Cornec *et al.* 2015; Wiedmann *et al.* 2016).

Porosity calculations of this study were based on Alldredge and Gotschalk (1988), defining the aggregate boundary as ellipse fitting the maximum aggregate height and width. Calculations revealed optical porosities between 0.8 and 0.97. Those were found to be 5 – 10 % lower than reported previously (Alldredge and Gotschalk 1988). One possible reason for this discrepancy could be the integration of multiple layers of matter across the section, leading to the omission of pore space and therefore underestimation of porosity. To minimize this effect, we proposed that sections should be cut as thinly as possible for porosity investigations.

The non-toxic behavior of the cryogel makes it an easy-to-use method in the field as well as a highly recommended medium for sediment traps. Due to structural preservation and the

possible application of a huge variety of structural stains on many consecutive sections of the same aggregate, cryogels can be used to study pore distribution within single aggregates, but also aggregation and densification effects, as well as the interaction of different exopolymeric compounds. Moreover, a combination of structural staining and FISH approaches allows new possibilities for investigations about the co-localization of special microbial groups with each other, as well as with selected substrates of the aggregate matrix. Thin-sectioning of embedded aggregates further allows high resolution studies of microbial colonization processes and dynamics in relation to small-scale aggregate structure and composition.

We considered this method an important step towards understanding the ecology and microbial connectivity within the pelagic zone with strong potential to open up new possibilities for research on microbial processes controlling the biological carbon pump and recycling of organic matter in the water column. The resolution of individual aggregate-associated micro-zones within settling marine particles will increase our knowledge of microbial ecology as a whole, shedding light on the spatial distribution of, and relations between, individual microbial groups, as well as their colonization and detachment processes. It could also be used to clarify the role of particles as vehicles for obligate anaerobic microorganisms through the oxygenated water column (see Paper I).

2.2.2 Towards precise single-cell activity measurements within sinking marine aggregates

Microscopic analyses alone, however, cannot uncover all the important attributes of particle-associated microbial assemblages. There are many examples from free-living microbes, where the most abundant organism is not the most important player in terms of matter cycling rates. One very well known, although special, case is the oligotrophic, meromictic lake Cadagno, where the anaerobic phototrophic bacteria *Chromatium okenii* contributes 40 % to total ammonium uptake and 70 % to total carbon uptake, but only represents 0.3 % of the total microbial cell abundance (Musat 2008). This study exemplifies the strength of a key method: nano-scale secondary ion mass spectrometry (NanoSIMS), which enables the simultaneous quantification of 6-7 secondary ion masses in each investigated field of view. NanoSIMS measurements following incubation experiments using stable isotope labelled nutrients and cell identification, allow the calculation of isotope ratios or abundances and, hence, the investigation of single-cell element uptake.

SIMS has become a common method in microbiology during the last decade, but the fragile nature of sinking aggregates has prevented the application of such methods for aggregate-associated microbes. Cryogels (Paper II) do not help here, since the slicing of a cryogel does not provide an even surface, and the risk of outgassing and shrinking prevents accurate measurements and calculations of biovolume corrected enrichments. This is of special importance when comparing groups of microbial organisms with different mean cell sizes as described in Paper I. Therefore, I developed an optimized preparation method for NanoSIMS-based uptake measurements of single cells within marine snow (Paper III).

PAPER III

Hard and soft plastic resin embedding for single-cell element uptake investigations of marine-snow-associated microorganisms using nano-scale secondary ion mass spectrometry

Andreas Rogge [iD],*[1] Clara M. Flintrop,[1,2,3] Morten H. Iversen [iD],[1,2] Ian Salter,[1,4] Allison A. Fong,[1] Angela Vogts,[5] Anya M. Waite [iD][1,6]

[1]Alfred Wegener Institute Helmholtz Centre for Polar and Marine Research (AWI), Bremerhaven, Bremen, Germany
[2]Marum and University of Bremen, Bremen, Germany
[3]Max-Planck-Institute for Marine Microbiology, Bremen, Germany
[4]Faroe Marine Research Institute, Tórshavn, Faroe Islands
[5]Leibniz Institute for Baltic Sea Research Warnemünde (IOW), Rostock-Warnemünde, Mecklenburg-Vorpommern, Germany
[6]FB2 Biology/Chemistry, University of Bremen, Bremen, Germany

Abstract

Marine snow aggregates are microhabitats for diverse microbial communities with various active metabolic pathways. Rapid recycling and symbiotic transfer of nutrients within aggregates poses a significant challenge for accurately assessing aggregate-associated turnover rates. Although single-cell uptake measurements are well-established for free-living microorganisms, suitable methods for cells embedded in marine snow are currently lacking. Comparable cell-specific measurements within sinking pelagic aggregates would have the potential to address core questions regarding aggregate-associated fluxes. However, the capacity to perform microscale studies is limited by the difficulty of sampling and preserving the fragile aggregate structure. Furthermore, the application of nano-scale secondary ion mass spectrometry (NanoSIMS) to aggregates is complicated by technical requirements related to vacuum and ablation resistance. Here, we present a NanoSIMS-optimized method for fixation, embedding, and sectioning of marine snow. Stable isotope labeling of laboratory-generated aggregates enabled visualization of label incorporation into prokaryotic and eukaryotic cells embedded in the aggregate structure. The current method is also amenable to various staining procedures, including transparent exopolymer particles, Coomassie stainable particles, nucleic acids, and eukaryotic cytoplasm. We demonstrate the potential for using structural stains to generate three-dimensional (3D) models of marine snow and present a simplified calculation of porosity and fractal dimension. This multipurpose method enables combined investigations of 3D aggregate structure, spatial microbial distribution, and single-cell activity within individual aggregates and provides new possibilities for future studies on microbial interactions and elemental uptake within marine snow.

Marine aggregates play a crucial role in the sequestration of photosynthetically produced organic matter, moving carbon from the euphotic zone to the deep ocean, which has an important impact on the global carbon budget (Turner 2015). They range from small conglomerates of organisms to aggregates of several millimeters in diameter, which also includes marine snow (aggregates > 500 μm; Alldredge and Silver 1988). The primary components of marine snow are phytodetritus, discarded appendicularian houses, fecal pellets, and other detrital material which stick together due to a matrix of exuded polymeric substances, including transparent exopolymer particles (TEP) (Passow et al. 1994; Passow et al. 2001; Turner 2015). The latter are defined as discrete exopolymers that consist predominantly of surface-active acidic polysaccharides and that are stainable with Alcian Blue (Alldredge et al. 1993; Cisternas-Novoa et al. 2015). Early studies revealed the importance of non-TEP extracellular polymeric substances (Stoderegger and Herndl 1999; Waite et al. 2005), and proteinaceous Coomassie stainable particles (CSP) (Long and Azam 1996) for aggregate structure. The first marine snow microstructure investigations also confirmed

*Correspondence: andreas.rogge@awi.de

these findings and provided insights into organism distribution (Heissenberger et al. 1996a; Leppard et al. 1996).

Microorganisms within organic aggregates benefit from highly concentrated substrate conditions (Shanks and Trent 1979; Lyons and Dobbs 2012) which characterize them as microscale nutrient patches in an otherwise homogeneous water column. Microbial abundances can be 10^3–10^5-fold higher than in the surrounding water column (Waite et al. 2000) and are typically associated with comparatively high-metabolic activity (Lyons and Dobbs 2012). Direct measurements of primary and bacterial production (Gotschalk and Alldredge 1989; Turley and Stutt 2000) and extracellular enzymatic activity (Karner and Herndl 1992; Zoppini et al. 2005) typically display enhanced values on aggregates relative to the water column.

Genomic profiling has also revealed that phylogenetic diversity of microbial assemblages associated with aggregates can differ from free-living communities (DeLong et al. 1993; Rath et al. 1998; Fontanez et al. 2015). Additionally, phylogenetic analyses revealed the presence of microbial communities capable of performing rare pelagic nutrient cycling processes such as ammonification (Shanks and Trent 1979), nitrification (Phillips et al. 1999), or methane production by archaea (Marty 1993; Maarel et al. 1999). Early studies suggested the potential existence of sub- or anoxic microzones within aggregates (Gowing and Silver 1983; Paerl and Pinckney 1996), and more recent work has demonstrated sub- and anoxic metabolic processes, such as anammox (Woebken et al. 2007), sulfate reduction (Vojvoda et al. 2014), or even chemolithoautotrophy (Swan et al. 2011) within aggregates from oxic or suboxic environments.

Based on a size-resolved particle model, Bianchi et al. (2018) estimated very recently that the anaerobic niche in the world oceans is expanded by particle-associated microenvironments which increases the rates of denitrification and sulfate reduction in the water column massively. Direct quantification of those and other nutrient turnover rates associated with marine snow, however, is difficult because numerous aggregates are required to generate results above measurable threshold values. This in turn necessitates bulk measurements which can be challenging to interpret due to the heterogeneous nature of aggregates. Furthermore, there is potential overlap of opposing metabolic pathways that can result in cryptic elemental cycling within single aggregates, as recently observed for the pelagic sulfur cycle in the Peruvian OMZ (Canfield et al. 2010). Emerging techniques such as single-cell measurements using nanoscale secondary ion mass spectrometry (NanoSIMS), or other modern technologies requiring vacuum conditions like electron dispersive X-ray, are powerful tools with the potential to yield insights into aggregate-associated nutrient fluxes. However, microzone investigations on marine aggregates that combine single-cell visualization, uptake measurements, and porosity measurements pose a significant challenge. Notable difficulties include (1) the preservation and handling of fragile

marine snow to reduce material loss, (2) the possibility for specific structural staining processes with reduced sample loss and dye precipitation, (3) the preservation of the three-dimensional (3D) structure enabling structure reconstruction for calculations of porosity and 3D fractal dimension, (4) the suitability for stable isotope enrichment measurements using NanoSIMS analyses with minimal enrichment dilution, and finally (5) stable storage conditions to ensure effective analyses in the field and at shore-based laboratories.

Here, we present a multidisciplinary method synthesis to address the challenges stated above, resulting in a widely applicable approach for microscopic investigations of marine snow, uptake measurements employing NanoSIMS, and structure reconstruction to facilitate porosity calculations. The characteristics of the resulting specimen matrix, including vacuum stability and negligible nitrogen and sulfur content, provide great potential for NanoSIMS-based flux investigations of individual organisms within an aggregate. Moreover, a streamlined workflow for biological and structural fixation combined with stable storage enables effective analyses in the field or at shore-based laboratories. Our preliminary investigations, as well as the recent literature (McGlynn et al. 2015), indicate that the fixation and storage conditions optimized for NanoSIMS and structural staining are potentially compatible with taxonomic staining procedures, such as fluorescence in situ hybridization (FISH) or catalyzed reporter deposition in situ fluorescence hybridization (CARDFISH), but this aspect of the method requires further optimization beyond the scope of the present objectives (*see* Supporting Information Chapter 1). A complementary embedding approach based on cryogel embedding is described in the companion paper by Flintrop et al. (2018), which enables taxonomic identification using FISH. We provide direct comparison of the two approaches (*see* "Discussion" section).

Using the plastic resin embedding procedure and structural stains, we describe a simplified calculation to determine porosity and fractal dimension based on a 3D reconstruction model. We also provide an alternative embedding protocol for aggregates comprised of very dense and/or terrigenous material, which allows structure-preserving bright field investigations and NanoSIMS measurements. A detailed description of the current methods and proposed applications is provided, as well as a field test of the embedding and structural staining. Our preliminary application of this approach demonstrates its potential to address existing gaps in our knowledge concerning biogeochemical fluxes as anaerobic cycling and microbial ecology of marine snow.

Methods

The final method for embedding of marine snow into an acrylic or epoxy resin consists of eight major steps (see Flowchart in Fig. 1): (1) The inactivation of biological activity and aggregate fixation with formaldehyde solution with subsequent washing in sterile seawater. Fixed aggregates are
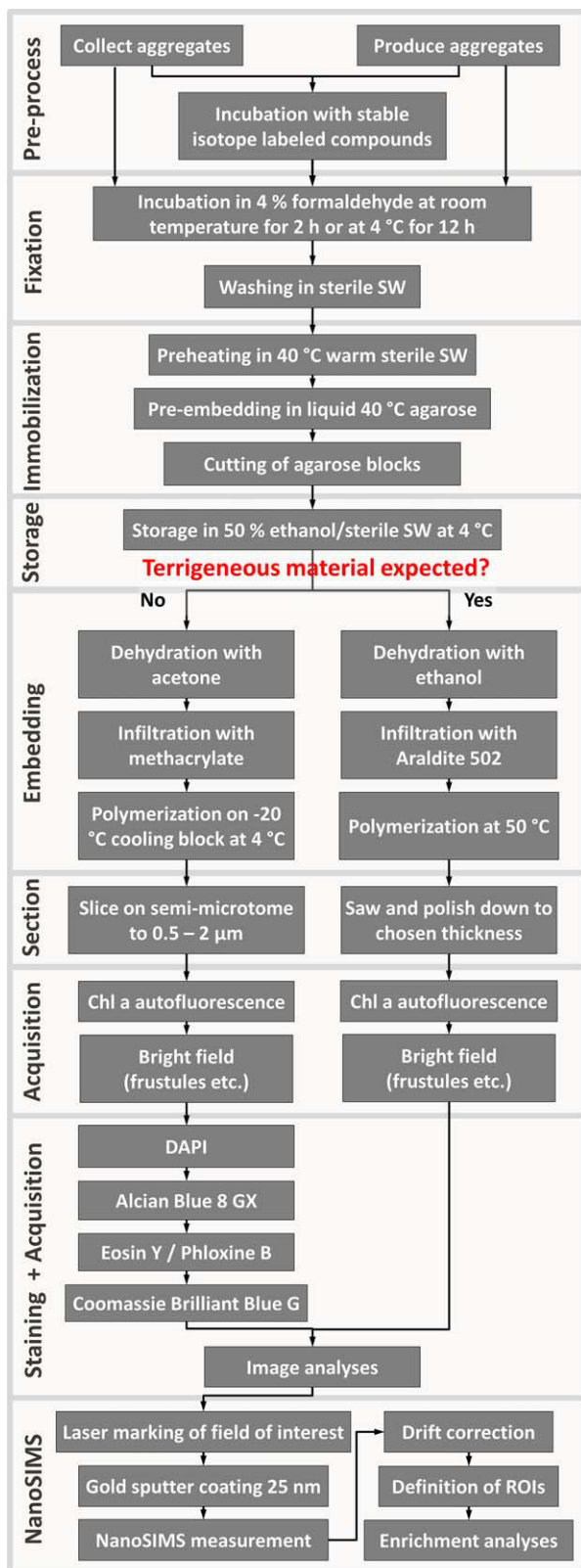
Fig. 1. Schematic outline of the presented method.

subsequently (2) immobilized and stabilized by pre-embedding in liquid agarose which can be followed by a storage step in ethanol solution. The stabilized aggregate is then (3) embedded in an acrylic or epoxy resin of choice, resulting in final structural and biological preservation, (4) sectioned and (5) stained using different structural, histological, and molecular dyes. Images of stained TEP, CSP, cytoplasm, and nucleic acid compounds as well as chlorophyll *a* (Chl *a*) auto-fluorescence are acquired and (6) structure is reconstructed in two or three dimensions, to allow porosity calculations. Finally, (7) embedded slices are prepared for NanoSIMS investigations, including laser-marking of the fields of interest, sputter coating, and fitting into the sample holder, followed by (8) NanoSIMS- and post-analysis.

In order to create a method suitable for structural staining and NanoSIMS analyses, we performed laboratory tests using a range of laboratory-generated aggregates, produced under controlled conditions (see details below). Mixed plankton communities were supplemented with natural marine bacterioplankton, and then incubated for 24 h with stable isotope-labeled glucose, nitrate, and sulfate (see below). We tested agarose as a pre-embedding matrix and the histological resin methacrylate as a final embedding medium. We applied several staining procedures, including Alcian Blue staining for TEP, Coomassie Blue staining for proteins, DAPI staining for nucleic acids, and eosin staining for eukaryotic cytoplasm proteins. The different structural signals were merged and a 3D model was created to illustrate the preserved structural features. NanoSIMS measurements were performed on one of the test aggregates to demonstrate the capacity to investigate single-cell element uptake employing the presented approach. To assess potential difficulties during the slicing process for aggregates with dense or terrigenous material, we also performed a test on dense aggregates, using agarose as a pre-embedding matrix and the resin Araldite 502 as a final embedding medium. This enables more precise sectioning for dense aggregates.

Generation of aggregates from laboratory phytoplankton cultures and surface water

Laboratory aggregates for methacrylate embeddings tests included a mixture of *Thalassiosira hyalina*, *T. marinoii*, *Emiliania huxleyi*, and *Micromonas pusilla* cultures in equal parts. This ensures applicability of the method for a diversity of aggregates by including soft as well as hard compounds, such as diatom frustules and coccoliths. Cultures were grown in F/2r medium (Guillard and Ryther 1962) with 12/12 h dark/light cycles for 7 d until the culture was opaque (cell numbers or growth phase not determined) before transfer of 1.8 L of culture mix into 2.1 L roller tanks. For bacterial colonization, 300 mL of 2 μm prefiltered North Seawater sampled in May off Bremerhaven (Germany) was added to the roller tanks (cell numbers not determined). The cultures were allowed to aggregate for 2 d at 2 rpm and 15°C in roller tanks in the dark.

In order to create very dense aggregates for alternative Araldite 502 embeddings, surface water sampled in March off Helgoland (Germany) was aggregated in roller tanks as described above for 4 weeks followed by direct fixation and embedding (*see* iii (b) "Methods" section) without prior incubation with stable isotope labeled compounds.

Stable isotope enrichment incubations

Aggregates containing stable-isotope-enriched organisms for NanoSIMS tests were formed by incubating laboratory generated aggregates in roller tanks with ^{13}C-labeled glucose, ^{15}N-labeled potassium nitrate, and ^{34}S-labeled sodium sulfate (see details below). Background concentrations of nitrate and sulfate in the sterile (0.2 μm filtered) North Seawater (sNSW) were measured prior to incubation using a QuAAtro39 Auto-Analyzer (Seal Analytical) to ensure correct labeling of ^{15}N and ^{34}S. All aggregate handlings and transfers were performed very gently, using either a bore pipette or a 1 mL pipette with cut pipette tips (*see* Table 1).

The lab aggregates were separated from free-living microorganisms by transferring each aggregate into a 50 mL centrifugation tube filled with sNSW. The aggregates were allowed to settle in the tube without reaching the bottom and then transferred into another tube with fresh sNSW, followed by transfer into a 50 mL roller tank. Triplicate 50 mL roller tanks, including 20–30 "washed" aggregates, were spiked with 10% ^{15}NO$_3$ (Cambridge Isotope Laboratories, Cat.-No. NLM-765-PK) and 15% ^{34}SO$_4$ (Sigma-Aldrich; Cat.-No. 718882) of the respective ambient concentration (12.47 μM NO$_3$, 25.44 mM SO$_4$), as well as 100 nM ^{13}C-glucose (D-glucose-^{13}C$_6$; Sigma-Aldrich; Cat.-No. 389374; background concentration not determined). Roller tanks were closed with a silicon stopper and rotated at 1.25 rpm and 15°C in the dark for 24 h before harvesting and embedding. To ascertain enrichment detection, triplicate controls were incubated with the same amount of unlabeled compounds and both groups analyzed to ensure an appropriate number of enriched aggregates for the analyses.

Aggregate embedding and analysis protocol

Biological fixation in formaldehyde solution and washing followed by immobilization in agarose is the first step in the procedure (Fig. 1). This step is the only step executed in the field. This prevents the risk of disaggregation during subsequent procedure and enables quick and easy sample handling during field campaigns as well as stable storage. The following dehydration, infiltration, and polymerization with resin enables thin sectioning of the aggregates in preparation for microscopy and SIMS analyses. A list of materials required is provided in Table 1.

i. Inactivation of biological activity and aggregate fixation

At the end of the 24 h aggregate incubation period, or immediately after aggregation in case of dense surface-water aggregates, aggregates were fixed in petri dishes filled with 0.2 μm-filtered 4% (v/v) formaldehyde/sNSW solution for 2 h at room temperature or at 4°C overnight (12 h). Stable isotope-labeled aggregates were subsequently washed in sNSW for 10 min and dense aggregates were washed for 30 min.

ii. Pre-embedding in liquid agarose and storage

Agarose solution was heated to boiling using a microwave. It was then kept at 40°C, along with the sNSW, in a hot water bath.

Following fixation, aggregates of both types were pre-heated by transferring them into 40°C warm sNSW for 10 min before transferring them into liquid, 40°C warm 6% (w/v) low-melting-point agarose (Omnipur® Agarose Low-Melting; EMD Chemicals) within silicon embedding molds. After cooling of the agarose at 4°C for 2 h, aggregates were cut out of the solid block using a sterile scalpel and forceps and transferred immediately into 2 mL centrifugation tubes filled with 0.2-μm-filtered 50% (v/v) ethanol/sNSW solution (molecular biology grade undenaturated absolute ethanol; Serva) to reduce biological degradation. Samples were stored at 4°C for 2 months.

iii. Embedding in acrylic resins

Final preservation was accomplished by embedding aggregates in an artificial resin resulting in solid, dehydrated, and sectionable blocks. Many resins for embedding were excluded prior to testing due to background fluorescence, polymerization temperatures above 60°C, or significant nitrogen and sulfur content rendering them unsuitable for potential rRNA-based hybridizations and NanoSIMS analyses, respectively. Moreover, hard materials such as sediments from terrigenous sources lead to rupture of the sections during the slicing process. Therefore, we tested the histology-originated methacrylate embedding medium for common "open ocean" aggregate samples which were sliced using a steel knife. We also tested the geology and soil sciences originated epoxy resin Araldite 502 which we sawed and polished to the desired thickness (40–140 μm).

(a) Methacrylate embedding for aggregates without terrigenous material

The methacrylate embedding protocol has been modified from the standard protocol (Velde et al. 1977). Dehydration was carried out in an increasing concentration series of acetone: Pre-embedded aggregates were transferred into snap cap vials and incubated twice with 50%, 70%, and 100% acetone on a tumbler for 1 h at room temperature. The methacrylate monomer was prepared by thoroughly mixing together 240 mL 2-hydroxyethyl methacrylate (Sigma Aldrich), 36 mL ethylene glycol butyl ether (Sigma Aldrich), and 0.81 g benzoyl peroxide (Luperox® A75; Sigma Aldrich). Infiltration started with a washing step with methacrylate monomer for 30 min followed by infiltration with monomer on a tumbler overnight at room temperature. Activator was

Table 1. List of required materials and instruments (n. d. = not determined).

Material	Company
Fixation	
Formaldehyde	Sigma Aldrich
sterile (0.2 μm filtered) seawater	n. d.
Petri dish	n. d.
Pre-embedding	
1 mL pipette	Eppendorf
Cut 1 mL pipette tips	Eppendorf
Bore pipette	n. d.
Agarose low-melting	Omnipur®; EMD chemicals
Sterile (0.2 μm filtered) seawater	n. d.
Embedding molds	n. d.
Microwave	Sharp
Water bath	Thermo Fisher Scientific
Scalpell	n. d.
Forceps	n. d.
50 mL centrifugation tubes	Sarstedt
Storage	
2 mL centrifuge tubes	Eppendorf
Ethanol (undenaturated for molecular biology)	Serva
Sterile (0.2 μm filtered) seawater	n. d.
Methacrylate embedding	
Forceps	n. d.
Scalpell	n. d.
Embedding molds	n. d.
Holder blocks	Custom made
Tumbler	Custom made
Refrigerator (4°C)	n. d.
Cooling blocks	n. d.
Snap cap vials	n. d.
Ultra-pure water	Millipore
Acetone	Sigma Aldrich
2-hydroxyethyl methacrylate	Sigma Aldrich
Ethylene glycol butyl ether	Sigma Aldrich
Benzoyl peroxide Luperox® A75	Sigma Aldrich
Polyethylene glycol 200	Sigma Aldrich
N,N-dimethylaniline	Sigma Aldrich
Methacrylate slicing	
Semi-automatic microtome	Leica
Humidity chamber	n. d.
Ultra-pure water	Millipore
Acetone	Sigma Aldrich
Biobond	EMS
Slides	Unimark
Heat plate	n. d.
Araldite 502 embedding	
Forceps	n. d.
Scalpell	n. d.
Embedding molds	n. d.
Tumbler	Custom made

TABLE 1. Continued

Material	Company
Snap cap vials	n. d.
Oven	n. d.
Ultra-pure water	Millipore
Ethanol (undenaturated for molecular biology)	Serva
Propylene oxide	Sigma Aldrich
Araldite 502 kit including DDSA and DMP-30	Electron microscopy sciences
Araldite 502 sectioning	
Grinding wheel	Wirtz
Carbid powder	Theodor Ehrich
Tap water	n. d.
Ethanol	n. d.
Körapox 439	Sikora
Stone saw Woco 50	Conrad
Grinding machine MPS 2 120	G&N
Grinding machine MPS 2 R 300	G&N
Aluminium oxide powder	Bühler
DAPI counterstaining	
Cover slips	Thermo Fisher Scientific
Ethanol for cleaning	Merck
4′,6-diamidino-2-phenylindole	Sigma Aldrich
Citifluor	Electron microscopy sciences
Vectashield	Vector laboratories
Ultra-pure water	Millipore
Sodium dodecyl sulfate	Merck
Alcian Blue staining	
Alcian Blue 8GX	Sigma Aldrich
Ultra-pure water	Millipore
Acetic acid	Merck
Ethanol (undenaturated for molecular biology)	Serva
Eosin staining	
Alcoholic eosin Y/phloxine B solution	Merck
Ultra-pure water	Millipore
Acetic acid	Merck
Coomassie Brilliant Blue staining	
Coomassie Brilliant Blue G	Sigma Aldrich
Ultra-pure water	Millipore
Ethanol (undenaturated for molecular biology)	Serva
Acetic acid	Merck

prepared by mixing 2 mL polyethylene glycol 200 (Sigma Aldrich) and 0.2 mL N,N-dimethyl aniline (Sigma Aldrich). All the infiltrated agarose blocks were carefully placed into individual embedding molds before 2 mL activator was added to 92 mL methacrylate monomer. The activated resin was added quickly into the molds, a holder block was placed on top of the molds and the embedding form was carefully

placed on a $-20°C$ precooled cooling block and transferred into a 4°C refrigerator to avoid high temperatures during the exothermic reaction. After polymerization, resin blocks were cleaned of nonpolymerized resin using paper towel and were allowed to dry for several days at room temperature to finalize the hardening.

(b) Alternative Araldite 502 embedding for aggregates containing hard or terrigenous material

In order to embed dense aggregates, we used the Araldite 502 Kit (Electron Microscopy Sciences; Cat.-No. 13900). Embedding medium, consisting of 100 mL Araldite 502 (Sigma-Aldrich), 110 mL dodecenyl succinic anhydride (DDSA), and 4 mL 2,4,6-Tris(dimethylaminomethyl)phenol (DMP-30) was mixed thoroughly and stored at 4°C in sealed syringes until further processing.

Agarose blocks were dehydrated in snap-cap-vials on a tumbler, using an increasing concentration series of ethanol (molecular biology grade undenaturated absolute ethanol; Serva): 70% ethanol for 10 min, followed by two times 100% ethanol for 10 min. Afterward, ethanol was replaced by propylene oxide by incubating the blocks twice for 10 min in 100% propylene oxide, which enhanced the following infiltration with monomer.

Dehydrated agarose blocks were incubated in snap-cap-vials on a specimen rotator in an increasing concentration series of embedding medium and propylene oxide: starting with 25%, 50%, and finally 75% Araldite embedding medium in propylene oxide for 1 h, respectively. At last, agarose blocks were incubated in 100% embedding medium overnight (12 h) before transferring them into embedding molds and removing air bubbles in a desiccator under vacuum. Afterward, polymerization was carried out at 60°C for a minimum of 12 h.

i. Sectioning

To study the microscale 3D structure in aggregates of different densities, embeddings were sectioned using different approaches. Methacrylate embeddings were sliced on a semi-automatic microtome using steel knives, similar to the preparation of biological tissue samples, while Araldite 502 embeddings were sectioned by sawing and polishing; similar to petrographic thin sections.

In order to reconstruct the aggregate structure in three dimensions, we sectioned a 142 μm thick portion of one of our methacrylate embedded laboratory aggregate. To demonstrate the possibility for porosity and 3D fractal dimension estimation, we used 23 of the resulting 71 planes for the structural model.

(a) Sectioning of methacrylate embeddings

Methacrylate resin blocks were sliced with a thickness of 2 μm on a semi-automatic microtome (Leica) using a steel knife. Prior to slicing, resin blocks were placed in a humidity chamber (wet paper towel in closed plastic box) for at least 30 min to soften them and ease the slicing process. Slices

were placed on a drop of ultrapure water (UW; 18.2 Ω) on a clean glass slide (Unimark) followed by drying on a heat plate for 1 h ($< 50°C$).

(b) Sectioning of Araldite 502 embeddings

Alternative Araldite 502 embeddings were grinded and polished to different thicknesses down to 40 μm at the geology section of the University of Bremen. Samples were polished on a grinding wheel (Wirtz) using silicon carbid powder (Theodor Erich) and tap water until samples were level before they were cleaned with ethanol and adhered without air bubbles onto a transparent specimen holder using Körapox 439 resin (Sikora). Specimens were sawed using a Woco 50 stone saw (Conrad) to a thickness of 500–1000 μm before rough polishing down to the approximate thickness using a MPS 2 120 grinding machine (G&N). Finally, fine grinding to the final thickness of 40–140 μm and ultra-plane surface was done on a MPS 2 R 300 grinding machine (G&N) using aluminum oxide powder (Bühler).

ii. Structural and histological staining

To prevent overlapping of individual stains, staining and microscopy was performed in succession. After DAPI staining, DAPI signal and Chl a auto-fluorescence was acquired, followed by Alcian Blue staining and acquisition, eosin/phloxine staining and acquisition, and finally, Coomassie Blue staining and acquisition.

(a) DNA staining

Methacrylate slices were embedded with DAPI oil, consisting of 1% (v/v) 4′,6-diamidino-2-phenylindole (DAPI; Sigma-Aldrich) solution (100 μg mL^{-1}), 85% (v/v) Citifluor AF1 (Electron Microscopy Sciences) and 14% (v/v) Vectashield (Vector Laboratories), and closed with a cover slip (Thermo Fisher Scientific). After image acquisition (*see* vi in "Methods" section) of the DAPI and Chl a signal, the cover slip was removed very gently and DAPI-oil was washed off the specimen using 1% (v/v) sodium dodecyl sulfate solution for 15 min at room temperature followed by a washing step in UW for 10 min at room temperature and air drying.

(b) TEP staining

Alcian Blue, a polyvalent basic dye, was used to stain the TEP-fraction of aggregates. Alcian Blue stain solution consisted of 0.125% (w/v) Alcian Blue 8GX (Sigma Aldrich), 10% (v/v) acetic acid, 25% (v/v) ethanol, and 64.875% UW. Destain solution consisted of 25% ethanol, 10% acetic acid, and 65% UW. Sliced samples were incubated for 18 h in 0.2 μm filtered Alcian Blue stain solution at 4°C followed by a washing step in destain solution for 30 min to remove excess stain and to enhance contrast before 1 min of UW-washing and air drying.

(c) Cytoplasm staining

Cytoplasm structures, including proteins were stained with Eosin; a negatively charged acidic dye that stains basic and acidophilic structures. A mixture of eosin Y and phloxine B was used to enhance bright field signal intensity. Due

to the fluorescent properties of phloxine B, this combination of stains improved signal isolation during subsequent overlapping of images required for the structural model. Acetic acid was added to alcoholic eosin Y/phloxine B solution (Merck) to a final concentration of 0.25% (v/v). Samples were incubated at room temperature for 8 min in 0.2 μm filtered stain solution and subsequently washed in 0.25% (v/v) acetic acid in 90% ethanol/UW (v/v) for 30 min at room temperature to remove excess stain and to enhance contrast before 1 min of UW washing and air drying.

(d) Protein staining

Protein staining was accomplished by using the triphenylmethane dye Coomassie Brilliant Blue in an alcoholic and acetic solution. Coomassie Brilliant Blue solution consisted of 0.1% (w/v) Coomassie Brilliant Blue G 250 (Sigma Aldrich), 20% ethanol, and 3.75% acetic acid in UW. Slides were incubated in 0.2 μm filtered Coomassie Brilliant Blue solution for 1 h at 4°C, and washed for 30 min in 20% ethanol and 0.4% acetic acid at room temperature in UW to remove stain and enhance contrast. After a short washing step (1 min) in UW, the samples were air dried.

iii. Image acquisition, two-dimensional and three-dimensional reconstruction, and porosity calculation

Images were acquired on an Axioskop 2 plus epifluorescence microscope (Zeiss) equipped with a Ph1 Plan-Neofluar 10× objective and an Axiocam MRc5 camera (Zeiss) using Zeiss' Axiovision software. Alcian Blue, eosin Y/phloxine B, and Coomassie Blue images were acquired using bright field whereas DAPI, Chl *a* autofluorescence, and phloxine using the respective excitation and emission filter set. Using the software GIMP 2 (GNU Image Manipulation Program; Kimball et al. 1997–2017), images were contrast and brightness corrected. For overlap images, respective specific original channels (Coomassie and Alcian Blue, blue; DAPI, blue and cyan; Chl *a* autofluorescence as well as eosin/phloxine, red) were overlapped whereas residual channels were converted to the transparent alpha channel. For better visibility, colors were changed, i.e., when combining Alcian Blue and Coomassie Blue resulting in two blue channels (See figure descriptions). For the 3D model, aggregate positions of the individual planes were aligned manually (shift and rotation function) followed by aligning the dimensions (cut function). Construction of the 3D model was accomplished by importing all planes per channel as hyperstack into the FijiBundle (Schindelin et al. 2012) of ImageJ (Schneider et al. 2012; Schindelin et al. 2015) using the importer of the Bioformats plugin (Linkert et al. 2010). The selected channel stacks were merged and the model calculated using the 3D-Viewer plugin (Schmid et al. 2010).

Porosity calculations were accomplished by merging all channels and thresholding the resulting stack with the optimal value to a binary stack. In every plane, the aggregate was defined manually by using the ROI-Manager tool (region of interest [ROI]) followed by interpolating those ROIs into three dimensions using the Interpolate ROIs tool of the ImageJ plugin BoneJ (Doube et al. 2010). Afterward, the percentage of pore volume to total aggregate volume inside the interpolated 3D-ROI was calculated using the surface mesh-based Volume Fraction function of BoneJ resulting in % of empty space or % porosity. The aggregate inside the interpolated 3D ROI (surface mesh) was visualized within the 3D-Viewer plugin of ImageJ.

Three-dimensional fractal dimension was calculated using the Fractal Dimension tool of BoneJ. The tool estimated the fractal dimension of the binary image stack by applying the box-counting algorithm as described for trabecular bone elsewhere (Fazzalari and Parkinson 1996). The program scanned boxes of diminishing size over the images and the number of boxes of each size containing foreground (aggregate) is counted. As the box size decreases, the proportion of boxes containing foreground increases in a fractal structure. The slope of the resulting linear function equals the fractal dimension.

iv. NanoSIMS preparations

Laser marking of spots of interest as well as bright field and DAPI image acquisition for later identification was carried out using a LMD7000 microscope (Leica) for labeled samples as well as controls. LMD-marked samples were cut to sample holder size using a glass cutter (Silberschnitt) and sputter coated with 25 nm gold using a 108 auto sputter coater (Cressington).

v. NanoSIMS measurements of single cells, image acquisition, and data processing

In order to measure single-cell uptake of stable-isotope-labeled glucose, nitrate, and sulfate, NanoSIMS imaging was performed using a NanoSIMS 50L instrument (Cameca, France) at the Leibniz-Institute for Baltic Sea Research Warnemünde (IOW). A $^{133}Cs^+$ primary ion beam was used to erode and ionize atoms of the sample surface. Six mass detectors equipped with electron multipliers (Hamamatsu) were used to record the received secondary ions $^{12}C^-$, $^{13}C^-$, $^{12}C^{14}N^-$, $^{12}C^{15}N^-$, $^{32}S^-$, and $^{34}S^-$ from the LMD-marked areas simultaneously. To suppress interferences, the mass resolving power was adjusted, allowing the separation of, e.g., $^{12}C^{15}N^-$ from interfering ions such as $^{13}C^{14}N^-$. Sample areas were sputtered for 1 min with 600 pA prior to analysis to reach the steady state of secondary ion formation. The primary ion beam current during the analysis was 2–3 pA; the scanning parameters were 512 × 512 px for areas of 20 × 20 μm to 60 × 60 μm, with a dwell time of 250 μs per pixel. Up to 120 planes were recorded.

The scans of each mass were accumulated and shift-corrected using the software Look@NanoSIMS (LANS; Polerecky et al. 2012). Cells were defined as ROI based on the $^{12}C^{14}N$ signal using the interactive threshold tool of the

same software. Isotope abundances for ^{13}C, ^{15}N, and ^{34}S were calculated and exported for each cell. Prokaryotic and algal cells were identified by shape using the DAPI, Chl *a*, and Bright Field image acquired prior to analysis.

Isotope abundances of individual ROIs of the labeled samples were corrected using the methacrylate resin as internal standard. The average stable isotope abundance of the resin of the unlabeled control measurements was subtracted from the stable isotope abundance of the resin of each measurement of each labeled sample. The resulting correction value was then added to each ROI of the respective measurement.

Enrichment threshold was defined for each type of heavy isotope as the maximum Poisson Error, calculated by LANS, of the unlabeled standard cells, respectively. Cells containing values greater than the threshold were defined as enriched. NanoSIMS images of the different isotope ratios were prepared as hue, saturation, and intensity (HSI) images using the software ImageJ and the plug-in OpenMIMS (Gormanns et al. 2012).

Field test using in situ collected marine snow

Aggregate samples were collected during the research cruise PS99 in July 2016 on board RV Polarstern west off Svalbard (78°58.85′N, 9°30.58′E) using a marine snow catcher (Osil, UK) with a volume of 100 L at 50 m depth. After recovery of the marine snow catcher, aggregates were allowed to settle down to the bottom chamber. The bottom chamber was then removed, and aggregates were harvested by hand using a 1 mL pipette with cut pipette tips. Fixation, storage, and methacrylate embedding as well as sectioning, DAPI, and TEP staining were performed as described in the main protocol above.

Assessment

The key challenges of microscale research on intact marine snow are (1) to reduce the loss of material, (2) ensure specific staining of structural compounds, (3) preserve the 3D structure to enable structure reconstruction for calculations of porosity and fractal dimension, (4) produce suitable samples for stable isotope enrichment measurements using nano-scale secondary ion mass spectrometer analyses with reduced enrichment dilution, and (5) to optimize the storage period to ensure effective analyses in the field and at shore-based laboratories. We tested how the method overcomes these challenges on laboratory-generated phytodetritus and also provide a (6) field test of the embedding principle by applying nucleic acid and TEP stain on methacrylate embedded marine snow sampled west off Svalbard.

Loss of material

While our method prevents loss of insoluble material during the washing and staining procedures that follow embedding, it is very difficult to estimate any loss of material during the embedding process itself. Appropriate approaches to address material loss during handling are currently lacking. Considering the limited physical interaction with the aggregate surface following pre-embedding, it is reasonable to assume that the risk of losing insoluble material is limited to the period prior to completion of pre-embedding. Until this point, however, aggregates should be handled very carefully to reduce material loss and retain structural integrity during transfer. In particular, it is important to minimize the volume of water surrounding the aggregate to < 200 μL when it is transferred into agarose. Otherwise, dilution effects can result in soft pre-embeddings that perturb structure. Following these careful handling techniques, TEP structures and proteins remain undisturbed and are clearly arranged around algal cells (Fig. 2A,C, Supporting Information Fig. S1), demonstrating the procedure is capable of preserving aggregate structure.

It is also difficult to fully account for the loss of soluble material in water and the organic solvents (acetone or ethanol) used during resin embedding and the staining process. Nevertheless, we could clearly observe visible pigments in the chlorophyll auto-fluorescence signal (Fig. 2B), suggesting that pigments remain intact and can be used to visualize chloroplasts.

One possible limitation of our method is that the presence of very hard compounds, such as terrigenous material and diatom frustules, may lead to rupture of the specimen during the slicing process. We found that ensuring the use of newly sharpened knives on the microtome was able to prevent sample rupture in the presence of numerous diatom frustules. However, this is more problematic in the case of terrigenous material since the risk of damaging the microtome knife is very high. For aggregates of this nature, we recommend Araldite 502, instead of methacrylate, which is a more appropriate resin for hard embeddings (Fig. 3). Araldite 502 can be sawed and polished down to different section thicknesses. The equipment we had available when applying the Araldite 502 embedding procedure produced relatively thick sections (> 40 μm) that showed optimal characteristics for NanoSIMS as reported elsewhere (Herrmann et al. 2007; Mueller et al. 2012; Kaiser et al. 2015). However, structural staining was not applicable to Araldite 502 slices > 40 μm and it was only possible to prepare one slice per aggregate.

During the staining of methacrylate resin slices, detachment of the slice from the microscope slide may lead to the establishment of folds and sample loss. In order to address this limitation, we experimented with the use of adhesive coated slides (Biobond; Electron Microscopy Sciences), which proved successful for structural staining. However, also other adhesives, such as poly-L-lysine are widely used for this purpose (Huang et al. 1983; McGlynn et al. 2015). In our tests, also the use of a mixture of 2–10% acetone in UW as bedding between the slide and slice resulted in improved bonding characteristics that eliminated folding artifacts.
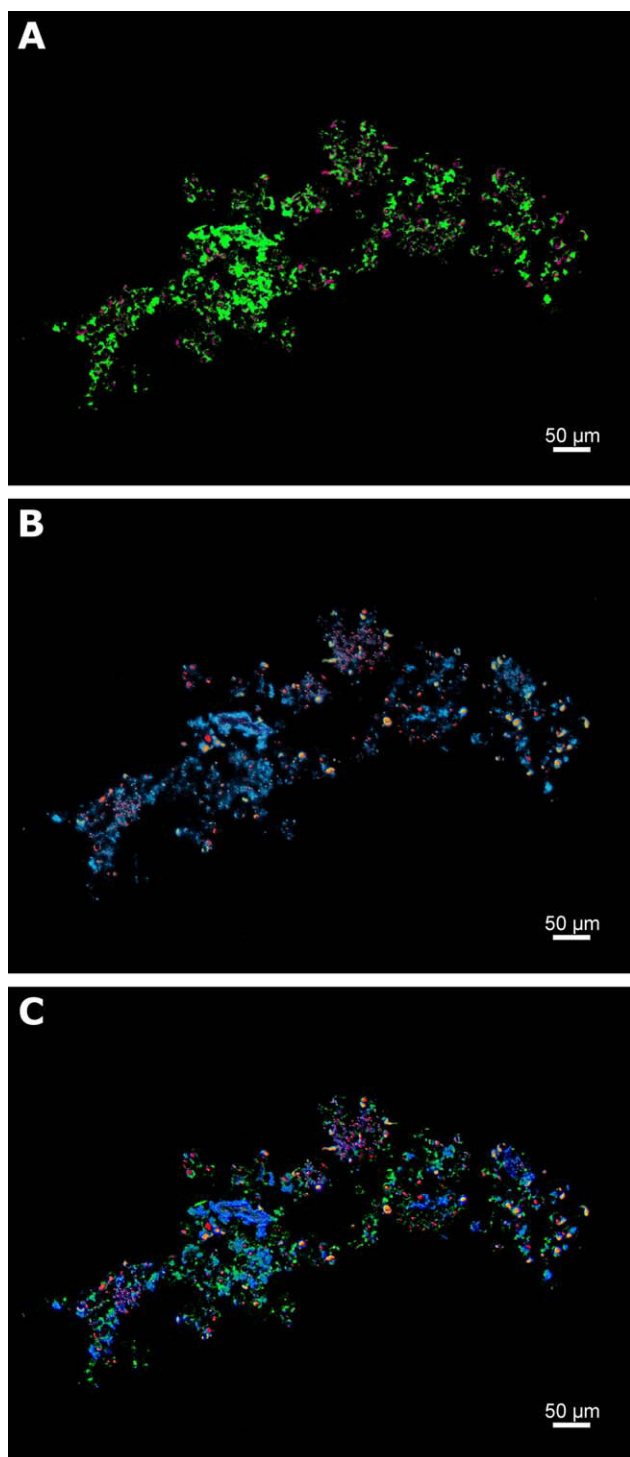
Fig. 2. Image overlap of the staining approaches. (**A**) Structural compounds TEP (green) and Coomassie stained proteins (magenta). (**B**) Distribution of nucleic acids stained with DAPI (blue), chlorophyll (red), and eukaryotic cytoplasm stained with eosin Y/phloxine B (yellow). (**C**) Overlap of all compounds mentioned above. Note that nucleic acid-rich areas without chlorophyll represent prokaryotes. Prokaryotes are distributed around algal cells and within a TEP matrix. Original images of each channel are provided in the Supporting Information Figs. S2–S7.
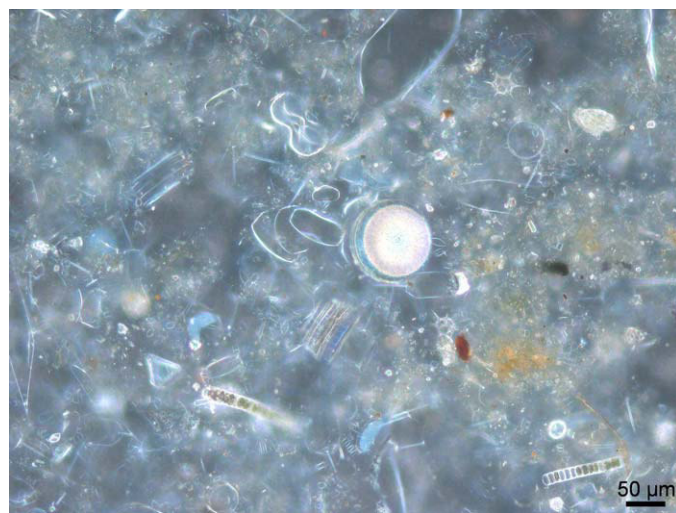

Fig. 3. Bright-field micrograph of an 80 μm thick slice through an Araldite 502 embedded aggregate formed from surface water off Helgoland, Germany. The resin did not allow structural staining, but valves and pigments are clearly visible. Araldite 502 sections are also amenable to NanoSIMS.

Stainability

The result of the different staining approaches for polysaccharides, proteins, cytoplasm, and nucleic acids are summarized in Fig. 2. Figure 2A exemplifies structural TEP and CSP staining, Fig. 2B shows organism distribution by visualizing nucleic acids, chlorophyll, and eosin, and Fig. 2C is an overlap of all channels. Examples for original images are provided in the Supporting Information Figs. S2–S7.

DAPI staining showed clear results that were distinguishable from background values, especially under higher magnification (Fig. 4). Prokaryotic cells were densely distributed around algal cells embedded within TEP-structures (Fig. 2B and Supporting Information Fig. S2). While the use of DAPI-oil is fast and convenient, we observed that even with anti-fading solution (Vectashield) bleaching of the dye occurred relatively quickly, by observation with UV-light ($\sim$ 5 min). An aqueous staining approach followed by embedding in anti-fading solution as reported for methacrylate embedded tissue might provide better results in cases where longer observation times are required (Bako et al. 2015).

Staining with Alcian Blue is a well-established method, which enables the visualization of negatively charged, sulfated, and carboxylated polysaccharides (Decho 1990) and was first reported for transparent exopolymeric particles by Alldredge et al. (1993). There are no reports of Alcian Blue staining of TEP-compounds with methacrylate embedded samples; however, we were able to achieve successful staining when applied in an ethanol solution. The stain is distinctly visible and the localization of TEP around algal cells follows the expectation that phytoplankton exudates would be present in aggregates (Fig. 2A, Supporting Information
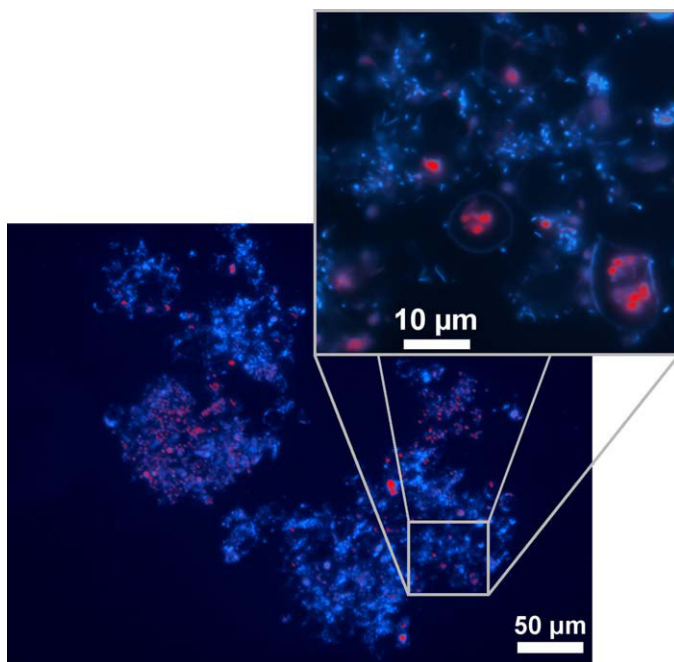
Fig. 4. Two micrometer thick slice of the methacrylate embedded aggregate used for NanoSIMS: The overlap of the DAPI stained nucleic acid channel in blue and the red Chl *a* autofluorescence channel enables the identification and distribution of prokaryotes and algae. Bigger cells with red compartments are chloroplast containing algae which are mostly surrounded by small prokaryotes without chlorophyll. The inset area represents area analyzed by NanoSIMS (*see* "Utility for stable isotope enrichment measurements" section). Note that cells and compartments that are not in focus are located in deeper slice layers and might not appear in the surface based NanoSIMS image.

Fig. S1). Importantly, dye coagulation or interference with salts which lead to overestimations of TEP signals as reported for staining in situ or on filters (Passow and Alldredge 1995; Cisternas-Novoa et al. 2015), can be excluded here. Since aggregate sections are still embedded within the resin during the staining process, it is possible to remove Alcian Blue particles by intense washing without risking sample loss.

Eosin, a halogenated derivative of fluorescein, binds to basic poly-amino acids, such as histidine, arginine, lysine, and tryptophan under acidic conditions (Waheed et al. 2000). It is a well-established and commonly used method to stain eukaryotic cytoplasm in histology (e.g., Veta et al. 2014), whereas mainly negatively charged bacterial cytoplasm may be stained with other dyes instead (Becerra et al. 2016). In combination with phloxine B, a chemically related compound to eosin Y, it is possible to increase bright-field intensity and enhance fluorescence signals (Carvalho and Taboga 1996; Aylon et al. 2016) (Fig. 2B, Supporting Information Figs. S5, S6). In our laboratory aggregates, the signal of eosin Y/phloxine B overlapped with chlorophyll, which is expected since eukaryotic organisms were the only cytoplasm containing cells stainable with eosin. This results in a

combined approach necessary for total cytoplasm visualization in future studies.

Coomassie Brilliant Blue, originally used to stain proteins in polyacrylamide gels (Fazekas et al. 1963), is a common dye for proteinaceous particles in the water column (Long and Azam 1996). We show that when applied in an alcoholic and acidified solution, it is also possible to stain methacrylate sections (Supporting Information Fig. S7). However, we only detected distinct CSP signals within internal algae structures (Fig. 2A), i.e., no external signals were visible. It is possible that since Coomassie Brilliant Blue staining was done after TEP staining the stains overlapped precluding the identification of CSP structures within the aggregate. Alternatively, the lack of areas with exclusive extracellular CSP labeling might also be explained by aggregate composition. Differences would be expected in aggregates with TEP-producing eukaryotic algae and microbes only, compared to different types of particles (CSP) produced by different species such as cyanobacteria at different growth phases (Cisternas-Novoa et al. 2015). However, due to the observation of stained protein-containing algal structures, CSP remains a possibility for staining in future studies. As reported for Alcian Blue staining above, an overestimation of CSP by dye precipitation can be excluded by intense washing of the specimen without sample loss.

Alternative Araldite 502 embeddings for dense aggregates were not stainable with any of the dyes tested above. However, observation of nontransparent compounds, such as frustules and pigments was possible (Fig. 3).

Three-dimensional aggregate structure

Two-dimensional visualizations enable investigations on organism distributions, including algae-bacteria associations or inter-cellular material distributions such as TEP or CSP (*see* Fig. 5C). However, structural investigations on porosity or fractal dimension require the implementation of the third dimension. Therefore, we demonstrate the reconstruction of a 3D structure using 23 of 71 planes of a 142 μm thick segment of a laboratory-generated aggregate (Fig. 5).

Using the plugin BoneJ, we calculated the number of voxels (volumetric pixels) filled by particulate material (merged channels of TEP, CSP, nucleic acid chlorophyll, and cytoplasm) and the total number of voxels. Definition of the aggregate boundary is difficult and controversial, and currently beyond the scope of this study. To illustrate the possibility of porosity calculation, using our embedding method, we defined the boundary manually as close as possible to the particulate material while including pores (*see* Fig. 5C). For future investigations, we recommend a standardized approach to define the boundary, such as by applying a modified script of the automatic ROI definition tool in ImageJ or elliptical approximations of the boundary using the estimated cross-sectional area as reported elsewhere (Dörgens et al. 2015; Flintrop et al. 2018). In this
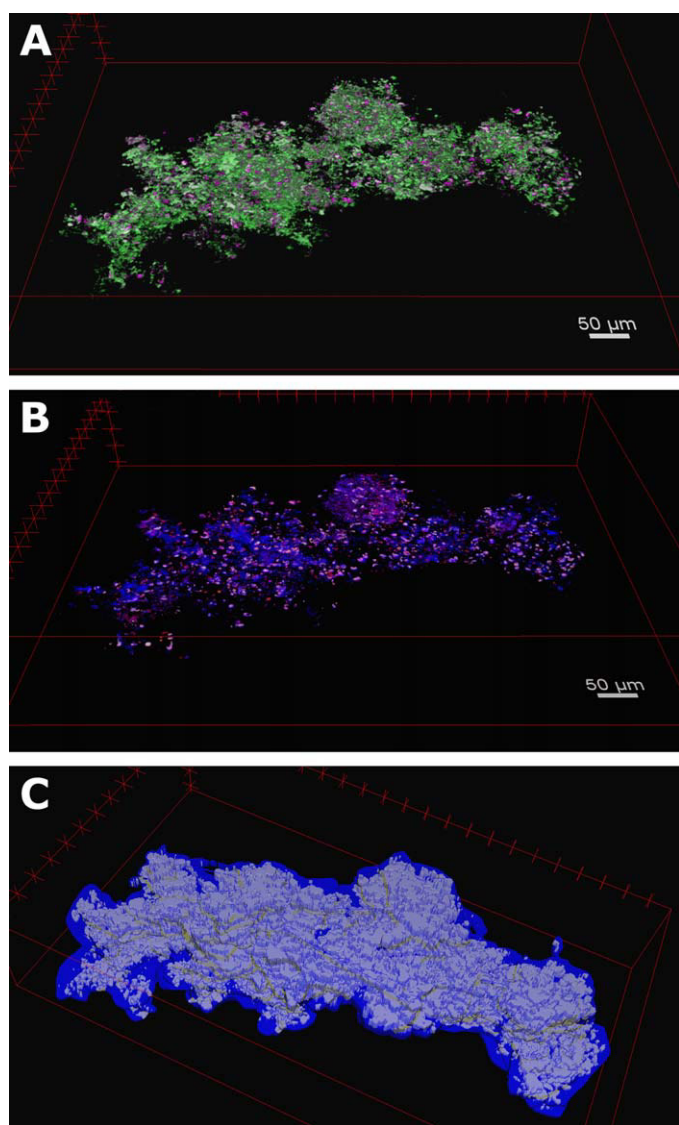
Fig. 5. Three-dimensional reconstruction of an aggregate segment. (**A**) Structural compounds TEP (green) and Coomassie Brilliant Blue stained proteins (magenta). (**B**) Nucleic acids (blue) and chlorophyll (red) as well as eukaryotic cytoplasm (yellow). (**C**) Visualization of the porosity calculation using BoneJ. All channels were merged and converted to a binary stack, whereas a 3D ROI (blue) defined the boundary of the aggregate.

demonstration, we used 23 of 71 planes, but we recommend using as many planes as possible to increase precision. We estimated a porosity of 66.5% in our test aggregate compartment. This is somewhat low compared to other calculations of phytodetritus aggregates (97–99.9%; Alldredge and Gotschalk 1988) and is closer to values reported for copepod fecal pellets (Ploug et al. 2008). Previous estimates of marine aggregate porosity are based on volume to dry weight ratios (Alldredge and Gotschalk 1988; Ploug et al. 2008). The approach employed here was based exclusively on volumetric ratios, i.e., the ratio of stained hydrated compounds to

total aggregate volume. Water-containing compounds in bacteria or algae, as well as TEP or CSP may have higher volumes when hydrated leading to lower porosity estimates in our approach. This is of course a matter of definition, but when considering, that these values may be used in hydrodynamic models for aggregate and particle settling behavior, our approach might provide realistic results because water does not flow through enclosed water intrusions such as organisms, or hydrated matter as TEP or CSP. For the same aggregate portion, we also calculated a 3D fractal dimension of 2.13. Natural aggregates are characterized by fractal dimensions between 1 (tenuous and stringy) and 3 (dense and opaque) (Kranenburg 1994). The fractal dimension calculated in this approach is comparable to aggregates sampled at depths > 400 m (Risović 1998), when considering the likely differences that exists between laboratory-generated and natural aggregates.

Utility for stable isotope enrichment measurements

Methacrylate embedded samples investigated via NanoSIMS were characterized by a plane surface and a stabilized structure under ultra-high vacuum conditions with no outgassing observed. This is also evident from comparisons of epifluorescence (Fig. 4) and secondary electron images of the same region (Fig. 6). The airlock reached full vacuum (3.7–8 mbar) in 60 h after loading three 2 μm thick methacrylate samples into the chamber. When the samples were loaded into the NanoSIMS analysis chamber, normal operation vacuum (2.5–10 mbar) was reached within 15 min. This behavior indicates negligible outgassing of methacrylate when applying a slice thickness of 2 μm. Several failures on the surface, such as scratches and holes could be observed in the secondary electron image (Fig. 6), which was likely due to slightly rough handling while placing the sample into the holder. Negative effects, such as ablation, however, were not observed.

Element uptake into single cells was successfully visualized and calculated based on NanoSIMS measurements of methacrylate embedded aggregates. We observed one ^{15}N and several ^{34}S enriched organisms in laboratory generated aggregates incubated with stable isotope tracer compounds occurring predominantly in prokaryotic cells (Figs. 7 and 8). The low number of ^{15}N enriched cells may, next to inactive cells, be explained by the use of alternative nitrogen sources such as ammonia. Moreover, the location of enzymes involved in prokaryotic nitrate reduction may prevent uptake: only assimilatory reductase enzymes (Nas) are located within the cytoplasm, whereas respiratory (Nar), and dissimilatory nitrate reductase (Nap) enzymes are membrane-bound or located in the periplasm, respectively (Moreno-Vivián et al. 1999). The latter enzyme leads to direct export of nitrate reduction products out of the cell after uptake inside the periplasm.
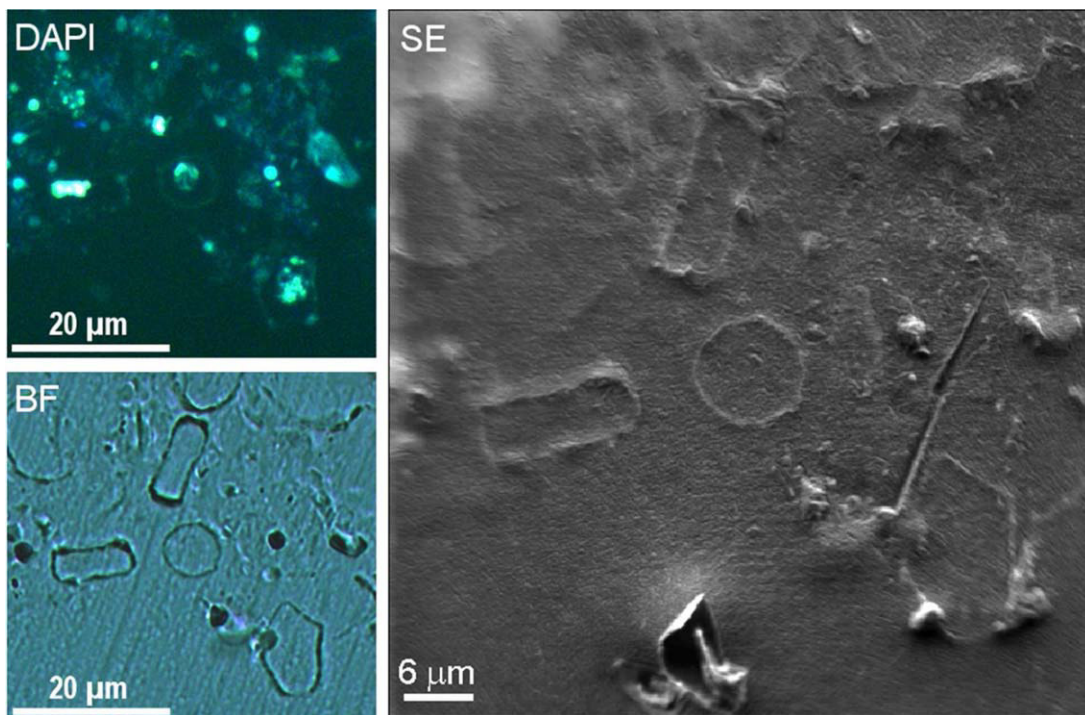
Fig. 6. Structural characteristics of methacrylate embeddings during the NanoSIMS measuring process: DAPI and bright field (BF) images were taken on a Laser Micro Dissection microscope (LMD7000, Leica) and the secondary electron image was acquired in the NanoSIMS 50L (Cameca). Structural differences caused by ultra-high vacuum as inflation, contraction, or detachment could not be observed compared to the sample structure at atmospheric pressure. Visible effects as the hole on the bottom or the scratch in the right middle were caused by sample treatment using forceps. Note that fluorescence differences to Fig. 4 are caused by removed DAPI stain and immersion oil prior to Laser marking.

Original abundance values of cells from ^{13}C incubations have on average an approximately 1‰ lower ^{13}C abundance compared to control incubations (Supporting Information Fig. S16). Higher Poisson errors associated with these cells indicate internal measurement effects as a likely explanation for this difference. These may include a different angle of the primary ion beam or slightly shifted detector positions on the mass peak of the respective isotopes due to the separation of measurements by several days. Based on the fact that all our methacrylate samples were embedded using the same batch of resin mixture at the same time, we were able to use an abundance correction approach based on resin abundances serving as internal standard. This calculation eliminates the internal measurement effects and enables correct result interpretation (Fig. 8 vs. Supporting Information Fig. S16). Taking these considerations into account, we might interpret a trend toward enrichment for a small number of ^{13}C-incubated cells as well. It is also probable that a matrix effect leads to dilution of the ^{13}C-signal in methacrylate resin embeddings. However, quantifying the dilution factor is challenging because of variable and unconstrained infiltration in different aggregates that is partly related to material density. This should be considered when combining quantitative measurements, as, e.g., total uptake measurements, with

qualitative NanoSIMS measurements of aggregates of different density. The background content of N and S in methacrylate resin is negligible, resulting in stronger signals and low dilution of ^{15}N and ^{34}S enrichments (Fig. 7). Secondary ion yields were comparable to previous applications, such as bacterial samples on gold sputtered polycarbonate filters (Rogge et al. 2017), signifying adequate ionization efficiencies in embedded samples.

The utility of Araldite 502 embeddings for ultra-high vacuum applications, such as NanoSIMS, has been demonstrated previously (Herrmann et al. 2007; Clode et al. 2009; Mueller et al. 2012; Kaiser et al. 2015). Key attributes include very low outgassing characteristics as well as structural stability without ablation. In this study, we did not specifically test its efficacy.

Storage life

In our tests, we started the final resin embedding 2 months after sampling when the agarose blocks were still intact. This time should be sufficient for sample storage during periods between most field collections and lab-based processing. We observed that 50% sterile seawater and storage above the freezing point prevents cell bursting and the presence of ethanol serves as biological preservative. Ethanol is also used as a rRNA preservative for FISH (Shiraishi et al.
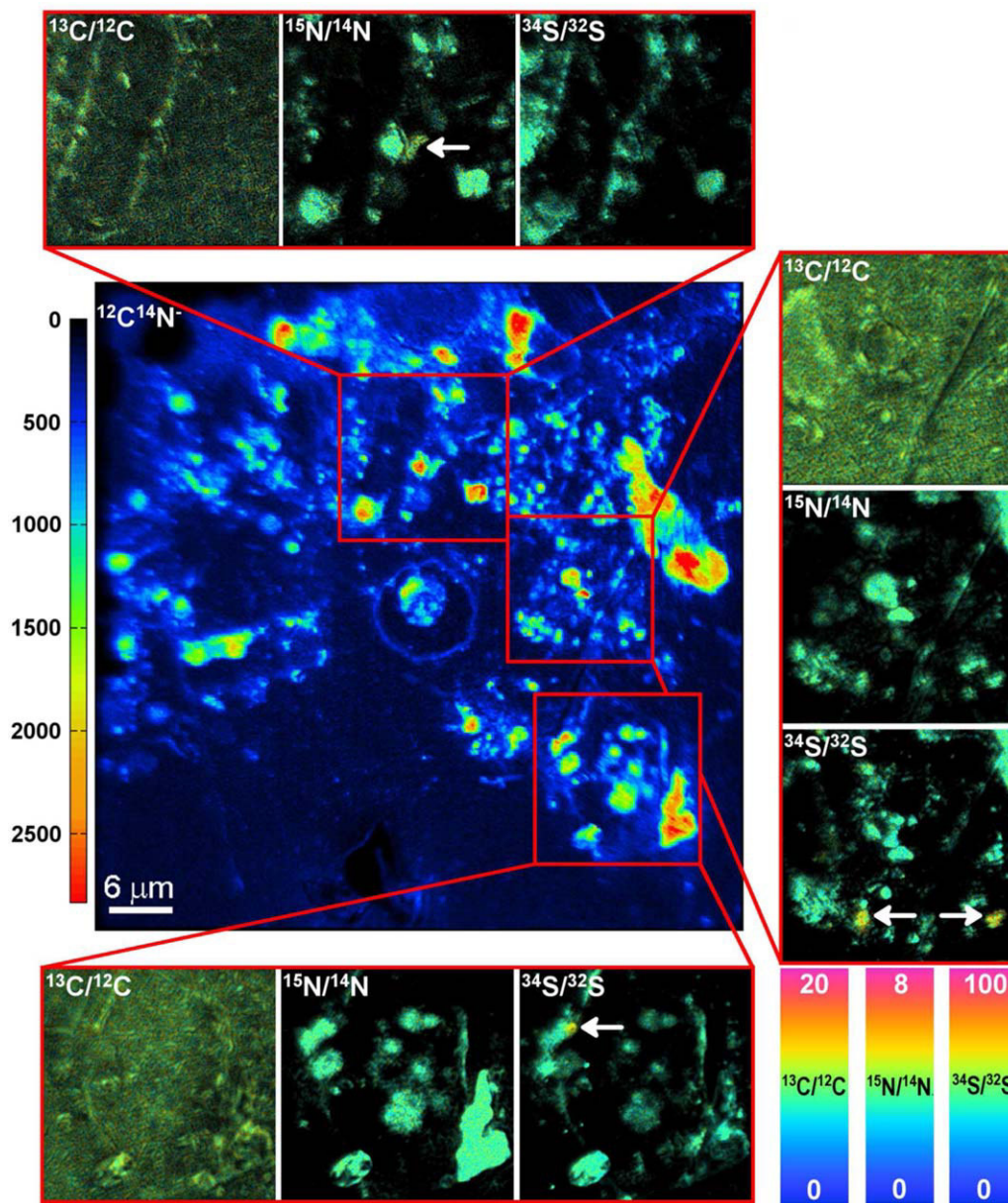
Fig. 7. Secondary ion mass spectrometry measurements on a 2 μm thick methacrylate embedded lab aggregate: The $^{12}C^{14}N^{-}$ signal as overview image was used to identify biomass and to locate spots for detailed ratio measurements. Significant and visible enrichments of ^{15}N could be detected in one prokaryotic cell in the upper spot while significant and visible enrichments of ^{34}S could be detected in the middle and lower spot. A low background in the N and S signal enables the precise definition of cells. Isotope ratios are presented as HSI-image enabling brightness adjustion of each pixel based on respective ion counts whereas black areas correspond to areas with low ion counts. The scales of isotope ratios are presented in per mill.

2008). We did not perform a time-course study of preservation properties of agarose-embedded and preserved aggregates, as it was secondary to the main issue of optimizing embedding techniques for NanoSIMS analyses. However, given previous findings using ethanol as a preservation solution for both nucleic acids and biofilm samples (Shiraishi et al. 2008), we are confident that biological components were stabilized.

Field test using in situ collected marine snow

To test aggregate handling and pre-embedding in more realistic conditions at sea, we performed aggregate sampling in Fram Strait close to the coast of Svalbard using a marine snow catcher. No difficulty in aggregate handling, leading to material loss due to disaggregation during transfer steps, could be observed. Even though the aggregates were relatively close to the coast and Kongsfjorden, the content of terrigenous material was low, so that slicing of methacrylate
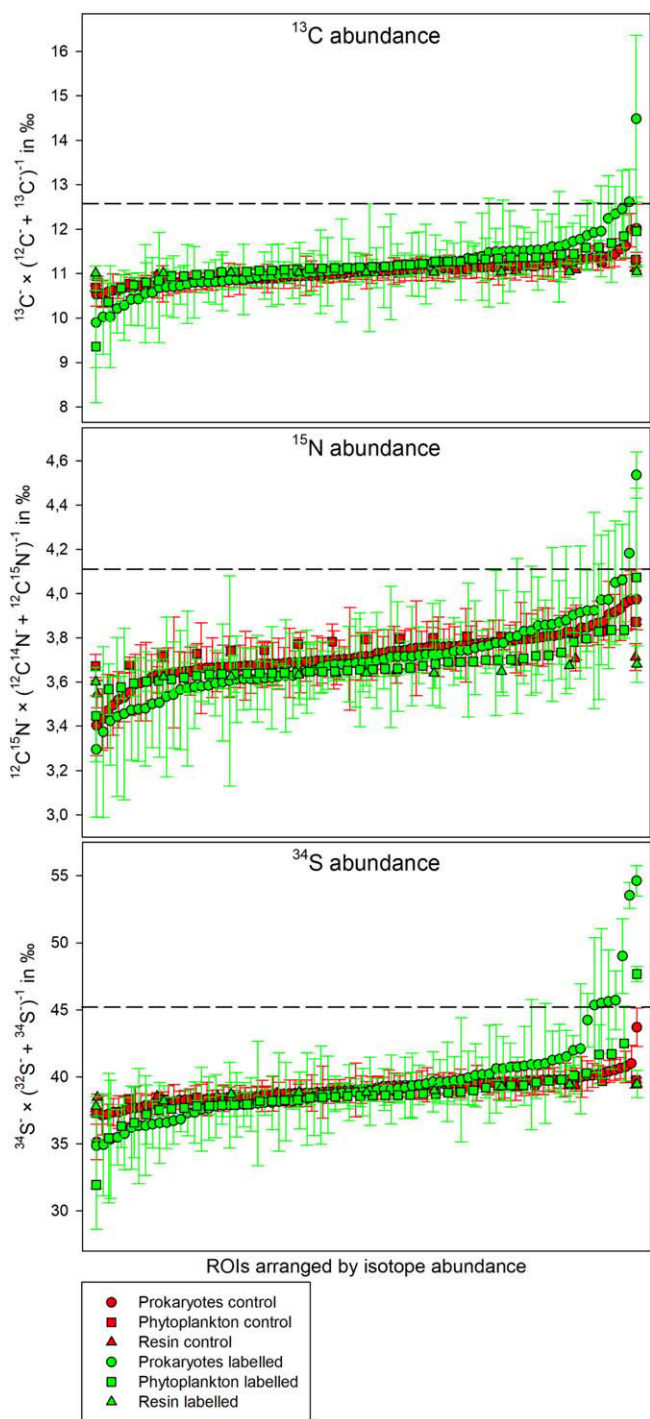
Fig. 9. Overlap micrograph of marine snow sampled off Svalbard, Norway: DAPI stained nucleic acids (blue) and Chl *a* (red) as well as Alcian Blue stained TEP (green) in top image of a slice through the whole aggregate. The bottom image, showing a part of the aggregate in higher magnification, exemplifies nucleic acid staining (blue) and Chl *a* (red).

trip: samples were resin embedded approximately 3 months after sampling and pigment localization and concentration as well as the structure is still undisturbed.

Discussion

The microstructure of marine snow is likely to impact the scale and availability of diverse microbial niches within these particles. In turn, microbially mediated transformations of particulate matter can influence the regeneration of (sometimes limiting) nutrients and carbon-specific remineralization rates. These specific processes within marine snow may affect the efficiency of the biological carbon pump, pelagic-benthic coupling, and physical transport of microbial communities. Understanding the importance of these processes within aggregates is currently limited by a lack of suitable methods. To broaden our knowledge on microscale structures, microbial communities, and uptake rates associated with marine snow, we sought to develop a multipurpose method for the preservation and slicing of marine snow that was compatible with different structural stains and NanoSIMS investigations.

Several approaches for the investigation of marine snow have been developed during recent decades. To date, these have mainly focused on characterizing features on whole aggregates, such as Alcian Blue and Coomassie Blue staining on membrane filters for total exopolymer equivalents (Busch et al. 2017) or fingerprinting and sequencing techniques for aggregate-associated microbial community structure (DeLong et al. 1993; Rath et al. 1998; Fontanez et al. 2015). For such

Fig. 8. Isotope abundances in ‰ including Poisson Errors as error bars, of all measured prokaryotic and phytoplankton cells as well as the resin itself corrected by using the resin as internal standard. The dashed line indicates the enrichment threshold (maximum value of the Poisson error of controls). Respective ROIs are shown in Supporting Information Figs. S8–S15.

was successful. As shown in Fig. 9, chlorophyll and nucleic acid signals are distinct and TEP compounds are intensely stained. Also the storage time was adequate for this field
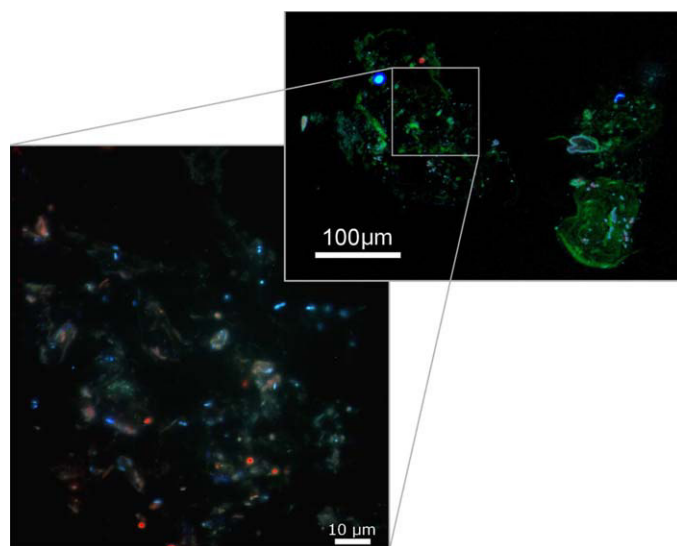
objectives, capturing particles and aggregates on membrane filters is sufficient. However, such sampling methods lead to loss of 3D structure and material and are not suitable for addressing the microscale structure of individual marine aggregates. The idea of slicing marine snow was developed for TEM investigations using the melamine resin Nanoplast® (Heissenberger et al. 1996b; Leppard et al. 1996). This resin, however, requires high-hardening temperatures of 60°C, which does not ensure intact rRNA for potential taxonomic staining (see below). Moreover, melamine contains high amounts of nitrogen, which leads to dilution of nitrogen enrichments within organisms.

Other embedding matrices for CARDFISH and NanoSIMS analyses of other types of samples include paraffin (e.g., Jaekel et al. 2013 or Musat et al. 2007) and cryogels (e.g., Wilbanks et al. 2014). Those are, however, not useful for detailed single-cell analyses in marine snow due to the impossibility of section preparations thinner than 5 μm. Additionally, paraffin must be removed after sectioning to allow staining and secondary ion mass spectrometry which increases the risk of material loss due to the high fragility of the marine snow sections dramatically. Cryogels, on the other hand, enable uninterrupted staining but the vacuum resistancy is likely to be suboptimal, and shrinking can be expected, limiting the use for biovolume-corrected enrichment calculations.

As described by Kopf et al. (2015), hard plastic resins are often too dense to allow a variety of staining techniques including CARDFISH. Kopf et al. (2015) and McGlynn et al. (2015) used Technovit, a commercially available acrylic resin. In our tests it turned out, that the also broadly used acrylic resin LR-white (Nussbaumer et al. 2006; Gros and Maurin 2008) showed a high-background fluorescence and was thus not useful for fluorescent stains, such as DAPI.

For our study, we chose a well-established embedding medium mixture based on methacrylate. Key benefits of this medium are that it enables the dissipation of heat during the exothermic polymerization and is characterized by negligible nitrogen and sulfur contents which can affect the significance of enrichment measurements. The medium was optimized for the investigation of human and animal tissue (Burkhardt 1966; Velde et al. 1977) which, like most eumetazoan tissues, contains collagen that acts as a stabilizing matrix during embedding. In contrast, the absence of collagen in marine aggregates leads to disaggregation during the dehydration and infiltration steps. In order to circumvent this limitation, our method employs a pre-embedding step to supplement marine snow with an agarose matrix. Agarose has been used previously as an embedding matrix for marine snow pellets concentrated by centrifugation (Biddanda 1986; Carlough 1994) or for small zooplankton fecal pellets (Gowing and Silver 1983). Agar embedding has been intensively used as for methanotrophic consortia from marine sediments (McGlynn et al. 2015) as well as centrifuged pellets of

bacteria and algae cells (Slaveykova et al. 2009; Kopf et al. 2015). However, as far as we are aware, our method is the first application of an agarose pre-embedding step for preserving structure of undisturbed marine snow. We used low melting-point agarose (liquid state above gelling range of 24–29°C), which facilitates infiltration into typically porous marine aggregates. Furthermore, carbon and hydrogen, the only constituents of agarose, are an advantage when performing isotopic enrichments with nitrogen and sulfur. Combined with the very low nitrogen and sulfur content in the methacrylate resin, dilutions of those elements are reduced. Carbon uptake measurements, on the other hand, require a higher labeling concentration for precise enrichment identification under the same conditions.

The objective of the present study was to develop a working protocol capable of coupling observations of the physical microstructure of marine snow with single-cell uptake rates of organisms within the aggregates. The aggregates, when treated with agarose-methacrylate embedding method, could be consistently sliced to a thickness of 2 μm and exhibited no background fluorescence from the embedding matrix.

Furthermore, we were able to demonstrate the successful staining of methacrylate embedded slices with Alcian Blue for TEP structure, Coomassie Brilliant Blue for proteins, eosin Y for cytoplasm proteins, and DAPI for nucleic acids. Microbes embedded within TEP exudates around algal cells within individual aggregates could be clearly visualized. In contrast, extracellular proteinaceous compounds were not observed in significant amounts, in the aggregates we studied. Moreover, excess Alcian Blue and Coomassie Brilliant Blue dye could be removed without sample loss, reducing any overestimation of TEP and CSP due to precipitation (Passow and Alldredge 1995; Cisternas-Novoa et al. 2015).

We were able to reconstruct the 3D structure of an aggregate portion with its biological (bacterial, algae, eukaryotic cytoplasm) as well as structural (TEP, CSP) compounds. Moreover, we provided a first step toward alternative porosity and 3D fractal dimension calculations using the software BoneJ and its tools originally constructed for trabeculae bone analyses. We have identified further need for a standardized aggregate boundary definition approach.

Thin methacrylate (2 μm) embedded slices had sufficient structural integrity for NanoSIMS analyses under ultra-high vacuum conditions (10^{-10} mbar) with workable ionization efficiencies. Retention of specimen structural integrity is absolutely critical for the calculation of cell volume-corrected elemental enrichments. This was recently demonstrated with pelagic bacteria (Rogge et al. 2017), and is important for calculating the differential uptake of specific elements by heterogeneously sized environmental microorganisms.

We were able to detect and localize prokaryotic uptake of nitrate and sulfate in our sliced marine aggregate preparations. While a dilution of carbon enrichment signals is likely given the C-rich embedding media, even in incubations with

low glucose concentrations (100 nM), a trend toward enrichments was observed visually. The use of higher labeling concentrations in future studies should provide more pronounced results. Moreover, the resin surrounding the organic matter of the aggregate can be used as internal standard to correct abundance calculations and enables precise interpretations.

As an alternative approach for very dense marine snow or marine particles with incorporated terrigenous material, we performed Araldite 502 embeddings. Resulting specimens could be sectioned to a minimum thickness of 40 μm. The applicability for NanoSIMS has already been proven elsewhere (Herrmann et al. 2007; Mueller et al. 2012; Kaiser et al. 2015). Structural staining, however, was not possible with the greater thicknesses, thereby restricting the use of this resin to investigations of nontransparent compounds, such as frustules, pigments, or terrigenous material, and uptake measurements using NanoSIMS.

Finally, we show that our method is also effective for natural aggregates, and we demonstrate the method using aggregates from polar waters off Svalbard. Even though NanoSIMS analyses were not performed on these samples, the reduction of material loss during processing as well as adequate stainability properties could be exemplified. We used the same resin and slice thickness for these samples as for the lab-generated aggregates, and the natural marine snow particles were characterized by identical or similar vacuum resistance specifications as our laboratory generated aggregates.

Future applications for marine snow would benefit from a combination of single cell uptake measurements with identification methods such as rRNA-based catalyzed reporter deposition in situ hybridization (CARDFISH) and related approaches, as demonstrated by several authors for pelagic bacteria (Musat et al. 2008; Krupke et al. 2013; Rogge et al. 2017). This would enable the investigation of physical and metabolic co-location and community structure analyses in marine snow as shown for microbial consortia from marine sediments (McGlynn et al. 2015). In parallel tests, which were not the main focus of this study, we achieved corresponding signals to both positive and negative controls. However, final hybridization optimization and stringency was never achieved and further development would be required. The protocol applied is provided in the Supporting Information Chapter 1 and a similar approach presented by McGlynn et al. (2015).

The method synthesis developed in the present study meets our objective for investigations on marine snow. The pre-embedding procedure maintains 3D structure of the samples and minimizes sample loss primarily because aggregate sections remain embedded in resin during staining process. We demonstrated the ability to identify structural components such as TEP and alkaline amino acids. The identification of prokaryotes and photoautotrophic organisms was also possible using a combination of successful nucleic acid

and eukaryotic cytoplasm staining as wells as Chl *a* autofluorescence of the embedded aggregate slices. Critically, rRNA stays intact during sample preparations with methacrylate resins enabling potential taxonomic staining using CARD-FISH techniques in future applications.

The present protocol provides an opportunity to preserve the structure of marine snow sampled at sea, and investigate microbial activity at the single-cell level within aggregates. We envisage that when our method is applied more broadly to a range of field samples, it will facilitate the development of new insights into aggregate types, sizes and structures, microbial interactions, and aggregate transformation. It will provide input for a new understanding of particle dynamics, as well as for microbial ecology.

We note that in our laboratory-generated aggregates, we also observed the uptake of SO_4, a result which will be of particular interest to follow up in the field, as it points to the potential use of alternative electron acceptors in anoxic microzones within aggregates. The global distribution of aggregate-associated anoxia which increases the global rate of sulfate reduction in the water column was very recently predicted by Bianchi et al. (2018) and our work protocol represents the first tool to investigate those processes in the marine environment. Additionally, slight modifications of the sampling and pre-embedding protocol, such as preaccumulation of aggregates using an elutriation system (Peterson et al. 2005) would enable the investigation of smaller less visible aggregates (< 500 μm). High vacuum tolerance of methacrylate and Araldite resins also allows the use of other modern technologies such as scanning transmission electron microscopy coupled to electron dispersive X-ray analyses, ultimately enabling quantitative element measurements inside organisms, and thus even further possibilities for future applications. A combination of aggregate-related turnover rates with noninvasive optical quantification systems, such as the Underwater Vision Profiler or other systems (Iversen et al. 2010; Picheral et al. 2010; Biard et al. 2016) would ultimately allow us to calculate the contribution of different size classes of aggregates as well as the proportion of involved organisms on regional turnover rates.

We envisage future incorporation into our method of the wide variety of staining protocols already available, enabling further development of application for diverse future investigations.

The cryogel approach presented by Flintrop et al. (2018) focused on structural investigation of marine snow sampled with a Marine Snow Catcher or directly from drifting sediment traps coupled to taxonomic microbial identification using FISH. An overview of major differences and overlaps between plastic resin and the cryogel embedding methods utilized by Flintrop and coworkers is presented in Supporting Information Table S1. In brief, use of a cryogel enables more detailed observations of hydrous compounds due to minimized dehydration, while the resin-embedding process' use

of formaldehyde for chemical fixation, and ethanol or acetone for dehydration, leads to potential loss of diffusible compounds (Grovenor et al. 2006; Kilburn and Clode 2014). If desirable, samples for SIMS analyses of diffusible compounds can be dehydrated using the freeze-approach as described for X-ray microanalyses by Marshall (1980) and more recently for NanoSIMS by Kilburn and Clode (2014). For analyses of nondiffusive compounds, however, acetone dehydration and plastic resin embedding is in fact a widely used method (Herrmann et al. 2007; Clode et al. 2009; Slaveykova et al. 2009; Mueller et al. 2012; Kaiser et al. 2015). Soft and hard plastic embedding resins, particularly methacrylate and Araldite 502, are characterized by ultra-high vacuum-stability, such as minimized shrinking and ablation. Those features, together with the low N and S content, enable cell-volume corrected enrichment calculations with as low as possible isotope dilution effects as reported elsewhere (Rogge et al. 2017). In combination with applicable basic stains (*see* Supporting Information Table S1), detailed elemental uptake investigations of single cells with mechanically undisturbed localization within surrounding organic matrices are possible. Smearing of embedded samples during slicing can go undetected, despite the fact that such smearing significantly reduces their optical resolution and overall effectiveness for analysis. In contrast, any distortion of the sample in a resin can immediately detected because of instantaneous rupture of the slice. Moreover, the alternative embedding matrix Araldite 502, described in this manuscript, enables uptake investigations of marine snow containing very hard compounds as, e.g., terrigenous material. A complementary application of the methods described in this and the manuscript by Flintrop et al. (2018) would enable a wide variety of possible investigations of the microbial ecology and biogeochemical cycling within marine snow as well as effects on the biological carbon pump.

References

Alldredge, A. L., and C. C. Gotschalk. 1988. In situ settling behavior of marine snow. Limnol. Oceanogr. **33**: 339–351. doi:10.4319/lo.1988.33.3.0339

Alldredge, A. L., and M. W. Silver. 1988. Characteristics, dynamics and significance of marine snow. Prog. Oceanogr. **20**: 41–82. doi:10.1016/0079-6611(88)90053-5

Alldredge, A. L., U. Passow, and B. E. Logan. 1993. The abundance and significance of a class of large, transparent organic particles in the ocean. Deep-Sea Res. Part I Oceanogr. Res. Pap. **40**: 1131–1140. doi:10.1016/0967-0637(93)90129-Q

Aylon, Y., and others. 2016. The LATS2 tumor suppressor inhibits SREBP and suppresses hepatic cholesterol accumulation. Genes Dev. **30**: 786–797. doi:10.1101/gad.274167.115

Bako, P., M. Bassiouni, A. Eckhard, I. Gerlinger, C. Frick, H. Löwenheim, and M. Müller. 2015. Methyl methacrylate embedding to study the morphology and immunohistochemistry of adult guinea pig and mouse cochleae. J. Neurosci. Methods **254**: 86–93. doi:10.1016/j.jneumeth.2015.07.017

Becerra, S. C., D. C. Roy, C. J. Sanchez, R. J. Christy, and D. M. Burmeister. 2016. An optimized staining technique for the detection of Gram positive and Gram negative bacteria within tissue. BMC Res. Notes **9**: 216. doi:10.1186/s13104-016-1902-0

Bianchi, D., T. Weber, S. R. Kiko, and C. Deutsch. 2018. Global niche of marine anaerobic metabolisms expanded by particle microenvironments. Nat. Geosci. **65**: 36. doi:10.1038/s41561-018-0081-0

Biard, T., and others. 2016. In situ imaging reveals the biomass of giant protists in the global ocean. Nature **532**: 504–507. doi:10.1038/nature17652

Biddanda, B. A. 1986. Structure and function of marine microbial aggregates. Oceanol. Acta **9**: 209–211.

Burkhardt, R. 1966. Präparative Voraussetzungen zur klinischen histologie des menschlichen Knochenmarkes. Blut **14**: 30–46. doi:10.1007/BF01633163

Busch, K., S. Endres, M. H. Iversen, J. Michels, E.-M. Nöthig, and A. Engel. 2017. Bacterial colonization and vertical distribution of marine gel particles (TEP and CSP) in the Arctic Fram Strait. Front. Mar. Sci. **4**: 1131. doi:10.3389/fmars.2017.00166

Canfield, D. E., F. J. Stewart, B. Thamdrup, L. De Brabandere, T. Dalsgaard, E. F. Delong, N. P. Revsbech, and O. Ulloa. 2010. A cryptic sulfur cycle in oxygen-minimum-zone waters off the Chilean coast. Science **330**: 1375–1378. doi:10.1126/science.1196889

Carlough, L. A. 1994. Origins, structure, and trophic significance of amorphous seston in a blackwater river. Freshw. Biol. **31**: 227–237. doi:10.1111/j.1365-2427.1994.tb00857.x

Carvalho, H. F., and S. R. Taboga. 1996. Fluorescence and confocal laser scanning microscopy imaging of elastic fibers in hematoxylin-eosin stained sections. Histochem. Cell Biol. **106**: 587–592. doi:10.1007/BF02473274

Cisternas-Novoa, C., C. Lee, and A. Engel. 2015. Transparent exopolymer particles (TEP) and Coomassie stainable particles (CSP). Mar. Chem. **175**: 56–71. doi:10.1016/j.marchem.2015.03.009

Clode, P. L., M. R. Kilburn, D. L. Jones, E. A. Stockdale, J. B. Cliff, A. M. Herrmann, and D. V. Murphy. 2009. In situ mapping of nutrient uptake in the rhizosphere using nanoscale secondary ion mass spectrometry. Plant Physiol. **151**: 1751–1757. doi:10.1104/pp.109.141499

Decho, A. W. 1990. Microbial exopolymer secretions in ocean environments: Their role(s) in food webs and marine processes. Oceanogr. Mar. Biol. **28**: 73–153.

DeLong, E. F., D. G. Franks, and A. L. Alldredge. 1993. Phylogenetic diversity of aggregate-attached vs. free-living marine bacterial assemblages. Limnol. Oceanogr. **38**: 924–934. doi:10.4319/lo.1993.38.5.0924

Dörgens, A. L., S. Ahmerkamp, J. Müssig, R. Stocker, M. M. M. Kuypers, A. Khalili, and K. Kindler. 2015. A laboratory model of marine snow. Limnol. Oceanogr.: Methods **13**: 664–671. doi:10.1002/lom3.10056

Doube, M., and others. 2010. BoneJ: Free and extensible bone image analysis in ImageJ. Bone **47**: 1076–1079. doi:10.1016/j.bone.2010.08.023

Fazekas, S., S. Groth, R. G. Webster, and A. Datyner. 1963. Two new staining procedures for quantitative estimation of proteins on electrophoresis strips. Biochim. Biophys. Acta **71**: 377–391. doi:10.1016/0006-3002(63)91092-8

Fazzalari, N. L., and I. H. Parkinson. 1996. Fractal dimension and architecture of trabecular bone. J. Pathol. **178**: 100–105. doi:10.1002/(SICI)1096-9896(199601)178:1 < 100:: AID-PATH429 > 3.0.CO;2-K

Flintrop, C., A. Rogge, S. Miksch, A. M. Waite, and M. H. Iversen. 2018. Embedding and slicing of intact in situ collected marine snow. Limnol. Oceanogr.: Methods. **16**: 339–355. doi:10.1002/lom3.10251

Fontanez, K. M., J. M. Eppley, T. J. Samo, D. M. Karl, and E. F. DeLong. 2015. Microbial community structure and function on sinking particles in the North Pacific Subtropical Gyre. Front. Microbiol. **6**: 469. doi:10.3389/fmicb.2015.00469

Gormanns, P., S. Reckow, J. C. Poczatek, C. W. Turck, and C. Lechene. 2012. Segmentation of multi-isotope imaging mass spectrometry data for semi-automatic detection of regions of interest. PLoS One **7**: e30576. doi:10.1371/journal.pone.0030576

Gotschalk, C. C., and A. L. Alldredge. 1989. Enhanced primary production and nutrient regeneration within aggregated marine diatoms. Mar. Biol. **103**: 119–129. doi:10.1007/BF00391070

Gowing, M. M., and M. W. Silver. 1983. Origins and microenvironments of bacteria mediating fecal pellet decomposition in the sea. Mar. Biol. **73**: 7–16. doi:10.1007/BF00396280

Gros, O., and L. C. Maurin. 2008. Easy flat embedding of oriented samples in hydrophilic resin (LR White) under controlled atmosphere: Application allowing both nucleic acid hybridizations (CARD-FISH) and ultrastructural observations. Acta Histochem. **110**: 427–431. doi:10.1016/j.acthis.2007.11.001

Grovenor, C. R. M., K. E. Smart, M. R. Kilburn, B. Shore, J. R. Dilworth, B. Martin, C. Hawes, and R. E. M. Rickaby. 2006. Specimen preparation for NanoSIMS analysis of biological materials. Appl. Surf. Sci. **252**: 6917–6924. doi:10.1016/j.apsusc.2006.02.180

Guillard, R. L. L., and J. H. Ryther. 1962. Studies of marine planktonic diatoms. I. Cyclotella nana Hustedt, and Detonula confervacea (cleve) Gran. Can. J. Microbiol. **8**: 229–239. doi:10.1139/m62-029

Heissenberger, A., G. G. Leppard, and G. J. Herndl. 1996a. Relationship between the intracellular integrity and the morphology of the capsular envelope in attached and free-living marine bacteria. Appl. Environ. Microbiol. **62**: 4521–4528.

Heissenberger, A., G. G. Leppard, and G. J. Herndl. 1996b. Ultrastructure of marine snow. II. Microbiological considerations. Mar. Ecol. Prog. Ser. **135**: 299–308. doi:10.3354/meps135299

Herrmann, A. M., P. L. Clode, I. R. Fletcher, N. Nunan, E. A. Stockdale, A. G. O'Donnell, and D. V. Murphy. 2007. A novel method for the study of the biophysical interface in soils using nano-scale secondary ion mass spectrometry. Rapid Commun. Mass Spectrom. **21**: 29–34. doi:10.1002/rcm.2811

Huang, W. M., S. J. Gibson, P. Facer, J. Gu, and J. M. Polak. 1983. Improved section adhesion for immunocytochemistry using high molecular weight polymers of l-lysine as a slide coating. Histochemistry **77**: 275–279. doi:10.1007/BF00506570

Iversen, M. H., N. Nowald, H. Ploug, G. A. Jackson, and G. Fischer. 2010. High resolution profiles of vertical particulate organic matter export off Cape Blanc, Mauritania: Degradation processes and ballasting effects. Deep-Sea Res. Part I Oceanogr. Res. Pap. **57**: 771–784. doi:10.1016/j.dsr.2010.03.007

Jaekel, U., N. Musat, B. Adam, M. Kuypers, O. Grundmann, and F. Musat. 2013. Anaerobic degradation of propane and butane by sulfate-reducing bacteria enriched from marine hydrocarbon cold seeps. ISME J. **7**: 885–895. doi:10.1038/ismej.2012.159

Kaiser, C., M. R. Kilburn, P. L. Clode, L. Fuchslueger, M. Koranda, J. B. Cliff, Z. M. Solaiman, and D. V. Murphy. 2015. Exploring the transfer of recent plant photosynthates to soil microbes: Mycorrhizal pathway vs direct root exudation. New Phytol. **205**: 1537–1551. doi:10.1111/nph.13138

Karner, M., and G. J. Herndl. 1992. Extracellular enzymatic activity and secondary production in free-living and marine-snow-associated bacteria. Mar. Biol. **113**: 341–347. doi:10.1007/BF00347289

Kilburn, M. R., and P. L. Clode. 2014. Elemental and isotopic imaging of biological samples using NanoSIMS. Methods Mol. Biol. **1117**: 733–755. doi:10.1007/978-1-62703-776-1_33

Kimball, S., and P. Mattis, and GIMP Development Team. 1997–2017. GIMP2; [accessed 2018 June 27]. Available from www.gimp.org

Kopf, S. H., S. E. McGlynn, A. Green-Saxena, Y. Guan, D. K. Newman, and V. J. Orphan. 2015. Heavy water and ^{15}N labelling with NanoSIMS analysis reveals growth rate-dependent metabolic heterogeneity in chemostats. Environ. Microbiol. **17**: 2542–2556. doi:10.1111/1462-2920.12752

Kranenburg, C. 1994. The fractal structure of cohesive sediment aggregates. Estuar. Coast. Shelf Sci. **39**: 451–460. doi:10.1016/S0272-7714(06)80002-8

Krupke, A., N. Musat, J. L. Roche, W. Mohr, B. M. Fuchs, R. I. Amann, M. M. M. Kuypers, and R. A. Foster. 2013. In situ identification and N_2 and C fixation rates of uncultivated cyanobacteria populations. Syst. Appl. Microbiol. **36**: 259–271. doi:10.1016/j.syapm.2013.02.002

Leppard, G. G., A. Heissenberger, and G. J. Herndl. 1996. Ultrastructure of marine snow. I. Transmission electron microscopy methodology. Mar. Ecol. Prog. Ser. **135**: 289–298. doi:10.3354/meps135289

Linkert, M., and others. 2010. Metadata matters. J. Cell Biol. **189**: 777–782. doi:10.1083/jcb.201004104

Long, R. A., and F. Azam. 1996. Abundant protein-containing particles in the sea. Aquat. Microb. Ecol. **10**: 213–221. doi:10.3354/ame010213

Lyons, M. M., and F. C. Dobbs. 2012. Differential utilization of carbon substrates by aggregate-associated and water-associated heterotrophic bacterial communities. Hydrobiologia **686**: 181–193. doi:10.1007/s10750-012-1010-7

Maarel, M. J. E. C., W. Sprenger, R. Haanstra, and L. J. Forney. 1999. Detection of methanogenic archaea in seawater particles and the digestive tract of a marine fish species. FEMS Microbiol. Ecol. **173**: 189–194. doi:10.1111/j.1574-6968.1999.tb13501.x

Marshall, A. T. 1980. Freeze-substitution as a preparation technique for biological X-ray microanalysis. Scan. Electron Microsc. 395–408.

Marty, D. G. 1993. Methanogenic bacteria in seawater. Limnol. Oceanogr. **38**: 452–456. doi:10.4319/lo.1993.38.2.0452

McGlynn, S. E., G. L. Chadwick, C. P. Kempes, and V. J. Orphan. 2015. Single cell activity reveals direct electron transfer in methanotrophic consortia. Nature **526**: 531–535. doi:10.1038/nature15512

Moreno-Vivián, C., P. Cabello, M. Martínez-Luque, R. Blasco, and F. Castillo. 1999. Prokaryotic nitrate reduction: Molecular properties and functional distinction among bacterial nitrate reductases. J. Bacteriol. **181**: 6573–6584.

Mueller, C. W., A. Kölbl, C. Hoeschen, F. Hillion, K. Heister, A. M. Herrmann, and I. Kögel-Knabner. 2012. Submicron scale imaging of soil organic matter dynamics using Nano-SIMS – from single particles to intact aggregates. Org. Geochem. **42**: 1476–1488. doi:10.1016/j.orggeochem.2011.06.003

Musat, N., O. Giere, A. Gieseke, F. Thiermann, R. Amann, and N. Dubilier. 2007. Molecular and morphological characterization of the association between bacterial endosymbionts and the marine nematode *Astomonema* sp. from the Bahamas. Environ. Microbiol. **9**: 1345–1353. doi:10.1111/j.1462-2920.2006.01232.x

Musat, N., and others. 2008. A single-cell view on the ecophysiology of anaerobic phototrophic bacteria. Proc. Natl. Acad. Sci. USA **105**: 17861–17866. doi:10.1073/pnas.0809329105

Nussbaumer, A. D., C. R. Fisher, and M. Bright. 2006. Horizontal endosymbiont transmission in hydrothermal vent tubeworms. Nature **441**: 345–348. doi:10.1038/nature04793

Paerl, H. W., and J. L. Pinckney. 1996. A mini-review of microbial consortia: Their roles in aquatic production and biogeochemical cycling. Microb. Ecol. **31**: 225–247. doi:10.1007/BF00171569

Passow, U., A. L. Alldredge, and B. E. Logan. 1994. The role of particulate carbohydrate exudates in the flocculation of diatom blooms. Deep-Sea Res. Part I Oceanogr. Res. Pap. **41**: 335–357. doi:10.1016/0967-0637(94)90007-8

Passow, U., and A. L. Alldredge. 1995. A dye-binding assay for the spectrophotometric measurement of transparent exopolymer particles (TEP). Limnol. Oceanogr. **40**: 1326–1335. doi:10.4319/lo.1995.40.7.1326

Passow, U., R. F. Shipe, A. Murray, D. K. Pak, M. A. Brzezinski, and A. L. Alldredge. 2001. The origin of transparent exopolymer particles (TEP) and their role in the sedimentation of particulate matter. Cont. Shelf Res. **21**: 327–346. doi:10.1016/S0278-4343(00)00101-1

Peterson, M. L., S. G. Wakeham, C. Lee, M. A. Askea, and J. C. Miquel. 2005. Novel techniques for collection of sinking particles in the ocean and determining their settling rates. Limnol. Oceanogr.: Methods **3**: 520–532. doi:10.4319/lom.2005.3.520

Phillips, C. J., Z. Smith, T. M. Embley, and J. I. Prosser. 1999. Phylogenetic differences between particle-associated and planktonic ammonia-oxidizing bacteria of the β subdivision of the class *Proteobacteria* in the northwestern Mediterranean Sea. Appl. Environ. Microbiol. **65**: 779–786.

Picheral, M., L. Guidi, L. Stemmann, D. M. Karl, G. Iddaoud, and G. Gorsky. 2010. The underwater vision profiler 5. Limnol. Oceanogr.: Methods **8**: 462–473. doi:10.4319/lom.2010.8.462

Ploug, H., M. H. Iversen, and G. Fischer. 2008. Ballast, sinking velocity, and apparent diffusivity within marine snow and zooplankton fecal pellets: Implications for substrate turnover by attached bacteria. Limnol. Oceanogr. **53**: 1878–1886. doi:10.4319/lo.2008.53.5.1878

Polerecky, L., B. Adam, J. Milucka, N. Musat, T. Vagner, and M. M. M. Kuypers. 2012. Look@NanoSIMS–a tool for the analysis of nanoSIMS data in. Environ. Microbiol. **14**: 1009–1023. doi:10.1111/j.1462-2920.2011.02681.x

Rath, J., K. Y. Wu, G. J. Herndl, and E. F. DeLong. 1998. High phylogenetic diversity in a marine-snow-associated bacterial assemblage. Aquat. Microb. Ecol. **14**: 261–269. doi:10.3354/ame014261

Risović, D. 1998. On correlation of fractal dimension of marine particles with depth. J. Colloid Interface Sci. **197**: 391–394. doi:10.1006/jcis.1997.5277

Rogge, A., A. Vogts, M. Voss, K. Jürgens, G. Jost, and M. Labrenz. 2017. Success of chemolithoautotrophic SUP05 and Sulfurimonas GD17 cells in pelagic Baltic Sea redox zones is facilitated by their lifestyles as K- and r-strategists.

Environ. Microbiol. **19**: 2495–2506. doi:10.1111/1462-2920.13783

Schindelin, J., and others. 2012. Fiji: An open-source platform for biological-image analysis. Nat. Methods **9**: 676–682. doi:10.1038/nmeth.2019

Schindelin, J., C. T. Rueden, M. C. Hiner, and K. W. Eliceiri. 2015. The ImageJ ecosystem. Mol. Reprod. Dev. **82**: 518–529. doi:10.1002/mrd.22489

Schmid, B., J. Schindelin, A. Cardona, M. Longair, and M. Heisenberg. 2010. A high-level 3D visualization API for Java and ImageJ. BMC Bioinf. **11**: 274. doi:10.1186/1471-2105-11-274

Schneider, C. A., W. S. Rasband, and K. W. Eliceiri. 2012. NIH image to ImageJ. Nat. Methods **9**: 671–675. doi:10.1038/nmeth.2089

Shanks, A. L., and J. D. Trent. 1979. Marine snow: Microscale nutrient patches. Limnol. Oceanogr. **24**: 850–854. doi:10.4319/lo.1979.24.5.0850

Shiraishi, F., B. Zippel, T. R. Neu, and G. Arp. 2008. In situ detection of bacteria in calcified biofilms using FISH and CARD-FISH. J. Microbiol. Methods **75**: 103–108. doi:10.1016/j.mimet.2008.05.015

Slaveykova, V. I., C. Guignard, T. Eybe, H.-N. Migeon, and L. Hoffmann. 2009. Dynamic NanoSIMS ion imaging of unicellular freshwater algae exposed to copper. Anal. Bioanal. Chem. **393**: 583–589. doi:10.1007/s00216-008-2486-x

Stoderegger, K. E., and G. J. Herndl. 1999. Production of exopolymer particles by marine bacterioplankton under contrasting turbulence conditions. Mar. Ecol. Prog. Ser. **189**: 9–16. doi:10.3354/meps189009

Swan, B. K., and others. 2011. Potential for chemolithoautotrophy among ubiquitous bacteria lineages in the dark ocean. Science **333**: 1296–1300. doi:10.1126/science.1203690

Turley, C. M., and E. D. Stutt. 2000. Depth-related cell-specific bacterial leucine incorporation rates on particles and its biogeochemical significance in the Northwest Mediterranean. Limnol. Oceanogr. **45**: 419–425. doi:10.4319/lo.2000.45.2.0419

Turner, J. T. 2015. Zooplankton fecal pellets, marine snow, phytodetritus and the ocean's biological pump. Prog. Oceanogr. **130**: 205–248. doi:10.1016/j.pocean.2014.08.005

Velde, J. T., R. Burkhardt, K. Kleiverda, L. Leenheers-Binnendijk, and W. Sommerfeld. 1977. Methyl-methacrylate as an embedding medium in histopathology. Histopathology **1**: 319–330. doi:10.1111/j.1365-2559.1977.tb01671.x

Veta, M., J. P. W. Pluim, P. J. van Diest, and M. A. Viergever. 2014. Breast cancer histopathology image analysis: A review. IEEE Trans. Biomed. Eng. **61**: 1400–1411. doi:10.1109/TBME.2014.2303852

Vojvoda, J., D. Lamy, E. Sintes, J. A. L. Garcia, V. Turk, and G. J. Herndl. 2014. Seasonal variation in marine-snow-associated and ambient-water prokaryotic communities in the northern Adriatic Sea. Aquat. Microb. Ecol. **73**: 211–224. doi:10.3354/ame01718

Waheed, A. A., K. S. Rao, and P. D. Gupta. 2000. Mechanism of dye binding in the protein assay using eosin dyes. Anal. Biochem. **287**: 73–79. doi:10.1006/abio.2000.4793

Waite, A. M., K. A. Safi, J. A. Hall, and S. D. Nodder. 2000. Mass sedimentation of picoplankton embedded in organic aggregates. Limnol. Oceanogr. **45**: 87–97. doi:10.4319/lo.2000.45.1.0087

Waite, A. M., Ö. Gustafsson, O. Lindahl, and P. Tiselius. 2005. Linking ecosystem dynamics and biogeochemistry: Sinking fractionation of organic carbon in a Swedish fjord. Limnol. Oceanogr. **50**: 658–671. doi:10.4319/lo.2005.50.2.0658

Wilbanks, E. G., and others. 2014. Microscale sulfur cycling in the phototrophic pink berry consortia of the Sippewissett Salt Marsh. Environ. Microbiol. **16**: 3398–3415. doi:10.1111/1462-2920.12388

Woebken, D., B. M. Fuchs, M. M. M. Kuypers, and R. I. Amann. 2007. Potential interactions of particle-associated anammox bacteria with bacterial and archaeal partners in the Namibian upwelling system. Appl. Environ. Microbiol. **73**: 4648–4657. doi:10.1128/AEM.02774-06

Zoppini, A., A. Puddu, S. Fazi, M. Rosati, and P. Sist. 2005. Extracellular enzyme activity and dynamics of bacterial community in mucilaginous aggregates of the northern Adriatic Sea. Sci. Total Environ. **353**: 270–286. doi:10.1016/j.scitotenv.2005.09.019

Acknowledgments

Conflict of Interest

None declared.

2.2.2.1 How can single-cell uptake measurements be applied to sinking particles?

In Paper III, I demonstrated that the combination of immobilization in liquid agarose, and the final embedding in plastic resin, showed the required structural integrity for NanoSIMS in ultra-high vacuum conditions, as well as a high secondary ion yield. Most importantly, the resin consisted mainly of hydrocarbons, which reduced tracer dilutions of nitrogen and sulfur isotopes in the cells to be analyzed. Methacrylate, the plastic resin of choice, also showed a hydrophilic nature, enabling structural stainings, as well as the potential for phylogenetic identification based on the monoFISH approach.

I was able to observed one ^{15}N and several ^{34}S enriched organisms, predominantly prokaryotes, in laboratory generated aggregates incubated with stable isotope labelled compounds. It also emerged that the resin can be used as internal standard if the embeddings were performed with the same batch of agarose and resin. This is a great benefit of the method since internal effects can affect the NanoSIMS, leading to slightly different secondary ion counts of the respective masses if the single measurements are separated by several days. The detailed application of this internal standard is explained in Paper III.

During our tests we discovered that hard compounds, such as terrigenous material or diatom frustules may lead to sample rupture during the slicing process. Therefore, we also tested the soil research-based resin Araldite 502, which is known for its sufficient behavior in the NanoSIMS but low stainability (Herrmann *et al.* 2007; Clode *et al.* 2009; Mueller *et al.* 2012; Kaiser *et al.* 2015). Although this material requires a more complex sectioning approach based on polishing, which produces only relatively thick sections (> 40 µm), it enables new insights on the single-cell level as well. One useful application would be detailed uptake investigations within mineral-ballasted particles.

Unfortunately, compatibility with advanced FISH approaches, such as CARDFISH, could not be proven with our method. However, McGlynn *et al.* (2015) reported the successful application of monoFISH on methacrylate embedded samples, which could be very useful in future investigations coupling microbial identity and activity.

The application of the presented method allows detailed investigations on biogeochemical cycling within sinking aggregates. We demonstrated the uptake of nitrogen and sulfur from nitrate and sulfate, which suggests the use of alternative electron acceptors. More detailed investigations applying incubations with stable isotope labelled electron

acceptors or donors might enable important investigations on matter cycling within the often postulated anoxic micro-zones in the oxygenated water column with potentially tremendous effects on our understanding of global matter cycling (Canfield *et al.* 2010; Bianchi *et al.* 2018).

2.2.2.2   How can anoxic micro-zones be identified within sinking particles?

The first NanoSIMS analyses of sliced marine snow also provided evidence for sulfur-rich particulate matter, which was not presented in Paper III (Fig. 5). Interestingly, this material did not seem to be closely associated with living cells, because it showed neither nucleic acid content, nor chlorophyll in the microscopic images (see also Fig 4 in Paper III). Moreover, the nitrogen content was too low for living cells. Hence, internal storage can be excluded here.
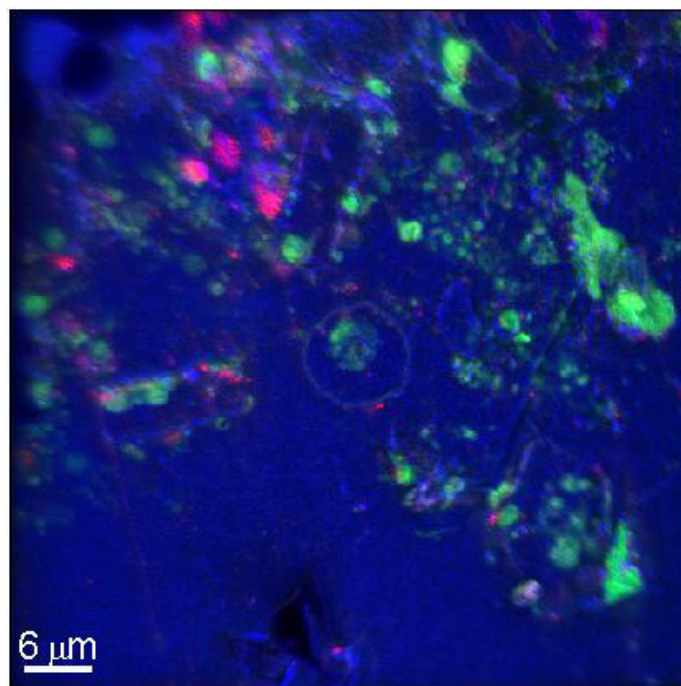
Figure 5: Overlap of ^{12}C (blue), ^{12}C^{14}N (green), and ^{34}S ion counts (red). Red regions represent particulate material with strikingly low nitrogen but high sulfur content. This material could potentially represent biologically reduced particulate sulfur compounds, such as elemental sulfur or iron sulfides, or abiotically precipitated barium sulfate.

Biologically, elemental sulfur can be produced during sulfate reduction, or sulfide oxidation (Jasińska *et al.* 2012). Based on our measurements, we could not identify an

enrichment of [34]S in the identified particulate sulfur rich compounds. Thus, formation from [34]S labelled sulfate can be excluded (See also Fig. 7 in Paper III). However, the lack of enrichment could also be explained by a delay of isotope transfer caused by a combination of slow diffusion into the aggregate and a too short incubation time. Abiotically, sulfur rich particulate material can be produced from a reaction of sulfides and iron ions (Jasińska *et al.* 2012) – a process which finally produces pyrite (FeS_2); the largest fraction of reduced sulfur in the environment (Jasińska *et al.* 2012). Also, abiotically precipitated barium sulfate could explain the observed sulfur-rich material. In Palaeooceanography, geochemical investigations in geological records showed high contents of barium throughout earth's history. It could be shown, that dissolved barium ions precipitate under anoxic conditions with sulfate ions and form particulate barium sulfate. Due to these properties, it is commonly used as a proxy to study the cycling of sulfate in the early earth oceans (e.g. Farquhar *et al.* 2000; Shen *et al.* 2001; Roerdink *et al.* 2012). Moreover, earlier studies suggest that the process of barium precipitation is present in particles of organic matter within an oxygenated ocean (Fig. 6; Chow and Goldberg 1960; Horner *et al.* 2017). The proof of anaerobically produced sulfur particles, but also under anoxic conditions precipitated pyrite or barite particles would clearly identify anoxic zones within particles.
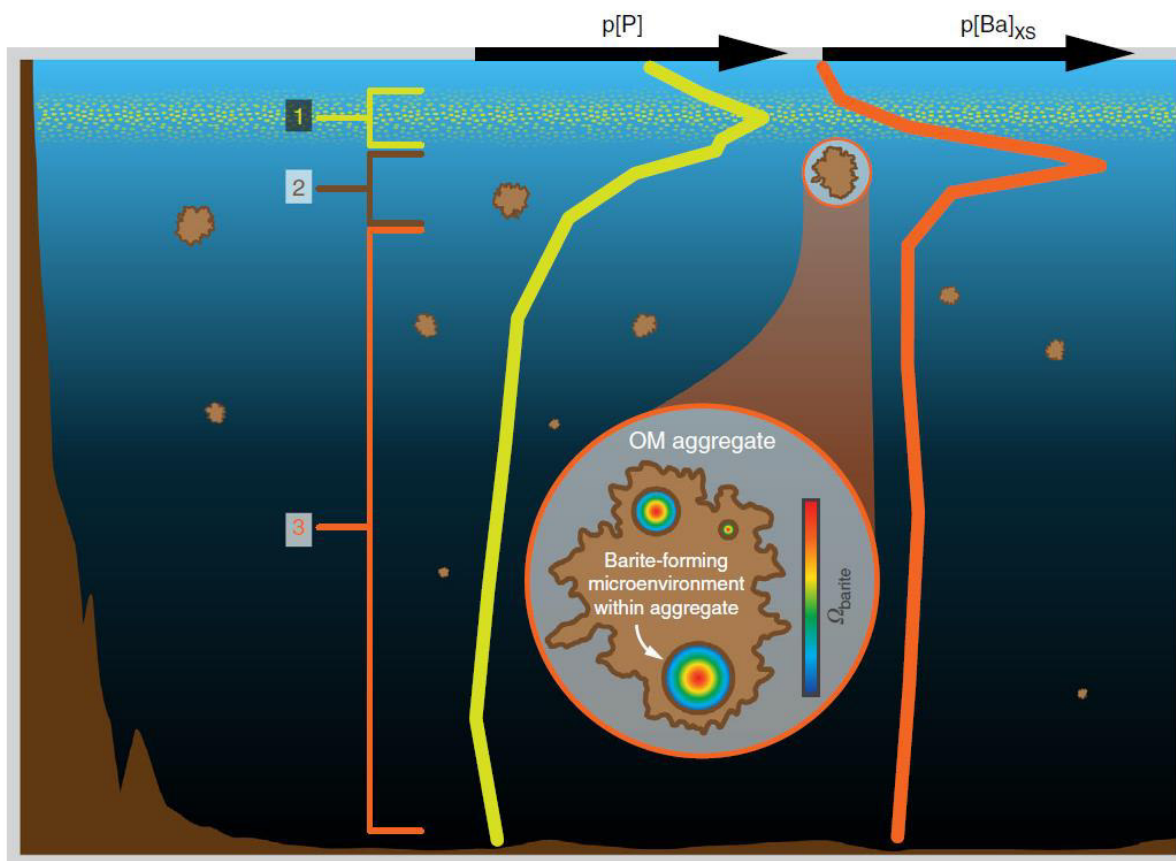
Figure 6: Conceptual model of barium cycling in the water column. Depth profiles of sinking particles (p[P]) and particulate barium (p[Ba]$_{XS}$) are separated into 3 zones: (1) Autotrophic production leads to a peak in organic matter near the surface, indicated by the maximum in p[P]. (2) Microbial respiration within aggregates of decaying particles leads to development of barite-supersaturated microenvironments and precipitation of barium sulfate. (3) Continued degradation leads to attenuation of the particle flux and destroys microenvironments, preventing further buildup of barite; settling barites are exposed to undersaturated waters and may start to dissolve (From Horner *et al.* 2017).

As presented in Paper I and Paper III, NanoSIMS has the potential to measure sulfur as $^{32}S^-$, but also iron as $^{56}Fe^{16}O^-$ and barium as $^{138}Ba^+$ secondary ions, using a Cs^+ or O^- primary beam, respectively (Sano *et al.* 2005; Newsome *et al.* 2018). Using the embedding method presented in Paper III, one could identify the spatial extent of e.g. sulfur and barium or sulfur and iron as tracers to calculate the extent of anoxic micro-zones within particles. Moreover, the EDX technology, as applied in Paper A1, has the potential to quantify sulfur, iron, and barium more precisely than NanoSIMS alone (Liberge *et al.* 2001). The application would provide precise element ratios for the exact identification of compounds involved. Furthermore, active microorganisms within those zones can be identified using monoFISH or

advanced CARDFISH and MiL-FISH approaches, and the embedding method of Paper II. Initial identification of abundant microbial groups, e.g. by using molecular sequencing protocols of whole particles, would, furthermore, help to choose the right phylogenetic probes for FISH investigations. This joint approach would open up new ways to investigate the biological carbon pump and its associated microorganisms.

2.3 The influence of particle composition on vertical microbial connectivity

Large scale investigations of the biological pump, can be achieved using optical particle quantification methods, such as the Underwater Vision Profiler (e.g. Guidi *et al.* 2008; Waite *et al.* 2016). General information about particle-associated organism communities, such as phytoplankton (Guidi *et al.* 2016), as well as prokaryotic communities can thereby be achieved using parallel molecular sequencing approaches of whole aggregates.

Microbes have a restricted range of motility (Purcell 1977), which makes sinking particles an important vehicle for microbial connectivity (Thiele *et al.* 2015; Paper IV). The gravitational sinking of particles enables them to penetrate stratified water masses of different density from surface waters down to the deep sea. After primary colonization of particles by microorganisms in surface waters, the particle-associated microbial community composition changes with time of particle settling due to the formation of micro-niches (Woebken *et al.* 2007; Thiele *et al.* 2015; Bristow 2018). The composition similarity of the particle-associated and the free-living microbial communities is thereby decreasing (Salazar *et al.* 2015; Mestre *et al.* 2017; Paper IV). Moreover, taxonomic exchange between particle-associated and free-living microbial communities may shape the microbiological ecology of the water column and potentially of biogeochemical cycling as a whole (Simon *et al.* 2002; Grossart *et al.* 2003; Grossart *et al.* 2006; Stocker 2012).

The depth to which particles sink, however, is mainly influenced by the sinking velocity (Iversen and Ploug 2010). For phytoplankton aggregates it could be shown, that the sinking velocity depends on the composition of the phytoplankton species they are formed from, i.e. the ballasting compounds, such as diatom frustules, they introduce into the aggregate structure (Iversen and Ploug 2010) or by inclusion of lithogenic material within the aggregates (Iversen *et al.* 2010; Iversen and Robert 2015; van der Jagt *et al.* 2018).

In the Arctic Ocean, a general shift from diatom dominated phytoplankton communities in ice-covered regions towards flagellate dominated phytoplankton communities (i.e. *Phaeocystis spp.*) in ice-free regions could be observed in previous studies (Lasternas and Agusti 2010; Nöthig *et al.* 2015). This shift is most likely a result of sea ice decrease due to global warming (Lasternas and Agusti 2010; Notz and Stroeve 2016; Engel *et al.* 2017). Decreased sinking velocities of aggregates, such as those formed by *Phaeocystis spp.*, increase their residence time in the upper water column, leading to increased remineralization

rates of those aggregates in shallower waters and, hence, decreased particle export towards the deep sea (Ploug *et al.* 2008a; Ploug *et al.* 2008b; Iversen and Ploug 2010). This raises the question of how the observed shift in the surface phytoplankton community of the Arctic influences the vertical connectivity of microbes towards the Arctic deep sea.

In Paper IV, we performed microbial source tracking based on 16S rRNA gene sequences of the particle-associated and free-living microbial community and combined those results with particle characterization and spatial distributions based on flow chamber measurement of size-specific sinking velocities and high resolution Underwater Vision Profiler measurements in the Fram Strait. We used those results to investigate the influence of sea ice coverage on the microbial vertical connectivity in the Arctic.

PAPER IV

1 <u>**Classification:**</u> **BIOLOGICAL SCIENCES – Microbiology**

2

3 <u>**Title:**</u> **Arctic sea ice enhances vertical connectivity of microbial**

4 **communities through sinking particles**

5

6 <u>**Short title:**</u> **Vertical microbial connectivity in Arctic Ocean**

7

8 <u>**Author Affiliation:**</u>

9 **Eduard Fadeev[1,2], Morten H. Iversen[1,3], Claudia Wekerle[1], Ian Salter[1,4], Christina**

10 **Bienhold[1,2], Andreas Rogge[1,5], Anya M. Waite[1,6], Laura Hehemann[1], Antje Boetius[1,2]**

11

12 [1] Alfred Wegener Institute, Helmholtz Center for Polar and Marine Research, D-27570

13 Bremerhaven, Germany

14 [2] Max Planck Institute for Marine Microbiology, D-28359 Bremen, Germany

15 [3] MARUM and University of Bremen, D-28359 Bremen, Germany

16 [4] Faroe Marine Research Institute, FO 100 Tórshavn, Faroe Islands

17 [5] Institute for Ecosystem Research, University of Kiel, D-24118 Kiel, Germany

18 [6] Ocean Frontier Institute, NS B3H 4R2 Halifax, Canada

19

20 <u>**Corresponding Author:**</u>

21   Eduard Fadeev - eduard.fadeev@awi.de

22   Address: Celsiusstr. 1, D-28359 Bremen, Germany

23   Phone number: +49 421 2028-876

24   ORCID - 0000-0002-2289-2949

25 <u>**Keywords:**</u> microbial source tracking, deep ocean, particles colonization, sinking particles,

26 marine snow

Abstract

The Arctic Ocean is characterized by a single seasonal phytoplankton bloom in late spring that is terminated both by nutrient depletion and strong grazing pressure. A substantial export of sinking particles follows, including decaying phytoplankton, fecal pellets and other forms of particulate matter. By combining *in situ* measurements with Lagrangian modeling we reconstructed sinking trajectories of marine particles across the Fram Strait (0-2500 m water depth), and showed that ice-covered regions were characterized by larger (1-2 mm diameter) and faster-sinking (40-80 m d^{-1}) particles, composed mainly of diatoms. Marine particles are colonized at the surface by diverse microbes, however, little is known about the succession of the particle-associated community during its descent to the deep ocean. Using high-throughput sequencing of the 16S rRNA gene, we investigated differences in particle-associated (> 5 µm) and free-living (0.2-5 µm) microbial communities throughout the water column. We showed that particles were colonized mainly in surface waters by heterotrophic bacteria (e.g., *Flavobacteria*), which were traced in deep ocean particle-associated communities (> 1000 m depth) using microbial source tracking. This vertical connectivity of microbial communities was especially strong in regions with sea ice, where almost half of the particle-associated communities at 1000 m depth were linked to surface-derived microbes. Our study reveals the magnitude at which surface-derived microbes may be transported to the deep ocean via sinking particles. Highlighting that further sea-ice loss in the Arctic Ocean may impact this microbial connectivity, and alter current biogeochemical cycling in the Arctic.

Significance

Sinking particles are formed from organic matter that is produced by phytoplankton in the surface ocean, and are responsible for the sequestration of one third of the atmospheric anthropogenic carbon dioxide. These particles fuel productivity in the deep ocean, and distribute chemical compounds and microbes through the water column. Our data shows that particles formed in ice-covered waters of the Arctic Ocean sink faster to the deep ocean and promote a higher vertical connectivity of microbial communities compared to ice-free waters. This rapidly exports carbon and transports microbes to the deep ocean. We propose that the predicted ice-free summers in the second half of this century will weaken this vertical export altering biogeochemical cycles in the Arctic Ocean.

110

Introduction

Global warming and climate change is currently affecting the Arctic Ocean at an unprecedented rate, causing warming at rates much faster than any other ocean (1, 2). Arctic sea ice has declined by approximately 50% since the late 1950s (3, 4), and current projections suggest that the Arctic Ocean may experience ice-free summers by the second half of this century (5–7). These remarkable environmental changes are likely to increase primary production in the water column (8–10), change phytoplankton and grazers communities, and the alter the biological carbon pump (11, 12). Shifts from diatom to flagellate (e.g., *Phaeocystis spp.*) dominated phytoplankton communities has been already observed after the record Arctic sea-ice minimum of 2006 (13–15).

The particulate organic matter produced by phytoplankton in the surface ocean is exported to the deep ocean through formation and gravitational settling of aggregates (16). In comparison to aggregates of diatoms, aggregates formed by *Phaeocystis spp.* are more buoyant and sink slowly. Thus, they remain longer in the surface ocean, allowing more recycling of the organic matter in the upper water column (17–19). This is supported by recent model predictions that suggest that an ice-free Arctic Ocean will have a more active microbial loop in surface waters and less carbon export to the deep ocean (20, 21), where the availability of organic matter is usually extremely low (22, 23).

Marine aggregates of particulate organic matter (further addressed as 'particles') are subject to colonization by microorganisms and are hotspots of microbial activity in the ocean (24, 25). The microbes play key roles in the recycling of particulate organic matter in the aggregates by hydrolytic enzymatic activity, and the release of dissolved organic matter and nutrients into the water (26–29). There is strong experimental evidence showing that the particle-associated (PA) communities originate from the surface ocean and are subsequently altered by internal succession through formation of microniches (e.g., anoxic conditions)(30–32), as well as, a continuous taxonomic exchange with the ambient free-living (FL) microbial communities (26, 33–39). From surface down to bathypelagic waters (0-4000 m depth), PA microbial communities have been shown to differ in composition from the surrounding FL communities (40, 41). Furthermore, phylogenetic analyses showed that in the deep ocean, FL and PA communities are phylogenetically distant, and cases of microbes being present in both fractions are rare (41). It has also been demonstrated, using a wide range of size-fractionated

90   FL and PA communities, that sinking aggregates may act as vertical dispersal vectors between

91   surface and deep ocean microbial communities, in tropical and subtropical waters (42).

92

93   Unlike other open ocean environments, surface and deep waters of the Arctic Ocean both

94   maintain similar near freezing point temperatures (43), which may allow PA microbes from

95   surface waters to survive in the deep ocean, despite the increasing hydrostatic pressure (44).

96   Evidence for a potential connectivity of microbial communities from sea ice, water column

97   and seafloor in the central Arctic was provided by the identification of roughly 20%

98   taxonomic overlap at the level of operational taxonomic units (OTUs) between these

99   environments (45). In contrast, in the Pacific Ocean only 12% of the OTUs were shared

100   between the water column and the deep-sea sediment (46). However, in order to further

101   understand the relevance of sinking particles to vertical connectivity of microbial

102   communities in the Arctic Ocean, a better characterization of PA communities and an

103   identification of their sources are required.

104

105   Here, we characterized and compared sinking particles dynamics in ice-free and ice-covered

106   (partially or entirely covered by sea ice) regions at the FRAM Observatory in the Fram Strait

107   (47), the only deep water gateway to the Arctic Ocean. Vertical profiles of particle abundance

108   and size-distribution were obtained from the Underwater Vision Profiler (UVP)(48).

109   Individual aggregates were collected *in situ* with a Marine Snow Catcher, their composition

110   was determined microscopically, and measurements of their sizes and sinking velocities were

111   conducted in a vertical flow chamber (49, 50). By combining direct measurements of particle

112   sinking velocities and a Lagrangian modeling approach, we reconstructed back-trajectories of

113   sinking particles from the deep ocean to their origin in the surface waters. We collected water

114   samples in ice-covered and ice-free stations across the Fram Strait (9 stations in total). The

115   water samples were divided into two size fractions: 0.2-5 μm and > 5 μm, in order to

116   distinguish between free-living and particle-associated communities, respectively. Based on

117   high-throughput sequencing of the 16S rRNA gene, we investigated the particle-associated

118   and the free-living archaeal and bacterial communities (further referred to as 'microbes') at 4

119   distinct water layers down to 2500 m depth. Then, using Bayesian microbial source tracking

120   algorithm ('SourceTracker')(51) we assessed the potential connectivity between surface and

121   deep Arctic Ocean microbial communities mediated by association with particles.

122

Results and Discussion

The Fram Strait has two main distinct oceanographic regimes. Based on the geographical location, the sea-ice conditions, and the physical characteristics (temperature and salinity) of the water (52), the epipelagic waters (0-200 m) of the sampled area were divided into ice-free and ice-covered regions (Fig. 1). The ice-free region consisted of the 'HG' stations and the southernmost station 'S3', all in the West Spitsbergen Current (53). The ice-covered regions consisted of the entirely ice-covered stations 'EG' in the East Greenland Current (54), as well as, the partially ice-covered stations 'N' associated with the highly productive marginal ice zone (55–57). These distinct regions have been previously shown to have different dynamics in the development of the seasonal phytoplankton bloom (58, 59). At the time of sampling, the chlorophyll *a* concentrations integrated over the depth of the euphotic zone reached 50 to 95 mg m^{-2} (*SI Appendix*, Fig. S1). Thus, suggesting an ongoing phytoplankton bloom conditions across all sampled stations (58, 59).

The deeper layers (below 200 m) of the Fram Strait were more homogeneous and did not show differences in temperature and salinity characteristics between the regions (*SI Appendix*, Fig. S2). However, a clear vertical layering of the deep water column was observed. The mesopelagic waters (200 - 1000 m) mainly consisted of mixed Atlantic Water, which transitioned into Eurasian Basin Deep Water at bathypelagic depths (> 1000 m) (60).

Marine particles in different regions of the Fram Strait differ in their size distribution, composition and sinking velocities. The vertical profiles of total particle volume (acquired using the UVP) showed maxima at the upper 100 m of the water column (Table 1; *SI Appendix*, Fig. S3). The ice-free and ice-covered regions exhibited similar distributions of both small (64-512 µm) and large (0.512- 0.3 mm; i.e., "marine-snow") particles within the epipalgic waters (0-200 m). In the mesopelagic waters (100-1000 m) there was a significantly higher volume of large particles in the ice-free region (Mann–Whitney–Wilcoxon 'MWW' test, p < 0.001; Table 1). This was mainly due to elevated number of large particles between 600 and 900 m, in contrast to individual peaks of large particles volume in the ice-covered region (*SI Appendix*, Fig. 3S). Thus, suggesting a sustained vertical export of particles in ice-free region, and episodic vertical export events in the ice-covered region (61). Potential evidence for such episodic export events in ice-covered region is observations of the diatom *Melosira arctica* beneath the sea ice (Fig. 2), and independently recorded by high-resolution imaging large phytoplankton aggregates on the seafloor of the ice-covered region (62).

157 Aggregates of the sea ice associated diatom *M.arctica* have previously been shown to provide
158 an important vector for the rapid export of organic matter to the seafloor (12, 45). The
159 increasing abundance of small particles towards the seafloor in bathypelagic waters (> 1000
160 m) of the ice-free region potentially indicates re-suspended material of the nepheloid layer
161 (63).

162

163 The combination of size, structure (e.g., porosity, fractal geometry), and composition (e.g.,
164 biomineral content) of a marine particle determine its sinking velocity (17, 18). Intact
165 particles were collected with a marine snow catcher below the sub-surface chlorophyll *a*
166 maximum (~60 m) in both ice-free and ice-covered regions of the Fram Strait (Table 1). Size
167 measurement revealed that on average in the ice-covered region particles were significantly
168 larger (MWW test, $p < 0.001$). According to microscopic analyses, half of the particles
169 collected in the ice-free region (13 out of 24) were smaller than 512 µm and composed
170 primarily of flagellates, including *Phaeocystis spp.* (Fig. 2). On the other hand, almost all (33
171 out of 36) collected particles in the ice-covered region were large (> 512 µm) and were
172 dominated by diatoms (Fig. 2). The mean sinking velocity of particles in the ice-covered
173 region was significantly higher (52.77 ± 0.91 m d^{-1}) compared to the non-ballasted flagellate
174 dominated particles in the ice-free region (29.5 ± 0.67 m d^{-}1; MWW test, $p < 0.05$),
175 supporting previous observations of higher sinking velocities of silica-rich diatoms (18, 64,
176 65). Furthermore, recent observations suggested that *Phaeocystis spp.* in ice-covered waters
177 incorporates cryogenic gypsum that leads to higher sinking velocities (21). In accordance with
178 these observations, our results showed that small particles (< 512 µm) of *Phaeocystis spp.* in
179 the ice-covered regions, had also significantly (MWW test, $p < 0.05$) higher sinking velocities
180 (42.68 ± 8.14 m d^{-1}) in comparison to the small particles in the ice-free region (23.37 ± 3.98
181 m d^{-1}). Altogether our results support the recently observed dominance of flagellated
182 phytoplankton over diatoms in the ice-free water column (14), and suggest longer residence
183 times of more slowly sinking particles throughout the water column in ice-free waters.

184

185 **The sinking trajectories of particles to the deep ocean show little lateral transport**
186 **between the ice-covered and ice-free regions.** Using a Lagrangian particle tracking
187 algorithm (66), we combined the measured on board sinking velocities of particles, with
188 horizontal ocean velocities from a sea ice-ocean model FESOM (67), into statistical funnels
189 that describe the sinking trajectories of particles from the surface to the deep ocean. Based on
190 the mean sinking velocities measured in each of the sampled regions of the Fram Strait, the

191 sinking trajectories were reconstructed for the productive season of 2016 (March-July; Fig. 3).

192 The results revealed a significantly higher percentage of sinking particles originating directly

193 under the sea ice in the entirely ice-covered 'EG' stations compared to other regions

194 (Pearson's chi-squared test, p < 0.001; Table 2). The partially ice-covered 'N' stations were

195 characterized by mixed origin of particles from ice-free and ice-covered regions (Fig. 3).

196 However, overall the majority of particles reaching the deep waters in the ice-covered regions

197 are exported from waters partially or entirely covered by sea ice, and is not laterally

198 transported from ice-free regions, while particles reaching deep waters in the ice-free region

199 also originate in the ice-free surface waters.

200

201 It is important to note that the reconstructed sinking trajectories rely on a constant sinking

202 velocity, and do not take into account the time of the particle being suspended in surface

203 waters before sinking (68), as well as, changing characteristics of the particles or

204 disaggregation as they descend through the water column (e.g., as a result of microbial

205 degradation) (69, 70). Slower sinking velocities result in a stronger horizontal displacement of

206 the particles at depth (i.e., sinking trajectory length)(66). However, hypothetical sinking

207 velocities of 20 m d^{-1} and 60 m d^{-1}, selected based on previous studies in the region (71), did

208 not show strong differences in the proportion of particles originated below the sea ice (Table

209 2).

210

211 **Pelagic microbial communities in the Fram Strait show strong association with depth.**

212 The particle-associated (> 5 µm; 'PA') and free-living (0.2-5 µm; 'FL') microbial

213 communities were sampled in the water column of the ice-covered and ice-free regions (Fig.

214 1). Using Illumina 16S rRNA gene sequencing of the V4-V5 hypervariable region, we

215 obtained a final dataset of 3,384,300 sequences (amplicons) in 65 samples (*SI Appendix*,

216 Table S1), which were assigned to 17,631 operational taxonomic units (OTUs) associated

217 with bacterial and archaeal lineages. All OTUs which were taxonomically assigned to

218 chloroplasts or mitochondria were excluded from further analysis. In the FL fraction,

219 sequences were affiliated to a total of 12,796 OTUs (12,293 bacterial and 503 archaeal

220 OTUs), with a mean number of 1,901 ± 108 OTUs per sample. In the PA fraction, sequences

221 were affiliated to a total number of 10,265 OTUs (10,011 bacterial and 254 archaeal OTUs),

222 with a mean number of 1,172 ± 159 OTUs per sample. The rarefaction curves did not reach a

223 plateau in any of the samples, suggesting that additional OTUs could be expected with

224 additional sequencing effort (*SI Appendix*, Fig. S4). Based on the Chao1 richness estimator

115

the samples covered on overage 59% of the bacterial and archaeal community, with no

statistically significant differences in coverage between the fractions (*SI Appendix*, Table S1).

In both FL and PA fractions, there was a statistically significant increase of the mean Chao1

richness estimator with depth ('ANOVA', $F_{3,61} = 39.03$, $p < 0.001$; *SI Appendix*, Fig. S5 *A*).

Throughout the entire water column the PA communities exhibited a generally lower richness

in comparison to the FL communities, consistent with observations from other oceanic

regions (41). The bathypelgic PA communities of the stations HG1 and HG2 exhibited much

higher richness in comparison to their associated FL communities, potential evidence for re-

suspended particles of the nepheloid layer (*SI Appendix*, Fig. 3S)(63), which harbor rich

microbial communities of the seafloor (45, 72). The Pielou's evenness index (*J'*) showed

similar patterns to the richness estimates, with a statistically significant increase of evenness

with depth in both fractions ('ANOVA', $F_{3,61} = 21.695$, $p < 0.001$; *SI Appendix*, Fig. S5 *B*),

indicating that OTUs were more evenly distributed in the deep ocean communities. The deep

waters of the Arctic Ocean are less affected by the frequent ecological perturbations typical

for the surface waters (e.g., sea-ice dynamics and/or phytoplankton blooms)(59), thus our

results support previously suggested observations that high evenness is linked to a stability of

microbial ecosystems (73, 74).

The communities of both FL and PA fractions showed statistically significant ('ADONIS',

$F_{3,61} = 15.788$, $R^2 = 0.386$, $p < 0.001$) differences between the distinct pelagic layers of the

Fram Strait (Fig. 5; surface ~ 20 m, epipelagic - 100 m, mesopelagic - 1000 m and

bathypelagic – 1200-2500 m). The dissimilarity between FL and PA fractions exhibited a

statistically significant increase with depth (MWW test, $p < 0.001$; *SI Appendix*, Fig. S6 *A*).

However, no statistically significant increase in dissimilarity was observed between meso-

and bathypelagic waters. The FL communities exhibited significantly higher dissimilarity

between the distinct pelagic layers in comparison to the PA communities (MWW test, $p <$

0.001; *SI Appendix*, Fig. S6 *B*). This can be explained by a well stratified water column, with

little vertical mixing between pelagic layers (75), maintaining a strong vertical structure of FL

communities. In contrast, the lower dissimilarity of PA communities throughout the water

column suggests enhanced connectivity between pelagic layers, likely mediated through

sinking particles (42).

Particle-associated communities undergo internal succession throughout the water

column. Sinking particles mostly originate, and are thus initially colonized, in epipelagic

waters (42, 76). There are notable changes in PA community structure as a function of depth, but it is still a matter of debate to what extent this reflects "internal-succession" of the original PA community compared to subsequent colonization by deeper FL communities during sinking (33, 37, 77). In order to test which taxonomic groups prevail on marine particles with depth, we conducted enrichment tests of OTUs between the PA communities of consecutive pelagic layers: surface-epipelagic, epipelagic-mesopelagic, mesopelagic-bathypelagic. The OTUs with a $\log_2$ fold change (in their sequence abundance) of absolute value higher than 1 and an adjusted p value < 0.1 were defined as enriched.

Our results revealed that altogether 1,270 OTUs showed a significant enrichment with depth in the PA communities (222 OTUs between surface and epipelagic waters; 452 OTUs between epipelagic and mesopelagic waters; 596 OTUs between mesopelagic and bathypelagic waters). With increasing depth the PA communities became enriched by members of the *Gammaproteobacteria* (122 OTUs) and *Bacteroidia* (99 OTUs; Fig. 5), corresponding to various taxonomic groups that have previously been defined as 'master recyclers' (78). These taxa are known for possessing a wide range of carbohydrate-active enzymes to decompose algal-derived organic matter (78–80), and were previously described in association with phytoplankton blooms (81). Consequently, they have been identified as potential candidates for the downward propagation of temporally variable microbial communities to the deep ocean (82, 83), and our enrichment analysis supports that scenario.

The PA microbial communities of meso- and the bathypelagic waters showed a strong increase in diversity relative to the surface and epipelagic communities (Fig. 5; *SI Appendix*, Table S1). The largest number of enriched OTUs with depth was associated with various classes within the phylum *Planctomycetes* (in total 257 OTUs) and the class *Deltaproteobacteria* (181 OTUs; Fig. 6). It has been suggested that the high oxygen consumption by organic matter degrading bacteria (e.g., *Gammaproteobacteria* or *Bacteroidia*) creates anoxic and nutrient-enriched patches within marine particles (30, 31, 84). Subsequently these microniches are occupied by microorganisms with anaerobic oxidation capabilities, such as anaerobic oxidation of ammonium by *Planctomycetes* (85, 86) or sulfate-reduction by *Deltaproteobacteria* (87, 88). Thus, the concomitant enrichment of these taxonomic groups suggests an internal succession of the PA community, as biogeochemical niches within the particle evolve (89). However, as these taxonomic groups are also present in

292 the deep waters FL communities, one cannot rule out a secondary effect of further
293 colonization of the particle.

294

295 **Sinking particles as potential vectors for the transport of surface-derived microbial taxa**
296 **to the deep Arctic Ocean.** In order to estimate whether the observed PA community patterns
297 are a result of internal succession within the sinking particles or a result of further
298 colonization by surrounding microbes, we implemented the microbial source tracking (MST)
299 Bayesian algorithm 'SourceTracker' (51). This approach has been previously applied to
300 identify contamination between microbial communities in coastal waters and lakes (90, 91),
301 and it is based on the assumption that the diversity in various 'source' communities (i.e., FL)
302 and corresponding 'sink' communities (i.e., PA) will allow the identification of statistically
303 probable links between them based on their microbial signatures. To our knowledge this
304 approach has so far only been applied once in microbial oceanography to correlate total
305 microbial communities and water mass advections in the Southern Ocean (92).

306

307 It has been previously shown that surface microbial communities are strongly associated with
308 the epipelagic water masses across the Fram Strait (59). Therefore, the surface and epipelagic
309 FL communities were grouped together based on their origin in ice-covered region (Polar
310 Water) and ice-free region (Atlantic Water; *SI Appendix*, Fig. S2). The meso- and
311 bathypelagic FL communities on the other hand, did not show strong dissimilarity between
312 the regions (Fig. 4), therefore, were grouped by the water layer across the entire strait. In
313 order to test the predictive accuracy of the grouped FL communities, we used the statistical
314 learning validation approach 'leave-one-out' (93). Each FL sample was removed, in turn,
315 from the training dataset, and its origin was predicted based on the rest of the FL samples in
316 the dataset. The assessed performance of the algorithm showed that the predicted source of
317 each FL community matched its actual origin with high statistical significance ('ADONIS',
318 $R^2 = 0.83$, $p < 0.001$; Fig. 6), indicating a strong signal of the distinct FL communities in the
319 dataset. The MST algorithm showed that PA communities in the surface and epipelagic
320 depths were mostly associated with the FL communities of the epipelagic water masses (Fig.
321 6). In contrast, the meso- and bathypelagic FL microbes contributed much less to the
322 respective PA communities, supporting previous observations of rare transitions between FL
323 and PA lifestyles at depth (41, 76). It is important to note that size-fractionated filtration may
324 lead to different observations compared to bulk filtration (94). Although we did not observe
325 clogging of filters in this study, we cannot exclude potential effects on the observed patterns.

118

The use of only two size fractions clusters all particles larger than 5 μm into one pool. Consequently, our estimates represent an integration of small and large sinking particles, as well as, suspended particles, all of which may differ in their associated communities (95–97). This integration may influence our observations, especially in the deep ocean where suspended particles become more abundant (98, 99). Thus, we suggest that a considerable part of estimated bathypelagic FL communities contribution to the PA fraction may represent suspended deep ocean particles. Furthermore, the relatively high linkage between bathypelagic FL and PA communities in stations HG1 and HG2 may represent re-suspended particles of the nepheloid layer (*SI Appendix*, Fig. 3S)(63). The unresolved sources of the deep ocean PA communities at the southernmost station S3, combined with the sinking trajectories of particles in the ice-free region (Fig. 3), which follow the northward flowing West Spitsbergen Current (53), suggest that the origin of sinking particles in this station is southern of the sampled area.

The epipelagic FL communities contributed, as sources, up to 53% and 42% of the PA communities in meso- and bathypelagic waters, respectively (*SI Appendix,* Table S2). The vast majority of the contribution was associated with FL communities of the ice-covered waters. Furthermore, up to 60% of the PA communities in meso- and bathypelagic waters was not assigned to any FL source. Taking into account the apparent colonization of particles in epipelagic waters, and the described sinking velocities (30-50 m d^{-1}), there is a time lag of 1-2 months between the observation of PA communities in the meso- and bathypelagic waters, and their colonization by FL microbes in the surface. A recent study of surface microbial communities across the Fram Strait in 2014, showed that in summer the differences in community composition across the Strait are closely related to a slower development of the seasonal phytoplankton bloom in the ice-covered waters, compared to the ice-free waters (59). It is possible therefore, that the contribution of FL microbes from the ice-covered waters in the ice-free PA communities is a result of a retained signal, within the PA communities, of earlier stages of the seasonal phytoplankton bloom. Furthermore, it is possible that as a result of the seasonal microbial communities succession during a bloom (100, 101), that 1-2 months ago the surface waters contained FL communities with different composition compared to the time of sampling, and therefore their source remained unknown.

The estimated contribution of surface FL communities to the deep-water PA communities of the ice-covered region was on average three times higher than for the ice-free region (Fig. 6; *SI Appendix,* Table S2), retaining an increased contribution of epipelagic community

members. The presence of sea ice has already been considered a major factor influencing vertical fluxes in the Arctic Ocean (47, 102) by controlling primary production of rapidly sinking organic matter beneath the sea ice (12, 45) and in the ice-melt regions (56, 57). In our study, we also observed significantly larger and faster-sinking particles in ice-covered regions ('EG' and 'N') that evidently rapidly reach the seafloor. Taken together with our community turnover projections, we conclude that sea ice promotes formation of particles with a higher sinking velocity, leading to decreased retention times in the different water layers on their way down. The attenuated turnover of communities, in turn, retains larger proportions of surface community members in these particles, and promotes a stronger connectivity between the surface and the deep ocean.

Conclusions

The impact of current Arctic sea ice decline on microbial communities in the water column remains largely unknown. Here we focused on the vertical connectivity between surface and deep ocean microbial communities in ice-covered and ice-free regions of the Fram Strait. Our data suggest that the vertical flux of particulate organic matter and the associated microbial communities during the Arctic summer is strongly associated with the sea ice conditions. The variation in size and composition of particles (e.g., the type of phytoplankton) influences sinking velocities between the regions, with larger and faster-sinking particles in ice-covered waters. The microbial communities associated with the sinking particles change throughout the different water layers, and are increasingly dissimilar from the ambient free-living microbes. Identified using microbial source tracking particle colonization and vertical connectivity patterns showed that in ice-covered regions surface water free-living microbes had a stronger contribution to the deep ocean particle-associated communities than in ice-free regions. Due to lower sinking velocities of particles in ice-free regions, the associated communities have more time for internal succession and exchanges with ambient free-living microbes. Thus, the export of surface-derived microbes to the deep ocean is significantly smaller in ice-free region. Overall, considering the similar conditions between the surface and the deep waters of the Arctic Ocean (e.g., temperature, oligotrophy), these surface-derived microbes may remain active and play an important role in remineralization of the sinking particles at depth.

In conclusion, the observed vertical microbial connectivity provides an important evidence for the biological carbon pump functioning, under distinct sea ice conditions in the Arctic Ocean. The effectively mediated connectivity by sinking marine particles in ice-covered waters suggests rapid vertical export of particulate organic matter from surface to the deep ocean and eventually to the seafloor. In contrast, the slow sinking particles of the ice-free waters mediate a substantially weaker microbial connectivity, which suggests stronger remineralization of the sinking particles in the upper layers of the water column. These scenarios can be directly projected to future decline in sea ice cover of the Arctic Ocean, suggesting strong impact on the biogeochemical processes in the water column and the seafloor.

Materials and methods

Sampling campaign. The sampling was performed during RV Polarstern expedition PS99.2 to the LTER observatory HAUSGARTEN in the Fram Strait (June 24th – July 16th 2016). The *in situ* profiling of marine particles was carried out using Underwater Vision Profiler 5hd (UVP; Hydroptic, France) mounted to the water sampler rosette (48). The UVP measures numbers and sizes of particles within a defined volume of water, which provides quantitative information on the size distribution of particles throughout the water column. Using a marine snow catcher (MSC) we sampled intact particles, at 60 m depth. The particles were measured on board for their size, composition, and sinking velocities. To investigate the vertical structure and connectivity of free-living and particle-associated microbial communities, size fractionated water samples (0.22 μm and 5 μm) were collected from 4 distinct water layers throughout the entire water column. Detailed information on the sampling procedures can be found in *SI Materials and Methods*.

Modeled particles sinking trajectories. We use a Lagrangian particle tracking algorithm to determine the sinking trajectories of particles in different regions of the sampling area (71). The algorithm integrates sinking velocities of particles with horizontal currents from the sea ice-ocean model FESOM (67). Detailed description of the model can be found in *SI Materials and Methods*.

Microbial community analyses. Genomic bacterial and archaeal DNA was isolated and the 16S rRNA gene was amplified using 515F-Y and 926R primers (103). The amplicon sequencing procedure on the Illumina MiSeq platform was conducted following the standard

instructions of the 16S Metagenomic Sequencing Library Preparation protocol (Illumina, Inc., San Diego, CA, USA).

After quality control and merging the amplicons were clustered into OTU with Swarm v2.0 (104), and taxonomically classified using SINA v1.2.11 (105) against Silva reference database release 132 (106). All the statistical analyses were conducted using R v3.4.1 (http://www.Rproject.org/). Detailed information on the bioinformatics procedures and statistical analyses can be found in *SI Materials and Methods*.

Microbial source tracking. To determine potential colonization of marine particles by free-living microbes, and their export from surface water to the deep ocean, we used the Bayesian MST algorithm 'SourceTracker' v1.0 (51). Based on the assumption that the particles-associated microbial communities (i.e., 'sink' communities) are result of various events of colonization of particles by free-living microbes (i.e., 'source' communities), the 'algorithm provided estimated proportions of each of the different 'source' communities within the 'sink' community (further described in *SI Materials and Methods*).

Data availability. The data is accessible via the Data Publisher for Earth & Environmental Science PANGAEA (www.pangaea.de): vertical profiles of total particle volume - doi: 10.1594/PANGAEA.896047. Raw paired-end sequence, primer-trimmed reads were deposited in the European Nucleotide Archive (ENA) (107) under accession number PRJEB30254. The data were archived using the brokerage service of the German Federation for Biological Data (GFBio) (108). Scripts for processing data can be accessed at https://github.com/edfadeev/XXX.

459 interactions with the biological pump": VH-NG-1000. This publication is Eprint ID XXX of

460 the Alfred Wegener Institute for Polar and Marine Research, Bremerhaven, Germany.

461

References

463 1. Dobricic S, Vignati E, Russo S (2016) Large-scale atmospheric warming in winter and
464   the arctic sea ice retreat. *J Clim* 29(8):2869–2888.

465 2. Sun L, Perlwitz J, Hoerling M (2016) What caused the recent "Warm Arctic, Cold
466   Continents" trend pattern in winter temperatures? *Geophys Res Lett* 43(10):5345–5352.

467 3. Kwok R, Rothrock DA (2009) Decline in Arctic sea ice thickness from submarine and
468   ICESat records: 1958-2008. *Geophys Res Lett* 36(15):n/a-n/a.

469 4. Peng G, Meier WN (2017) Temporal and regional variability of Arctic sea-ice coverage
470   from satellite data. *Ann Glaciol*:1–10.

471 5. Notz D, Stroeve J (2016) Observed Arctic sea-ice loss directly follows anthropogenic
472   CO 2 emission. *Science (80-)* 354(6313):747–750.

473 6. Polyakov I V., et al. (2017) Greater role for Atlantic inflows on sea-ice loss in the
474   Eurasian Basin of the Arctic Ocean. *Science (80-)* 356(6335):285–291.

475 7. Overland JE, Wang M (2013) When will the summer Arctic be nearly sea ice free?
476   *Geophys Res Lett* 40(10):2097–2101.

477 8. Tremblay J-É, et al. (2015) Global and regional drivers of nutrient supply, primary
478   production and CO2 drawdown in the changing Arctic Ocean. *Prog Oceanogr*
479   139:171–196.

480 9. Arrigo KR, van Dijken GL (2015) Continued increases in Arctic Ocean primary
481   production. *Prog Oceanogr* 136:60–70.

482 10. Randelhoff A, et al. (2018) Seasonality of the Physical and Biogeochemical
483   Hydrography in the Inflow to the Arctic Ocean Through Fram Strait. *Front Mar Sci*
484   5(June):224.

485 11. Li WKW, McLaughlin FA, Lovejoy C, Carmack EC (2009) Smallest Algae Thrive As
486   the Arctic Ocean Freshens. *Science (80-)* 326(5952):539–539.

487 12. Boetius A, et al. (2013) Export of Algal Biomass from the Melting Arctic Sea Ice.
488   *Science (80-)* 339(6126):1430–1432.

489 13. Nöthig E-M, et al. (2015) Summertime plankton ecology in Fram Strait—a compilation
490   of long- and short-term observations. *Polar Res* 34(1):23349.

491 14. Engel A, et al. (2017) Inter-annual variability of transparent exopolymer particles in the
492   Arctic Ocean reveals high sensitivity to ecosystem changes. *Sci Rep* 7(1):4129.

493   15.   Lasternas S, Agustí S (2010) Phytoplankton community structure during the record
494   Arctic ice-melting of summer 2007. *Polar Biol* 33(12):1709–1717.

495   16.   Ducklow H, Steinberg D, Buesseler K (2001) Upper Ocean Carbon Export and the
496   Biological Pump. *Oceanography* 14(4):50–58.

497   17.   Iversen MH, Ploug H (2010) Ballast minerals and the sinking carbon flux in the ocean:
498   carbon-specific respiration rates and sinking velocity of marine snow aggregates.
499   *Biogeosciences* 7(9):2613–2624.

500   18.   Ploug H, Iversen MH, Fischer G (2008) Ballast, sinking velocity, and apparent
501   diffusivity within marine snow and zooplankton fecal pellets: Implications for substrate
502   turnover by attached bacteria. *Limnol Oceanogr* 53(5):1878–1886.

503   19.   Ploug H, Iversen MH, Koski M, Buitenhuis ET (2008) Production, oxygen respiration
504   rates, and sinking velocity of copepod fecal pellets: Direct measurements of ballasting
505   by opal and calcite. *Limnol Oceanogr* 53(2):469–476.

506   20.   Vernet M, Richardson TL, Metfies K, Nöthig E-M, Peeken I (2017) Models of
507   Plankton Community Changes during a Warm Water Anomaly in Arctic Waters Show
508   Altered Trophic Pathways with Minimal Changes in Carbon Export. *Front Mar Sci*
509   4(May):1–19.

510   21.   Wollenburg JE, et al. (2018) Ballasting by cryogenic gypsum enhances carbon export
511   in a Phaeocystis under-ice bloom. *Sci Rep* 8(1):7703.

512   22.   Herndl GJ, Reinthaler T (2013) Microbial control of the dark end of the biological
513   pump. *Nat Geosci* 6(9):718–724.

514   23.   Aristegui J, Gasol JM, Duarte CM, Herndl GJ (2009) Microbial oceanography of the
515   dark ocean's pelagic realm. *Limnol Oceanogr* 54(5):1501–1529.

516   24.   Azam F, Long RA (2001) Sea snow microcosms. *Nature* 414(6863):495–498.

517   25.   Azam F, Malfatti F (2007) Microbial structuring of marine ecosystems. *Nat Rev*
518   *Microbiol* 5(10):782–791.

519   26.   Grossart H, et al. (2006) Interactions between marine snow and heterotrophic bacteria:
520   aggregate formation and microbial dynamics. *Aquat Microb Ecol* 42(1):19–26.

521   27.   Arnosti C (2011) Microbial Extracellular Enzymes and the Marine Carbon Cycle. *Ann*
522   *Rev Mar Sci* 3(1):401–425.

523   28.   Karner M, Herndl GJ (1992) Extracellular enzymatic activity and secondary production
524   in free-living and marine-snow-associated bacteria. *Mar Biol* 113(2):341–347.

525   29.   Grossart H-P, Tang KW, KiÃ¸rboe T, Ploug H (2007) Comparison of cell-specific
526   activity between free-living and attached bacteria using isolates and natural

124

527   assemblages. *FEMS Microbiol Lett* 266(2):194–200.

528   30.   Bianchi D, Weber TS, Kiko R, Deutsch C (2018) Global niche of marine anaerobic

529   metabolisms expanded by particle microenvironments. *Nat Geosci* 11(April):1–6.

530   31.   Bristow LA (2018) Anoxia in the snow. *Nat Geosci* 11(April):1–2.

531   32.   Woebken D, Fuchs BM, Kuypers MMM, Amann R (2007) Potential interactions of

532   particle-associated anammox bacteria with bacterial and archaeal partners in the

533   Namibian upwelling system. *Appl Environ Microbiol* 73(14):4648–4657.

534   33.   Datta MS, Sliwerska E, Gore J, Polz MF, Cordero OX (2016) Microbial interactions

535   lead to rapid micro-scale successions on model marine particles. *Nat Commun*

536   7(May):11965.

537   34.   Simon M, Grossart HH, Schweitzer B, Ploug H (2002) Microbial ecology of organic

538   aggregates in aquatic ecosystems. *Aquat Microb Ecol* 28:175–211.

539   35.   Grossart H-P, Kiørboe T, Tang K, Ploug H (2003) Bacterial Colonization of Marine

540   Snow Particles: Growth and Inter-Specific Interactions. *Appl Environ Microbiol*

541   69(6):3500–3509.

542   36.   Kiørboe T, Grossart H-P, Ploug H, Tang K (2002) Mechanisms and rates of

543   colonisation of sinking aggregates. *Appl Environ Microbiol* 68(8):3996–4006.

544   37.   Stocker R (2012) Marine Microbes See a Sea of Gradients. *Science (80-)*

545   338(6107):628–633.

546   38.   Stocker R, Seymour JR, Samadani A, Hunt DE, Polz MF (2008) Rapid chemotactic

547   response enables marine bacteria to exploit ephemeral microscale nutrient patches.

548   105(11):4209–4214.

549   39.   Enke TN, Leventhal GE, Metzger M, Saavedra JT, Cordero OX (2018) Microscale

550   ecology regulates particulate organic matter turnover in model marine microbial

551   communities. *Nat Commun* 9(1):2743.

552   40.   Mestre M, et al. (2017) Spatial variability of marine bacterial and archaeal

553   communities along the particulate matter continuum. *Mol Ecol* 26(24):6827–6840.

554   41.   Salazar G, et al. (2015) Particle-association lifestyle is a phylogenetically conserved

555   trait in bathypelagic prokaryotes. *Mol Ecol* 24(22):5692–5706.

556   42.   Mestre M, et al. (2018) Sinking particles promote vertical connectivity in the ocean

557   microbiome. *Proc Natl Acad Sci* 115(29):E6799–E6807.

558   43.   Rudels B, et al. (2013) Observations of water masses and circulation with focus on the

559   Eurasian Basin of the Arctic Ocean from the 1990s to the late 2000s. *Ocean Sci*

560   9(1):147–169.

561 44. Tamburini C, Boutrif M, Garel M, Colwell RR, Deming JW (2013) Prokaryotic
562   responses to hydrostatic pressure in the ocean - a review. *Environ Microbiol*
563   15(5):1262–1274.

564 45. Rapp JZ, Fernández-Méndez M, Bienhold C, Boetius A (2018) Effects of ice-algal
565   aggregate export on the connectivity of bacterial communities in the central Arctic
566   Ocean. *Front Microbiol* 9(MAY). doi:10.3389/fmicb.2018.01035.

567 46. Walsh EA, et al. (2016) Bacterial diversity and community composition from
568   seasurface to subseafloor. *ISME J* 10(4):979–989.

569 47. Soltwedel T, et al. (2016) Natural variability or anthropogenically-induced variation?
570   Insights from 15 years of multidisciplinary observations at the arctic marine LTER site
571   HAUSGARTEN. *Ecol Indic* 65:89–102.

572 48. Picheral M, et al. (2010) The Underwater Vision Profiler 5: An advanced instrument
573   for high spatial resolution studies of particle size spectra and zooplankton. *Limnol*
574   *Oceanogr Methods* 8(9):462–473.

575 49. Ploug H, Jørgensen BB (1999) A net-jet flow system for mass transfer and micro
576   electrode studies in sinking aggregates. *Mar Ecol Prog Ser* 176(1987):279.

577 50. Ploug H, Terbrüggen A, Kaufmann A, Wolf-Gladrow D, Passow U (2010) A novel
578   method to measure particle sinking velocity in vitro, and its comparison to three other
579   in vitro methods. *Limnol Oceanogr Methods* 8(8):386–393.

580 51. Knights D, et al. (2011) Bayesian community-wide culture-independent microbial
581   source tracking. *Nat Methods* 8(9):761–763.

582 52. Rudels B, Nilsson J, Winsor P (2005) The interaction between waters from the Arctic
583   Ocean and the Nordic Seas north of Fram Strait and along the East Greenland Current :
584   results from the Arctic Ocean-02 Oden expedition. 55:1–30.

585 53. Beszczynska-Moller A, Fahrbach E, Schauer U, Hansen E (2012) Variability in
586   Atlantic water temperature and transport at the entrance to the Arctic Ocean, 1997-
587   2010. *ICES J Mar Sci* 69(5):852–863.

588 54. de Steur L, et al. (2009) Freshwater fluxes in the East Greenland Current: A decade of
589   observations. *Geophys Res Lett* 36(23):L23611.

590 55. Hebbeln D, Wefer G (1991) Effects of ice coverage and ice-rafted material on
591   sedimentation in the Fram Strait. *Nature* 350:409.

592 56. Schewe I, Soltwedel T (2003) Benthic response to ice-edge-induced particle flux in the
593   Arctic Ocean. *Polar Biol* 26(9):610–620.

594 57. Perrette M, Yool A, Quartly GD, Popova EE (2011) Near-ubiquity of ice-edge blooms

595   in the Arctic. *Biogeosciences* 8(2):515–524.

596 58. Nöthig E-M, et al. (2015) Summertime plankton ecology in Fram Strait—a compilation

597   of long- and short-term observations. *Polar Res* 34(1):23349.

598 59. Fadeev E, et al. (2018) Microbial communities in the East and West Fram Strait during

599   sea-ice melting season. *Front Mar Sci* 5:429.

600 60. von Appen W-J, Schauer U, Somavilla R, Bauerfeind E, Beszczynska-Möller A (2015)

601   Exchange of warming deep waters across Fram Strait. *Deep Sea Res Part I Oceanogr*

602   *Res Pap* 103:86–100.

603 61. Buesseler KO (1998) The decoupling of production and particle export in the surface

604   ocean. *Global Biogeochem Cycles* 12(2):297–310.

605 62. Bergmann M, Schewe I (2017) High resolution movies along OFOS profile PS99/048-

606   14. doi:10.1594/PANGAEA.873926.

607 63. Wells LE, Deming JW (2003) Abundance of bacteria, the Cytophaga-Flavobacterium

608   cluster and Archaea in cold oligotrophic waters and nepheloid layers of the Northwest

609   Passage, Canadian archipelago. *Aquat Microb Ecol* 31(1):19–31.

610 64. Reigstad M, Wassmann P (2007) Does Phaeocystis spp. contribute significantly to

611   vertical export of organic carbon? *Phaeocystis, Major Link in the Biogeochemical*

612   *Cycling of Climate-Relevant Elements* (Springer Netherlands, Dordrecht), pp 217–234.

613 65. Iversen MH, Ploug H (2010) Ballast minerals and the sinking carbon flux in the ocean:

614   carbon-specific respiration rates and sinking velocity of marine snow aggregates.

615   *Biogeosciences* 7(9):2613–2624.

616 66. Wekerle C, et al. (2018) Properties of Sediment Trap Catchment Areas in Fram Strait:

617   Results From Lagrangian Modeling and Remote Sensing. *Front Mar Sci* 5(November).

618   doi:10.3389/fmars.2018.00407.

619 67. Wang Q, et al. (2014) The Finite Element Sea Ice-Ocean Model (FESOM) v.1.4:

620   formulation of an ocean general circulation model. *Geosci Model Dev* 7(2):663–693.

621 68. De La Rocha CL, Passow U (2007) Factors influencing the sinking of POC and the

622   efficiency of the biological carbon pump. *Deep Res Part II Top Stud Oceanogr* 54(5–

623   7):639–658.

624 69. McDonnell AMP, Boyd PW, Buesseler KO (2015) Effects of sinking velocities and

625   microbial respiration rates on the attenuation of particulate carbon fluxes through the

626   mesopelagic zone. *Global Biogeochem Cycles* 29(2):175–193.

627 70. Iversen MH, Ploug H (2013) Temperature effects on carbon-specific respiration rate

628   and sinking velocity of diatom aggregates – potential implications for deep ocean

629   export processes. *Biogeosciences Discuss* 10(1):371–399.

630   71.   Wekerle C, Krumpen T, Dinter T, Iversen M, Salter I (2018) Origin and properties of
631   sediment trap catchment areas in Fram Strait : results from Lagrangian modelling and
632   remote sensing. *Front Mar Sci*:1–26.

633   72.   Bienhold C, Boetius A, Ramette A (2012) The energy-diversity relationship of
634   complex bacterial communities in Arctic deep-sea sediments. *ISME J* 6(4):724–732.

635   73.   Wittebolle L, et al. (2009) Initial community evenness favours functionality under
636   selective stress. *Nature* 458(7238):623–626.

637   74.   Frank AH, Garcia JAL, Herndl GJ, Reinthaler T (2016) Connectivity between surface
638   and deep waters determines prokaryotic diversity in the North Atlantic Deep Water.
639   *Environ Microbiol* 18(6):2052–2063.

640   75.   Marnela M, Rudels B, Goszczko I, Beszczynska-Möller A, Schauer U (2016) Fram
641   Strait and Greenland Sea transports, water masses, and water mass transformations
642   1999-2010 (and beyond). *J Geophys Res Ocean* 121(4):2314–2346.

643   76.   Thiele S, Fuchs BM, Amann R, Iversen MH (2015) Colonization in the Photic Zone
644   and Subsequent Changes during Sinking Determine Bacterial Community Composition
645   in Marine Snow. *Appl Environ Microbiol* 81(4):1463–1471.

646   77.   Yawata Y, et al. (2014) Competition-dispersal tradeoff ecologically differentiates
647   recently speciated marine bacterioplankton populations. *Proc Natl Acad Sci*
648   111(15):5622–5627.

649   78.   Buchan A, et al. (2014) Master recyclers: features and functions of bacteria associated
650   with phytoplankton blooms. *Nat Rev Microbiol* 12(10):686–698.

651   79.   Teeling H, et al. (2012) Substrate-Controlled Succession of Marine Bacterioplankton
652   Populations Induced by a Phytoplankton Bloom. *Science (80-)* 336(6081):608–611.

653   80.   Chow C-ET, et al. (2013) Temporal variability and coherence of euphotic zone
654   bacterial communities over a decade in the Southern California Bight. *ISME J*
655   7(12):2259–2273.

656   81.   Teeling H, et al. (2016) Recurring patterns in bacterioplankton dynamics during coastal
657   spring algae blooms. *Elife* 5(APRIL2016):1–31.

658   82.   Cram JA, et al. (2015) Cross-depth analysis of marine bacterial networks suggests
659   downward propagation of temporal changes. *ISME J* 9(12):2573–2586.

660   83.   Cram JA, et al. (2015) Seasonal and interannual variability of the marine
661   bacterioplankton community throughout the water column over ten years. *ISME J*
662   9(3):563–580.

128

663   84. Woebken D, Fuchs BM, Kuypers MMM, Amann R (2007) Potential interactions of

664   particle-associated anammox bacteria with bacterial and archaeal partners in the

665   Namibian upwelling system. *Appl Environ Microbiol* 73(14):4648–4657.

666   85. Strous M, et al. (2006) Deciphering the evolution and metabolism of an anammox

667   bacterium from a community genome. *Nature* 440(7085):790–794.

668   86. Kuypers MMM, et al. (2003) Anaerobic Ammonium Oxidation by Anammox Bacteria

669   in the Black Sea. *Nature* 422(6932):608–611.

670   87. Jones ZL, Jasper JT, Sedlak DL, Sharp JO (2017) Sulfide-Induced Dissimilatory

671   Nitrate Reduction to Ammonium Supports Anaerobic Ammonium Oxidation

672   (Anammox) in an Open-Water Unit Process Wetland. *Appl Environ Microbiol*

673   83(15):1–14.

674   88. Muyzer G, Stams AJM (2008) The ecology and biotechnology of sulphate-reducing

675   bacteria. *Nat Rev Microbiol* 6(6):441–454.

676   89. Cordero OX, Datta MS (2016) Microbial interactions and community assembly at

677   microscales. *Curr Opin Microbiol* 31(Figure 1):227–234.

678   90. Henry R, et al. (2016) Into the deep: Evaluation of SourceTracker for assessment of

679   faecal contamination of coastal waters. *Water Res* 93:242–253.

680   91. Neave M, et al. (2014) Multiple approaches to microbial source tracking in tropical

681   northern Australia. *Microbiologyopen* 3(6):860–874.

682   92. Wilkins D, Van Sebille E, Rintoul SR, Lauro FM, Cavicchioli R (2013) Advection

683   shapes Southern Ocean microbial assemblages independent of distance and

684   environment effects. *Nat Commun* 4(May):1–7.

685   93. Friedman J, Hastie T, Tibshirani R (2001) *The elements of statistical learning*

686   (Springer series in statistics New York, NY, USA:).

687   94. Padilla CC, et al. (2015) Standard filtration practices may significantly distort

688   planktonic microbial diversity estimates. *Front Microbiol* 6(JUN):1–10.

689   95. Duret MT, Lampitt RS, Lam P (2018) Prokaryotic Niche Partitioning Between

690   Suspended and Sinking Marine Particles. *Environ Microbiol Rep*. doi:10.1111/1758-

691   2229.12692.

692   96. Mestre M, Borrull E, Sala MM, Gasol JM (2017) Patterns of bacterial diversity in the

693   marine planktonic particulate matter continuum. *ISME J* 11(4):999–1010.

694   97. Mestre M, et al. (2017) Spatial variability of marine bacterial and archaeal

695   communities along the particulate matter continuum. *Mol Ecol* 26(24):6827–6840.

696   98. Bochdansky AB, Clouse MA, Herndl GJ (2016) Dragon kings of the deep sea: Marine

697   particles deviate markedly from the common number-size spectrum. *Sci Rep*
698   6(September 2015):4–10.

699   99.   Herndl GJ, Reinthaler T (2013) Microbial control of the dark end of the biological
700   pump. *Nat Geosci* 6(9):718–724.

701   100.   Teeling H, et al. (2016) Recurring patterns in bacterioplankton dynamics during coastal
702   spring algae blooms. *Elife* 5(APRIL2016):1–31.

703   101.   Bunse C, Pinhassi J (2017) Marine Bacterioplankton Seasonal Succession Dynamics.
704   *Trends Microbiol* 25(6):494–505.

705   102.   Leu E, Søreide JE, Hessen DO, Falk-Petersen S, Berge J (2011) Consequences of
706   changing sea-ice cover for primary and secondary producers in the European Arctic
707   shelf seas: Timing, quantity, and quality. *Prog Oceanogr* 90(1–4):18–32.

708   103.   Parada AE, Needham DM, Fuhrman JA (2016) Every base matters: assessing small
709   subunit rRNA primers for marine microbiomes with mock communities, time series
710   and global field samples. *Environ Microbiol* 18(5):1403–1414.

711   104.   Mahé F, Rognes T, Quince C, de Vargas C, Dunthorn M (2015) Swarm v2: highly-
712   scalable and high-resolution amplicon clustering. *PeerJ* 3:e1420.

713   105.   Pruesse E, Peplies J, Glöckner FO (2012) SINA: Accurate high-throughput multiple
714   sequence alignment of ribosomal RNA genes. *Bioinformatics* 28(14):1823–1829.

715   106.   Quast C, et al. (2013) The SILVA ribosomal RNA gene database project : improved
716   data processing and web-based tools. 41(November 2012):590–596.

717   107.   Silvester N, et al. (2018) The European Nucleotide Archive in 2017. *Nucleic Acids Res*
718   46(D1):D36–D40.

719   108.   Diepenbroek M, et al. (2014) Towards an integrated biodiversity and ecological
720   research data management and archiving platform: the German federation for the
721   curation of biological data (GFBio). *Informatik 2014*, eds Plödereder E, Grunske L,
722   Schneider E, Ull D (Gesellschaft für Informatik e.V., Bonn), pp 1711–1721.

Figures
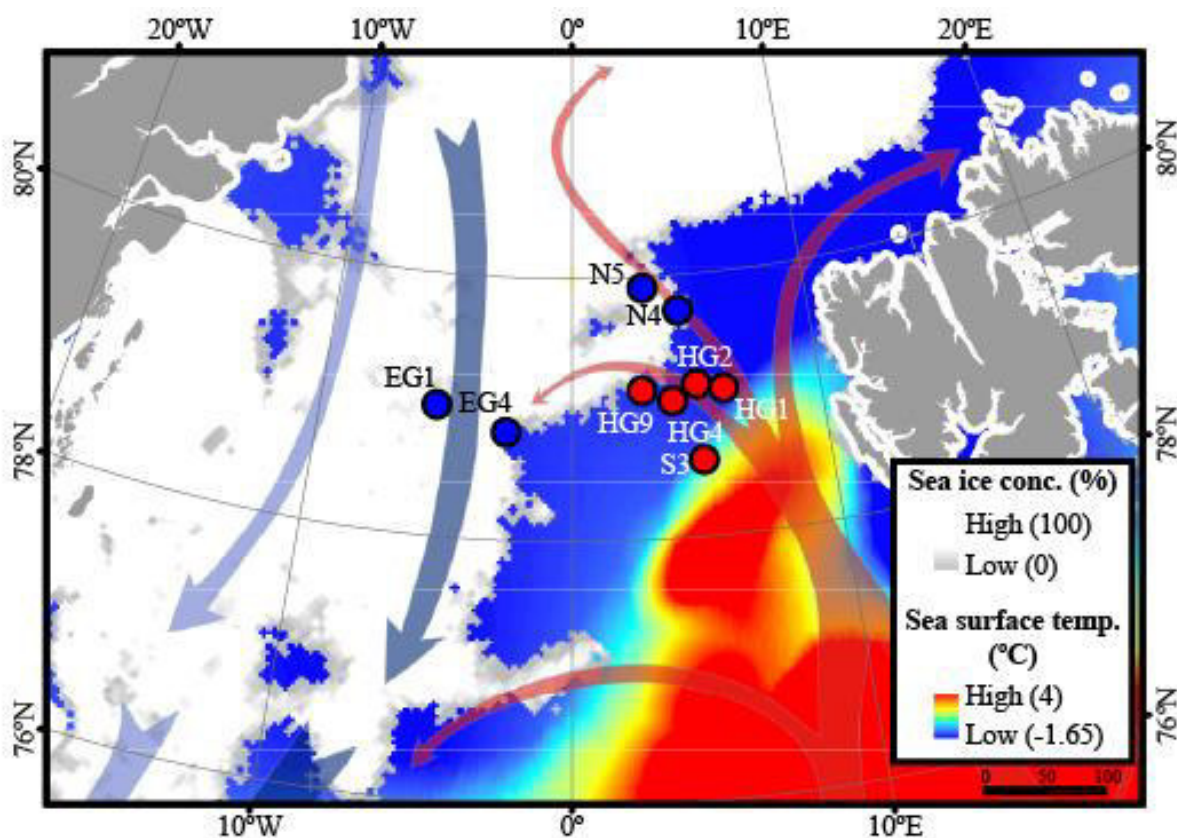
Fig. 1. Oceanographic overview of Fram Strait during July 2016. Monthly mean of sea-ice cover and sea surface temperature during July 2016. The sea ice concentration is represented by inverted grayscale (gray-low, white-high). The arrows represent general directions of the WSC (in red) and the EGC (in blue). Stations of water column sampling are indicated and colored according to their sea-ice conditions: ice-covered EG and N stations (blue), ice-free HG stations (red). The map was generated using ArcMap (v.10.5) with Esri world countries dataset (www.esri.com) in a WGS 1984 Arctic Polar Stereographic map projection.

732
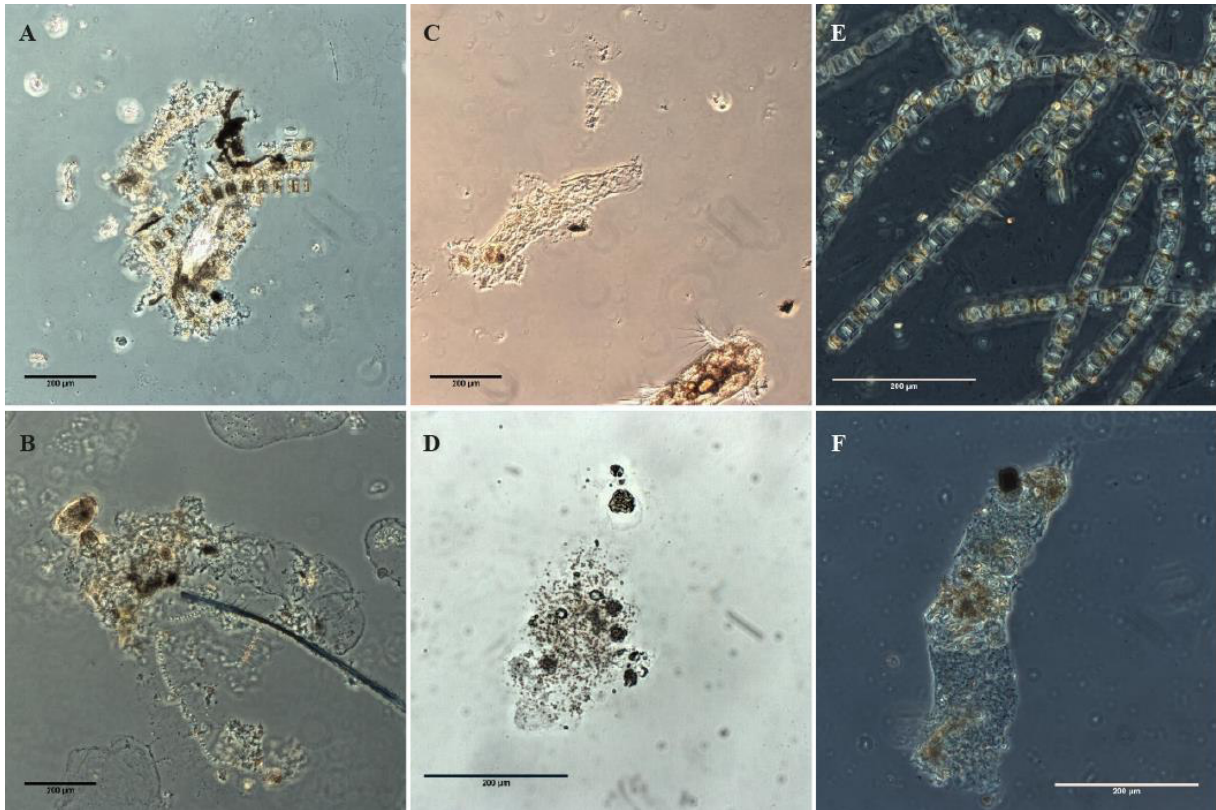
Fig. 2. Exemplary light microscopy images of marine aggregates in Fram Strait. (*A,B*) Aggregates dominated by diatoms from ice-covered region -'EG', where *A* is mainly diatoms and *B* is diatoms together with *Phaeocystis*. (*C,D*) Aggregates dominated by flagellates in ice-free region - 'HG', where *C* is a copepod fecal pellet produced from flagellates and *D* is a marine snow aggregate formed from *Phaeocystis* colonies. (*E*) Chains of *Melosira spp.*, diatoms growing under the sea ice. (*F*) *Calanus spp.* (copepod) fecal pellets collected at the partially ice-covered region - 'N' and formed from mainly *Phaeocystis* colonies with a few diatoms. All scale bars are 200 µm long. White arrows point towards diatom chains and black arrows point towards colonies of flagellates.

132

742
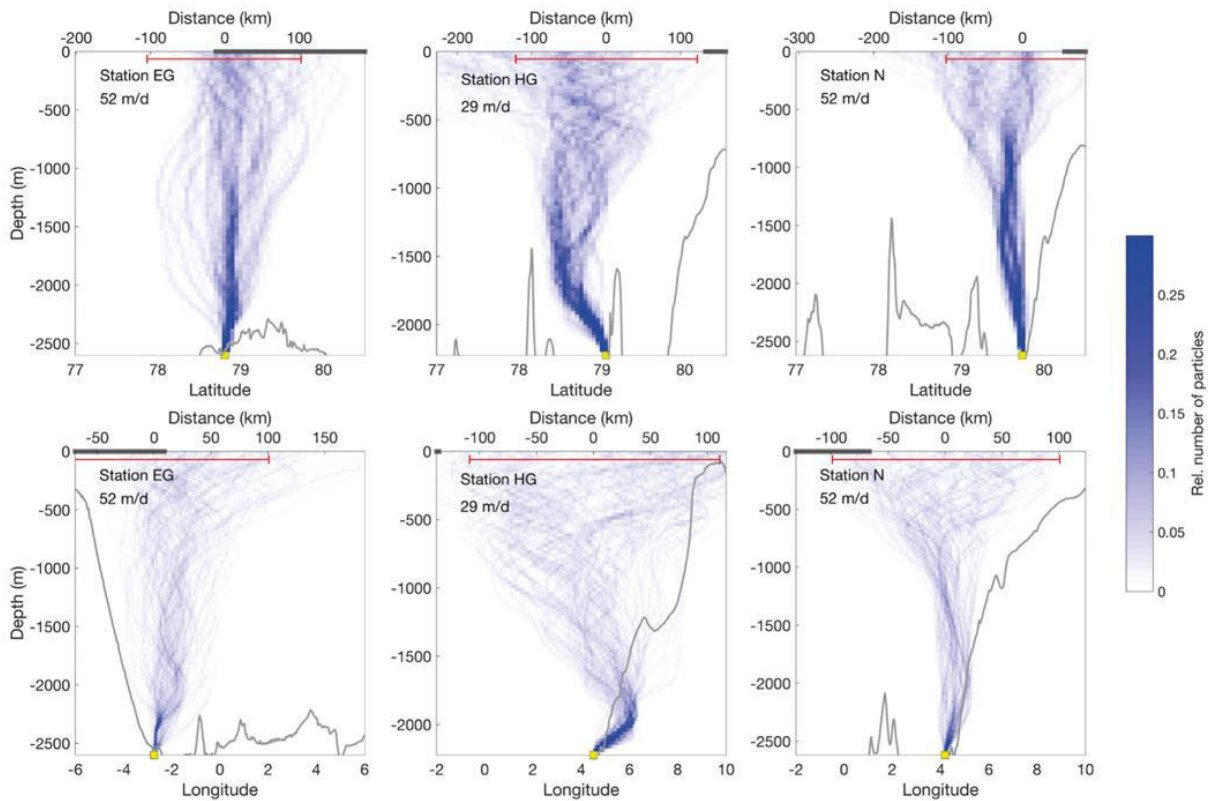
Fig. 3. Sinking trajectories of particles across the Fram Strait. Distribution of particle origin in surface (A), and sinking trajectories as a function of latitude (B) and longitude (C). The backward particle trajectories were computed for the time period March-July 2016, based on measured mean sinking velocities (Table 1). In panel A light blue dots represent particles originated in ice-covered waters, and dark blue dots represent particles originated in ice-free waters. The yellow square indicates the starting point of the backward particle trajectory calculation. The dark gray bar on the top of the figures indicates the presence of sea ice in July 2016 (> 15% concentration).
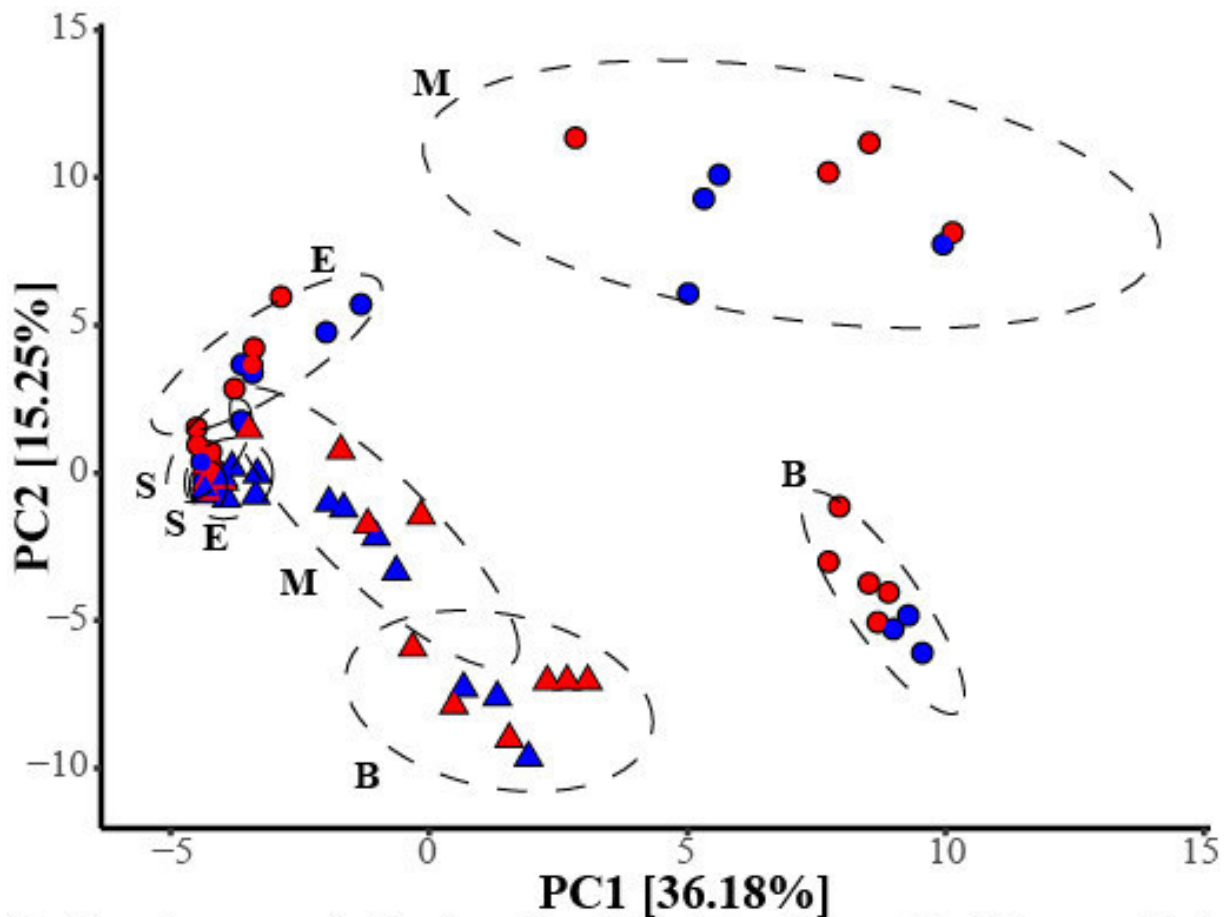
Region ● Ice-covered ● Ice-free **Fraction** ○ Free-living △ Particle-associated

Fig. 4. Free-living and particle-associated community patterns throughout the water column of Fram Strait. Principal component analysis (PCA) of microbial communities, based on Euclidean distances. Colors represent different geographic origins, and the shapes indicate free-living (FL) and particle-associated (PA) community fractions. Ellipses encompass clustering of each of the fractions by water layer (S-surface, E-epipelagic, M-mesopelagic, B-bathypelagic), with normal confidence of 0.95. The percentages on both axes represent the explained variance of the axis.
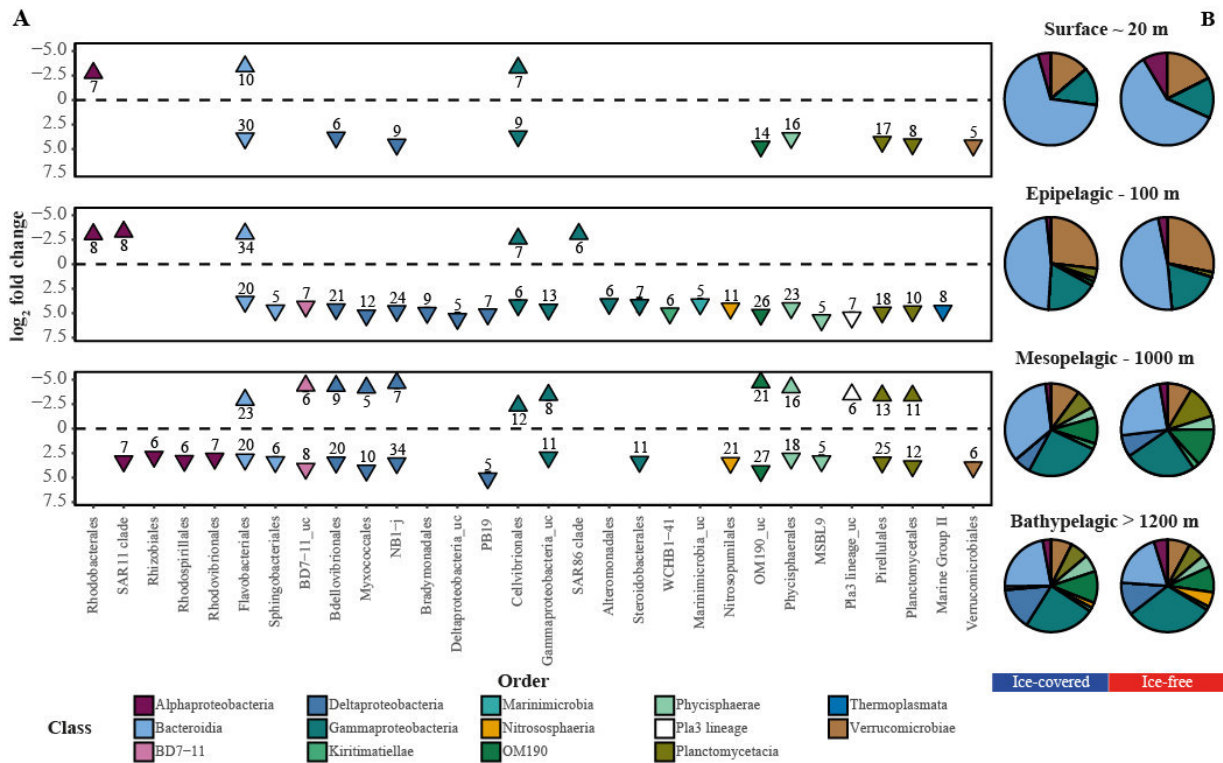
Fig. 5. Differences in particle-associated (PA) community composition between the distinct water layers. (A) Enriched OTUs between each two consecutive depths (ordered according to labels in panel B). The y axis represents the mean log$_2$ fold change for orders with more than 5 OTUs (standard error is smaller than the point). The numbers below the symbols represent the number of OTUs enriched in the depth. The x axis is ordered according to the different taxonomic classes, represented by the color code. (B) A mean PA community composition in ice-covered and ice-free regions. Only taxonomic classes with sequence abundances above 1% were included in the visualization.
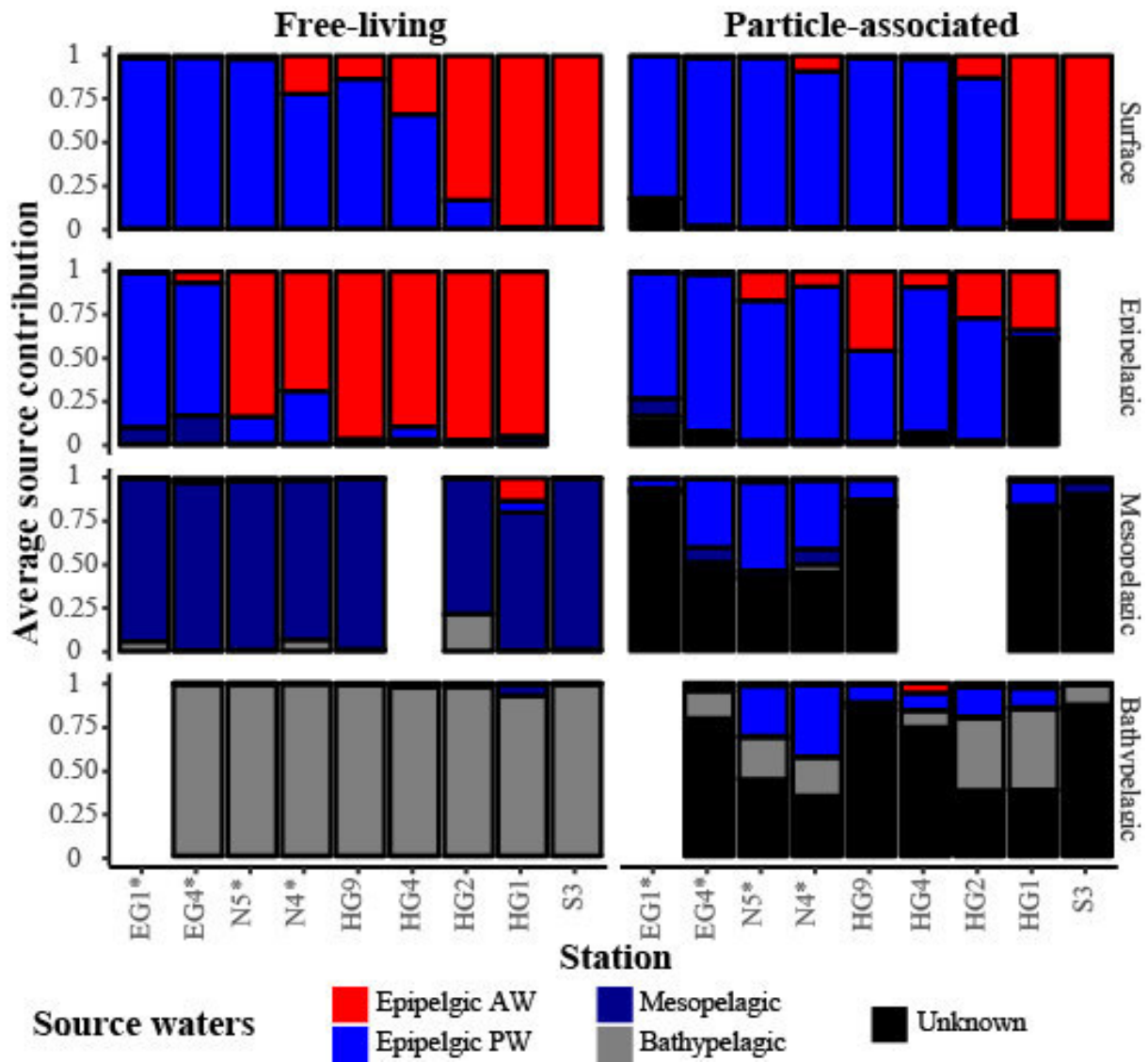
Fig. 6. Water mass source proportion estimates for microbial communities along the water column, conducted using 'SourceTracker'. The source estimates for the free-living (FL) communities were estimated using the leave-one-out approach, and the sources of the particle-associated (PA) communities were estimated based on the FL communities. The ice-covered stations are marked with an asterisk.

2.3.1 How does sea ice coverage affect the vertical connectivity of the microbial community in the Arctic?

In Paper IV, we investigated the impact of sea ice coverage on the particle composition, size distribution, size-specific sinking velocities and the associated microbial communities to shed light on the vertical connectivity between surface and deep ocean microbial communities in the Arctic.

We could observe a sustained particle export down to 1000 m in ice-free regions, whereas the water column of ice-covered regions was generally characterized by lower particle abundances but with episodic export of larger particles towards deeper layers. Flow chamber measurements of aggregate composition, size, and sinking velocity demonstrated that larger aggregates from ice-covered regions were characterized by a high sinking velocity and consisted mainly of diatoms, such as *Melosira arctica*. This diatom species is associated with sea ice and known to cause rapid export of organic matter (Boetius *et al.* 2013; Rapp *et al.* 2018). On the other hand, slow sinking and smaller aggregates, sampled in ice-free regions, consisted mainly of *Phaeocystis spp.*, which confirmed earlier studies regarding the influence of sea ice coverage on phytoplankton communities and particle-specific sinking velocities in the Arctic (Iversen and Ploug 2010; Lasternas and Agusti 2010; Nöthig *et al.* 2015; Engel *et al.* 2017).

The free-living microbial community was strongly impacted by a stratified water column, visible as a strong dissimilarity in community composition between different water masses. The particle-associated community, however, showed less dissimilarity in different layers, indicating a high vertical connectivity. Microbial source tracking revealed that particle-associated microbial communities of surface and epipelagic waters were most closely genetically related to epipelagic free-living communities, whereas the free-living community in the deep sea had much less impact on the deep particle-associated community. This indicated a low level of genetic exchange between free-living and particle-associated communities in deep layers, which confirmed earlier studies (Salazar *et al.* 2015; Thiele *et al.* 2015). In addition, the increasing dissimilarity between free-living and particle-associated communities with depth promoted these observations.

Most importantly, we could show that the contribution of the free-living microbial community from surface waters on the particle-associated community in the deep sea was on average three times higher in ice-covered regions compared with ice-free regions. This

observation was most likely linked to the high sinking velocities of larger aggregates formed from sea ice-associated diatoms: their lower retention times caused decreased degradation, which led to increased export depths. This effect promoted a much stronger vertical connectivity of microbial communities in the ice-covered water column.

We concluded that fast-sinking particles cause a strong vertical connection of microbial communities, which is in the Arctic most pronounced in sea ice-covered regions. A further decline in sea-ice coverage, induced by global warming, might reduce the deep export of particles in the future due to a shift towards primary producers without biominerals, e.g. *Phaeocystis spp.*, This may lead to a decreased vertical connectivity of microbial communities in the deep ocean and, thus, have an impact on the deep sea biogeochemical cycling.

Interestingly, we could also observe microbial community succession towards potentially sub- or anoxic organisms within particles. This gives additional evidence for anaerobic metabolism in particle-associated micro-environments. Investigations on the influence of global warming on these small-scale processes could be achieved in further studies using slicing and single-cell uptake methods as described in Paper II and III.

2.4 Physical effects on the biological carbon pump

Effects of small-scale processes, such as carbon dioxide or nutrient production due to respiration or remineralization, respectively, can cumulate with increasing scale of observation due to the high abundance of particles in many regions of the ocean. Here, general oceanographic phenomena, which shape the biological carbon pump (BCP), become important. Coastal upwelling regions (Lavik *et al.* 2009; Waldron *et al.* 2009) and the equatorial divergence (Kiko *et al.* 2017), for instance, are characterized by high production and carbon export associated with deep particles plumes of thousands of meters. Nutrient depleted gyres, on the other hand, are generally characterized by low carbon export (Thomalla *et al.* 2006). One logically following piece of the puzzle is, thus, to understand the impact of oceanographic phenomena on the BCP, such as velocity fields on nutrient input or strong density gradients on particle settling.

The physical properties of meso-scale eddies can also shape the particle distribution (Dufois *et al.* 2016). Meso-scale processes can increase the amount of exported carbon due to increased primary production (Lévy *et al.* 1998) or directly by very high particle sinking velocities caused by high vertical velocities at the perimeter of mesoscale eddies (van Haren *et al.* 2006). The Underwater Vision Profiler can be used to measure or infer lateral and vertical movement of particles across hundreds of kilometers in the horizontal and thousands of meters in the vertical, yielding insight into the interactions of meso- and sub-mesoscale motions with the biological pump (Waite *et al.* 2016; Kiko *et al.* 2017). Using this technology, it could be shown that anticyclonic eddies cause enhanced particle concentration and sedimentation by subsurface convergence, generated by a combination of secondary circulation and eddy relaxation (Waite *et al.* 2016). The effect of cyclonic eddies on particle distribution and export, however, remains unclear.

In the following chapter, I present a study based on high resolution Acoustic Doppler Current Profiler and Underwater Vision Profiler measurements, which demonstrates how a combination of physical sub-mesoscale phenomena and biological processes shape the BCP in a cyclonic eddy of the South Atlantic (Paper V).

PAPER V

Supplementary Information is presented in the Appendix

1 **Sub-mesoscale driven deep particle export in a cyclonic eddy of the South**

2 **Atlantic**

3 Andreas Rogge[1], Johannes Karstensen[2], Alannah Paulina Prondzinsky[3], Morten H. Iversen[4],

4 Anya M. Waite[1,5,6]

5 [1] Alfred-Wegener-Institute Helmholtz-Zentrum für Polar- und Meeresforschung (AWI),

6 Bremerhaven, Germany; [2]GEOMAR Helmholtz Centre for Ocean Research Kiel, Kiel,

7 Germany; [3]Earth-Life Science Institute, Tokyo Institute of Technology, Tokyo, Japan;

8 [4]Marum, Zentrum für Marine Umweltwissenschaften, Bremen, Germany; [5]University of

9 Bremen FB2 Biology / Chemistry, Bremen, Germany; [6]Ocean Frontier Institute, Dalhousie

10 University, Halifax, Canada

11

12 **Running title:** Increased deep particle export by cyclonic eddy.

13

14 *Correspondence: Andreas Rogge

15 E-mail: andreas.rogge@awi.de

16

Abstract

While mesoscale anticyclonic eddies globally have been shown to affect particle export to the deep sea, the influence of cyclonic eddies on carbon export is more poorly understood. Combining particle counting and imaging data with ocean currents data, we analyzed particle production and export processes associated with a mesoscale cyclonic eddy close to the Agulhas retroflection. We infer that the interaction of mesoscale and sub-mesoscale horizontal velocity shear supported high productivity and particle generation via enhanced vertical flux of nutrients into the euphotic zone and disturbance of the gravitational settling by strong flow, respectively. Enhanced primary productivity was measurable as an increase in chlorophyll and small particle abundance (< 0.5 mm) in surface waters above the perimeter of the eddy. Grazing, repackaging, and coprorhexy led to enrichments of detritus particles, most likely fecal pellet fragments. The vertical pattern of the horizontal flow field of the mesoscale cyclonic eddy altered the gravitational settling of particles that appeared in a characteristic V-shape. In combination with reduced degradation activities in the water column below, this effect led to an intense carbon export event with threefold increased flux values, compared to surrounding waters, down to 3000 m and below. We conclude that coupled physicobiological processes associated with propagating cyclonic eddies may lead to regularly occurring deep punctual export events in oligotrophic gyres including enhanced sequestration of carbon.

144

Introduction

The biological carbon pump (BCP) represents an important process within the global carbon cycle[1]. Estimations suggest, that up to 15 % of the total primary production in the marine euphotic zone can be exported passively by sinking particles[2], whereas usually only 5 % of the surface export reaches the deep sea at 3000 m[3]. Regional carbon export is often linked to various physical processes, such as upwelling and mixing, introducing important nutrients into the euphotic zone which increases net primary production.

In the South-East Atlantic, the amount of exported carbon differs drastically: upwelling regions, such as the Benguela upwelling region[4] and the equatorial divergence[5] show high carbon export, in contrast, the South Atlantic subtropical gyre is usually nutrient depleted and a less productive region[6]. It has been shown that mesoscale eddies can increase productivity in the subtropical gyre and enhance carbon export events[7]. On the other hand, eddies can also inhabit specialized flux feeders, such as salps[8] or pelagic polychaetes[9], which reduce the amount of exported carbon drastically. However, grazing of algae and phytodetritus by e.g. copepods[10,11] or salps[8] also causes the production of dense fecal pellets with a highly increased sinking velocity. Thus, the final efficiency of regional carbon export in mesoscale eddies towards the deep sea is the result of a complex interaction of biological and physical processes.

The Cape Basin in the eastern South Atlantic is populated with mesoscale eddies. Long-lived anticyclonic "Agulhas Rings" emerge from the retroflection region and subsequently propagate north-westwards through the South Atlantic Gyre towards the South American coast[12]. Agulhas Rings are characterized by a very high energy content and deep mixing, what typically promotes primary production and carbon export[13]. Moreover, anticyclonic eddies also alter particle dynamics by physical effects alone: in anticyclonic eddies with vertical shear in horizontal velocity, subsurface convergence with velocities on the order of 0.05 m s^{-1}, generated by secondary circulation and/or eddy relaxation, have been seen to enhance particle concentrations and sedimentation fluxes, a process known as the "wine glass effect"[14].

Cyclonic mesoscale eddies are formed in the eastern South Atlantic by a flow detachment process in the lee of the Agulhas Bank and by instability processes of the coastal current system, usually stay close to the retroflection, and finally propagate back into the Indian Ocean[12,15]. Mesoscale dynamics in cyclonic eddies lead to a shoaling of the mixed layer towards the eddy center that may suggest that the nutrient pool below the mixed layer is exposed to light in the eddy center which, in turn, drives increased productivity and surface export[16]. However, in order to supply nutrient pool below the mixed layer need to be

70 maintained by a certain process as the recycling of nutrients in a self-maintained way would

71 render significant carbon export impossible.

72

73 *Cyclonic eddy survey in the Cape Basin*

74 Here we performed a high-resolution ship survey across a cyclonic mesoscale eddy located in

75 the eastern South Atlantic at 34.5 °S to analyze the biological/physical coupling. Quasi-

76 continuous shipboard Acoustic Doppler Current Profiler (sADCP) data revealed the current

77 structure of the upper 1.5 km of the water column. We combined this data with full depth (up

78 to 5 km) station data, taken with a horizontal distance of about 36 km, of velocity profile

79 observations (lADCP) and detailed optical particle analysis using an Underwater Vision

80 Profiler (UVP 5hd). Vertical carbon flux and degradation rates based on the particle size

81 distribution were estimated[17]. Moreover, UVP images were analyzed for grazers and detritus

82 classes considering all particles > 1 mm.

83 Satellite altimetry data revealed, that at the time of our survey, the eddy was located between

84 34 and 35 °S and 11 and 16 °E and most probably shed by a flow detachment process in the

85 lee of the Agulhas Bank[15] (Fig. 1A). The maximum swirl velocity was at the surface and

86 about 1 m s^{-1} suggesting a full rotation takes about 40 h to complete, which was about twice

87 the inertial period at 34.5 °S (21 h). Tracking the maximum swirl velocity with depth, we

88 observed a decrease in eddy diameter with decrease in velocity.

89 We report increased deep particle export associated with the cyclonic eddy, and show how

90 vorticity patterns, horizontal shear, and coprorhexic feeding behavior of grazers at the eddy

91 perimeter shaped the particle distribution. This led, in combination with low degradation rates

92 below the eddy core, to increased carbon export patterns in a V-shape down to a depth of >

93 3000 m.

94 General physicochemical properties support earlier studies of cyclonic eddies[16], showing an

95 upwelling core of nutrient rich deep waters with maximum values of ~30 µmol L^{-1} in the

96 central core (500 m) and ~10 µmol L^{-1} at 100 m, (Fig. 1B-C). This core, however, did not

97 totally reach the euphotic zone, which was visible as a sharp decrease in nitrate concentrations

98 above 100 m. Instead, intrusions of nitrate (3.5 and 5 µmol L^{-1}) above the flanks of the core

99 reached up to ~50 m of the water column and caused production, visible as twice the

100 chlorophyll concentration (~2 mg m^{-3}) than in the residual chlorophyll maximum (~0.8 - 1.2

101 mg m^{-3}; Fig 3; Fig. S1). These patterns suggest upwelling at the eddy rim possibly related to a

102 vertical flux of nutrients. It has been suggested earlier that the vertical shear in horizontal

103 currents, driven by the vertical propagation of near-inertial gravity waves (NIW), could be

one reason for this vertical nutrient flux. The strong horizontal current shear that could be found at the periphery of the eddy caused a change in the vertical component of the horizontal vorticity vector (relative vorticity "zeta"). Zeta is strongly negative (anticyclonal) just outside of the eddy and positive (cyclonal) inside. This zeta pattern forced NIW to propagate downward in the anticyclonic skirt of the eddy, a process commonly known as the "inertial chimney"[18]. We assume that these internal waves caused mixing and the intrusion of nitrate into the euphotic zone. This was also visible as a turbulent vorticity field in the upper 1300 m of the eddy flanks (Fig. 1D) and an intense and structured horizontal shear at those stations (Fig. 2).

Particle and zooplankton distribution

The distribution of small sinking particles (0.08 – 0.51 mm) showed a distinct shallow maximum of up to ~$2x10^5$ particles per m³ (further part. m⁻³) in the upper 100 m throughout the eddy, following more or less the 1026 kg m⁻³ isopycnal (Fig. 3). The co-occurrence of the small particle maximum with the chlorophyll maximum suggested particle formation induced by primary production in this layer. Small particle abundances generally followed the Martin curve with depth, which was induced by degradation and/or aggregation towards larger particles[19]. In the eddy center, however, a second, deep maximum could be observed above the 1027 kg m⁻³ isopycnal at ~260 m, where abundances reached maximum values of up to $1.0x10^5$ part. m⁻³. Sinking of small particles is suggested to be forced by viscous, rather than inertial forces[20], and in combination with low chlorophyll concentrations in this depth we suggested that particle retention at the density interface may have caused this deep maximum. Intermediate sized particles (0.51 – 1.02 mm) and large identified detritus (> 1 mm) were most abundant within the upper 150 m of the flanks of the cold core ($8x10^3$ part. m⁻³ and $6x10^2$ part. m⁻³, respectively). Particle retention could not be observed. Instead, particle maxima followed the anticyclonic zeta with depth until ~3500 m, where abundances reached ambient values (see also Fig. 1C). The zeta pattern constrains the way particles of certain size classes sink. Because of the bended zeta pattern towards the eddy center with depth, the particles also followed this pattern. In anticyclonic eddies, this pattern appears as a "wine glass" shape[14]. Here it resulted in a V-shaped particle distribution with an intense particle minimum between the upper 150 – 500 m of the eddy core, where abundances did not exceed 10² and 10^1 part. m⁻³, respectively.

136   Optical identification of large detritus (> 1 mm) revealed, that the total particle volume

137   (including particles > 1 mm) at the surface was volumetrically dominated by intact fecal

138   pellets, followed by increasing proportions of porous grey detritus between 200 and 800 m at

139   the flanks of the eddy (Fig. 4), most likely formed by aggregation of phytodetritus and feces.

140   Interestingly, we also found the major accumulation of grazers, i.e. Copepod like organisms,

141   in this zone (~350 – 800 m), which are known to feed on phytodetritus, but also fecal

142   pellets[21,22]. Copepods are known to break up fecal pellets – a process known as coprorhexy

143   which produces fecal pellet fragments with a relatively low sinking velocity, compared to

144   intact fecal pellets.[23,24] Indeed, the major proportion on total particle volume in the converged

145   particle maximum zone in the deep eddy center below 900 m was contributed by relatively

146   small and dark particles (> 1 mm), which were most likely fecal pellet fragments.

147

Carbon flux and carbon specific degradation

149   Carbon flux was estimated based on relationships between particle size, carbon content, and

150   sinking speed according to Guidi et al. (2008)[17]. Maximum values ranged between 30 and 43

151   mg C m^{-2} d^{-1} below the chlorophyll maximum at the flanks of the eddy, followed by a

152   decrease down to 3 and 7 mg C m^{-2} d^{-1} at 1000 m (Fig. 3; see also Fig. S2). Below this depth,

153   carbon export decreased rapidly at the flanks, but stays at a level of ~3 mg C m^{-2} d^{-1} down to

154   > 3000 m below the cold upwelled eddy core. This equals a three-fold export value compared

155   to ambient deep waters. One exception is the easternmost station in the study area, where high

156   export rates can be explained by off-shelf transport of particulate material form the productive

157   African shelf. An explanation for the high export below the eddy center might be reduced

158   degradation activity in the deep, which is also visible in calculated carbon specific

159   degradation rates. Highest values were located above the 1027 kg m³ isopycnal at the flanks

160   of the cold core, where degradation rates reached maximum values between 0.1 and 0.31 d^{-1}.

161   This was also the region where grazers, i.e. Copepods were most abundant. On the other hand,

162   degradation rates below the eddy core did not exceed 0.005 d^{-1}. It was suggested that fecal

163   pellet fragments, produced by coprorhexy promote carbon degradation by bacteria and

164   protozooplankton caused by increased surface to volume ratios and available degradation time

165   due to reduced sinking speeds[24]. Data on microbial or protozooplankton abundances or

166   activity was not available for this study, but based on the low degradation activity with

167   simultaneous large amounts of available material, we could argue that there was a delay in the

168   response of degrading organisms to the observed export event which led to relatively high

169 numbers of fecal pellet fragments reaching the Deep Sea. Kiko et al. (2017)[5] reported a major

170 contribution of particles < 0.5 mm to bathypelagic export in the equatorial divergence. They

171 concluded that those small particles may be generated at depth through shedding from or

172 disintegration of larger, fast sinking particles, following a period of several weeks of

173 microbial colonization and attack. Low numbers of this particle size class in bathypelagic

174 depths of our study area could confirm our hypothesis of a response delay of degrading

175 organisms.

176

Conclusions

178 Our results suggest that vertical energy propagation at the perimeter of a cyclonic eddy, due to

179 the 'inertial chimney' effect, caused mixing and the intrusion of nutrients into the euphotic

180 zone above. Small sized particles, formed by resulting increased primary production,

181 aggregated, got grazed and subsequently repackaged by grazers, i.e. Copepods. Most likely

182 the process of coprorhexy lead to increasing abundances of fecal pellet fragments, which

183 converged below the tip of the cold-water core at about 1500 m, while following the zeta

184 pattern. Reduced degradation activity, most likely caused by a response delay of degrading

185 organisms below led in consequence to a threefold increased carbon flux compared to

186 surrounding waters down to a depth of more than 3000 m. We conclude that this

187 physicobiological coupling may lead to regular export events connected with the formation

188 and propagation of cyclonic eddies in the region of the Agulhas retroflection and most

189 probably in other eddy formation regions worldwide.

190

Methods

Methods, including statements of data availability and any associated accession codes and references, are available in the online version of this paper.

References

1. Zhang, C. *et al.* Evolving paradigms in biological carbon cycling in the ocean. *National Science Review* **5,** 481–499; 10.1093/nsr/nwy074 (2018).

2. Siegel, D. A. *et al.* Prediction of the Export and Fate of Global Ocean Net Primary Production: The EXPORTS Science Plan. *Front. Mar. Sci.* **3,** 4; 10.3389/fmars.2016.00022 (2016).

3. Barker, S., Higgins, J. A. & Elderfield, H. The future of the carbon cycle: review, calcification response, ballast and feedback on atmospheric CO2. *Philosophical transactions. Series A, Mathematical, physical, and engineering sciences* **361,** 1977-98; discussion 1998-9; 10.1098/rsta.2003.1238 (2003).

4. Waldron, H. N., Monteiro, P. M. S. & Swart, N. C. Carbon export and sequestration in the southern Benguela upwelling system: lower and upper estimates. *Ocean Sci. Discuss.* **6,** 1173–1192; 10.5194/osd-6-1173-2009 (2009).

5. Kiko, R. *et al.* Biological and physical influences on marine snowfall at the equator. *Nature Geosci* **10,** 852–858; 10.1038/ngeo3042 (2017).

6. Thomalla, S., Turnewitsch, R., Lucas, M. & Poulton, A. Particulate organic carbon export from the North and South Atlantic gyres: The 234Th/238U disequilibrium approach. *Deep Sea Research Part II: Topical Studies in Oceanography* **53,** 1629–1648; 10.1016/j.dsr2.2006.05.018 (2006).

7. Dufois, F. *et al.* Anticyclonic eddies are more productive than cyclonic eddies in subtropical gyres because of winter mixing. *Science advances* **2,** e1600282; 10.1126/sciadv.1600282 (2016).

8. Everett, J. D., Baird, M. E. & Suthers, I. M. Three-dimensional structure of a swarm of the salp Thalia democratica within a cold-core eddy off southeast Australia. *J. Geophys. Res.* **116,** 60; 10.1029/2011JC007310 (2011).

9. Christiansen, S. *et al.* Particulate matter flux interception in oceanic mesoscale eddies by the polychaete Poeobius sp. *Limnol. Oceanogr.* (2018).

150

222 10. Ploug, H., Iversen, M. H. & Fischer, G. Ballast, sinking velocity, and apparent diffusivity
223   within marine snow and zooplankton fecal pellets: Implications for substrate turnover by
224   attached bacteria. *Limnol. Oceanogr.,* 1878–1886 (2008).

225 11. Laurenceau-Cornec, E. C. *et al.* The relative importance of phytoplankton aggregates and
226   zooplankton fecal pellets to carbon export. Insights from free-drifting sediment trap
227   deployments in naturally iron-fertilised waters near the Kerguelen Plateau. *Biogeosciences*
228   **12,** 1007–1027; 10.5194/bg-12-1007-2015 (2015).

229 12. Casanova-Masjoan, M. *et al.* Characteristics and evolution of an Agulhas ring. *J.*
230   *Geophys. Res. Oceans* **122,** 7049–7065; 10.1002/2017JC012969 (2017).

231 13. Villar, E. *et al.* Environmental characteristics of Agulhas rings affect interocean plankton
232   transport. *Science,* 1–11 (2015).

233 14. Waite, A. M. *et al.* The wineglass effect shapes particle export to the deep ocean in
234   mesoscale eddies. *Geophys. Res. Lett.* **43,** 9791–9800; 10.1002/2015GL066463 (2016).

235 15. Penven, P., Lutjeharms, J. R. E., Marchesiello, P., Roy, C. & Weeks, S. J. Generation of
236   cyclonic eddies by the Agulhas Current in the Lee of the Agulhas Bank. *Geophys. Res.*
237   *Lett.* **28,** 1055–1058; 10.1029/2000GL011760 (2001).

238 16. Singh, A., Gandhi, N., Ramesh, R. & Prakash, S. Role of cyclonic eddy in enhancing
239   primary and new production in the Bay of Bengal. *Journal of Sea Research* **97,** 5–13;
240   10.1016/j.seares.2014.12.002 (2015).

241 17. Guidi, L. *et al.* Relationship between particle size distribution and flux in the mesopelagic
242   zone. *Deep Sea Res., Part I* **55,** 1364–1374; 10.1016/j.dsr.2008.05.014 (2008).

243 18. Lee, D.-K. & Niiler, P. P. The inertial chimney: The near-inertial energy drainage from
244   the ocean surface to the deep layer. *J Geophys. Res. (Journal of Geophysical Research)*
245   (1998).

246 19. Martin, J. H., Knauer, G. A., Karl, D. M. & Broenkow, W. W. VERTEX: carbon cycling
247   in the northeast Pacific. *Deep Sea Res A* **34,** 267–285; 10.1016/0198-0149(87)90086-0
248   (1987).

249 20. Kindler, K., Khalili, A. & Stocker, R. Diffusion-limited retention of porous particles at
250   density interfaces. *Proceedings of the National Academy of Sciences of the United States*
251   *of America* **107,** 22163–22168; 10.1073/pnas.1012319108 (2010).

252 21. Wotton, R. S. & Malmqvist, B. Feces in Aquatic Ecosystems. *BioScience* **51,** 537;
253   10.1641/0006-3568(2001)051[0537:FIAE]2.0.CO;2 (2001).

254   22. Martin, P. *et al.* Iron fertilization enhanced net community production but not downward
255   particle flux during the Southern Ocean iron fertilization experiment LOHAFEX. *Global*
256   *Biogeochem. Cycles* **27,** 871–881; 10.1002/gbc.20077 (2013).

257   23. Lampitt, R. S., Noji, T. & Bodungen, B. von. What happens to zooplankton faecal pellets?
258   Implications for material flux. *Mar. Biol.* **104,** 15–23; 10.1007/BF01313152 (1990).

259   24. Iversen, M. H. & Poulsen, L. K. Coprorhexy, coprophagy, and coprochaly in the copepods
260   Calanus helgolandicus, Pseudocalanus elongatus, and Oithona similis. *Mar. Ecol. Prog.*
261   *Ser.* **350,** 79–89; 10.3354/meps07095 (2007).

262

263

264   **Acknowledgements**

269

270   **Additional information**

271   Supplementary information is available in the online version of the paper. Reprints and
272   permissions information is available online at www.nature.com/reprints. Publisher's note:
273   Springer Nature remains neutral with regard to jurisdictional claims in published maps and
274   institutional affiliations. Correspondence and requests for materials should be addressed to
275   A.R.

276

277   **Competing financial interests**

278   The authors declare no competing financial interests.
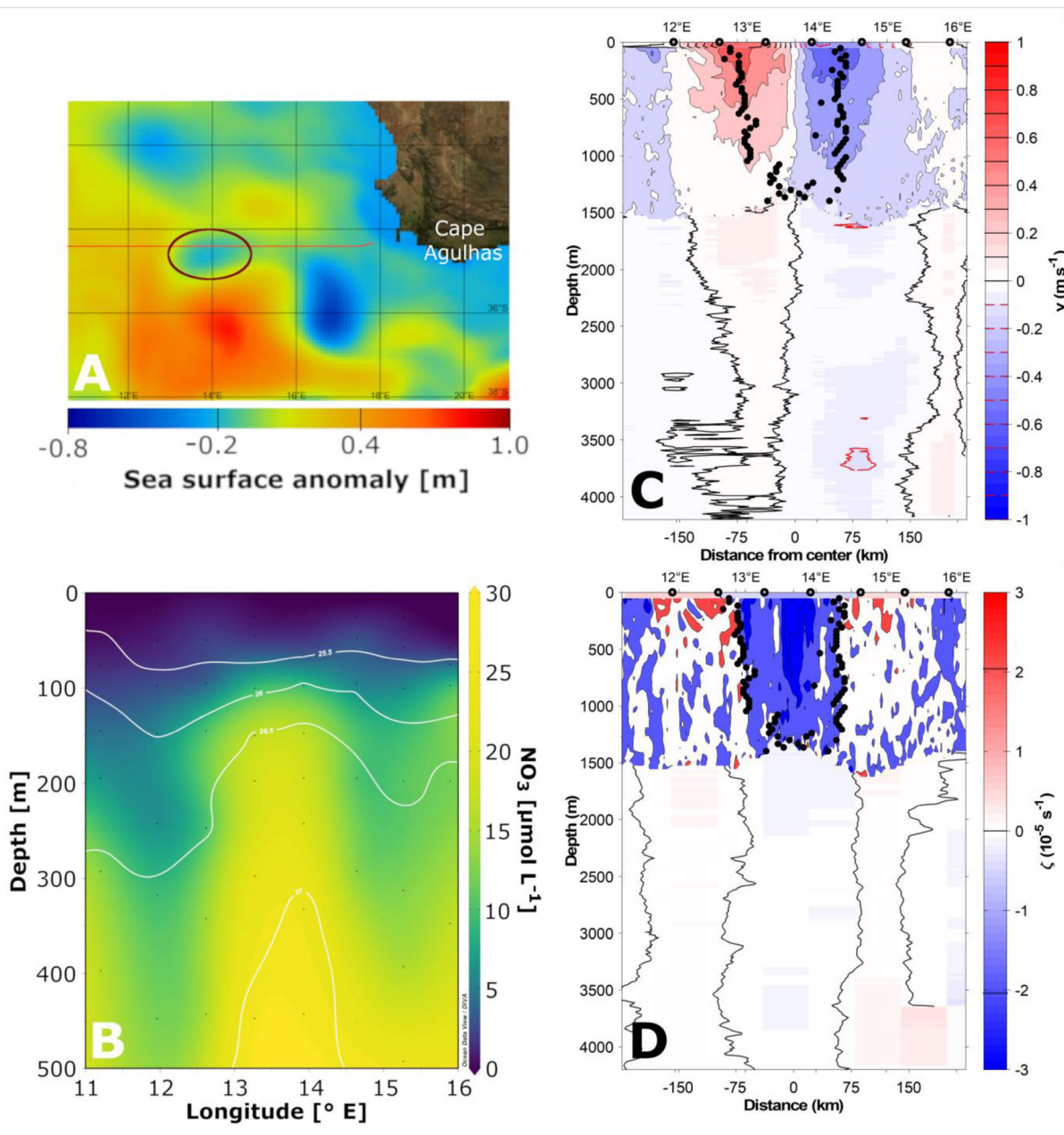
Figure 1: Physicochemical features of the observed cyclonic eddy. A: Sea surface anomaly in meters above geoid illustrates the localization of the investigated cyclonic eddy (dark red ellipse) west of Cape Agulhas (South Africa). The Cruise track is marked as red line. B: Nitrate concentration in the upper 500 m of the water column exemplifies the tip of the upwelled, nutrient rich deep water. White lines indicate isopycnals in kg m⁻³ ($\rho - 1000$ kg m⁻³). Note the increase in nitrate concentration at the flanks of the deep water core in the euphotic zone (~50 m). C: Meridional velocity shows intense clockwise rotation. Black dots mark speed maxima [u + i*v]. D: Vorticity calculation exemplifies cyclonal (blue) and anticyclonal areas (red) within the eddy. While the center of the eddy is characterized by cyclonal, upwelling waters, the flanks are characterized by turbulent waters or in deeper

290 layers also anticyclonal downwelling. C and D: Note that the upper part (0 - ~1500m} has
291 been acquired using high resolution shipboard ADCP (sADCP) while the lower part consists
292 of data from the lowered ADCP (lADCP).

293
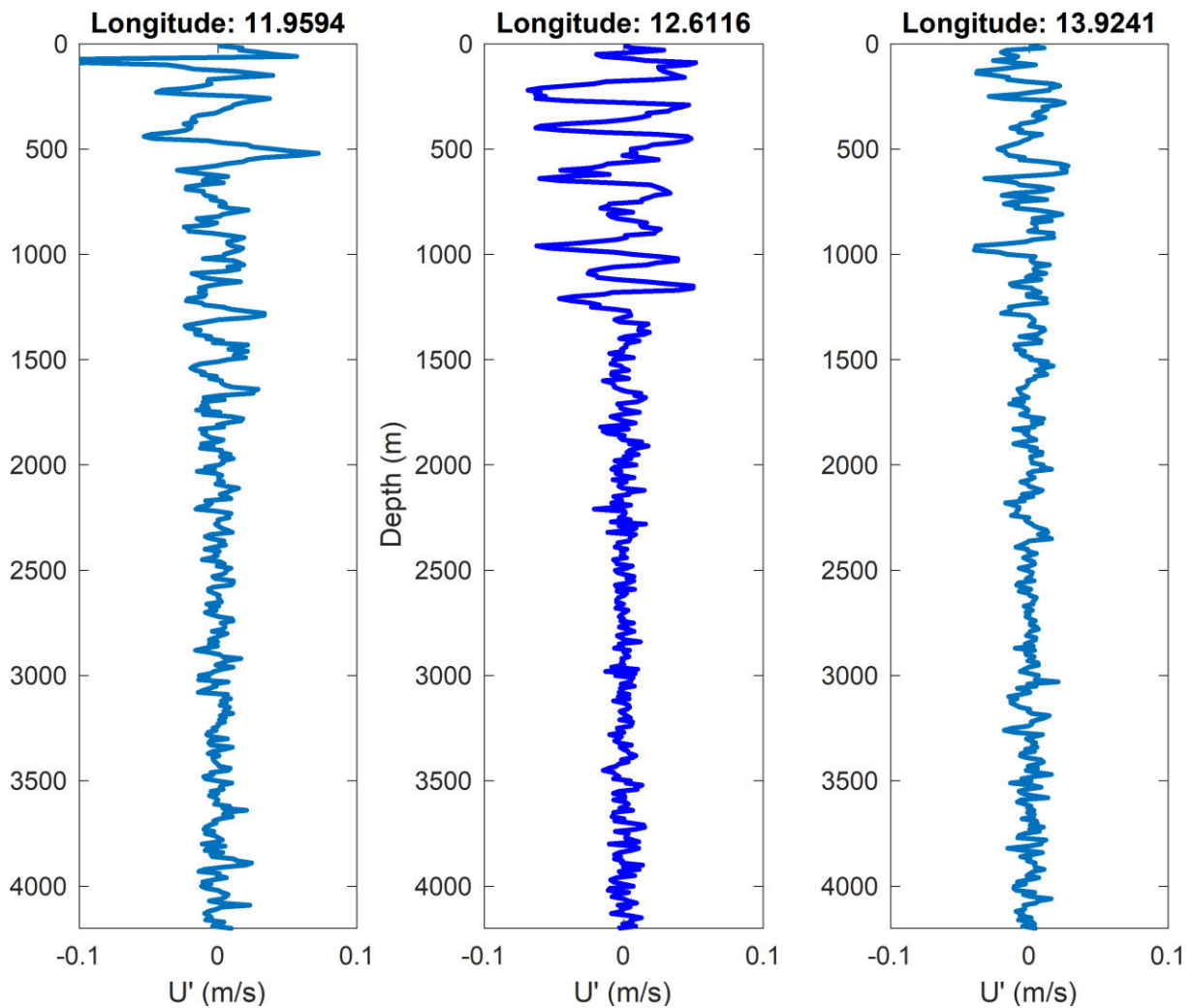
294

295 Figure 2: Speed anomaly profiles of selected stations shows strong and structured horizontal
296 shear at the flank of the eddy (background velocity removed). Station 11.96 °E (left)
297 exemplifies area outside of the eddy, station 12.61 °E (middle) the flank of the eddy and
298 station 13.92 (right) the eddy centre.

299
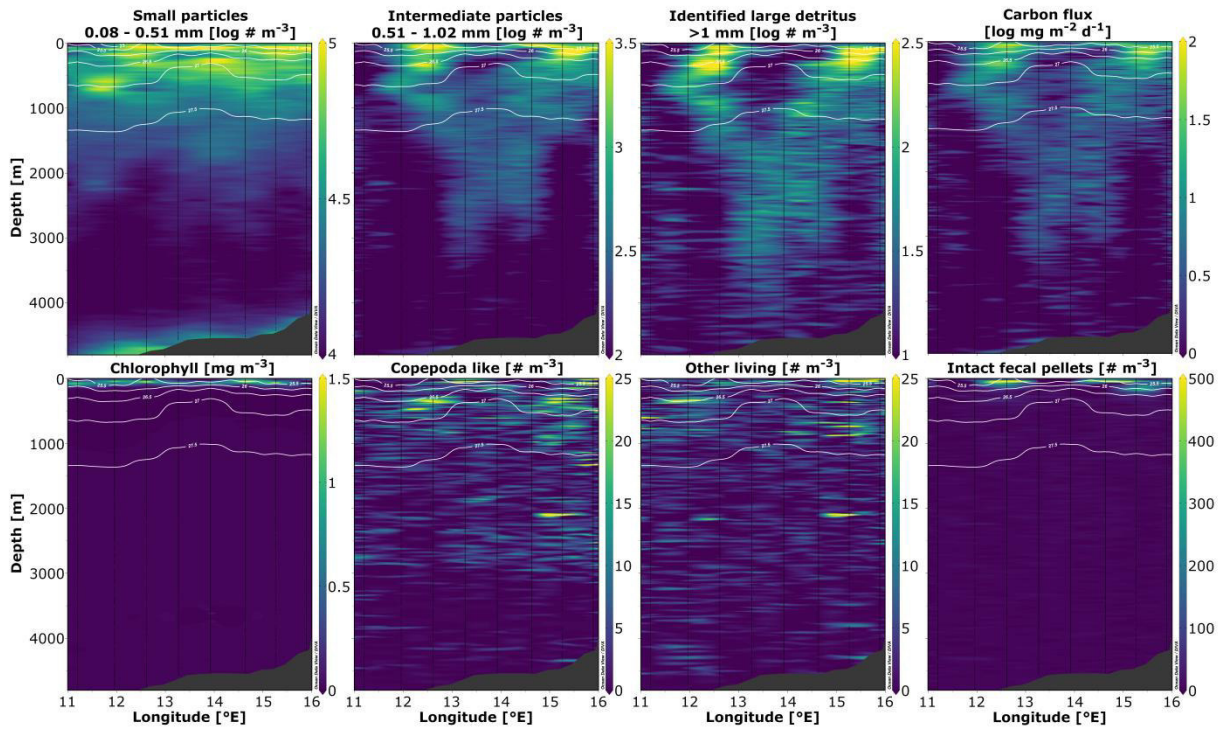
Figure 3: Particle and biological characterization of the cyclonic eddy. Upper panels show particle classes of increasing size and the resulting carbon flux calculation. Small and intermediate particle classes represent total particulate material including organisms. Note that upper panels are presented as logarithmic values ($\log_{10}[x]$). Lower panels show biological features of fluorometer sensor based chlorophyll measurements as well as abundances of identified Copepods, other organisms, and intact fecal pellets. White lines indicate isopycnals in kg m^{-3} (ρ – 1000 kg m^{-3}).
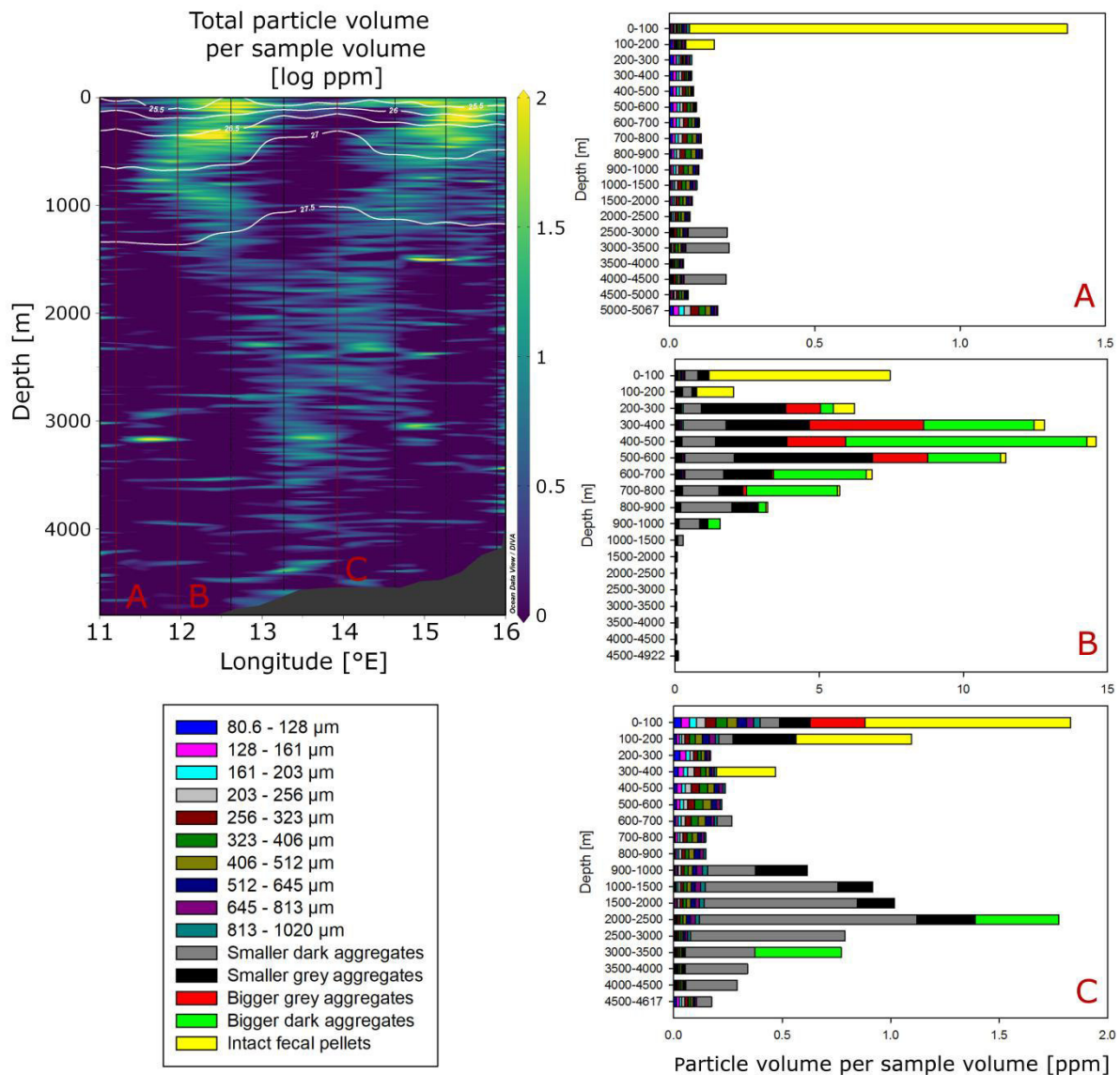
Figure 4: Median contribution of different particle size classes and types on total particle volume in different zones of the cyclonic eddy. Total particle volume per sample volume calculations include total particulate material with an ESD between 0.08 and 1 mm, identified detritus > 1mm, and intact fecal pellets. White lines indicate isopycnals in kg m⁻³ (ρ – 1000 kg m⁻³).

313
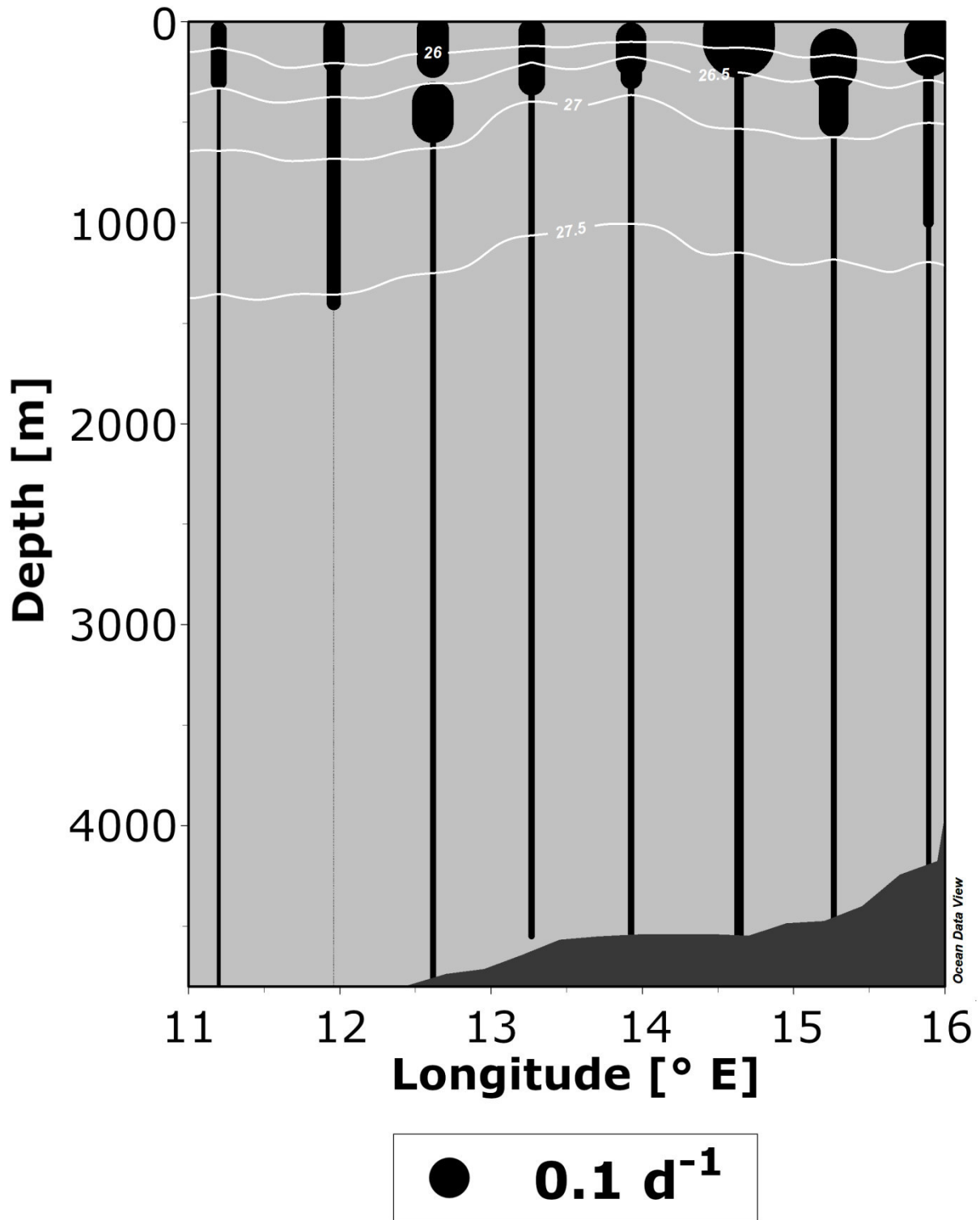
Figure 5: Calculated carbon specific degradation rates illustrate increased activity in the upper 500 m, while below the eddy core only low degradation could be observed. Dot size indicates amount of carbon degradation.

2.4.1 How does a cyclonic eddy influence the particle-driven BCP and what are the main drivers?

To investigate the influence of a cyclonic eddy and its related physical and biological forcings on the BCP, I performed several full depth profiles along a transect at 34.4 °S through a cyclonic eddy close to the South African coast in early 2017. I combined shipboard Acoustic Doppler Current Profiler (sADCP) data with high resolution lowered ADCP (lADCP) and Underwater Vision Profiler (UVP) data and used image analyses of particles > 1 mm to localize grazers and differentiate large aggregate classes. Finally, I calculated vertical carbon flux and degradation rates based on the particle size distribution.

I could identify 4 major processes involved in the export event: (1) vertical inertial wave energy propagation due to the 'inertial chimney' effect caused mixing at the eddy perimeter and nutrient injection into the euphotic zone. The resulting increased primary production supported formation of small particles at the eddy perimeter. (2) Repackaging of phytoplankton aggregates and coprorhexy by grazers led to increasing abundances of fecal pellet fragments at depths ~150 m below the small particle maximum. Particles generally followed the vorticity field of the eddy and converged below the tip of the cold upwelled eddy core at about 1500 m. (4) Reduced degradation activity, most likely caused by a response delay of degrading organisms to the rapid export event, led to the observed threefold increased carbon flux down to a depth of more than 3000 m.

I concluded that the observed physical-biological coupling may cause regular rapid and deep export events connected with the formation and propagation of cyclonic eddies in the otherwise oligotrophic southeast Atlantic and most probably in other eddy formation regions worldwide.

The increase in particle concentration at depth might also increase the impact of alternative metabolic pathways in particle-associated microenvironments on element cycling of the deep sea. More detailed investigations on element cycling, microbial diversity and activity might help to understand the impact of these phenomena on the BCP and biogeochemical cycling as a whole.

3 CONCLUSIONS

Sinking particles represent an important habitat and food source in the pelagic environment due to their substrate richness and heterogeneity in terms of redox gradients and structure (Paper II). The dynamics of important elemental fluxes moderating the BCP, such as the intensity of remineralization and respiration, depend on fundamental microbial ecological processes, such as niche separation and colonization strategies, which occur at the micro-scale (Paper I, Paper II, Paper III). Detailed investigations on microbial strategies, however, were historically limited to free-living bacteria in former times (Paper I). Continuous advances of method development and optimization have enabled new perspectives on microbial life in more complex environments, including those of fragile sinking aggregates (Paper II, Paper III). The BCP, in turn, also shapes microbial ecology, due to its influence on vertical connectivity of microbial communities (Paper IV). Physical factors, such as individual particle sinking velocities, drive particle export, but are, in turn, also determined by biological drivers, such as the phytoplankton communities involved in particle formation (Paper IV, Paper V). In the Arctic, the composition of particle-associated microbial communities is influenced by drivers at global scale that affect sea ice-coverage. The trajectories and sinking velocities of particles, however, are not linear (Paper IV). Advection, fronts, filaments, and eddies make the oceans heterogeneous at multiple scales. Interaction of particle formation and flux with this complex physical oceanography at the mesoscale and sub-mesoscale can lead to regular rapid export events in otherwise oligotrophic gyres. (Paper V). In turn, the BCP represents a biogeochemical link between large-scale and micro-scale processes, which best be investigated through interdisciplinary approaches at multiple scales.

4   OUTLOOK

Global warming represents, from my point of view, the most challenging problem of our time, and the biological carbon pump (BCP) may be heavily impacted by this phenomenon. A perturbed BCP may result in a positive feedback of temperature increase due to decreased carbon retention in the oceans. My thesis demonstrates the potential of new technologies and methods in biological oceanography in resolving important biogeochemical fluxes at multiple scales. The ocean is still a sparsely sampled system, and linkages between small and fragile elements and phenomena at larger scales remain unresolved. I am optimistic that the methods and results presented in this thesis will help to provide some of these linkages, as well as identifying remarkable new survival strategies and interactions of microbes. Another important area of investigation remains how deep currents affect the BCP, as well as the associated microbial ecology in the deep sea. I will provide one answer to this question for the Arctic boundary current in a following project. Global warming represents, from my point of view, the most challenging problem of our time and the BCP may be heavily affected by this phenomenon. Moreover, a perturbed BCP may result in a positive feedback of temperature increase due to decreased carbon retention in the oceans. To answer another one piece of this question I am investigating the temporal consequences of sea ice coverage on the Arctic BCP, using a moored optical particle quantification and imaging system for long-term observation of particle distribution in the marginal ice zone.

Other new questions raised by my work include:

Is the particle-specific average brightness, acquired by Underwater Vision Profilers, directly related to particle density? How can we use this data to calculate more precise carbon export estimations?

Hypothesis: Average brightness of particles is directly linked to density and carbon content and can be implemented into carbon export calculations based on UVP data sets.

How does an increased riverine input of dissolved organic matter (DOM), caused by melting of permafrost, affect microbial activity and particle dynamics in the Arctic Ocean?

Hypothesis: Riverine input of especially labile and semi-labile DOM increases free-living microbial abundance and activity, which promotes colonization of particles by degrading microorganisms, and increases flux attenuation.

Which organisms and metabolic processes are associated with resuspended particles, i.e. from nepheloid layers, and how do they affect biogeochemical cycles?

Hypothesis: Resuspended particles are inhabited by particle-associated as well as benthic microbes. Resuspension promotes carbon specific degradation and decreases carbon sequestration, due to the repeated exposition of particulate organic matter and its associated microbial community to oxygen.

Is there a passive transfer of terrestrial microorganisms to sinking particles due to dust input and how do those affect the microbial ecology of aggregates?

Hypothesis: Dust particles represent a vehicle for terrestrial microorganisms, which colonize aggregates after deposition and increase respiration and remineralization.

How do micro-plastic particles interact with natural aggregates? How do they influence particle sinking velocities and the BCP as a whole?

Hypothesis: Plastic particles, i.e. polyethylene particles, included in aggregates increase carbon export due to increased aggregate density. Moreover, they promote aggregation because they act as "aggregation nuclei", analogous to condensation nuclei for rain drop formation.

What is the influence of glyphosate and other anthropogenic chemicals enriched in the marine environment on the BCP?

Hypothesis: Glyphosate enriched in sea water interferes with essential metabolic pathways in algae, bacteria, archaea, and fungi and, thus, decreases primary production, aggregate formation, and microbial decomposition, which decreases the BCP.

I am looking forward to addressing some of these interesting questions in my future research.

REFERENCES

Alldredge, A. L., and C. C. Gotschalk. 1988. *In situ* settling behavior of marine snow. Limnol Oceanogr **33:** 339–351. doi:10.4319/lo.1988.33.3.0339.

Alldredge, A. L., and M. W. Silver. 1988. Characteristics, dynamics and significance of marine snow. Prog Oceanogr **20:** 41–82. doi:10.1016/0079-6611(88)90053-5.

Andrews, J. H., and R. F. Harris. 1986. r- and K-selection in microbial ecology. Adv Microb Ecol **9**: 99–147. doi:10.1007/978-1-4757-0611-6_3.

Axell, L. B. 1998. On the variability of Baltic Sea deepwater mixing. J Geophys Res **103:** 21667–21682. doi:10.1029/98JC01714.

Barker, S., J. A. Higgins, and H. Elderfield. 2003. The future of the carbon cycle: review, calcification response, ballast and feedback on atmospheric CO_2. Phil Trans A Math Phys Eng Sci **361:** 1977-98; discussion 1998-9. doi:10.1098/rsta.2003.1238.

Berg, C., V. Vandieken, B. Thamdrup, and K. Jürgens. 2015. Significance of archaeal nitrification in hypoxic waters of the Baltic Sea. ISME J **9**: 1319–1332. doi:10.1038/ismej.2014.218.

Bianchi, D., T. S. Weber, R. Kiko, and C. Deutsch. 2018. Global niche of marine anaerobic metabolisms expanded by particle microenvironments. Nature Geosci **65:** 36. doi:10.1038/s41561-018-0081-0.

Boetius, A., S. Albrecht, K. Bakker, C. Bienhold, J. Felden, M. Fernández-Méndez, and S. Hendricks, *et al.* 2013. Export of algal biomass from the melting Arctic sea ice. Science **339:** 1430–1432. doi:10.1126/science.1231346.

Brettar, I., M. Labrenz, S. Flavier, J. Botel, H. Kuosa, R. Christen, and M. G. Höfle. 2006. Identification of a *Thiomicrospira denitrificans*-like Epsilonproteobacterium as a catalyst for autotrophic denitrification in the central Baltic Sea. Appl Environ Microbiol **72:** 1364–1372. doi:10.1128/AEM.72.2.1364-1372.2006.

Brettar, I., and G. Rheinheimer. 1991. Denitrification in the central Baltic: evidence for H_2S-oxidation as motor of denitrification at the oxic-anoxic interface. Microb Ecol **77:** 157–169. doi:10.3354/meps077157.

Bristow, L. A. 2018. Anoxia in the snow. Nat Geosci **11**: 226–227. doi:10.1038/s41561-018-0088-6.

Brüchert, V., B. B. Jørgensen, K. Neumann, D. Riechmann, M. Schlösser, and H. Schulz. 2003. Regulation of bacterial sulfate reduction and hydrogen sulfide fluxes in the central namibian coastal upwelling zone. Geochim Cosmochim Acta **67**: 4505–4518. doi:10.1016/S0016-7037(03)00275-8.

Buesseler, K. O., A. N. Antia, M. Chen, S. W. Fowler, W. D. Gardner, O. Gustafsson, and K. Harada, *et al.* 2007a. An assessment of the use of sediment traps for estimating upper ocean particle fluxes. J Mar Res **65**: 345–416. doi:10.1357/002224007781567621.

Canfield, D. E., F. J. Stewart, B. Thamdrup, L. de Brabandere, T. Dalsgaard, E. F. DeLong, and N. P. Revsbech, *et al.* 2010. A cryptic sulfur cycle in oxygen-minimum-zone waters off the Chilean coast. Science **330**: 1375–1378. doi:10.1126/science.1196889.

Carini, P., L. Steindler, S. Beszteri, and S. J. Giovannoni. 2012. Nutrient requirements for growth of the extreme oligotroph '*Candidatus Pelagibacter ubique*' HTCC1062 on a defined medium. ISME J **7:** 592–602. doi:10.1038/ismej.2012.122.

Carolan, M., and J. M. Beman. 2015. Transcriptomic evidence for microbial sulfur cycling in the eastern tropical North Pacific oxygen minimum zone. Front Microbiol **6**: 334. doi:10.3389/fmicb.2015.00334.

Chow, T. J., and E. D. Goldberg. 1960. On the marine geochemistry of barium. Geochim Cosmochim Acta **20**: 192–198. doi:10.1016/0016-7037(60)90073-9.

Cisternas-Novoa, C., C. Lee, and A. Engel. 2015. Transparent exopolymer particles (TEP) and Coomassie stainable particles (CSP). Differences between their origin and vertical distributions in the ocean. Mar Chemistry **175:** 56–71. doi:10.1016/j.marchem.2015.03.009.

Clode, P. L., M. R. Kilburn, D. L. Jones, E. A. Stockdale, J. B. Cliff, A. M. Herrmann, and D. V. Murphy. 2009. *In situ* mapping of nutrient uptake in the rhizosphere using nanoscale secondary ion mass spectrometry. Plant Physiol **151:** 1751–1757. doi:10.1104/pp.109.141499.

Cypionka, H., F. Widdel, and N. Pfennig. 1985. Survival of sulfate-reducing bacteria after oxygen stress, and growth in sulfate-free oxygen-sulfide gradients. FEMS Microbiol Lett **31**: 39–45. doi:10.1111/j.1574-6968.1985.tb01129.x.

Dickey, T. D. 2003. Emerging ocean observations for interdisciplinary data assimilation systems. J Mar Syst **40-41:** 5–48. doi:10.1016/S0924-7963(03)00011-3.

Dufois, F., N. J. Hardman-Mountford, J. Greenwood, A. J. Richardson, M. Feng, and R. J. Matear. 2016. Anticyclonic eddies are more productive than cyclonic eddies in subtropical gyres because of winter mixing. Sci Adv **2:** e1600282. doi:10.1126/sciadv.1600282.

Dunne, J. P., J. L. Sarmiento, and A. Gnanadesikan. 2007. A synthesis of global particle export from the surface ocean and cycling through the ocean interior and on the seafloor. Global Biogeochem Cy **21:** n/a-n/a. doi:10.1029/2006GB002907.

Ebersbach, F., and T. W. Trull. 2008. Sinking particle properties from polyacrylamide gels during the KErguelen Ocean and Plateau compared Study (KEOPS): Zooplankton control of carbon export in an area of persistent natural iron inputs in the Southern Ocean. Limnol Oceanogr **53:** 212–224. doi:10.4319/lo.2008.53.1.0212.

Engel, A., J. Piontek, K. Metfies, S. Endres, P. Sprong, I. Peeken, and S. Gäbler-Schwarz, *et al.* 2017. Inter-annual variability of transparent exopolymer particles in the Arctic Ocean reveals high sensitivity to ecosystem changes. Sci Rep **7**: 4129. doi:10.1038/s41598-017-04106-9.

Everett, J. D., M. E. Baird, and I. M. Suthers. 2011. Three-dimensional structure of a swarm of the salp *Thalia democratica* within a cold-core eddy off southeast Australia. J Geophys Res **116:** 60. doi:10.1029/2011JC007310.

Farquhar, J., H. Bao, and M. Thiemens. 2000. Atmospheric influence of earth´s earliest sulfur cycle. Science **289**: 756–758. doi:10.1126/science.289.5480.756.

Franks, P. J.S. 1992. Sink or swim, accumulation of biomass at fronts. Mar Ecol Prog Ser **82:** 1–12. doi:10.3354/meps082001.

Frey, C., S. Hietanen, K. Jürgens, M. Labrenz, and M. Voss. 2014. N and O isotope fractionation in nitrate during chemolithoautotrophic denitrification by *Sulfurimonas gotlandica*. Environ Sci Technol **48:** 13229–13237. doi:10.1021/es503456g.

Friedrich, C. G., F. Bardischewsky, D. Rother, A. Quentmeier, and J. Fischer. 2005. Prokaryotic sulfur oxidation. Curr Opin Microbiol **8:** 253–259. doi:10.1016/j.mib.2005.04.005.

Fuchs, B. M., D. Woebken, M. V. Zubkov, P. H. Burkill, and R. Amann. 2005. Molecular identification of picoplankton populations in contrasting waters of the Arabian Sea. Aquat Microb Ecol **39:** 145–157. doi:10.3354/ame039145.

Ganesh, S., D. J. Parris, E. F. DeLong, and F. J. Stewart. 2013. Metagenomic analysis of size-fractionated picoplankton in a marine oxygen minimum zone. ISME J **8:** 187–211. doi:10.1038/ismej.2013.144.

Gao, Z., X. Wang, A. K. Hannides, F. J. Sansone, and G. Wang. 2011. Impact of redox-stratification on the diversity and distribution of bacterial communities in sandy reef sediments in a microcosm. Chin J Ocean Limnol **29:** 1209–1223. doi:10.1007/s00343-011-0316-z.

Giere, O. 1993. Meiobenthology. The microscopic fauna in aquatic sediments. Springer Berlin Heidelberg.

Gilly, W. F., J. M. Beman, S. Y. Litvin, and B. H. Robison. 2013. Oceanographic and biological effects of shoaling of the oxygen minimum zone. Ann Rev Mar Sci **5:** 393–420. doi:10.1146/annurev-marine-120710-100849.

Giovannoni, S. J., J. Cameron Thrash, and B. Temperton. 2014. Implications of streamlining theory for microbial ecology. ISME J **8:** 1553–1565. doi:10.1038/ismej.2014.60.

Glaubitz, S., K. Kießlich, C. Meeske, M. Labrenz, and K. Jürgens. 2013. SUP05 dominates the gammaproteobacterial sulfur oxidizer assemblages in pelagic redoxclines of the central Baltic and Black Seas. Appl Environ Microbiol **79:** 2767–2776. doi:10.1128/AEM.03777-12.

Gowing, M. M., and M. W. Silver. 1983. Origins and microenvironments of bacteria mediating fecal pellet decomposition in the sea. Mar. Biol. **73**: 7–16. doi:10.1007/BF00396280.

Grossart, H.-P., T. Kiørboe, K. Tang, and H. Ploug. 2003. Bacterial colonization of particles. growth and interactions. Appl Environ Microbiol **69:** 3500–3509. doi:10.1128/AEM.69.6.3500-3509.2003.

Grossart, H.-P., T. Kiørboe, K. W. Tang, M. Allgaier, E. M. Yam, and H. Ploug. 2006. Interactions between marine snow and heterotrophic bacteria: aggregate formation and microbial dynamics. Aquat Microb Ecol: 19–26. doi:10.3354/ame042019.

Grote, J., M. Labrenz, B. Pfeiffer, G. Jost, and K. Jürgens. 2007. Quantitative distributions of *Epsilonproteobacteria* and a *Sulfurimonas* Subgroup in pelagic redoxclines of the central Baltic Sea. Appl Environ Microbiol **73:** 7155–7161. doi:10.1128/AEM.00466-07.

Grote, J., T. Schott, C. G. Bruckner, F. O. Glöckner, G. Jost, H. Teeling, and M. Labrenz, *et al.* 2012. Genome and physiology of a model Epsilonproteobacterium responsible for sulfide detoxification in marine oxygen depletion zones. Proc Natl Acad Sci USA **109:** 506–510. doi:10.1073/pnas.1111262109.

Guidi, L., S. Chaffron, L. Bittner, D. Eveillard, A. Larhlimi, S. Roux, and Y. Darzi, *et al.* 2016. Plankton networks driving carbon export in the oligotrophic ocean. Nature **532:** 465–470. doi:10.1038/nature16942.

Guidi, L., G. A. Jackson, L. Stemmann, J. C. Miquel, M. Picheral, and G. Gorsky. 2008. Relationship between particle size distribution and flux in the mesopelagic zone. Deep Sea Res Part I **55:** 1364–1374. doi:10.1016/j.dsr.2008.05.014.

Herrmann, A. M., P. L. Clode, I. R. Fletcher, N. Nunan, E. A. Stockdale, A. G. O'Donnell, and D. V. Murphy. 2007. A novel method for the study of the biophysical interface in soils using nano-scale secondary ion mass spectrometry. Rapid Commun Mass Spectrom **21:** 29–34. doi:10.1002/rcm.2811.

Holland, H. D. 2002. Volcanic gases, black smokers, and the great oxidation event. Geochim Cosmochim Acta **66:** 3811–3826. doi:10.1016/S0016-7037(02)00950-X.

Horner, T. J., H. V. Pryer, S. G. Nielsen, P. W. Crockford, J. M. Gauglitz, B. A. Wing, and R. D. Ricketts. 2017. Pelagic barite precipitation at micromolar ambient sulfate. Nat Commun **8:** 1342. doi:10.1038/s41467-017-01229-5.

Iversen, M. H., N. Nowald, H. Ploug, G. A. Jackson, and G. Fischer. 2010. High resolution profiles of vertical particulate organic matter export off Cape Blanc, Mauritania. Degradation processes and ballasting effects. Deep Sea Res Part I **57:** 771–784. doi:10.1016/j.dsr.2010.03.007.

Iversen, M. H., and H. Ploug. 2010. Ballast minerals and the sinking carbon flux in the ocean. Carbon-specific respiration rates and sinking velocity of marine snow aggregates. Biogeosciences **7:** 2613–2624. doi:10.5194/bg-7-2613-2010.

Iversen, M. H., and M. L. Robert. 2015. Ballasting effects of smectite on aggregate formation and export from a natural plankton community. Mar Chem **175:** 18–27. doi:10.1016/j.marchem.2015.04.009.

Jakobs, G., G. Rehder, G. Jost, K. Kießlich, M. Labrenz, and O. Schmale. 2013. Comparative studies of pelagic microbial methane oxidation within the redox zones of the Gotland Deep and Landsort Deep (central Baltic Sea). Biogeosciences **10:** 7863–7875. doi:10.5194/bg-10-7863-2013.

Jasińska, A., D. Burska, and J. Bolałek. 2012. Sulfur in the marine environment. Oceanol Hydrobiol Stud **41:** 72–82. doi:10.2478/s13545-012-0019-x.

Jørgensen, B. B. 2006. Bacteria and Marine Biogeochemistry, p. 169–206. In H. D. Schulz and M. Zabel [eds.], Marine Geochemistry. Springer-Verlag.

Jørgensen, B. B., H. Fossing, C. O. Wirsen, and H. W. Jannasch. 1991. Sulfide oxidation in the anoxic Black Sea chemocline. Deep Sea Res A **38:** 1083-1103. doi:10.1016/S0198-0149(10)80025-1.

Kaiser, C., M. R. Kilburn, P. L. Clode, L. Fuchslueger, M. Koranda, J. B. Cliff, and Z. M. Solaiman, *et al.* 2015. Exploring the transfer of recent plant photosynthates to soil microbes. Mycorrhizal pathway vs direct root exudation. New Phytol **205:** 1537–1551. doi:10.1111/nph.13138.

Kalvelage, T., M. M. Jensen, S. Contreras, N. P. Revsbech, P. Lam, M. Gunter, and J. LaRoche, *et al.* 2011. Oxygen sensitivity of anammox and coupled N-cycle processes in oxygen minimum zones. PloS One **6:** e29299. doi:10.1371/journal.pone.0029299.

Karstensen, J., L. Stramma, and M. Visbeck. 2008. Oxygen minimum zones in the eastern tropical Atlantic and Pacific oceans. Prog in Oceanogr **77:** 331–350. doi:10.1016/j.pocean.2007.05.009.

Keeling, R. E., A. Körtzinger, and N. Gruber. 2010. Ocean deoxygenation in a warming world. Ann Rev Mar Sci **2:** 199–229. doi:10.1146/annurev.marine.010908.163855.

Kiko, R., A. Biastoch, P. Brandt, S. Cravatte, H. Hauss, R. Hummels, and I. Kriest, *et al.* 2017. Biological and physical influences on marine snowfall at the equator. Nature Geosci **10:** 852–858. doi:10.1038/ngeo3042.

Kiørboe, T. 2001. Formation and fate of marine snow: small-scale processes with large-scale implications. Sci Mar **65**: 57–71. doi:10.3989/scimar.2001.65s257.

Krupke, A., N. Musat, J. LaRoche, W. Mohr, B. M. Fuchs, R. I. Amann, and M. M. M. Kuypers, *et al.* 2013. *In situ* identification and N₂ and C fixation rates of uncultivated cyanobacteria populations. Syst Appl Microbiol **36:** 259–271. doi:10.1016/j.syapm.2013.02.002.

Labrenz, M., I. Brettar, R. Christen, S. Flavier, J. Botel, and M. G. Höfle. 2004. Development and application of a real-time PCR approach for quantification of uncultured bacteria in the central Baltic Sea. Appl Environ Microbiol **70:** 4971–4979. doi:10.1128/AEM.70.8.4971-4979.2004.

Labrenz, M., J. Grote, K. Mammitzsch, Boschker, H. T. S., M. Laue, G. Jost, and S. Glaubitz, *et al.* 2013. *Sulfurimonas gotlandica* sp. nov., a chemoautotrophic and psychrotolerant epsilonproteobacterium isolated from a pelagic redoxcline, and an emended description of the genus *Sulfurimonas*. Int J Syst Evol Microbiol **63:** 4141–4148. doi:10.1099/ijs.0.048827-0.

Labrenz, M., G. Jost, and K. Jürgens. 2007. Distribution of abundant prokaryotic organisms in the water column of the central Baltic Sea with an oxic–anoxic interface. Aquat Microb Ecol **46:** 177–190. doi:10.3354/ame046177.

Labrenz, M., E. Sintes, F. Toetzke, A. Zumsteg, G. J. Herndl, M. Seidler, and K. Jürgens. 2010. Relevance of a crenarchaeotal subcluster related to *Candidatus Nitrosopumilus maritimus* to ammonia oxidation in the suboxic zone of the central Baltic Sea. ISME J **4:** 1496–1508. doi:10.1038/ismej.2010.78.

Lam, P., and M. M. M. Kuypers. 2011. Microbial nitrogen cycling processes in oxygen minimum zones. Ann Rev Mar Sci **3:** 317–345. doi:10.1146/annurev-marine-120709-142814.

Lasternas, S., and S. Agusti. 2010. Phytoplankton community structure during the record Arctic ice-melting of summer 2007. Polar Biol **33**: 1709–1717. doi:10.1007/s00300-010-0877-x.

Laurenceau-Cornec, E. C., T. W. Trull, D. M. Davies, S. G. Bray, J. Doran, F. Planchon, and F. Carlotti, *et al.* 2015. The relative importance of phytoplankton aggregates and zooplankton fecal pellets to carbon export. Insights from free-drifting sediment trap

deployments in naturally iron-fertilised waters near the Kerguelen Plateau. Biogeosciences **12:** 1007–1027. doi:10.5194/bg-12-1007-2015.

Lavik, G., T. Stührmann, V. Brüchert, Van der Plas, Anja, V. Mohrholz, P. Lam, and M. Mußmann, *et al.* 2009. Detoxification of sulphidic African shelf waters by blooming chemolithotrophs. Nature **457:** 581–584. doi:10.1038/nature07588.

Lévy, M., L. Mémery, and G. Madec. 1998. The onset of a bloom after deep winter convection in the northwestern Mediterranean Sea: mesoscale process study with a primitive equation model. J Mar Syst **16:** 7–21. doi:10.1016/S0924-7963(97)00097-3.

Martin, J. H., G. A. Knauer, D. M. Karl, and W. W. Broenkow. 1987. VERTEX: carbon cycling in the northeast Pacific. Deep Sea Res A **34:** 267–285. doi:10.1016/0198-0149(87)90086-0.

McGlynn, S. E., G. L. Chadwick, C. P. Kempes, and V. J. Orphan. 2015. Single cell activity reveals direct electron transfer in methanotrophic consortia. Nature **526:** 531–535. doi:10.1038/nature15512.

Mestre, M., I. Ferrera, E. Borrull, E. Ortega-Retuerta, S. Mbedi, H.-P. Grossart, and J. M. Gasol, *et al.* 2017. Spatial variability of marine bacterial and archaeal communities along the particulate matter continuum. Mol Ecol **26:** 6827–6840. doi:10.1111/mec.14421.

Michotey, V., and P. Bonin. 1997. Evidence for anaerobic bacterial processes in the water column: denitrification and dissimilatory nitrate ammonification in the northwestern Mediterranean Sea. Mar Ecol Prog Ser **160**: 47–56. doi:10.3354/meps160047.

Milucka, J., T. G. Ferdelman, L. Polerecky, D. Franzke, G. Wegener, M. Schmid, and I. Lieberwirth, *et al.* 2012. Zero-valent sulphur is a key intermediate in marine methane oxidation. Nature **491:** 541–546. doi:10.1038/nature11656.

Mueller, C. W., A. Kölbl, C. Hoeschen, F. Hillion, K. Heister, A. M. Herrmann, and I. Kögel-Knabner. 2012. Submicron scale imaging of soil organic matter dynamics using NanoSIMS – From single particles to intact aggregates. Org Geochem **42:** 1476–1488. doi:10.1016/j.orggeochem.2011.06.003.

Musat, N., R. A. Foster, T. Vagner, B. Adam, and M. M. M. Kuypers. 2012. Detecting metabolic activities in single cells, with emphasis on nanoSIMS. FEMS Microbiol Rev **36:** 486–511. doi:10.1111/j.1574-6976.2011.00303.x.

Newsome, L., R. Lopez Adams, H. F. Downie, K. L. Moore, and J. R. Lloyd. 2018. NanoSIMS imaging of extracellular electron transport processes during microbial iron(III) reduction. FEMS Microbiol Ecol **94**. doi:10.1093/femsec/fiy104.

Nöthig, E.-M., A. Bracher, A. Engel, K. Metfies, B. Niehoff, I. Peeken, and E. Bauerfeind, *et al.* 2015. Summertime plankton ecology in Fram Strait—a compilation of long- and short-term observations. Polar Res **34**: 23349. doi:10.3402/polar.v34.23349.

Notz, D., and J. Stroeve. 2016. Observed Arctic sea-ice loss directly follows anthropogenic CO_2 emission. Science **354**: 747–750. doi:10.1126/science.aag2345.

Paerl, H. W., and J. L. Pinckney. 1996. A mini-review of microbial consortia. Their roles in aquatic production and biogeochemical cycling. Microb Ecol **31:** 225–247. doi:10.1007/BF00171569.

Passow, U. 2002. Transparent exopolymer particles (TEP) in aquatic environments. Prog Oceanogr **55:** 287–333. doi:10.1016/S0079-6611(02)00138-6.

Picheral, M., L. Guidi, L. Stemmann, D. M. Karl, G. Iddaoud, and G. Gorsky. 2010. The Underwater Vision Profiler 5. An advanced instrument for high spatial resolution studies of particle size spectra and zooplankton. Limnol Oceanogr: Methods **8:** 462–473. doi:10.4319/lom.2010.8.462.

Planavsky, N. J., D. Asael, A. Hofmann, C. T. Reinhard, S. V. Lalonde, A. Knudsen, and X. Wang, *et al.* 2014. Evidence for oxygenic photosynthesis half a billion years before the Great Oxidation Event. Nat Geosci **7:** 283 EP -. doi:10.1038/ngeo2122.

Ploug, H., M. H. Iversen, and G. Fischer. 2008a. Ballast, sinking velocity, and apparent diffusivity within marine snow and zooplankton fecal pellets: Implications for substrate turnover by attached bacteria. Limnol Oceanogr **53**: 1878–1886. doi:10.4319/lo.2008.53.5.1878.

Ploug, H., M. H. Iversen, M. Koski, and Buitenhuis E. T. 2008b. Production, oxygen respiration rates, and sinking velocity of copepod fecal pellets: Direct measurements of ballasting by opal and calcite. Limnol Oceanogr **53**: 469–476. doi:10.4319/lo.2008.53.2.0469.

Ploug, H., and U. Passow. 2007. Direct measurement of diffusivity within diatom aggregates containing transparent exopolymer particles. Limnol Oceanogr **52:** 1–6. doi:10.4319/lo.2007.52.1.0001.

Prairie, J. C., K. Ziervogel, R. Camassa, R. M. McLaughlin, B. L. White, C. Dewald, and C. Arnosti. 2015. Delayed settling of marine snow. Effects of density gradient and particle properties and implications for carbon cycling. Mar Chem **175:** 28–38. doi:10.1016/j.marchem.2015.04.006.

Proctor, L. M. 1997. Nitrogen-fixing, photosynthetic, anaerobic bacteria associated with pelagic copepods. Aquat Microb Ecol **12:** 105–113. doi:10.3354/ame012105.

Purcell, E. M. 1977. Life at low Reynolds number. Am J Phys **45:** 3–11. doi:10.1119/1.10903.

Rapp, J. Z., M. Fernández-Méndez, C. Bienhold, and A. Boetius. 2018. Effects of ice-algal aggregate export on the connectivity of bacterial communities in the central arctic ocean. Front Microbiol **9:** 1035. doi:10.3389/fmicb.2018.01035.

Roerdink, D. L., P. R. Mason, J. Farquhar, and T. Reimer. 2012. Multiple sulfur isotopes in Paleoarchean barites identify an important role for microbial sulfate reductioom in the early environment. Earth Planet Sci Lett **331**–**332**: 177–186. doi:10.1016/j.epsl.2012.03.020.

Roslev, P., M. B. Larsen, D. Jørgensen, and M. Hesselsoe. 2004. Use of heterotrophic CO_2 assimilation as a measure of metabolic activity in planktonic and sessile bacteria. J Microbiol Methods **59:** 381–393. doi:10.1016/j.mimet.2004.08.002.

Salazar, G., F. M. Cornejo-Castillo, E. Borrull, C. Díez-Vives, E. Lara, D. Vaqué, and J. M. Arrieta, *et al.* 2015. Particle-association lifestyle is a phylogenetically conserved trait in bathypelagic prokaryotes. Mol Ecol **24:** 5692–5706. doi:10.1111/mec.13419.

Sano, Y., K. Shirai, N. Takahata, T. Hirata, and N. C. Sturchio. 2005. Nano-SIMS analysis of Mg, Sr, Ba and U in natural calcium carbonate. Anal Sci **21:** 1091–1097. doi:10.2116/analsci.21.1091.

Schulz, H. N., and B. B. Jørgensen. 2001. Big bacteria. Annu Rev Microbiol **55:** 105–137.

Seager, S., M. Schrenk, and W. Bains. 2012. An astrophysical view of Earth-based metabolic biosignature gases. Astrobiology **12:** 61–82. doi:10.1089/ast.2010.0489.

Shah, V., B. X. Chang, and R. M. Morris. 2017. Cultivation of a chemoautotroph from the SUP05 clade of marine bacteria that produces nitrite and consumes ammonium. ISME J: 263–271. doi:10.1038/ismej.2016.87.

Shen, Y., R. Buick, and D. E. Canfield. 2001. Isotopic evidence for microbial sulphate reduction in the early Archaean era. Nature **410**: 77–81. doi:10.1038/35065071.

Simon, M., H.-P. Grossart, B. Schweitzer, and H. Ploug. 2002. Microbial ecology of organic aggregates in aquatic ecosystems. Aquat Microb Ecol **28:** 175–211. doi:10.3354/ame028175.

Smith, M. W., L. Z. Allen, A. E. Allen, L. Herfort, and H. M. Simon. 2013. Contrasting genomic properties of free-living and particle-attached microbial assemblages within a coastal ecosystem. Front Microbiol **4**:120. doi:10.3389/fmicb.2013.00120.

Stewart, F. J. 2011. Dissimilatory sulfur cycling in oxygen minimum zones: an emerging metagenomics perspective. Biochem Soc Trans **39:** 1859–1863. doi:10.1042/BST20110708.

Stocker, R. 2012. Marine microbes see a sea of gradients. Science **338**: 628–633. doi:10.1126/science.1208929.

Stramma, L., G. C. Johnson, J. Sprintall, and V. Mohrholz. 2008. Expanding oxygen-minimum zones in the tropical oceans. Science **320:** 655–658. doi:10.1126/science.1153847.

Stramma, L., E. D. Prince, S. Schmidtko, J. Luo, J. P. Hoolihan, M. Visbeck, and Wallace, Douglas W. R., *et al.* 2011. Expansion of oxygen minimum zones may reduce available habitat for tropical pelagic fishes. Nat Clim Chang **2:** 33–37. doi:10.1038/nclimate1304.

Swan, B. K., M. Martinez-Garcia, C. M. Preston, A. Sczyrba, T. Woyke, D. Lamy, and T. Reinthaler, *et al.* 2011. Potential for chemolithoautotrophy among ubiquitous bacteria lineages in the dark ocean. Science **333:** 1296–1300. doi:10.1126/science.1203690.

Tang, K. W., R. N. Glud, A. Glud, S. Rysgaard, and T. G. Nielsen. 2011. Copepod guts as biogeochemical hotspots in the sea: Evidence from microelectrode profiling of Calanus spp. Limnol Oceanogr **56:** 666–672. doi:10.4319/lo.2011.56.2.0666.

Taylor, G. T., M. Iabichella, T.-Y. Ho, M. I. Scranton, R. C. Thunell, F. E. Muller-Karger, and R. Varela. 2001. Chemoautotrophy in the redox transition zone of the Cariaco Basin: A significant mid-water source of organic carbon production. Limnol Oceanogr **46:** 148–163. doi:10.4319/lo.2001.46.1.0148.

Thiele, S., B. M. Fuchs, R. I. Amann, and M. H. Iversen. 2015. Colonization in the photic zone and subsequent changes during sinking determine bacterial community composition in marine snow. Appl Environ Microbiol **81:** 1463–1471. doi:10.1128/AEM.02570-14.

Thomalla, S., R. Turnewitsch, M. Lucas, and A. Poulton. 2006. Particulate organic carbon export from the North and South Atlantic gyres: The 234Th/238U disequilibrium approach. Deep Sea Res Part II **53:** 1629–1648. doi:10.1016/j.dsr2.2006.05.018.

Turner, J. T. 2015. Zooplankton fecal pellets, marine snow, phytodetritus and the ocean's biological pump. Prog Oceanogr **130:** 205–248. doi:10.1016/j.pocean.2014.08.005.

van der Jagt, H., C. Friese, J.-B. W. Stuut, G. Fischer, and M. H. Iversen. 2018. The ballasting effect of Saharan dust deposition on aggregate dynamics and carbon export: Aggregation, settling, and scavenging potential of marine snow. Limnol Oceanogr **63:** 1386–1394. doi:10.1002/lno.10779.

van Haren, H., C. Millot, and I. Taupier-Letage. 2006. Fast deep sinking in Mediterranean eddies. Geophys Res Lett **33:** 263. doi:10.1029/2005GL025367.

Waite, A. M., K. A. Safi, J. A. Hall, and S. D. Nodder. 2000. Mass sedimentation of picoplankton embedded in organic aggregates. Limnol Oceanogr **45:** 87–97. doi:10.4319/lo.2000.45.1.0087.

Waite, A. M., L. Stemmann, L. Guidi, P. H. R. Calil, A. M. C. Hogg, M. Feng, and P. A. Thompson, *et al.* 2016. The wineglass effect shapes particle export to the deep ocean in mesoscale eddies. Geophys Res Lett **43:** 9791–9800. doi:10.1002/2015GL066463.

Waldron, H. N., P. M. S. Monteiro, and N. C. Swart. 2009. Carbon export and sequestration in the southern Benguela upwelling system: lower and upper estimates. Ocean Sci Discuss **6:** 1173–1192. doi:10.5194/osd-6-1173-2009.

Walsh, D. A., E. Zaikova, C. G. Howes, Y. C. Song, J. J. Wright, S. G. Tringe, and P. D. Tortell, *et al.* 2009. Metagenome of a versatile chemolithoautotroph from expanding oceanic dead zones. Science **326:** 578–582. doi:10.1126/science.1175309.

Wiedmann, I., M. Reigstad, M. Marquardt, A. Vader, and T. M. Gabrielsen. 2016. Seasonality of vertical flux and sinking particle characteristics in an ice-free high arctic fjord— Different from subarctic fjords? J Mar Syst **154:** 192–205. doi:10.1016/j.jmarsys.2015.10.003.

Woebken, D., B. M. Fuchs, M. M. M. Kuypers, and R. I. Amann. 2007. Potential interactions of particle-associated anammox bacteria with bacterial and archaeal partners in the Namibian upwelling system. Appl Environ Microbiol **73:** 4648–4657. doi:10.1128/AEM.02774-06.

Wolgast, D., A. Carlucci, and J. Bauer. 1998. Nitrate respiration associated with detrital aggregates in aerobic bottom waters of the abyssal NE Pacific. Deep Sea Res Part II **45**: 881–992. doi:10.1016/S0967-0645(98)00006-X.

Zaikova, E., D. A. Walsh, C. P. Stilwell, W. W. Mohn, P. D. Tortell, and S. J. Hallam. 2010. Microbial community dynamics in a seasonally anoxic fjord: Saanich Inlet, British Columbia. Environ Microbiol **12:** 172–191. doi:10.1111/j.1462-2920.2009.02058.x.

Zhang, C., H. Dang, F. Azam, R. Benner, L. Legendre, U. Passow, and L. Polimene, *et al.* 2018. Evolving paradigms in biological carbon cycling in the ocean. Nat Sci Rev **5:** 481–499. doi:10.1093/nsr/nwy074.

SPECIFIC CONTRIBUTION TO EACH PAPER

Table 2: Total contribution to respective Papers in %.

Paper	Project Planning	Preparations	Practical realization	Sample analyses	Data analyses	Manuscript writing
Paper I	20 *(0*)*	15 *(0*)*	20 *(0*)*	70 *(0*)*	80 *(30*)*	70 *(50*)*
PaperII	40	10	0	0	0	40
Paper III	50	90	90	90	90	50
Paper IV	10	20	20	0	20	20
Paper V	70	70	60	n.s.e.	40	90

* Contribution within the time registered as PhD-student (Feb.2015 – Feb. 2019)

n.s.e.: no sampling executed

VERSICHERUNG AN EIDES STATT

Ich, Andreas Rogge; Otto-Fisch-Straße 36, 28217 Bremen; Matr.-Nr.: 3025709

versichere an Eides Statt durch meine Unterschrift, dass ich die vorstehende Arbeit

selbständig und ohne fremde Hilfe angefertigt und alle Stellen, die ich wörtlich dem

Sinne nach aus Veröffentlichungen entnommen habe, als solche kenntlich gemacht

habe, mich auch keiner anderen als der angegebenen Literatur oder sonstiger

Hilfsmittel bedient habe.

Ich versichere an Eides Statt, dass ich die vorgenannten Angaben nach bestem

Wissen und Gewissen gemacht habe und dass die Angaben der Wahrheit

entsprechen und ich nichts verschwiegen habe.

Die Strafbarkeit einer falschen eidesstattlichen Versicherung ist mir bekannt,

namentlich die Strafandrohung gemäß § 156 StGB bis zu drei Jahren Freiheitsstrafe

oder Geldstrafe bei vorsätzlicher Begehung der Tat bzw. gemäß § 161 Abs. 1 StGB

bis zu einem Jahr Freiheitsstrafe oder Geldstrafe bei fahrlässiger Begehung.

_____   _____
Ort, Datum   Unterschrift

176

APPENDIX

TABLE OF CONTENTS

CONTRIBUTION TO PAPER AI

A-2

Table A1: Total contribution to Paper AI in %.

Paper	Project Planning	Preparations	Practical realization	Sample analyses	Data analyses	Manuscript writing
Paper A1	0	0	0	0	0	10

Paper AI

ISME

ARTICLE

Sulfurimonas subgroup GD17 cells accumulate polyphosphate under fluctuating redox conditions in the Baltic Sea: possible implications for their ecology

Lars Möller[1] · Peeter Laas[1,2,3] · Andreas Rogge[1,4] · Florian Goetz [1,5] · Rainer Bahlo[1] · Thomas Leipe[1] ·
Matthias Labrenz[1]

Abstract

The central Baltic Sea is characterized by a pelagic redox zone exhibiting high dark CO_2 fixation rates below the chemocline. These rates are mainly driven by chemolithoautotrophic and denitrifying *Sulfurimonas* GD17 subgroup cells which are motile and fast-reacting *r*-strategists. Baltic Sea redox zones are unstable and a measurable overlap of nitrate and reduced sulfur, essential for chemosynthesis, is often only available on small scales and short times due to local mixing events. This raises the question of how GD17 cells gain access to electron donors or acceptors over longer term periods and under substrate deficiency. One possible answer is that GD17 cells store high-energy-containing polyphosphate during favorable nutrient conditions to survive periods of nutrient starvation. We used scanning electron microscopy with energy-dispersive X-ray spectroscopy to investigate potential substrate enrichments in single GD17 cells collected from Baltic Sea redox zones. More specific substrate enrichment features were identified in experiments using *Sulfurimonas gotlandica* GD1^T, a GD17 representative. *Sulfurimonas* cells accumulated polyphosphate both in situ and in vitro. Combined genome and culture-dependent analyses suggest that polyphosphate serves as an energy reservoir to maintain cellular integrity at unfavorable substrate conditions. This redox-independent energy supply would be a precondition for sustaining the *r*-strategy lifestyle of GD17 and may represent a newly identified survival strategy for chemolithoautotrophic prokaryotes occupying eutrophic redox zones.

Introduction

Marine systems such as the Baltic Sea, Black Sea, and the Cariaco Basin are characterized by a practically permanent

✉ Matthias Labrenz
matthias.labrenz@io-warnemuende.de

1 Department of Biological Oceanography, Leibniz Institute for Baltic Sea Research Warnemünde (IOW), Rostock, Germany

2 Department of Marine Systems, Tallinn University of Technology, Tallinn, Estonia

3 Fort Lauderdale Research and Education Center, University of Florida, Davie, FL, USA

4 Alfred Wegener Institute (AWI), Bremerhaven, Germany

5 Woods Hole Oceanographic Institution, Falmouth, MA, USA

oxygen depletion zone [1–5]. In these systems, reduced sulfur compounds, especially hydrogen sulfide, are produced by the anaerobic microbial decomposition of organic matter [6, 7].

The typical transition zone between oxidized and reduced water bodies is referred to as the redox zone and it contains a high microbial abundance and activity. The latter includes the catalysis of important biogeochemical transformation processes [8]. In the Baltic Sea, one of the organismal groups predominating within its redox zones belongs to the *Epsilonproteobacteria*, represented by the *Sulfurimonas* GD17 subgroup. GD17 cell counts are highest below the chemocline, defined as the depth marked by the first appearance of sulfide [9–11]. Bacteria of the *Sulfurimonas* GD17 subgroup are anaerobic sulfur oxidizers and denitrifiers, adapted to waters with sulfide concentrations ranging from <10 to 20 µmol L^{-1} [12, 13].

The successful isolation of a representative of the GD17 subgroup, *Sulfurimonas gotlandica* strain GD1^T, has provided a model organism for studies of biogeochemical
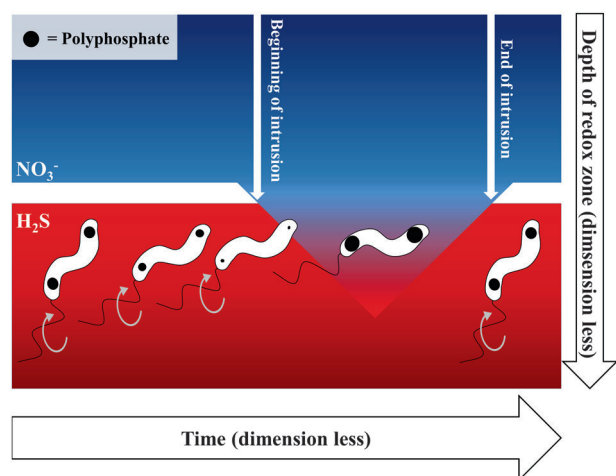
Fig. 1 Transition zones between oxidized and reduced water masses provide favorable habitats for chemolithoautophic microorganisms. Mixing events, such as micro-scale intrusions, create overlapping zones where suitable electron acceptors (including NO_3^-) and electron donors (including H_2S) co-localize. We hypothesize that under these conditions *S. gotlandica* GD1^T cells accumulate polyphosphate, using it as an energy source to sustain cellular integrity, which is a precondition to enable motility to new favorable zones

cycling in the Baltic Sea redox zone [12–14]. In the central Baltic Sea, even though the redox zone itself is relatively stable, local mixing events or lateral intrusions can occur [15], introducing nitrate-containing water masses in sulfidic zones and vice versa. The result is a redox zone of fluctuating redox potentials on smaller scales. In situ substrate incorporation analyses using nano secondary ion mass spectrometry (NanoSIMS) on a single-cell level showed that *S. gotlandica* subgroup GD17 cells are fast-reacting *r*-strategists that depend on these intrusions for growth [13]. However, in this fluctuating system, where the loss of essential donors or acceptors is a constant threat, it is unclear how *S. gotlandica* subgroup GD17 cells gain access to the energy sources they need for chemosynthesis. Accumulation and storage are possibilities and both have been well documented in other chemolithoautotrophic bacteria, such as *Beggiatoa*, *Thioploca*, and *Thiomargarita*, which store sulfur, nitrate, or both [16–19]. Although earlier studies suggested a similar ability for *Sulfurimonas* present in the Baltic Sea [11], it has yet to be demonstrated.

Thus, the aim of our study was to examine the potential substrate storage capabilities of *Sulfurimonas* subgroup GD17. However, with a mean volume of 0.6 μm^3 [13], *Sulfurimonas* cells are much smaller than the above-mentioned chemolithoautotrophic bacteria, limiting intracellular storage capacities. Thus, instead of sulfur or nitrate as only precursors for energy generation, we expected an enrichment of polyphosphate to be a more comprehensive and beneficial cellular storage system within unstable

marine redox zones. Polyphosphate consists of linear polymers based on tens to hundreds of phosphate residues which are linked by highly energetic phosphoanhydride bonds. As a final product it represents both a redox-independent and rich source of energy. Cellular polyphosphate enrichment is a well-known feature of numerous prokaryotic taxa and contributes to a wide variety of cellular functions. For instance, in *Beggiatoa*, polyphosphate may provide energy as part of a cellular "safety system" that is active in the absence of a suitable electron acceptor [20]. Polyphosphate can also be accumulated in response to certain conditions: for purposes of phosphorus storage [21–23], as an adenosine triphosphate (ATP) substitute [24, 25], as a factor in stress responses [20, 26–28], as an adaptation to the stationary phase of the cell cycle [29], as a pH buffer system [30], in the control of gene activity [31], for energy storage [32] and in the upkeep of motility [33, 34]. Recently, it has been shown for the oxic–anoxic interface in the water column of the ferruginous Lake Pavin that magnetotactic bacteria of the family Magnetococcaceae accumulate polyphosphates and could significantly contribute to the P cycle in this environment [35].

Our hypothesis was that, as shown in Fig. 1, mixing events in pelagic Baltic Sea redox zones provide areas where suitable electron acceptors and electron donors co-localize for the chemosynthesis of *Sulfurimonas* subgroup GD17. In these conditions *S. gotlandica* GD1^T cells accumulate polyphosphate. Preserving cellular integrity, potentially linked to motility, for a longer time period, this redox-independent energy supply would be a prerequisite for the maintenance of the *r*-strategy lifestyle of *Sulfurimonas* subgroup GD17/GD1^T.

The hypothesis was tested by polyphasic in situ and in vitro approaches. For our in situ approach, we took advantage of the fact that dark CO_2 fixation measurements have already demonstrated the high cellular density of most chemolithoautotrophic prokaryotes in sulfidic zones of the Baltic Sea [36]. As the major chemolithoautotrophic cluster in the redox zone, *Sulfurimonas* subgroup GD17 was expected to comprise these high-density cells. Accordingly, we isolated the chemolithoautotrophic cluster by flow cytometry, identified the bacterial composition, and determined the features of cellular substrate enrichment. In vitro experiments using *S. gotlandica* strain GD1^T were performed to identify the ecological features associated with the potential substrate storage capability of the cells.

Materials and methods

A detailed description of the material and methods used in this study is available online in the Supplementary Methods.
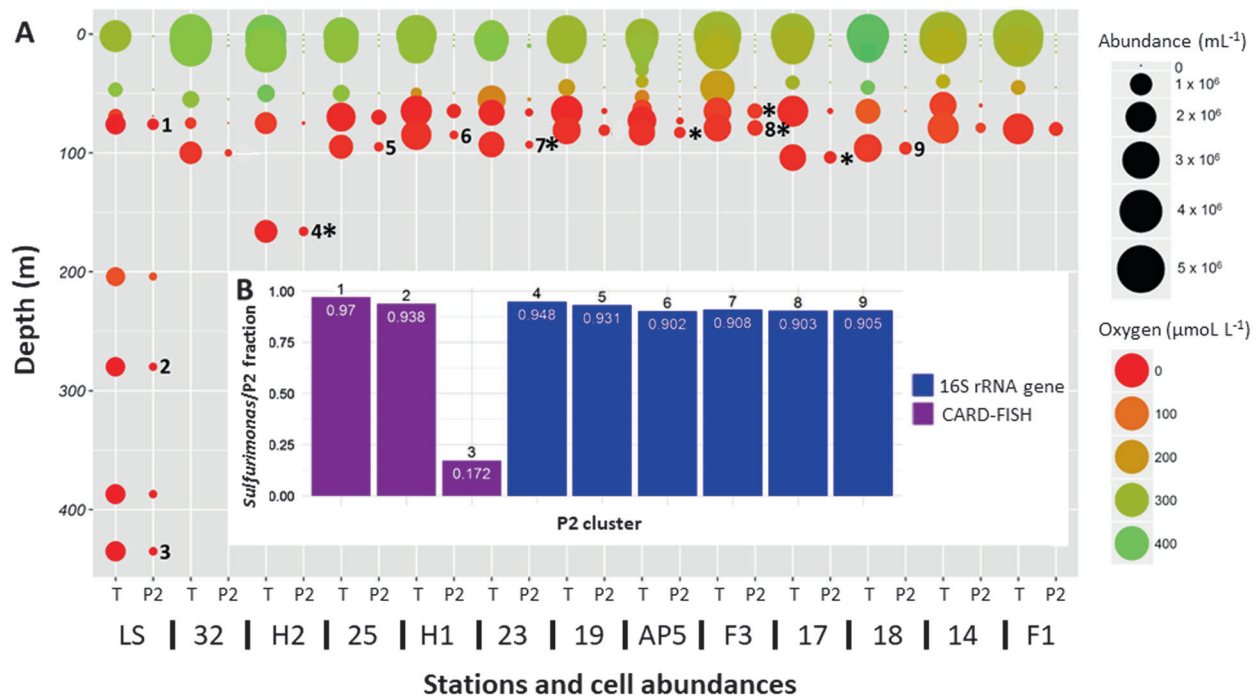
Fig. 2 In situ analyses. **a** Specific high nucleic acid-containing, high side scatter cluster P2 cell abundances and the total cell abundances (T) outside cluster P2 as determined at 13 different Baltic Sea stations. Nine P2 clusters (labeled 1–9) were selected for cell sorting, followed by CARD-FISH analyses or 16S rRNA gene identification. **b** Relative abundance of *S. gotlandica* strain GD1^{T}/GD17 cells determined by CARD-FISH (P2 clusters 1–3); 16S rRNA gene abundances of *Sulfurimonas* spp. (P2 clusters 4–9). *P2 cluster samples used for substrate enrichment analyses by SEM-EDX. Number of cells containing polyphosphate versus polyphosphate-free cells was: 1/294 (station H2), 3/143 (station 23), 1/217 (station AP5); 0/85 (77 m), 281/25 (79 m) (station F3), 0/103 (station 17)

Sulfurimonas subgroup GD17 in situ sampling and processing

Sampling

Water samples from the Gulf of Finland were collected on-board the R/V *Salme* in July 2014 and from the Landsort Deep on-board the R/V *Poseidon* in August 2015 (Supplementary Fig. S1; Supplementary Table S1). Flow cytometry samples for cellular-based analyses were fixed with paraformaldehyde and glutaraldehyde (P+G, final concentrations 1 and 0.05%, respectively; pH = 7.4) and incubated at 4 °C for 60 min. Subsamples for downstream molecular analyses were preserved in dimethyl sulfoxide (DMSO) at a final concentration of 15% and stored at −80 °C.

Cell isolation by flow cytometry

The cells were sorted on a BD FACSAria III (Becton, Dickinson and Company; see Supplementary Methods). Events within high nucleic acid and high side scatter clusters (HNA-hs) were attributed to GD17 (P2 cluster in Figs. 2–4). Cells within and without the P2 cluster were sorted, collecting between 500,000 and 1,000,000 cells in 2 mL Eppendorf tubes. The sorted samples were prepared and used for (a) scanning electron microscopy–energy-dispersive X-ray spectroscopy (SEM-EDX) analyses (P+G fixed) to detect cellular substrate enrichments; (b) GD17 identification by 16S rRNA gene analyses (DMSO-fixed); (c) GD17 quantification using the SUL90 gene probe and fluorescence in situ hybridization combined with catalyzed reporter deposition (CARD-FISH (P+G fixed)) [9].

Molecular identification and quantification

DMSO-preserved P2 cluster samples were pelleted and used for direct PCR amplification. Amplicons of the obtained 16S rRNA gene V2 hypervariable region were sequenced on the Illumina MiSeq platform (The Estonian Genome Center Core Facility) and phylogenetically analyzed as described earlier [37]. Sorted P2 samples from the Landsort Deep were used for CARD-FISH analyses.

Nucleotide sequence accession numbers

The 16S rRNA gene sequences determined in this study have been deposited in the National Center for Biotechnology Information (NCBI) Popset Database under accession numbers KT86004455220–KT860044.
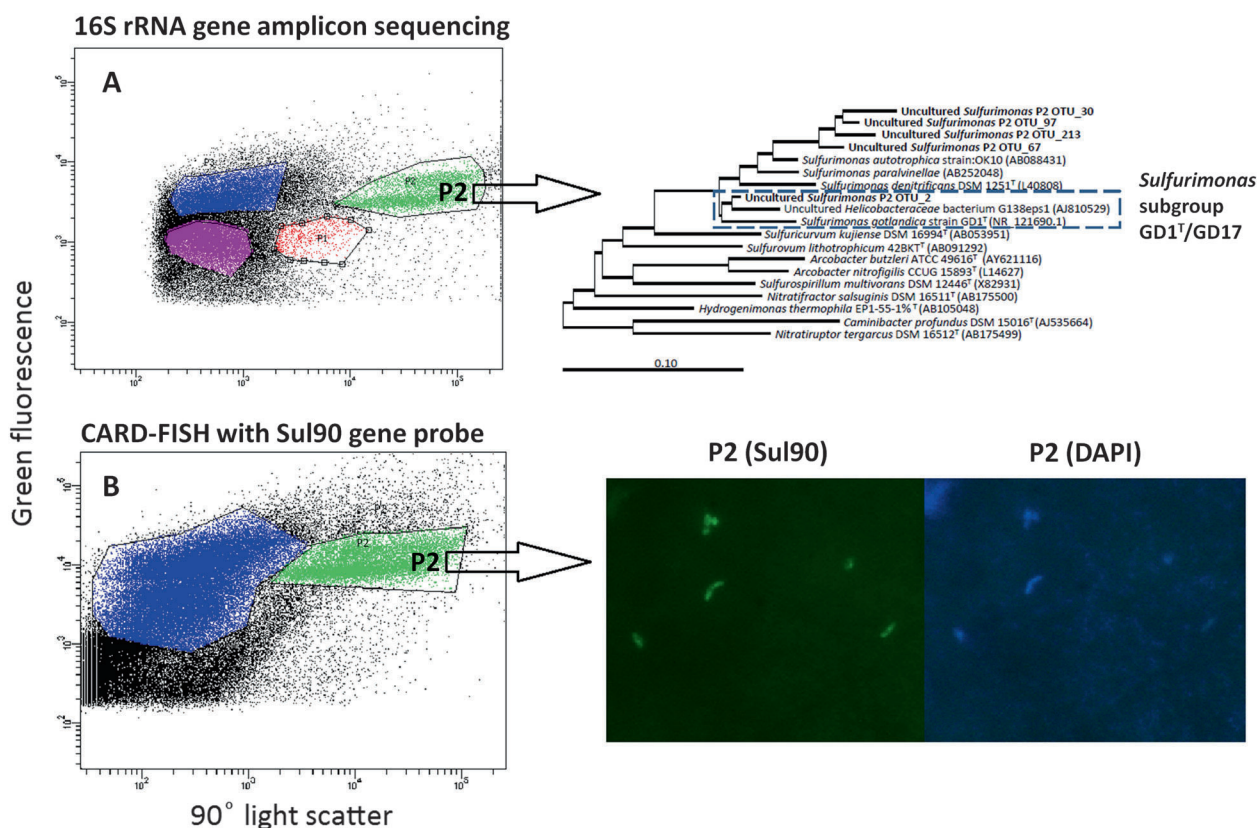
16S rRNA gene amplicon sequencing

CARD-FISH with Sul90 gene probe

Fig. 3 Approach to identify and quantify *Sulfurimonas* spp. cells in the high nucleic acid, high side scatter cluster P2. BD FACSAria III was used to sort out the P2 cluster (green gate) from SYBRGreen-I-stained samples. **a** Sorted cells were identified by parallel sequencing of 16S rRNA gene sequences amplified via direct PCR. OTU2, which clusters together with "uncultured *Helicobacteraceae* bacterium G138eps1" (the first 16S rRNA gene sequence published representing *Sulfurimonas* subgroup GD17 [10]), and *Sulfurimonas gotlandica* GD1^T were used to determine relative 16S rRNA gene abundance. **b** Quantification of sorted cells by CARD-FISH staining using the Sul90 probe which targets the *Sulfurimonas* GD1^T/GD17 subgroup

Polyphosphate identification

Cellular element composition was analyzed by SEM (Zeiss Merlin® Compact VP) combined with EDX (Oxford Instruments; AZtec 3.3. and Inca software) using X-MaxN80 EDX detector. The cells were filtered onto 0.2 μm polycarbonate filters (Whatman Nucleopore), dried at room temperature, and chrome-coated (vacuum sputter) before their analysis for electrical conductivity. A total of 25,396 potential particles (between 1494 and 5993 per sample) were automatically spotted by the AZtec program and their elemental composition identified by several measurements on the features. The accelerating voltage was 10 kV with a working distance of 8.5 and a microscope magnification of 3000. The EDX measurement was calculated by stoichiometry and normalized to 100%. Deconvolution elements were carbon and chrome. Eventually, particles were controlled by eye to discriminate abiotic particles from bacterial cells. Only those cells with phosphorus contents between 20 and 60% were labeled as phosphorus enriched. To identify polyphosphate, point identification was used for

elements nitrogen, phosphorus, sulfur, oxygen, magnesium, and calcium on 39 single cells. These selected cells were analyzed using the line scan mode with 200 points of measurement each.

Sulfurimonas GD1^T in vitro analyses

Cultivation

S. gotlandica strain GD1^T cells were cultivated in a modified artificial brackish water (ABW) medium under anoxic conditions [38], as described in Labrenz et al. [14]. NaHCO$_3$ was provided as the carbon source at a final concentration of 2 mmol L^{-1}. The medium was supplemented with 10 mmol KNO$_3$ L^{-1} (variations in some experiments, see Supplementary Methods) as the electron acceptor. One of two different compounds (thiosulfate, elemental sulfur) was used as the electron donor and added in variable concentrations depending on the experimental setup. All supplements were prepared anoxically and sterilized before usage: KNO$_3$ and thiosulfate was autoclaved

and sulfur tyndallized. The cultures were incubated at 15 °C in the dark. Cultures with elemental sulfur as the electron donor were incubated on a tilting table at 60 rpm. The cells were counted and observed by nucleic acid staining using DAPI (4,6-diamidino-2-phenylindol) and epifluorescence microscopy as described by Grote et al. [12].

Physiological and morphological *S. gotlandica* GD1^T features

A polyphasic approach was used to identify the potential role of polyphosphate for GD1^T. (a) The chemical composition of cellular element enrichments was identified in SEM-EDX analyses of 36 cells as described above. (b) Polyphosphate and protein production during the different GD1^T growth phases was quantified. Polyphosphate quantification was based on Martin and Van Mooy [39] with a slight modification in buffer composition according to Kulakova et al. [40]. For protein quantification Bio-Rad Quick StartTM Bradford Protein Assay was used. (c) The motility speed of cells grown in the presence of different electron donor and acceptor concentrations was measured. For this, GD1^T was cultivated as described above in ABW medium supplemented with 6 different electron thiosulfate/ nitrate concentrations, ranging from $10 \, \mu mol \, L^{-1}$ up to 10 $mmol \, L^{-1}$. Cultures were incubated for 7 days and then transferred on self-prepared objective slides with an anoxic chamber on it. Cells were recorded using a microscope (Zeiss AXIO star plus) mounted with a camera (Nikon D300s) for up to 10 s. Super©, a freeware tool, was used to extract data from all videos. Resulting bmp data were analyzed using the freeware program "Trace" (Heribert Cypionka, 2000–2010). Analogously to Fischer and Cypionka [41], individual cells were identified by the program and tracked over recorded times to measure the motility speed. Motility speeds of 436 cells were measured in total. (d) The influence of polyphosphate inclusions on GD1^T cell integrity was assayed in a 90-day incubation experiment, where only nitrate was supplemented as electron acceptor. The test design was based on Adler and Dahl [42] and the described gradient experiment to examine the influence of different polyphosphate concentration on cellular integrity. Defined numbers of nutrient-free ABW medium-washed high-polyphosphate-containing cells and low-polyphosphate-containing cells were placed on the bottom of glass tubes containing nutrient-free ABW soft agar with a nitrate-containing solid top agar. Tubes were incubated for 90 days in an anoxic atmosphere, at 15 °C in the dark. After incubation, tubes were split in 2 cm sections and the semi-solid agar of each part was prepared for DAPI counting. (e) An incubation experiment was carried out for 23 days to test chemotactic movement in a thiosulfate-nitrate gradient. Test tubes were prepared with semi-solid

agar in the middle flanked by solid top agar containing nitrate and solid bottom agar containing thiosulfate. Inoculated tubes were incubated for 23 days. After the incubation, the tubes were opened and the semi-solid medium was divided into $8 \times 1 \, mL$ sections. Cell counts in these layers were determined using DAPI staining.

Results

Identification and isolation of environmental *Sulfurimonas* subgroup GD17 cells

GD17 identification and quantification

Earlier $NaH_{14}CO_3$ tracer incubation experiments using central Baltic Sea redox zone waters followed by flow cytometric cell sorting and CO_2 fixation rate measurements identified already distinct flow cytometric high side scatter clusters with prokaryotes of high nucleic acid content being responsible for 65 to 100% of the total dark fixation [36]. As the major chemolithoautotrophic taxon in the redox zone [43], *Sulfurimonas* subgroup GD17 was expected to comprise these high-density cells [9–11, 36]. However, this hypothesis remained unproven and had to be confirmed first to enable a linkage between environmental *Sulfurimonas* identity and potential polyphosphate enrichment. Accordingly, we isolated the HNA-hs clusters, identified their bacterial composition and *Sulfurimonas* cell abundance. Water samples for flow cytometry analyses were collected from the Gulf of Finland and the Landsort Deep and revealed the presence of HNA-hs clusters in all hypoxic and sulfidic areas investigated (Figs. 2, 3; cluster P2). Parallel sequencing analyses of 16S rRNA gene amplicons based on six different samples demonstrated that *Sulfurimonas* spp. contributed 91.6% (±1.9%) of the 16S rRNA genes of the P2 clusters (Fig. 2b). The most abundant OTU2 (Fig. 3a) was a member of the *Sulfurimonas* GD1^T/GD17 subgroup (84.1% (±1.5%) of all 16S rRNA gene reads). *Sulfurimonas* GD1^T/GD17-specific CARD-FISH analyses using gene probe Sul90 confirmed these high 16S rRNA gene abundances for redox zone samples collected from the Landsort Deep under optimal H_2S concentrations of $6.8 \, \mu mol \, L^{-1}$ (Figs. 2a, 3b; Supplementary Table S2), in which *Sulfurimonas* GD1^T/ GD17 subgroup cell abundances within the P2 cluster were 94 and 97%. By contrast, in the control group (low side scatter cells), Sul90-positive cells contributed only between 0.7 and 2.1% of the cells outside the P2 cluster (Supplementary Table S2), and thus were at the detection limit of this approach. At the deepest depths and in a highly sulfidic zone, the fraction of Sul90-positive cells in the P2 cluster decreased down to 17% (Fig. 2).
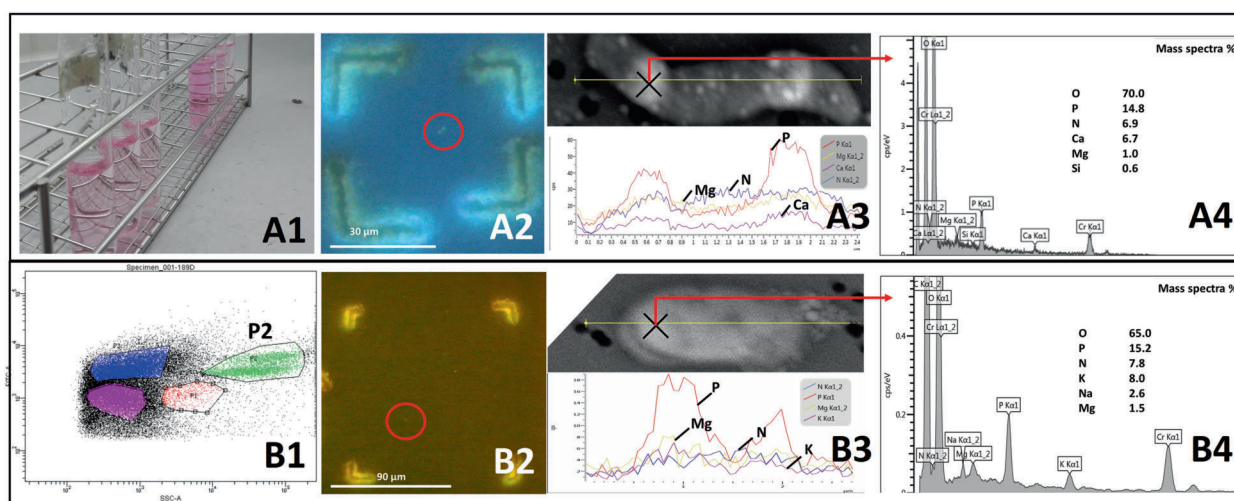
Fig. 4 Approach to detect polyphosphate inclusions in *Sulfurimonas* GD1^T/GD17 cells in culture and environmental samples. **a1** The cells were harvested directly from *S. gotlandica* GD1^T cultures. **b1** *Sulfurimonas* GD17 cells were collected by FACS from environmental samples. GD17 forms the distinct pattern P2 when analyzed by flow cytometry. **a2** Identification and marking of single *S. gotlandica* GD1^T cells with yellow inclusions after DAPI staining. **b2** SYBRGreen-stained *Sulfurimonas* GD17 cells isolated by FACS were identified by marking with the Laser Microdissection Microscope (LMD). **a3**, **b3** The marked cells were line-scanned for the distribution of phosphorus, nitrogen, magnesium, and potassium, or calcium over the whole cell body. The crosses mark the spots analyzed in greater detail by EDX point analysis (**a4**, **b4**). Specific cross-marked areas were analyzed for their elemental composition. Relative abundances (%) correspond to those elements in the marked spot included in the analysis. Two elements visible in the EDX spectra were excluded from calculation: carbon, which was the filter material, and chromium, used as the sputter element for conductivity

Polyphosphate accumulation in *Sulfurimonas* cells in situ and in vitro

In situ polyphosphate accumulation in *Sulfurimonas* subgroup GD17 cells

Following the sorting and identification of *Sulfurimonas* GD17/GD1^T dominated P2 clusters from the Gulf of Finland and the Landsort Deep, as described above, these samples were subjected to SEM-EDX particle analyses. The 5.9% ($\pm$5.1%) of the automatically detected particles could manually be identified as bacterial cells (1153 cells overall), with total numbers in the range from 85 to 295 cells per sample (Fig. 2). Of the cells originating from the P2 cluster of station F3, 91.8% (79 m) contained phosphorus. The P2 cluster taken 2 m above at 77 m depth did not contain phosphorus-positive cells anymore. All the other P2 clusters analyzed contained between 0.0 and 2.1% phosphorus-enriched cells. The evidence of inorganic polyphosphate in cells of the P2 cluster using the line scan mode was obtained from station F3 at 79 m (Fig. 4b3). At this depth, the abundance of the P2 cluster was high, $>4.36 \times 10^5$ cells mL^{-1} (Fig. 2). In comparison to cultured GD1^T cells, polyphosphate of the environmental P2 cluster cells contained potassium instead of calcium (Fig. 4b4). In contrast, sulfur or nitrate enrichments were undetectable in any cell or bulk of cells investigated by EDX. Thus, *Sulfurimonas* subgroup GD17 enriched polyphosphate in areas of pelagic redox zones where sulfide/nitrate overlaps may occur. To confirm these conditions as relevant ecological factors, the impact of different substrates and substrate concentrations on polyphosphate formation in *Sulfurimonas gotlandica* GD1^T cells were investigated.

In vitro polyphosphate accumulation in *Sulfurimonas gotlandica* GD1^T cells at different catabolite concentrations

Independent of the electron donor type, yellow inclusions were only seen in larger amounts in DAPI-stained, stationary-phase *S. gotlandica* strain GD1^T cells cultivated in the presence of high concentrations (5 or 10 mmol L^{-1}) of the electron donor/acceptor (thiosulfate: in 94.4% ($\pm$3.7%) of total cells; sulfur: in 7.5% ($\pm$5.2%) of total cells). Lower concentrations (100 μmol L^{-1}) resulted in cell growth but fewer or no visible inclusions (thiosulfate: in 0.1% ($\pm$0.3%) of total cells; sulfur: in 1.4% ($\pm$1.7%) of total cells). Point measurements as well as line scans during SEM-EDX-based elemental composition analyses of cells containing these inclusions (Fig. 4a3, 4) revealed the presence of phosphorus in combination with magnesium and calcium. In polyphosphate-free cells, phosphorus was below the detection limit of this approach.

Polyphosphate enrichment at different substrates and growth phases

Cellular polyphosphate and protein production depended on the applied electron donor and the growth phase (Table 1).

Table 1 The incubation of *S. gotlandica* strain GD1^T with 10 mmol Na$_2$S$_2$O$_3$ L^{-1} or 5 mmol sulfur L^{-1} revealed differences in polyphosphate formation over time

10 mmol Na$_2$S$_2$O$_3$ L^{-1}						
Incubation time (h)	0	60	84	108	132	156
Total cell count (cells mL^{-1})	1.00×10^4	1.31×10^6 (±3.81 × 10^5)	4.99×10^6 (±2.3 × 10^6)	4.06×10^7 (±3.03 × 10^6)	1.28×10^8 (±3.65 × 10^7)	1.79×10^8 (±5.43 × 10^7)
Protein conc. (fg cell^{-1})	n.m.	90.1 (±24.85)	35.7 (±25.93)	15.6 (±0.73)	17.0 (±4.72)	12.4 (±6.06)
PolyP conc. (amol cell^{-1})	n.m.	b.d.l. (±/)	0.265 (±0.191)	1.084 (±0.133)	1.509 (±0.380)	0.980 (±0.412)
PolyP:protein (amol fg^{-1})	n.m.	b.d.l.	0.007	0.069	0.089	0.079

5 mmol sulfur L^{-1}							
Incubation time (h)	0	72	120	144	192	216	240
Total cell count (cells mL^{-1})	4.00×10^4 (±/)	3.09×10^5 (±1.41 × 10^5)	2.09×10^6 (±1.33 × 10^6)	5.74×10^6 (±4.46 × 10^6)	1.7×10^7 (±4.11 × 10^6)	2.11×10^7 (±1.85 × 10^6)	1.94×10^7 (±4.08 × 10^6)
Protein conc. (fg cell^{-1})	n.m.	105.00 (±25.02)	25.3 (±11.42)	32.3 (±22.74)	30.5 (±9.46)	22.2 (±1.53)	24.8 (±3.93)
PolyP conc. (amol cell^{-1})	n.m.	1.925 (n.d.)	0.628 (±0.166)	0.720 (±0.649)	0.508 (±0.079)	0.545 (±0.039)	0.524 (±0.054)
PolyP: protein (amol fg^{-1})	n.m.	0.0183	0.025	0.022	0.017	0.025	0.021

Total cell counts, protein concentration per cell, polyphosphate concentration per cell, and polyphosphate/protein ratios are shown

Protein conc. protein concentration, *PolyP conc.* polyphosphate concentration, *PolyP* polyphosphate, *n.m.* no measurement, *n.d.* not determined, *b.d.l.* below detection limit

For cells grown on thiosulfate the exponential phase was between 60 and 132 h of incubation ($k = 0.066$), while for sulfur cultures the exponential growth phase was between 72 and 144 h ($k = 0.041$). In elemental sulfur incubations, the polyphosphate/protein ratio was nearly constant over time; between 0.017 and 0.025 amol (10^{-18}) fg^{-1}, with a mean polyphosphate enrichment of 0.81 (±0.55) amol per cell. In thiosulfate incubations, the polyphosphate/protein ratio followed the growth curve and increased over time from 0.007 up to 0.089 amol fg^{-1} at the end of the exponential phase (Table 1). Based on a polyphosphate content of 1.51 (±0.38) amol per cell, the maximal polyphosphate enrichment occurred after 132 h of incubation in thiosulfate medium.

Cellular integrity at different cellular polyphosphate concentrations

The theoretical benefit of polyphosphate enrichment could be the maintenance of cellular integrity at nutrient-limited conditions in a pelagic redox zone for a certain time. To gain first insights into this, *S. gotlandica* GD1^T cultures containing high and low cellular polyphosphate concentrations were incubated in electron donor-free media for 90 days and their survival rate determined.

Cells containing high or low amounts of polyphosphate were used (after two washing steps in nutrient-free ABW) at starting densities of 2.0×10^9 cells. The polyphosphate/protein ratio of the polyphosphate-rich approach was 0.049 amol fg^{-1}, with 98% of all DAPI-stained cells containing visible polyphosphate inclusions, and below the detection limit of 0.025 amol fg^{-1} for the polyphosphate-low approach. After 90 days, no polyphosphate was detectable anymore in both approaches. While cell abundances of both groups decreased (initially high-polyphosphate group by 84.0% (±9.0%) and low-polyphosphate group by 99.0% (±0.3%)), a significantly larger number of initially high-polyphosphate-containing cells (Mann–Whitney test, $p < 0.05$; with more than one magnitude difference) maintained visible cellular integrity.

Taken together, our data point to the role of polyphosphate as a cellular energy source under low-nutrient conditions.

Ecological features of *Sulfurimonas gotlandica* GD1^T potentially associated with polyphosphate generation

To reach favorable niches in an unstable environment, *Sulfurimonas* subgroup GD17/GD1^T requires the ability: (1) to identify zones of optimal nutrient conditions and (2) to reach these zones quickly before they disappear. In consequence, both the ability of GD1^T to identify optimal nutrient conditions within a thiosulfate-nitrate gradient and the maximal motility speed achieved were respectively investigated.

Cellular identification of optimal substrate concentrations in a thiosulfate-nitrate gradient

At all electron donor/acceptor concentrations tested in the gradient experiments, *S. gotlandica* GD1[T] formed distinct patterns in the glass tubes after 23 days of incubation. At higher nutrient concentrations, the fractions containing the highest cell abundances generally became proportionally larger, with the cells in those fractions moving towards the KNO_3-containing top agar. Thus, in a gradient system, GD1[T] actively moved and stayed in specific areas favorable for its growth (Supplementary Table S3).

Motility speed of GD1[T] cells

After their incubation for 7 days (late exponential growth phase), motile cells had a mean speed of 15–40 $\mu m\,s^{-1}$ (Supplementary Table S4; independent of the electron acceptor/donor concentration), but reached a maximum speed of 158 $\mu m\,s^{-1}$ (data not shown). There was no significant trend indicating a relationship between electron acceptor/donor concentrations and the speed of the motile cells.

Discussion

Our SEM-EDX analyses showed that *Sulfurimonas* cells became enriched in phosphorus in the form of polyphosphate, as they were detected together with an increase in magnesium and potassium (environmental samples) or calcium (cultures). Negatively charged polyphosphate is typically associated with positively charged ions, with valences of both +1 and +2 [44–46]. Similar EDX results have already been reported for polyphosphate inclusions [47, 48]. In addition, GD1[T] DAPI-stained cells contained bright yellow inclusions and thus differed in their appearance from otherwise blue DAPI-staining cells. This metachromatic shift was due to the interaction of the dye with a polyanionic substance, in this case polyphosphate [49, 50]. While there are alternative, multiple, negatively charged substances possibly explaining this spectral change [48, 51, 52], the combination of phosphorous detected in EDX analyses and the observed metachromatic shift provided reliable evidence that the *Sulfurimonas* inclusions consisted of polyphosphate.

Requirements for polyphosphate accumulation in *S. gotlandica* GD1[T]

Polyphosphate inclusions in cells of *S. gotlandica* strain GD1[T] were also detected in situ, in analyses of environmental samples, thus confirming that our results were not a culture-dependent artifact. However, among all the environmental samples analyzed, in only one such sample (which co-occurred with maximum abundances of the GD17/GD1[T] cluster) was polyphosphate detected in 98.1% of all cells, whereas for all the other samples it was ≤2.1%. The considerably higher cell abundance in this zone suggests that it provides favorable environmental conditions for GD1[T] cells. This was confirmed in the cultivation experiments, in which high concentrations of electron donors resulted in more pronounced polyphosphate inclusions, and low concentrations exhibited either low amounts or no polyphosphate inclusions at all. These results suggested that significant polyphosphate accumulation, evidenced by distinguishable inclusions, occur only under favorable conditions. Yet, while distinguishable inclusions were consistently seen in batch cultures, they were a rare occurrence in environmental samples.

The presence of different available electron donors resulted in different polyphosphate contents in GD1[T] cultures and also in variations of polyphosphate formation timing (Table 1). Polyphosphate accumulation in accordance with the growth phase and available energy source has been demonstrated in other microorganisms [53, 54]. In culture medium containing thiosulfate, polyphosphate was formed during the exponential growth phase. However, as soon as the cells entered stationary phase, the polyphosphate content remained constant or began to decrease. This is probably due to the complete consumption of electron donors during that growth phase [55].

In cultures supplemented with elemental sulfur, the nearly constant amount of polyphosphate may have reflected the fact that elemental sulfur hardly dissolves in pure water and even less in sea water [56]. Under the tested conditions, <10 nmol sulfur L^{-1} is dissolved in ABW medium [57]. Therefore, in addition to growth, polyphosphate production by GD1[T] seems to be highly dependent on the bioavailability of sulfur, such that only bacterial cells in direct contact with sulfur are probably able to produce high-energy-containing polyphosphate.

Thiosulfate was better than elemental sulfur in promoting polyphosphate production by GD1[T] cells. The probable difference can be explained by access to the electron donor, because the formation of high-energy-containing polyphosphate is only possible when an efficient supply is provided. Further investigations using other electron donors such as pyruvate and hydrogen sulfide will provide further insights into the relationship between polyphosphate formation and the availability of suitable electron donors.

Polyphosphate accumulation pathways in *S. gotlandica* GD1[T]

S. gotlandica GD1[T] contains a number of genes associated with both polyphosphate formation and degradation [12]
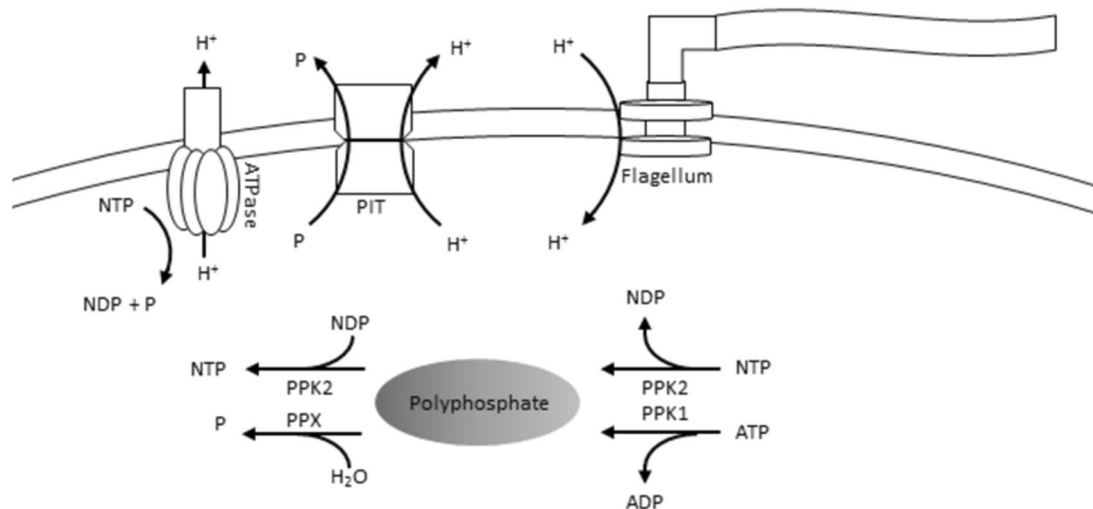
Fig. 5 Hypothesized use of polyphosphate for energy storage and motility of *S. gotlandica* GD1^T cells. Polyphosphate kinase 1 family (*ppk1*) enzymes catalyze the formation of polyphosphate from ATP. Polyphosphate kinase 2 family (*ppk2*) enzymes produce nucleoside triphosphate (NTP) from phosphate and nucleoside diphosphate (NDP). Exopolyphosphatase (*ppx*) hydrolyzes the terminal phosphate from polyphosphate; the low-affinity Pi transport system (PIT) generates a proton-motive force via the symport of polyphosphate and protons

and therefore also has the potential for polyphosphate anabolism and catabolism (Fig. 5). Three of these genes encode polyphosphate kinase enzymes belonging to the type 2 family (*ppk2* [12]) which, unlike the type 1 family (*ppk1*), preferentially degrade polyphosphate to achieve purine phosphorylation [58–60]. One of the *ppk2* genes in the GD1^T genome (NCBI accession: WP_008335082.1) was classified into the PA0141 family (using InterPro66.0), for which the activity has been tested in *Pseudomonas aeruginosa*. This enzyme catalyzes the synthesis of ATP in a reaction in which polyphosphate dephosphorylation is coupled to adenosine diphosphate (ADP) phosphorylation [59]. Another enzyme is an RNA degradosome polyphosphate kinase which is similar to the *ppk1* from *Escherichia coli* [P0A7B1]. The *S. gotlandica* strain GD1^T genome also contains an exopolyphosphatase (*ppx*) that catalyzes the hydrolysis of terminal phosphate residues from polyphosphate chains, as well as enzymes comprising a low-affinity Pi transport system (*Pit*) thought to play a role in the production of energy from polyphosphate through the generation of a proton-motive force [61, 62].

Members of the *Epsilonproteobacteria* isolated from marine sediments were recently shown to utilize all of the above-mentioned genes, particularly *ppk2*, under both anoxic and sulfidic conditions [63]. The authors proposed that these bacteria are able to concurrently engage in sulfur oxidation and polyphosphate degradation [63]. Our results show that the *S. gotlandica* strain GD1^T genome confers other possibilities for polyphosphate utilization which, analogously, may be widely distributed.

Possible implications of polyphosphate accumulation in *Sulfurimonas* GD17/GD1^T cells for their ecology

We hypothesized that *S. gotlandica* GD1^T cells accumulate polyphosphate in overlapping zones of pelagic redox zones where suitable electron acceptors and electron donors co-localize, using this polyphosphate as an energy source to sustain cellular integrity. Currently, the experimental results support important parts of our hypothesis. Specifically, the 90-day incubation experiment demonstrated that polyphosphate inclusions significantly assisted in maintaining the cellular integrity of *S. gotlandica* GD1^T cells under nutrient-limiting conditions for a 3-month time period.

However, more specifically in the context of maintenance energy, it could additionally be hypothesized that the sustainment of cellular integrity also sustains motility to reach new favorable zones under unfavorable conditions. Under nutrient starvation, maintenance energy defined as "…the energy consumed for functions other than the production of new cell material…" [64], including osmoregulation, synthesis of macromolecules, membrane energization and motility, has to be provided by endogenous substrates as, e.g., polyphosphate. It has been shown that prokaryotic cells can maintain motility under nutrient starvation. For instance, *Vibrio anguillarium* can stay motile for up to 8 days under these conditions [65] and *Methanocaldococcus jannaschii* only produces flagella related-polypeptides during energy limitation periods [66]. The reason is probably that motility, especially in combination

with chemotaxis, can improve the supply of catabolites and by this increase cellular fitness [67]. Thus, the maintenance of motility by polyphosphate may also be an important feature for the survival of *S. gotlandica* GD17/GD1^T in pelagic redox zones. In principal, the theoretical benefit of this form of energy storage, if solely used for movement, can be considered. For this we assumed that: (i) the storage of internal polyphosphate based on thiosulfate-grown cultures is between 0.27 and 1.51 amol cell^{-1} (Table 1), (ii) polyphosphate chain lengths are comparable in situ to those used in standard experiments (45 residues), (iii) the energy content of a phosphoric acid bond is 30.5 kJ mol^{-1} and (iv) bacterial swimming efficiency is in the range of 5.1×10^9 m J^{-1} to 7.3×10^9 m J^{-1} [68]. Under these conditions, the resulting maximum migration distance would be 0.2–1.5 cm (Supplementary material, text 1), which is sufficient to overcome small-scale turbulences. This hypothesis would be supported by the fact that GD1^T cells can, independent of their supply of electron donors and acceptors and the range of substrate concentrations tested, swim fast, with nearly 160 µm s^{-1}, thus enabling the cells to reach favorable zones quickly (Supplementary Table S4). Finally, it was shown that GD1^T cells can indeed actively localize these zones (Supplementary Table S3), probably based on chemotaxis towards nitrate [12].

The redox zone of the Baltic Sea is characterized by a changing redox potential induced by local mixing events [15] which introduce nitrate-containing water masses into sulfidic zones and vice versa. Given this turbulent environment, the ability to store polyphosphate to maintain cellular integrity, and potentially linked to motility, and thus improve localization would provide a valuable survival advantage and can therefore be considered a valuable niche adaption for motile bacteria in pelagic Baltic Sea redox zones. In fact, a comparative analysis of the functional capacity of Landsort Deep metagenomes showed that the proportion of genes responsible for chemotaxis and movement was much higher in cells from hypoxic water masses than in those from other ecosystems also characterized by redox gradients [69]. Even in ecosystems where there is no redox gradient, the micro-scale patchiness of available nutrients results in differences in bacterioplankton assemblages at a millimeter scale [70]. The adoption of a chemotactic response to micro-scale perturbations was previously shown to provide a significant advantage for heterotrophs, by enabling a much higher exposure to nutrients [71]. Our results could present a similar case for the chemolithoautotrophic bacteria that occupy redox gradients within eutrophic ecosystems perturbed by temporally and spatially limited mixing events; future analyses should especially aim to directly confirm this hypothesis with regard to maintenance of motility.

Conclusion

Our study demonstrated the storage of inorganic polyphosphate by cells of *Sulfurimonas* subgroup GD17/GD1^T cells, both in vitro and in situ. However, in environmental samples, polyphosphate storage was detected only in cells inhabiting a zone close to the chemocline and present in considerably higher abundances than in other parts of the redox zone. These results suggest that: (i) polyphosphate accumulates only under favorable conditions, defined as the exposure to sufficient amounts of electron acceptors/donors and (ii) that polyphosphate is used to maintain cellular integrity. This redox-independent energy supply could be a prerequisite for the maintenance of the *r*-strategy lifestyle of *Sulfurimonas* subgroup GD17/GD1^T and may generally represent a newly identified survival strategy for chemolithoautotrophic prokaryotes occupying eutrophic redox zones.

Compliance with ethical standards

Conflict of interest The authors declare that they have no conflict of interest.

References

1. Carstensen J, Andersen JH, Gustafsson BG, Conley DJ. Deoxygenation of the Baltic Sea during the last century. Proc Natl Acad Sci USA. 2014;111:5628–33.
2. Conley DJ, Björck S, Bonsdorff E, Carstensen J, Destouni G, Gustafsson BG, et al. Hypoxia-related processes in the Baltic Sea. Environ Sci Technol. 2009;43:3412–20.
3. Jørgensen BB, Fossing H, Wirsen CO, Jannasch HW. Sulfide oxidation in the anoxic Black Sea chemocline. Deep Sea Res Part 1 Oceanogr Res Pap. 1991;38:1083–103.
4. Taylor GT, Iabichella M, Ho TY, Scranton MI, Thunell RC, Muller-Karger F, et al. Chemoautotrophy in the redox transition zone of the Cariaco Basin: a significant mid-water source of organic carbon production. Limnol Oceanogr. 2001;46:148–63.
5. Brettar I, Rheinheimer G. Denitrification in the central Baltic: evidence for H$_2$S-oxidation as motor of denitrification at the oxic-anoxic interface. Mar Ecol Prog Ser. 1991;77:157–69.
6. Brüchert V, Jørgensen BB, Neumann K, Riechmann D, Schlösser M, Schulz H. Regulation of bacterial sulfate reduction and hydrogen sulfide fluxes in the central Namibian coastal upwelling zone. Geochim Chosmochim Acta. 2003;67:4505–18.
7. Canfield DE, Stewart FJ, Thamdrup B, De Brabandere L, Dalsgaard T, DeLong EF, et al. A cryptic sulfur cycle in oxygen-

minimum-zone waters off the Chilean Coast. Science. 2010;330:1375–8.

8. Lam P, Kuypers MM. Microbial nitrogen cycling processes in oxygen minimum zones. Ann Rev Mar Sci. 2011;3:317–45.

9. Grote J, Labrenz M, Pfeiffer B, Jost G, Jürgens K. Quantitative distributions of *Epsilonproteobacteria* and a *Sulfurimonas* subgroup in pelagic redoxclines of the central Baltic Sea. Appl Environ Microbiol. 2007;73:7155–61.

10. Labrenz M, Brettar I, Christen R, Flavier S, Botel J, Höfle MG. Development and application of a real-time PCR approach for quantification of uncultured bacteria in the central Baltic Sea. Appl Environ Microbiol. 2004;70:4971–9.

11. Brettar I, Labrenz M, Flavier S, Botel J, Kuosa H, Christen R, et al. Identification of a *Thiomicrospira denitrificans*-like epsilonproteobacterium as a catalyst for autotrophic denitrification in the central Baltic Sea. Appl Environ Microbiol. 2006;72:1364–72.

12. Grote J, Schott T, Bruckner CG, Glöckner FO, Jost G, Teeling H, et al. Genome and physiology of a model Epsilonproteobacterium responsible for sulfide detoxification in marine oxygen depletion zones. Proc Natl Acad Sci USA. 2012;109:506–10.

13. Rogge A, Vogts A, Voss M, Jürgens K, Günter J, Labrenz M. NanoSIMS analyses reveal different lifestyles of chemolithoautotrophic SUP05 and *Sulfurimonas* GD17 cells in a pelagic Baltic Sea redox zone. Env Microbiol. 2017;19:2495–506.

14. Labrenz M, Grote J, Mammitzsch K, Boschker HTS, Laue M, Jost G, et al. *Sulfurimonas gotlandica* sp. nov., a chemoautotrophic and psychrotolerant epsilonproteobacterium isolated from a pelagic redoxcline, and an emended description of the genus *Sulfurimonas*. Int J Syst Evol Micr. 2013;63:4141–8.

15. Axell LB. On the variability of Baltic Sea deepwater mixing. J Geophys Res Oceans. 1998;103:21667–82.

16. Otte S, Kuenen JG, Nielsen LP, Paerl HW, Zopfi J, Schulz HN, et al. Nitrogen, carbon, and sulfur metabolism in natural *Thioploca* samples. Appl Environ Microbiol. 1999;65:3148–57.

17. Pasteris JD, Freeman JJ, Goffredi SK, Buck KR. Raman spectroscopic and laser scanning confocal microscopic analysis of sulfur in living sulfur-precipitating marine bacteria. Chem Geol. 2001;180:3–18.

18. Preisler A, De Beer D, Lichtschlag A, Lavik G, Boetius A, Jørgensen BB. Biological and chemical sulfide oxidation in a *Beggiatoa* inhabited marine sediment. ISME J. 2007;1:341–53.

19. Schulz HN. The genus *Thiomargarita*. In: Dworkin M, Falkow S, Rosenberg E, Schleifer K-H, Stackebrandt E, editors. The prokaryotes. New York: Springer; 2006. p. S. 1156–63.

20. Brock J, Schulz-Vogt HN. Sulfide induces phosphate release from polyphosphate in cultures of a marine *Beggiatoa* strain. ISME J. 2011;5:497–506.

21. Harold FM. Depletion and replenishment of the inorganic polyphosphate pool in *Neurospora crassa*. J Bacteriol. 1962;83:1047–57.

22. Kornberg A. Inorganic polyphosphate: toward making a forgotten polymer unforgettable. J Bacteriol. 1995;177:491–6.

23. Baker AL, Schmidt RR. Induced utilization of polyphosphate during nuclear division in synchronously growing. Chlorella BBA Gen Subj. 1964;93:180–2.

24. Hsieh PC, Shenoy BC, Haase FC, Jentoft JE, Phillips NF. Involvement of tryptophan(s) at the active site of polyphosphate/ATP glucokinase from *Mycobacterium tuberculosis*. Biochemistry. 1993;32:6243–9.

25. Skorko R. Polyphosphate as a source of phosphoryl group in protein modification in the archaebacterium *Sulfolobus acidocaldarius*. Biochimie. 1989;71:1089–93.

26. Ault-Riché D, Fraley CD, Tzeng C-M, Kornberg A. Novel assay reveals multiple pathways regulating stress-induced accumulations of inorganic polyphosphate in *Escherichia coli*. J Bacteriol. 1998;180:1841–7.

27. Rao NN, Kornberg A. Inorganic polyphosphate supports resistance and survival of stationary-phase *Escherichia coli*. J Bacteriol. 1996;178:1394–400.

28. Sureka K, Dey S, Datta P, Singh AK, Dasgupta A, Rodrigue S, et al. Polyphosphate kinase is involved in stress-induced *mprAB-sigE-rel* signalling in mycobacteria. Mol Microbiol. 2007;65:261–76.

29. Kim HY, Schlictman D, Shankar S, Xie Z, Chakrabarty AM, Kornberg A. Alginate, inorganic polyphosphate, GTP and ppGpp synthesis co-regulated in *Pseudomonas aeruginosa*: implications for stationary phase survival and synthesis of RNA/DNA precursors. Mol Microbiol. 1998;27:717–25.

30. Pick U, Chitlaru E, Weiss M. Polyphosphate-hydrolysis-a protective mechanism against alkaline stress? FEBS Lett. 1990;274:15–8.

31. Blum E, Py B, Carpousis AJ, Higgins CF. Polyphosphate kinase is a component of the *Escherichia coli* RNA degradosome. Mol Microbiol. 1997;26:387–98.

32. Bonting CF, Kortstee GJ, Zehnder AJ. Properties of polyphosphate: AMP phosphotransferase of *Acinetobacter* strain 210A. J Bacteriol. 1991;173:6484–8.

33. Seufferheld MJ, Alvarez HM, Farias ME. Role of polyphosphates in microbial adaptation to extreme environments. Appl Environ Microbiol. 2008;74:5867–74.

34. Varela C, Mauriaca C, Paradela A, Albar JP, Jerez CA, Chávez FP. et al. New structural and functional defects in polyphosphate deficient bacteria: a cellular and proteomic study. BMC Microbiol. 2010;10:7

35. Rivas-Lamelo S, Benzerara K, Lefèvre CT, Monteil CL, Jézéquel D, Menguy N. et al. Magnetotactic bacteria as a new model for P sequestration in the ferruginous Lake Pavin. Geochem Persp Let. 2017;5:35–41.

36. Jost G, Zubkov MV, Yakushev E, Labrenz M, Jürgens K. High abundance and dark CO_2 fixation of chemolithoautotrophic prokaryotes in anoxic waters of the Baltic Sea. Limnol Oceanogr. 2008;53:14–22.

37. Laas P, Šatova E, Lips I, Lips U, Simm J, Kisand V, et al. Near-bottom hypoxia impacts dynamics of bacterioplankton assemblage throughout water column of the Gulf of Finland (Baltic Sea). PloS ONE. 2016;11:e0156147.

38. Bruns A, Cypionka H, Overmann J. Cyclic AMP and acyl homoserine lactones increase the cultivation efficiency of heterotrophic bacteria from the central Baltic Sea. Appl Environ Microbiol. 2002;68:3978–87.

39. Martin P, Van Mooy BA. Fluorometric quantification of polyphosphate in environmental plankton samples: extraction protocols, matrix effects, and nucleic acid interference. Appl Environ Microbiol. 2013;79:273–81.

40. Kulakova AN, Hobbs D, Smithen M, Pavlov E, Gilbert JA, Quinn JP, et al. Direct quantification of inorganic polyphosphate in microbial cells using 4′-6-diamidino-2-phenylindole (DAPI). Environ Sci Technol. 2011;45:7799–803.

41. Fischer JP, Cypionka H. Analysis of aerotactic band formation by *Desulfovibrio desulfuricans* in a stopped-flow diffusion chamber. FEMS Microbiol Ecol. 2006;55:186–94.

42. Adler J, Dahl MM. A method for measuring the motility of bacteria and for comparing random and non-random motility. J Gen Microbiol. 1967;46:161–73.

43. Grote J, Jost G, Labrenz M, Herndl GJ, Jürgens K. *Epsilonproteobacteria* represent the major portion of chemoautotrophic bacteria in sulfidic waters of pelagic redoxclines of the Baltic and Black Seas. Appl Environ Microbiol. 2008;74:7546–51.

44. Friedberg I, Avigad G. Structures containing polyphosphate in *Micrococcus lysodeikticus*. J Bacteriol. 1968;96:544–53.

45. Morrissey JH, Choi SH, Smith SA. Polyphosphate: an ancient molecule that links platelets, coagulation, and inflammation. Blood. 2012;119:5972–9.

46. Peverly JH, Adamec J, Parthasarathy MV. Association of potassium and some other monovalent cations with occurrence of polyphosphate bodies in *Chlorella pyrenoidosa*. Plant Physiol. 1978;62:120–6.

47. Gomes F, Ramos I, Wendt C, Girard-Dias W, De Souza W, Machado EA, et al. New insights into the *in situ* microscopic visualization and quantification of inorganic polyphosphate stores by 4', 6-diamidino-2-phenylindole (DAPI)-staining. Eur J Histochem. 2013;57:227–5.

48. Liu WT, Nielsen AT, Wu JH, Tsai CS, Matsuo Y, Molin S. *In situ* identification of polyphosphate-and polyhydroxyalkanoate-accumulating traits for microbial populations in a biological phosphorus removal process. Environ Microbiol. 2001;3:110–22.

49. Kulaev IS, Vagabov VM, Kulakovskaya TV. Localization of polyphosphates in cells of prokaryotes and eukaryotes. In: Kulaev IS, Vagabov VM, Kulakovskaya TV, editors. The biochemistry of inorganic polyphosphates. 2nd ed. Chichester: John Wiley & Sons; 2004. p. 53–4.

50. Tijssen JPF, Beekes HW, Van Steveninck J. Localization of polyphosphates in *Saccharomyces fragilis*, as revealed by 4', 6-diamidino-2-phenylindole fluorescence. BBA-Mol Cell Res. 1982;721:394–8.

51. Kolozsvari B, Parisi F, Saiardi A. Inositol phosphates induce DAPI fluorescence shift. Biochem J. 2014;460:377–85.

52. Streichan M, Golecki JR, Schön G. Polyphosphate-accumulating bacteria from sewage plants with different processes for biological phosphorus removal. FEMS Microbiol Ecol. 1990;6:113–24.

53. Chávez FP, Lünsdorf H, Jerez CA. Growth of polychlorinated-biphenyl-degrading bacteria in the presence of biphenyl and chlorobiphenyls generates oxidative stress and massive accumulation of inorganic polyphosphate. Appl Environ Microbiol. 2004;70:3064–72.

54. Clark JE, Beegen H, Wood HG. Isolation of intact chains of polyphosphate from" *Propionibacterium shermanii*" grown on glucose or lactate. J Bacteriol. 1986;168:1212–9.

55. Mammitzsch K, Jost G, Jürgens K. Impact of dissolved inorganic carbon concentrations and pH on growth of the chemolithoautotrophic epsilonproteobacterium *Sulfurimonas gotlandica* GD1^T. MicrobiologyOpen. 2014;3:80–88.

56. Tebbe FN, Wasserman E, Peet WG, Vatvars A, Hayman AC. Composition of elemental sulfur in solution: equilibrium of S6, S7 and S8 at ambient temperatures. J Am Chem Soc. 1982;104:4971–2.

57. Kamyshny JrA. Solubility of cyclooctasulfur in pure water and sea water at different temperatures. Geochim Cosmochim Acta. 2009;73:6022–8.

58. Ahn K, Kornberg A. Polyphosphate kinase from *Escherichia coli*. Purification and demonstration of a phosphoenzyme intermediate. J Biol Chem. 1990;265:11734–9.

59. Motomura K, Hirota R, Okada M, Ikeda T, Ishida T, Kuroda A. A new subfamily of polyphosphate kinase 2 (class III PPK2) catalyzes both nucleoside monophosphate phosphorylation and nucleoside diphosphate phosphorylation. Appl Environ Microbiol. 2014;80:2602–8.

60. Sureka K, Sanyal S, Basu J, Kundu M. Polyphosphate kinase 2: a modulator of nucleoside diphosphate kinase activity in mycobacteria. Mol Microbiol. 2009;74:1187–97.

61. Kawakoshi A, Nakazawa H, Fukada J, Sasagawa M, Katano Y, Nakamura S, et al. Deciphering the genome of polyphosphate accumulating actinobacterium *Microlunatus phosphovorus*. DNA Res. 2012;19:383–94.

62. Saunders AM, Mabbett AN, McEwan AG, Blackall LL. Proton motive force generation from stored polymers for the uptake of acetate under anaerobic conditions. FEMS Microbiol Lett. 2007;274:245–51.

63. Jones DS, Flood BE, Bailey JV. Metatranscriptomic insights into polyphosphate metabolism in marine sediments. ISME J. 2016;10:1015–9.

64. Pirt SJ. Maintenance energy of bacteria in growing cultures. Proc R Soc Lond B Biol Sci. 1965;163:224–31.

65. Larsen MH, Blackburn N, Larsen JL, Olsen JE. Influences of temperature, salinity and starvation on the motility and chemotactic response of *Vibrio anguillarum*. Microbiology. 2004;150:1283–90.

66. Mukhopadhyay B, Johnson EF, Wolfe RS. A novel p$_{H2}$ control on the expression of flagella in the hyperthermophilic strictly hydrogenotrophic methanarchaeaon *Methanococcus jannaschii*. Proc Natl Acad Sci USA. 2000;97:11522–7.

67. Stocker R, Seymour JR, Samadani A, Hunt DE, Polz MF. Rapid chemotactic response enables marine bacteria to exploit ephemeral microscale nutrient patches. Proc Natl Acad Sci USA. 2008;105:4209–14.

68. Li G, Tang JX. Low flagellar motor torque and high swimming efficiency of *Caulobacter crescentus* swarmer cells. Biophys J. 2006;91:2726–34.

69. Thureborn P, Lundin D, Plathan J, Poole AM, Sjöberg B-M, Sjöling S. A metagenomics transect into the deepest point of the Baltic Sea reveals clear stratification of microbial functional capacities. PLOS ONE. 2013;8:e74983.

70. Long RA, Azam F. Antagonistic interactions among marine pelagic bacteria. Appl Environ Microbiol. 2001;67:4975–83.

71. Stocker R. Marine microbes see a sea of gradients. Science. 2012;338:628–33.

Supplementary Information

for

Paper AI

Supplementary material
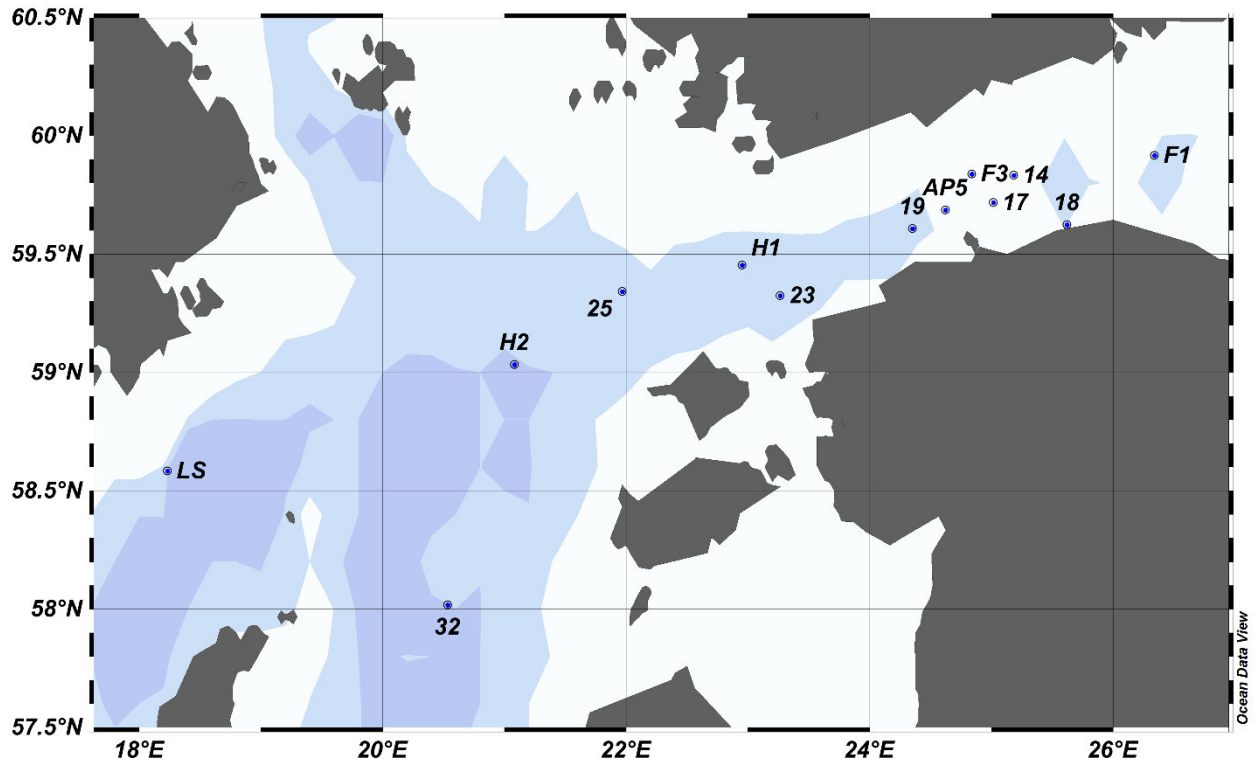
Supplementary Figure 1. Map of the study area central and eastern Baltic Sea. Latitude and longitude of stations sampled are given in Supplementary Table 1.

7   **Supplementary Table 1.** Latitude and longitude of stations sampled in the Baltic Sea.

Station	Date	Latitude (decimal degrees)	Longitude (decimal degrees)
F1	16.07.2017	59.91633	26.33980
14	16.07.2017	59.83315	25.18315
18	17.07.2017	59.62466	25.62069
17	16.07.2017	59.71772	25.01683
F3	16.07.2017	59.83872	24.83802
AP5	16.07.2017	59.68698	24.62341
19	16.07.2017	59.60833	24.35144
23	14.07.2017	59.32377	23.26534
H1	14.07.2017	59.45345	22.95264
25	14.07.2017	59.34195	21.96738
H2	14.07.2017	59.03317	21.08257
32	14.07.2017	58.01705	20.53432
LS	31.08.2015	58.583611	18.231389

8

9

10 **Supplementary Table 2.** *Sulfurimonas* GD1^T/GD17 subgroup cell abundances, determined by
11 CARD-FISH analyses using gene probe Sul90, within and outside the HNA-hs cluster P2 isolated
12 from a vertical profile of the Landsort Deep of different H$_2$S concentrations.

Depth (m)	*Sulfurimonas* GD1^T/GD17 subgroup cells in control cluster (%)	*Sulfurimonas* GD1^T/GD17 subgroup cells in cluster P2 (%)	H$_2$S (µmol L^{-1})
47	0.7	ND	0
68.5	1.2	ND	0
68.8	2.1	ND	1.5
76	0	97.0	6.8
280	0	93.8	36.1
435	0	17.2	26.8

13

14

15

Supplementary Table 3. The distribution of relative *S. gotlandica* strain GD1^T cell abundances

in a gradient experiment shows distinct cell enrichments at different nutrient concentrations after

23 days of incubation. Smaller fraction numbers indicate a closer location to the KNO$_3$ top agar,

larger fraction numbers a closer location to the Na$_2$S$_2$O$_3$ bottom agar. Dark gray areas indicate the

fractions of highest abundance in each approach.

Relative abundance of *S. gotlandica* strain GD1^T cells in gradient medium fractions (%)

KNO$_3$	(1 mmol L^{-1})	(5 mmol L^{-1})	(10 mmol L^{-1})	(100 mmol L^{-1})
Fraction 1	8.2	1.5	3.9	10.0
Fraction 2	7.2	3.6	15.5	18.3
Fraction 3	8.8	14.3	29.2	17.7
Fraction 4	5.4	27.3	15.5	14.2
Fraction 5	15.3	14.6	10.0	17.3
Fraction 6	36.0	8.5	14.4	3.9
Fraction 7	10.1	18.9	4.9	6.2
Fraction 8	9.1	11.3	6.5	12.6
Na$_2$S$_2$O$_3$	(1 mmol L^{-1})	(5 mmol L^{-1})	(10 mmol L^{-1})	(100 mmol L^{-1})

22

23

24 **Supplementary Table 4.** Average and median speed of *S. gotlandica* strain GD1^T cells

25 cultivated for 7 days in different concentrations of electron donors and acceptors. 436 cells

26 measured in total.

27

Nutrient concentration Na$_2$S$_2$O$_3$ / KNO$_3$ (mmol L^{-1})	10	5	1	0.5	0.1	0.01
Average cell speed (µm s^{-1})	20.9	29.8	15.6	17.3	38.8	25.5
Median cell speed (µm s^{-1})	16.8	22.8	12.4	15.8	20.3	23.8
Standard deviation	14.1	19.0	8.2	5.5	34.1	6.1
Number of cells analysed	137	255	13	8	7	16

28

29

30   **Supplementary text 1**. Calculations for theoretical migration distances for *Sulfurimonas*
31   *gotlandica* GD1^T using only polyphosphate in quantities that were observed during this study.

32

33   I: ATP_{PolyP} $[mol]$ = max $PolyP$ content $[mol] x$ phosphoric acid bounds per $PolyP - chain$

34   I: $ATP_{PolyP}[mol] = 1.51 \ x \ 10^{-18} \ [mol] \ x \ 44 = \ 6.64 \ x \ 10^{-17} \ [mol]$

35   II: $E_{PolyP}[J] = ATP_{PolyP} \ [mol] \ x \ \Delta G^0{}_{ATP} \ [J \ x \ mol^{-1}]$

36   II: $E_{PolyP}[J] = \ 6.64 \ x \ 10^{-17} \ [mol] \ x \ 30500 \ [J \ x \ mol^{-1}] = \ 2.03 \ x \ 10^{-12} \ [J]$

37   III: $s_{PolyP}[m] = \ E_{PolyP}[J] \ x \ \varepsilon \ [m \ x \ J^{-1}]$

38   IIIa: $s_{PolyP}[m] = \ 2.03 \ x \ 10^{-12} \ [J] \ x \ 7.3 \ x \ 10^9 \ [m \ x \ J^{-1}] = 0.015 \ [m]$

39   IIIb: $s_{PolyP}[m] = \ 2.03 \ x \ 10^{-12} \ [J] \ x \ 5.1 \ x \ 10^9 \ [m \ x \ J^{-1}] = 0.010 \ [m]$

40   ATP_{PoyP} = amount of ATP that can be formed out of polyphosphate

41   E_{PolyP} = energy content of the ATP that could be formed out of polyphosphate

42     $\Delta G^0{}_{ATP}$ = free energy of the reaction from ATP to ADP and P

43   ε = moving efficiency in the range of 5.1×10^9 [m J^{-1}] to 7.3×10^9 [m J^{-1}]

44   S_{PolyP} = distance that can be traveled by the energy from polyphosphate

45

46

Supplementary Methods

DAPI staining

To determine growth of the cultures, cell numbers were observed using DAPI staining. In short, cell suspension was mixed with 1/10 vol. formaldehyde (37 wt. %) to a final concentration of 3.36%. After 1 hour of fixation at room temperature in the dark, cells were filtered on a 0.2 μm filter (Whatman CyclPR Track Etched Membrane). Filters were stained with 36 mmol L^{-1} DAPI solution for 2 minutes and cells were counted in a fluorescence microscope (Zeiss, Axio Lab A1). At least 1,000 cells were counted at different spots of the filter and numbers were used to calculate cell density.

Polyphosphate identification in **S. gotlandica** *strain GD1^T*

S. gotlandica strain GD1^T was cultivated in acid cleaned glass tubes with 10 mL artificial brackish water. 1 of 2 electron donors were applied in 2 different concentrations: thiosulfate (10 mmol L^{-1} or 100 μmol L^{-1}) and elemental sulfur (5 mmol L^{-1} or 100 μmol L^{-1}). Growth dynamics were observed using DAPI-counting on a 2-day basis to determine the beginning of the stationary phase. In addition, stained cells were visibly checked for yellow inclusions in their cell bodies and their relative proportion on cell numbers determined. After reaching stationary phase, cells were filtered on 0.2 μm filters (Whatman CyclPR Track Etched Membrane BL Ø25mm, 7063-2502) and stained with DAPI. On the filters, single cells showing yellow-colored inclusions were spotted and marked with a laser in a Laser Microdissection Microscope (Leica LMD7000). For the analysis of potential nutrient storage (using SEM-EDX), marked filters were sputter-coated with chrome (Cressington H208) for 300 s at 80 mA resulting in a coating thickness of about 2 nm. The coated samples were checked using both an electron microscope (Zeiss, Merlin VP

70   Compact, 10 kV acceleration voltage, SE-Detector) and an EDX-detector (EDX-Detector Flash,

71   80 mm², peltier cooled, 8.5 mm working distance, 1 µm resolution at 30 kV, residence time of

72   150 µs/pixel, AZtex oxford system) to generate RX-distribution images and elemental line scans

73   of the marked cells.

74   ***Polyphosphate and protein quantification of* S. gotlandica *strain GD1ᵀ in different***

75   ***growth phases***

76   16 acid cleaned 250 mL bottles were filled with 100 mL anoxic ABW as described above and

77   were prepared with either 5 mmol L⁻¹ sulfur or 10 mmol L⁻¹ thiosulfate. Cultures were checked

78   for growth on a daily basis using DAPI staining. At different growth stages in the exponential and

79   stationary phase, 3 bottles were prepared for polyphosphate and protein quantification.

80   Polyphosphate quantification was based on Martin and van Mooy (2013) with a slight

81   modification in buffer composition according to Kulakova *et al.* (2011). Cells from different

82   growth stages were collected by centrifugation of 45 mL medium at 13 000 g for 30 minutes at 4

83   °C. Supernatant was removed by pipetting. Cells were resuspended in 3 mL sterile 0.9% NaCl-

84   solution. 1.5 mL of the suspension was transferred into a low DNA-binding tube and then

85   centrifuged again. The supernatant was removed and cells were stored at -80 °C until further

86   usage.

87   For polyphosphate and protein quantification, cells were resuspended in 200 µL HEPES-buffer

88   (Kulakova *et al.*, 2011). Half of the suspension was transferred into another tube and stored at

89   -20 °C for maximum 24 h for subsequent protein measurement. 1 spatula point of glass beads

90   (Ø 0.1 mm) was added to the cells. The cells were vortexed for 3 minutes at 2850 rpm (Disrupter

91   Genie, Scientific Industries). The mixture was boiled at 100 °C in a water bath for 5 minutes and

92   then kept on ice for further 5 minutes. 5 µl of DNaseI/RNaseTI-Mix (Roche Diagnostics Gmbh/

93   Life Technologies) were added (5/100 units per sample). The suspension was incubated at 37 °C

94   for 10 minutes while mixing at 300 rpm (Eppendorf Thermomixer Compact). Following this, 5 µl

95   of Proteinase K (Amresco) was added (100 µg per sample) and the tube was again incubated for

96   10 minutes at 37 °C while mixing at 300 rpm. The tubes were centrifuged at 10 000 x g for 3

97   minutes (Eppendorf Mini-Spin-Plus) and the clear supernatant, containing the polyphosphate,

98   was measured. For this measurement, 42 µl of clear supernatant were transferred into a well of a

99   low DNA binding microtiter plate (96 WELL Microplatte, µclear, black, Omnilab, No. 6468012).

100   5 µl of 3.61 mmol L^{-1} DAPI solution was placed onto the wall of each well. Then 250 µl of buffer

101   was added to each well. The plate was inserted into the plate reader (TECAN infinite 200 PRO®)

102   and was shaken in linear mode for 420 seconds and 3 mm amplitude at 452 rpm. The

103   fluorescence was measured with an excitation of 415 nm and an emission length of 500 nm. For

104   absolute quantification a standard was prepared in parallel containing between 14 µmol L^{-1} and

105   0.21 µmol L^{-1} polyphosphate 45 (chain length of 45 ±5 phosphate groups).

106   For protein quantification, cells were disrupted using glass beads and boiling, as described above.

107   The mixture was centrifuged at 3500 rpm for 5 minutes and supernatant was measured using the

108   Bio-Rad Quick Start^{TM} Bradford Protein Assay. Serum albumin in a range of 0-20 µg mL^{-1}

109   served as a reference.

110   ***Behaviour of* S. gotlandica *strain GD1^T in thiosulfate-nitrate gradient***

111   This test was used to demonstrate the behavior of GD1^T in electron donor and acceptor gradients,

112   simulating a possible natural scenario. 80 mL MilliQ water was mixed with 2.7 g agar for the

113   solid-top medium and 0.9 g agar was mixed with 100 mL MilliQ water for the semi-solid

114   medium. The solutions were autoclaved and kept at 80 °C until further usage. In parallel, ABW

115   water was prepared as described above and was supplemented with all the additional solutions for

116 cultivating (except nitrate and thiosulfate). The solid agar was then mixed with 80 mL of the

117 prepared ABW medium resulting in final agar content of 1.5% w/v and the semi-solid agar

118 solution was mixed with 260 mL ABW medium to a final concentration of 0.25% w/v agar. The

119 solid agar medium was then supplemented with the electron donor and 1 of 4 different electron-

120 acceptor concentrations. The concentrations used were 1 mmol L^{-1}, 5 mmol L^{-1}, 10 mmol L^{-1} and

121 100 mmol L^{-1}.

122 4 mL of solid agar medium containing thiosulfate were transferred into cleaned, sterile glass

123 tubes. After cooling, 8 mL of semi-solid agar medium was added on top. After 15 minutes of

124 cooling, the medium was incubated with 0.5 mL of GD1^T culture. Following this, 4 mL of solid

125 media, containing nitrate in the same concentration as thiosulfate in the bottom agar, was placed

126 on top. This resulted in test tubes with semi-solid agar in the middle flanked by solid-top agar

127 containing nitrate and solid bottom agar containing thiosulfate. The tubes were incubated for 23

128 days. After the incubation, the tubes were opened and the semi-solid medium was divided into 8

129 × 1 mL sections. Cell counts in these layers were determined using DAPI staining as described

130 previously.

131 **Influence of polyphosphate inclusions on GD1^T cell integrity**

132 This test was designed based on Adler and Dahl (1967) and the already described gradient

133 experiment to examine the influence of different polyphosphate concentration on cellular

134 integrity. The solid ABW- and semi-solid ABW-medium was prepared as described earlier. The

135 solid ABW contained no electron donor and KNO$_3$ in a final concentration of 1 mmol L^{-1}. The

136 semi-solid ABW contained no electron donor nor acceptor. Sterile glass tubes with a diameter of

137 1 cm and a length of 29 cm were sealed on one end with parafilm and isolation tape. Under

138 anaerobic conditions, 3 mL of solid ABW-Medium (at 80 °C) was poured into the tubes. After

139 cooling and hardening, the tubes were filled with 29 mL of semi-solid ABW. The tubes were

140 stored for 1 day at 15 °C in an anoxic atmosphere before inoculation with cells so a nitrate

141 gradient could establish in the tubes.

142 For inoculation, *S. gotlandica* strain GD1^T cells were cultivated in 1 L bottles with 400 mL APW

143 using potassium nitrate (10 mmol L^{-1}) as the electron donor and sodium thiosulfate (in 2 different

144 concentrations) as the electron acceptor. For generation of cells with low polyphosphate content,

145 100 µmol L^{-1} thiosulfate was applied, whilst for high polyphosphate content, 10 mmol L^{-1} was

146 applied. When the stationary phase was reached, 80 mL medium was used for polyphosphate and

147 protein quantification as described above. 160 mL of suspension was centrifuged in

148 polycarbonate vials at 13,000 g for 5 minutes and the medium was removed by decantation. A

149 second 160 mL cell-suspension was then centrifuged in the same vial. The cell pellet was washed

150 in 10 mL anaerobic APW-Medium without any electron acceptor or donor and centrifuged again.

151 Medium was again removed and the cell pellet was resuspended in 500 µL anaerobic APW (no

152 NO$_3^-$, no S$_2$O$_3^{2-}$) for cells grown in 100 µmol L^{-1} thiosulfate and in 2000 µL for cells grown in 10

153 mmol L^{-1} thiosulfate. The suspended cells were pipetted on top of the glass tube containing the

154 soft agar medium. The volume was adjusted so that the same amount of cells (approximately

155 2x10^9 cells) were applied into every tube. Tubes were then sealed using parafilm and isolation

156 tape. The tube was placed upside down resulting in the nitrate containing solid agar on top and

157 the GD1^T cells at the bottom. Finally, the tubes were incubated for 90 days in an anoxic

158 atmosphere, at 15 °C in the dark. After incubation, tubes were split in 2 cm sections and the semi-

159 solid agar of each part was prepared for DAPI counting as described above.

160

161 ***Sampling and flow-cytometric cell sorting from environmental samples***

162   Water samples from the Gulf of Finland were collected on aboard the R/V Salme in July of 2014

163   and from the Landsort Deep with R/V Poseidon in August of 2015 (Supplementary Figure S1).

164   The flow cytometry samples were fixed with paraformaldehyde and glutaraldehyde (final

165   concentrations 1% and 0.05%, respectively; pH = 7.4) and incubated at 4 °C for 60 minutes. The

166   samples were preserved in DMSO (with a final concentration of 15%) and stored at – 80 °C.

167   In the laboratory, water samples were slowly thawed at 4 °C. The samples for EDX-analysis were

168   gently mixed with 1:10 volume of sterile filtered formaldehyde (37%) to a final concentration of

169   3.36%; this step was skipped for samples used to verify the presence of *S. gotlandica* GD1^{T}.

170   After incubation (for 1 hour in the dark at room temperature), the cells were stained with

171   SYBRGreen^{TM} I. Therefore 5 µL of SYBRGreen^{TM} I 10,000x (InVitrogen) were mixed with 1445

172   µL Potassium citrate and DMSO solution (235.8 mmol L^{-1} and 16.955% respectively). Then 11

173   µL of the resulting staining solution were mixed with the 100 µL sample and incubated for 30

174   minutes in the dark. For cell sorting, a BD FACSAria^{TM} III was used with an excitation laser at

175   488 nm and a 530/30 detector for the fluorescence signal coupled with a 502 LP-filter. The side

176   scatter was detected with a 488/10 detector. The events were separated by both their fluorescence

177   signal and their side scatter (Fig. B1). Events with a high side scatter were assumed to be GD1^{T}

178   (P2 group in Fig. B1). GD1^{T} cells and non GD1^{T} cells were sorted and between 500,000 to

179   1,000,000 cells were collected in 2 mL Eppendorf tubes.

180   ***Preparation of sorted clusters for PCR***

181   The 2 mL centrifugation tubes containing sorted cells were centrifuged at 12 000 x g for 9

182   minutes. Most of the supernatant was discarded (5 – 10 µL left). Following this, a mix was

183   prepared consisting of 13 µL Smart-Taq Hot Red 2X PCR Mix (Naxo, Estonia), 3 µL of each

184   universal bacterial primer (BSF8 and BSR357; see Hamady *et al*., 2008; McKenna *et al*., 2008)

185 complimented with 8 nt index and Illumina adapter sequences with final concentration of 0.2

186 µmol L^{-1} of each primer. This mix was added to the sorted cell pellets and the mixture was

187 centrifuged for 1 minute before being transferred to 0.2 mL reaction tubes. Reaction volumes

188 were unified to 26 µL by adding MilliQ water and PCR was undertaken as described by Laas *et*

189 *al.* (2016).

190 ***Polyphosphate detection in GD1^T cells from environmental samples***

191 Some of the sorted samples were prepared for SEM-EDX analyses in order to detect

192 polyphosphate in cells collected from the environment. Collected cells were also prepared for

193 EDX-analysis as described above, and some cells were marked with the LMD in advance. With

194 the electron microscope, random and marked cells were checked for the occurrence of high

195 phosphorus and cation content, indicating the presence of polyphosphate.

196

197 ***CARD-FISH***

198 The sorted cells were filtered on a 0.2 µm polycarbonate filter (Whatmann, Nuclepore, 110606),

199 with a maximum of 200 mbar to avoid cell damage. Filters were stored at -20 °C untill use. The

200 filter was cut into several pieces (1 for each probe and 1 for the SEM-EDX, 4 pieces in total;

201 SUL90 (Grote *et al.*, 2007), EUB, NonEUB and for the EDX). The filter parts were embedded in

202 0.2% agarose by submerging them in heated agarose solution. After cooling the filters were

203 submerged in pure ethanol and then dried on paper tissue.

204 Lysozyme was prepared fresh (0.05 mol L^{-1} EDTA, 0.1 mol L^{-1} Tris/HCl pH 8, 1% [w/v]

205 lysozyme). The filters were put into a petri dish together with the lysozyme mixture and

206 incubated for 60 minutes at 37 °C. The incubated filters were transferred into 1xPBS, submerged

207 shortly, then transferred into autoclaved MilliQ, then into pure ethanol and finally air-dried.

208 Afterwards, the filters were transferred into an achromopeptidase solution (60 U/mL in 10 mmol

209 L^{-1} NaCl and 10 mmol L^{-1} Tris/HCl pH8) and incubated for 15 minutes at 37 °C. After

210 incubation, the filters were washed in 1xPBS, MilliQ-water and then in pure ethanol. The filters

211 were again air-dried. Filters were then incubated for 10 minutes in 0.01 mol L^{-1} HCl at room

212 temperature. After incubation, filters were washed in MilliQ-water and pure ethanol before again

213 being air-dried.

214 For each filter, 150 µL probe working solution was prepared by mixing 1 µL of probe (Sul90,

215 EUB-Mix, or NonEUB) with 149 µL hybridization-buffer (0.9 mol L^{-1} NaCl, 0.02 mol L^{-1}

216 Tris/HCl pH 7.4, 1% Blocking Reagent, 0.01 mol L^{-1} maleic acid, 10% dextran sulfate, 0.001%

217 SDS, and 35% formamid for Sul90 or 55% formamid the other 2 probes). Filters were transferred

218 to object slides and probe working solution was applied to the filters. Object slides were

219 transferred into a 50 mL falcon tubes with paper tissues at the bottom. On the paper tissues, 2 mL

220 of hybridization chamber buffer (0.9 mol L^{-1} NaCl, 0.02 mol L^{-1} Tris HCL pH 7.4, 0.001% SDS

221 and 35% / 55% formamid) were applied. Falcon tubes were closed and then transferred into oven

222 at 35 °C for 3 hours.

223 After incubation, object slides were put into new 50 mL falcon tubes filled with washing buffer

224 (0.05 mol L^{-1} EDTA, 0.02 mol L^{-1} Tris/HCl pH 7.4, 0.001% SDS, and 0.042 mol L^{-1} NaCl [for

225 SUL90] or 0.003 mol L^{-1} NaCl [for EUB and NonEUB] and were incubated at 37 °C for 15

226 minutes. Filters were then transferred into 1xPBS and incubated at 37 °C for 45 minutes. New

227 object slides were dipped into tyramid buffer (1.97 mol L^{-1} NaCl, 0.986% dextransulfate,

228 0.0986% blocking reagent, 0.00149% H_2O_2, achromopeptidase 0.72 U/mL) and filters were put

229 on top of the slides. Slides were transferred into a new 50 mL tube containing paper tissue, which

230 were drenched with 2 mL MilliQ-water. These were then incubated at 37 °C for 30 minutes.

231 Filters were then carefully dried on a paper tissue and transferred into 1xPBS for 15 minutes at

232 room temperature in the dark. Afterwards, filters were washed for 1 minute, in the dark, at room

233 temperature, first in MilliQ and then for 1 minute in pure ethanol. The filters were dried for 5

234 minutes on paper tissue in the dark.

235 For DAPI counterstaining, the filters were transferred into a DAPI solution (1 µg/mL) and

236 incubated for 5 minutes at room temperature in the dark. Then filters were shortly washed, first in

237 MilliQ-water and then pure ethanol. Filters were dried and then applied to an object slide and

238 covered with microscopy oil.

239

Literature, Supplementary material

241 Adler J, Dahl MM. (1967). A method for measuring the motility of bacteria and for comparing

242 random and non-random motility. *J Gen Microbiol* **46**:161-173.

243

244 Grote J, Labrenz M, Pfeiffer B, Jost G, Jürgens K. (2007). Quantitative distributions of

245 *Epsilonproteobacteria* and a *Sulfurimonas* subgroup in pelagic redoxclines of the central

246 Baltic Sea. *Appl Environ Microbiol* **73**:7155–7161

247

248 Hamady M, Walker JJ, Harris JK, Gold NJ, Knight R. (2008). Error-correcting barcoded primers

249 for pyrosequencing hundreds of samples in multiplex. *Nat Methods* **5**:235-237.

250

251   Kulakova AN, Hobbs D, Smithen M, Pavlov E, Gilbert JA, Quinn JP, *et al*. (2011). Direct

252   quantification of inorganic polyphosphate in microbial cells using 4′-6-diamidino-2-

253   phenylindole (DAPI). *Environ Sci Technol* **45**:7799-7803.

254

255   Laas P, Šatova E, Lips I, Lips U, Simm J, Kisand V, *et al*. (2016). Near-bottom hypoxia impacts

256   dynamics of bacterioplankton assemblage throughout water column of the Gulf of

257   Finland (Baltic Sea). *PloS one* **11**: e0156147.

258

259   Martin P, Van Mooy BA. (2013). Fluorometric quantification of polyphosphate in environmental

260   plankton samples: extraction protocols, matrix effects, and nucleic acid interference.

261   *Appl Environ Microbiol* **79**:273-281.

262

263   McKenna P, Hoffmann C, Minkah N, Aye PP, Lackner A, Liu Z, et al. (2008). The macaque gut

264   microbiome in health, lentiviral infection, and chronic enterocolitis. *PLoS Path* **4**: e20.

Supplementary Information

for

Paper I
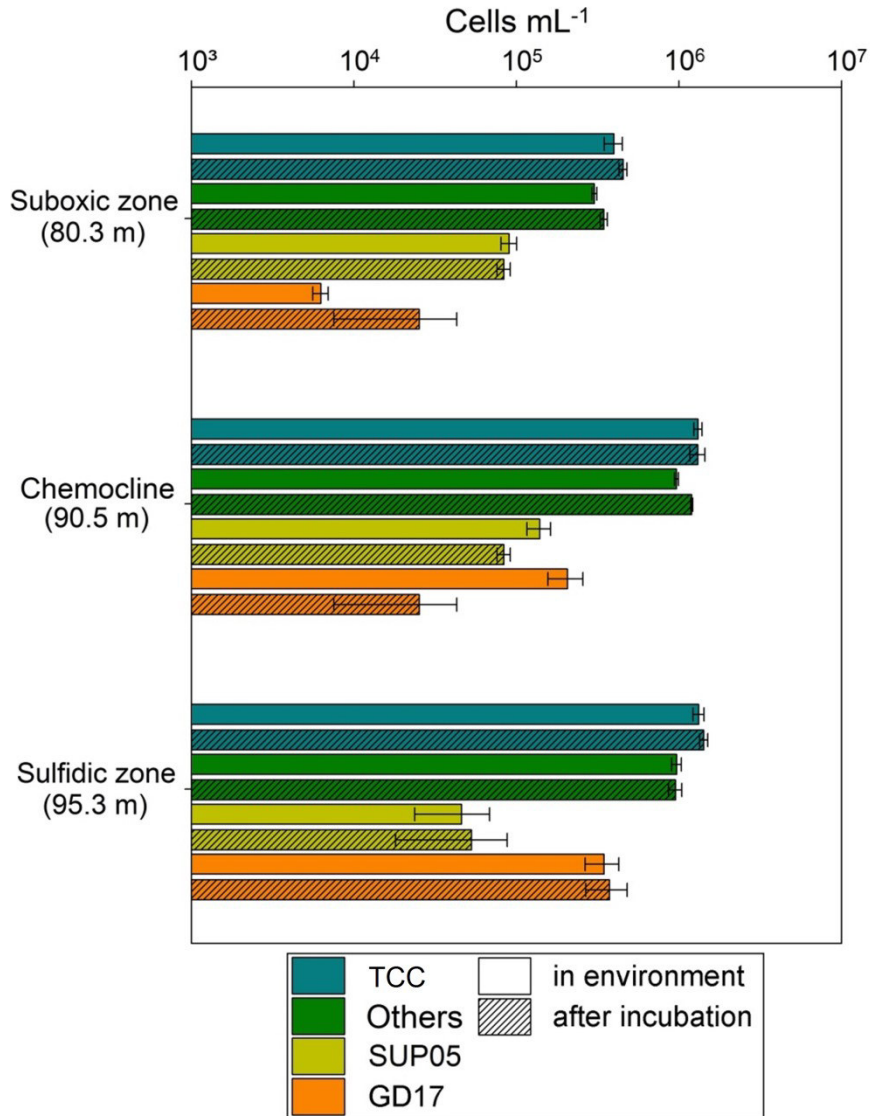
Figure S1

Cell numbers within the Gotland Deep redox zone and after stable isotope labeled substrate incubation. Cell numbers in the environment show typical overlapping abundance gradients of SUP05 and GD17. Total cell numbers were determined by flowcytometrical cell counting and the proportions of SUP05 by CARDFISH and of GD17 by FISH, whereas unidentified cells (others)

were calculated by subtracting the average cell numbers of SUP05 and GD17 from the average total cell number. Error bars indicate the standard deviation.

Cell numbers after individual incubation times and substrate concentrations show low stimulated conditions. Determination of cell numbers after incubations occurred analogously to the environmental samples. Error bars indicate the standard deviation of three independent replicates.

Figure S2

Individual cell volume adjusted ^{13}C, ^{15}N and ^{34}S enrichment (%) of SUP05 and *Sulfurimonas* GD17 cells with a higher isotope ratio than the unlabeled controls. Percentage drawings show proportion of cells of the particular group with a positive enrichment.
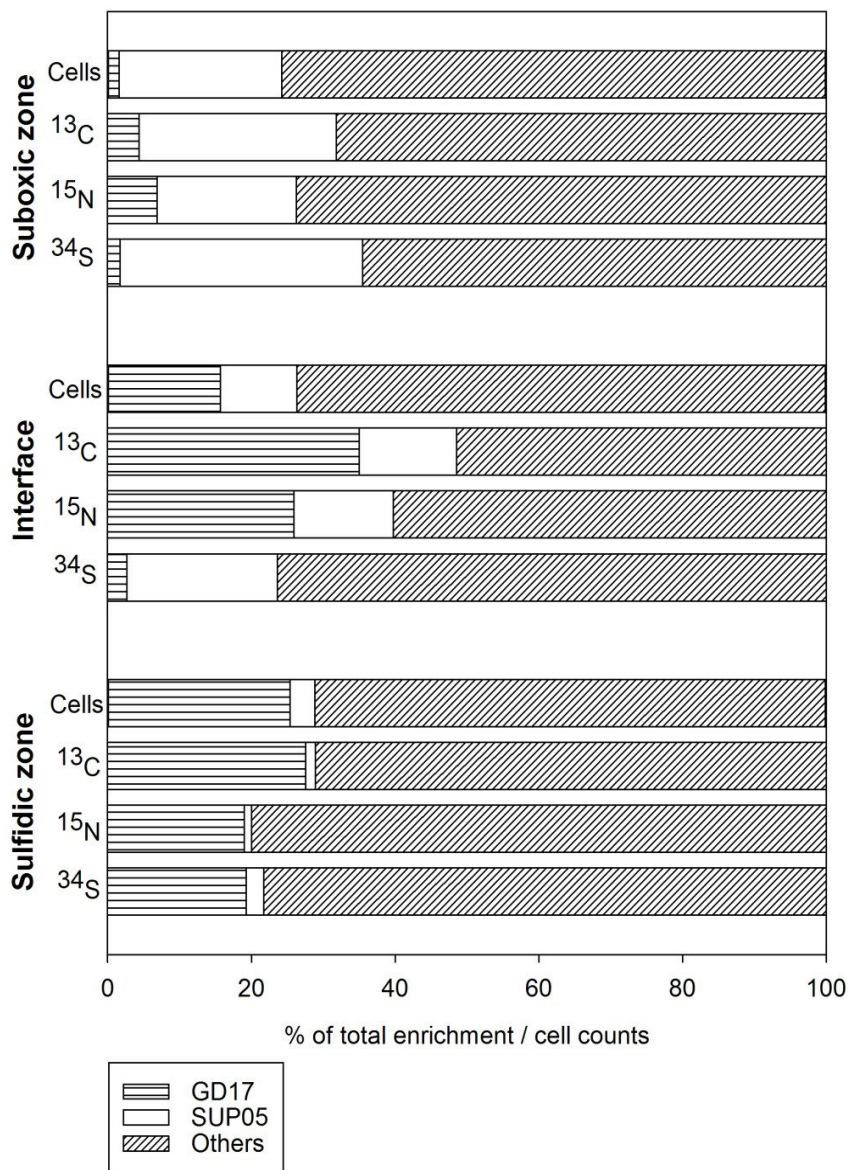
Figure S3

Average percentages of GD17, SUP05 and unidentified cells (others) on total cells (Cells bar) and on cellular ^{13}C, ^{15}N and ^{34}S enrichment on total isotope enriched cells (^{13}C-, ^{15}N- and ^{34}S-bar

shows). Visible is a high activity of SUP05 in the suboxic zone and a high activity of GD17 in the sulfidic zone and the chemocline, except for ^{34}S enrichment.
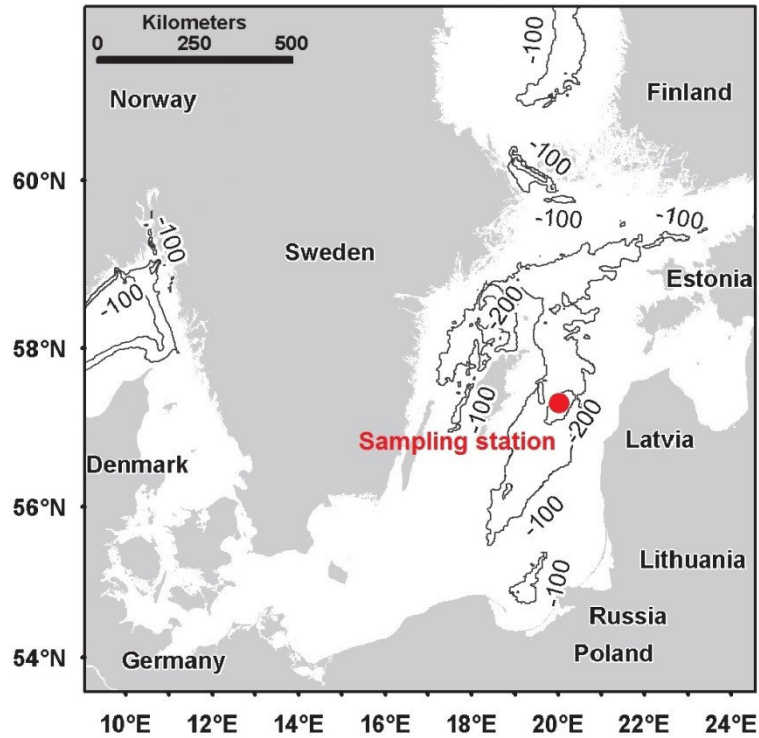
Figure S4

Position of the sampling station within the Eastern Gotland Deep of the Baltic Sea. Lines indicate deep basins of the Baltic Sea as depth contours. Modified after Schmale *et al.,* (2012)

Figure S5

^{13}C, ^{15}N and ^{34}S abundances in cells of *Sulfurimonas gotlandica* strain GD1^{T} after 12 and 24 hours of incubation with ^{13}C bicarbonate, ^{15}N nitrate and ^{34}S elemental sulfur. The incubation time had no effect on the saturation of the ^{13}C and ^{34}S abundance (α = 0.426; α = 0.668) and the ^{15}N abundance showed significant differences between the two incubation times (α = 0.003) but no further saturation.

Table S1

Number of measured parallels, spots, and cells of the stable isotope labelled substrate experiments. Others, unidentified cells.

Zone	Number of replicates		Number of spots		Number of identified cells			
	SUP05	GD17	SUP05	GD17	SUP05	GD17	Others	
	CARDFISH	FISH	CARDFISH	FISH	CARDFISH	FISH	Others-SUP05	Others-GD17
Suboxic zone	2	2	4	9	22	23	199	139
Chemocline	2	3	4	10	26	53	220	439
Sulfidic zone	2	3	3	9	3	83	242	255

Table S2

Number of measured parallels, spots, and cells of the unlabelled stable isotope substrate experiments. Others, unidentified cells.

Zone	Number of replicates		Number of spots		Number of identified cells			
	SUP05	GD17	SUP05	GD17	SUP05	GD17	Others	
	CARDFISH	FISH	CARDFISH	FISH	CARDFISH	FISH	Others-SUP05	Others-GD17
Suboxic zone	1	1	1	2	10	1	69	79
Chemocline	1	1	1	2	7	10	38	60
Sulfidic zone	1	1	1	1	0	8	37	47

Table S3

NanoSIMS based cell volumes and Length-Width ratios of single cells of SUP05 and GD17 in the particular zones indicate higher average biovolumes of GD17 than SUP05 in all zones. A: suboxic zone; B: chemocline; C: sulfidic zone.

		SUP05	GD17
Suboxic zone	Mean cell volume [µm³]	0.07 (± 0.09)	0.61 (±0.47)
	Median of cell volume [µm³]	0.03	0.58
	Mean length-width ratio	1.78 (± 0.56)	2.53 (± 1.25)
Chemocline	Mean cell volume [µm³]	0.06 (± 0.09)	0.26 (± 0.31)
	Median of cell volume [µm³]	0.04	0.17
	Mean length-width ratio	1.73 (± 0.41)	2.13 (± 0.64)
Sulfidic zone	Mean cell volume [µm³]	0.09 (± 0.04)	0.32 (± 0.53)
	Median of cell volume [µm³]	0.11	0.18
	Mean length-width ratio	1.45 (± 0.34)	2.16 (± 0.81)

Table S4

Overview of the sulfidic conditions in the global distributed environments of SUP05.

Study site	Ref.	H₂S concentration of highest SUP05 abundance		Investigated organism

Stratified marine or brackish environments

Study site	Ref.	H$_2$S concentration of highest SUP05 abundance		Investigated organism
Landsort Deep (Baltic Sea)	(Glaubitz *et al.,* 2013)	**< 1 µm L^{-1}** (4 10^5 cells mL^{-1}; 29 %)		SUP05 related cells (probe GSO1032)
Gotland Deep (Baltic Sea)	(Glaubitz *et al.,* 2013)	**6.95 µm L^{-1}** (2 10^5 cells ml^{-1}; 13 %)		SUP05 related cells (probe GSO1032)
Western Black Sea Basin	(Glaubitz *et al.,* 2013)	**4.9 µm L^{-1}** (7 x 10^4 cells mL^{-1})	**0.6 µm L^{-1}** (13 %)	SUP05 related cells (probe GSO1032)
Nitinat Lake (Canada)	(Schmidtova *et al.,* 2009)	**Near 0 µm L^{-1}** (2 x 10^3 SSU rRNA gene copies mL^{-1}) **~ 40 µM after inflow** (4 x 10^5 SSU rRNA gene copies mL^{-1})		SUP05 subgroup
Saanich Inlet (Canada)	(Walsh *et al.,* 2009)	**H$_2$S depleted** (5 × 10^5 SSU rRNA gene copies mL^{-1})		SUP05 SI-1 & SI-2 phylotypes
Benguela upwelling region (off Namibia)	(Lavik *et al.,* 2009)	**4 - 7 µm L^{-1}** (3 - ~5 x 10^5 cells mL^{-1})		Whole GSO cluster (probe GSO477)

Oxygen minimum zones

Study site	Ref.	H$_2$S concentration of highest SUP05 abundance		Investigated organism
Benguela upwelling zone (off Namibia & Angola)	(Morris *et al.,* 2012)	**Below deep chlorophyll maximum** (> 10% of total T-RFLP fragment area)		Members of GSO cluster
ETSP OMZ (off Peru)	(Canfield *et al.,* 2010)	**Core of the OMZ** (150m; 7 - 8 % of total protein coding genes matching NCBI-nr)		uncultured SUP05 cluster bacterium
ETSP OMZ (off northern Chile)	(Stewart *et al.,* 2012)	**Upper core of the OMZ** (200m; ~4 % of total protein coding genes matching NCBI-nr)		symbiont-like, uncultured SUP05 cluster bacterium

Hydrothermal vents	**Suiyo Seamount caldera** (off Japan)	(Sunamura *et al.,* 2004)	**Background seawater**	Arctic96BD-19
			Hydrothermal plume (6.6 x 10^4 cells mL^{-1}; 58 %)	SUP05 (probe SUP05-187)
	Guaymas Basin (Gulf of California)	(Lesniewski *et al.,* 2012)	**0 - 5 µm L^{-1}** (abundant and active in plume and background waters)	SUP05 group
	Guaymas Basin (Gulf of California)	(Anantharaman *et al.,* 2013)	**Hydrothermal deep waters with plume** (30%)	SUP05 GB-1 & GB-2
	Axial Seamount (Juan de Fuca Ridge)	(Mattes *et al.,* 2013)	**Hydrothermal plume**	SUP05 subclade
Other	**Polynya in Amundsen Sea** (Antarctica)	(Kim *et al.,* 2014)	**0 µm L^{-1}** (6-16 % in polynya deep waters)	Affiliated with ARCTIC96BD-19

Table S5

Overview of the sulfidic conditions in the global distributed environments of *Sulfurimonas* subgroup GD17 and *Sulfurimonas gotlandica* strain GD1^T.

	Study site	Ref.	H$_2$S concentration of highest GD17 cell concentration or abundance	Investigated organism / used probe
Pelagic, brackish Baltic Sea redox zones	**Gotland Deep**	(Brettar *et al.,* 2006)	**~ 16 µm L^{-1}** (1.4 x105 cells mL^{-1})	*Thiomicrospira denitrificans*-like bacterium
	Gotland Deep	(Grote *et al.,* 2007)	**~ 6 µm L^{-1}** (2.1 x 105 cells mL^{-1})	*Sulfurimonas* subgroup GD17 (gene probe SUL90)
	Gotland Deep	(Grote *et al.,* 2008)	**~ 14 µm L^{-1}** (31.8 %)	*Sulfurimonas* subgroup GD17 (gene probe SUL90)
	Farö Deep	(Grote *et al.,* 2007)	**~ 5 µm L^{-1}**	*Sulfurimonas* subgroup GD17 (gene probe SUL90)
	Landsort Deep	(Thureborn *et al.* 2013; Thureborn *et al.,* 2013)	**29.8 µm L^{-1}** (0.9% of the total archaeal/bacterial community at species level)	*Sulfurimonas gotlandica* GD1^T
Other brackish or marine pelagqic redox zones	**Black Sea**	(Vetriani *et al.,* 2003)	Abundant in sulfidic zone (interface at 100m; 12.5 and 21.4% of the recovered clones at 115 m and 217 m, respectively)	Related to *Thiomicrospira denitrificans*
	Black Sea	(Grote *et al.,* 2008)	**~ 8 µm L^{-1}** (4.9 %)	*Sulfurimonas* subgroup GD17 (gene probe SUL90)
	Nitinat Lake (Canada)	(Schmidtova *et al.,* 2009)	**~ 35 µm L^{-1}** (~40 % of all clones)	*Sulfurimonas* sp. rel. cluster
	Cariaco Basin (Off Venezuela)	(Madrid *et al.,* 2001)	**up to 23 µm L^{-1}** (clones generated)	Related to *Thiomicrospira denitrificans*

Others	**Suiyo Seamount caldera** (Off Japan)	(Sunamura *et al.*, 2004)	in plume layer (5 to 8% of the total cells)	SUP01 group (Gene probe SUP01-63)

Cell volume of SUP05 cells accordant to Glaubitz et al. (2013)

Glaubitz *et al.,* (2013) did not explicitly investigate the cell volume of SUP05 cells; therefore we performed it for this study using their protocol and comparable Baltic Sea samples. For this, SUP05 cells were hybridised using the CARD-FISH protocol of Glaubitz *et al.,* (2013) and counterstained with DAPI. Images taken with a Zeiss Axioskop epifluorescence microscope and the Software CellP were subsequently analysed using the software ACME tool 3 (Technobiology). In cells with adequate DAPI and CARD-FISH signals, the number of pixels of the DAPI image was exported. Together with the cell area and perimeter and the total image size, the cell volume was calculated assuming a cell shape of straight-sided rods with hemispherical ends (Zeder *et al.*, 2011).

References

Anantharaman, K., Breier, J.A., Sheik, C.S., and Dick, G.J. (2013) Evidence for hydrogen oxidation and metabolic plasticity in widespread deep-sea sulfur-oxidizing bacteria. Proc Natl Acad Sci 110: 330–335.

Brettar, I., Labrenz, M., Flavier, S., Botel, J., Kuosa, H., Christen, R., and Höfle, M.G. (2006) Identification of a *Thiomicrospira denitrificans*-Like epsilonproteobacterium as a catalyst for autotrophic denitrification in the central Baltic Sea. Appl Environ Microbiol 72: 1364–1372.

Canfield, D.E., Stewart, F.J., Thamdrup, B., Brabandere, L. de, Dalsgaard, T., DeLong, E.F., Revsbech, N.P., and Ulloa, O. (2010) A cryptic sulfur cycle in oxygen-minimum-zone waters off the Chilean coast. Science 330: 1375–1378.

Glaubitz, S., Kießlich, K., Meeske, C., Labrenz, M., and Jürgens, K. (2013) SUP05 dominates the gammaproteobacterial sulfur oxidizer assemblages in pelagic redoxclines of the central Baltic and Black Seas. Appl Environ Microbiol 79: 2767–2776.

Grote, J., Labrenz, M., Pfeiffer, B., Jost, G., and Jürgens, K. (2007) Quantitative distributions of *Epsilonproteobacteria* and a *Sulfurimonas* subgroup in pelagic redoxclines of the central Baltic Sea. Appl Environ Microbiol 73: 7155–7161.

Grote, J., Jost, G., Labrenz, M., Herndl, G.J., and Jürgens, K. (2008) Epsilonproteobacteria represent the major portion of chemoautotrophic bacteria in sulfidic waters of pelagic redoxclines of the Baltic and Black Seas. Appl Environ Microbiol 74: 7546–7551.

Kim, J.-G., Park, S.-J., Quan, Z.-X., Jung, M.-Y., Cha, I.-T., Kim, S.-J.*, et al.* (2014) Unveiling abundance and distribution of planktonic bacteria and archaea in a polynya in Amundsen Sea, Antarctica. Environ Microbiol 16: 1566–1578.

Lavik, G., Stührmann, T., Brüchert, V., Van der Plas, Anja, Mohrholz, V., Lam, P.*, et al.* (2009) Detoxification of sulphidic African shelf waters by blooming chemolithotrophs. Nature 457: 581–584.

Lesniewski, R.A., Jain, S., Anantharaman, K., Schloss, P.D., and Dick, G.J. (2012) The metatranscriptome of a deep-sea hydrothermal plume is dominated by water column methanotrophs and lithotrophs. ISME J 6: 2257–2268.

Madrid, V.M., Taylor, G.T., Scranton, M.I., and Chistoserdov, A. (2001) Phylogenetic diversity of bacterial and archaeal communities in the anoxic zone of the Cariaco Basin. Appl Environ Microbiol 67: 1663–1674.

Mattes, T.E., Nunn, B.L., Marshall, K.T., Proskurowski, G., Kelley, D.S., Kawka, O.E., *et al.* (2013) Sulfur oxidizers dominate carbon fixation at a biogeochemical hot spot in the dark ocean. ISME J **7**: 2349–2360.

Morris, R.M., Frazar, C.D., and Carlson, C.A. (2012) Basin-scale patterns in the abundance of SAR11 subclades, marine Actinobacteria (OM1), members of the *Roseobacter* clade and OCS116 in the South Atlantic. Environ Microbiol 14: 1133–1144.

Schmale, O., Blumenberg, M., Kießlich, K., Jakobs, G., Berndmeyer, C., Labrenz, M., Thiel, V., and Rehder, G. (2012) Aerobic methanotrophy within the pelagic redox-zone of the Gotland Deep (central Baltic Sea). Biogeosciences 9: 4969–4977.

Schmidtova, J., Hallam, S.J., and Baldwin, S.A. (2009) Phylogenetic diversity of transition and anoxic zone bacterial communities within a near-shore anoxic basin: Nitinat Lake. Environ Microbiol 11: 3233–3251.

Stewart, F.J., Ulloa, O., and DeLong, E.F. (2012) Microbial metatranscriptomics in a permanent marine oxygen minimum zone. Environ Microbiol 14: 23–40.

Sunamura, M., Higashi, Y., Miyako, C., Ishibashi, J.-i., and Maruyama, A. (2004) Two bacteria phylotypes are predominant in the Suiyo seamount hydrothermal plume. Appl Environ Microbiol 70: 1190–1198.

Thureborn, P., Lundin, D., Plathan, J., Poole, A.M., Sjöberg, B.-M., Sjöling, S., and Gilbert, J.A. (2013) A metagenomics transect into the deepest point of the Baltic Sea reveals clear stratification of microbial functional capacities. PLoS ONE 8: e74983.

Vetriani, C., Tran, H.V., and Kerkhof, L.J. (2003) Fingerprinting microbial assemblages from the oxic/anoxic chemocline of the Black Sea. Appl Environ Microbiol 69: 6481–6488 .

Walsh, D.A., Zaikova, E., Howes, C.G., Song, Y.C., Wright, J.J., Tringe, S.G., Tortell, P.D., and Hallam, S.J. (2009) Metagenome of a versatile chemolithoautotroph from expanding oceanic dead zones. Science 326: 578–582.
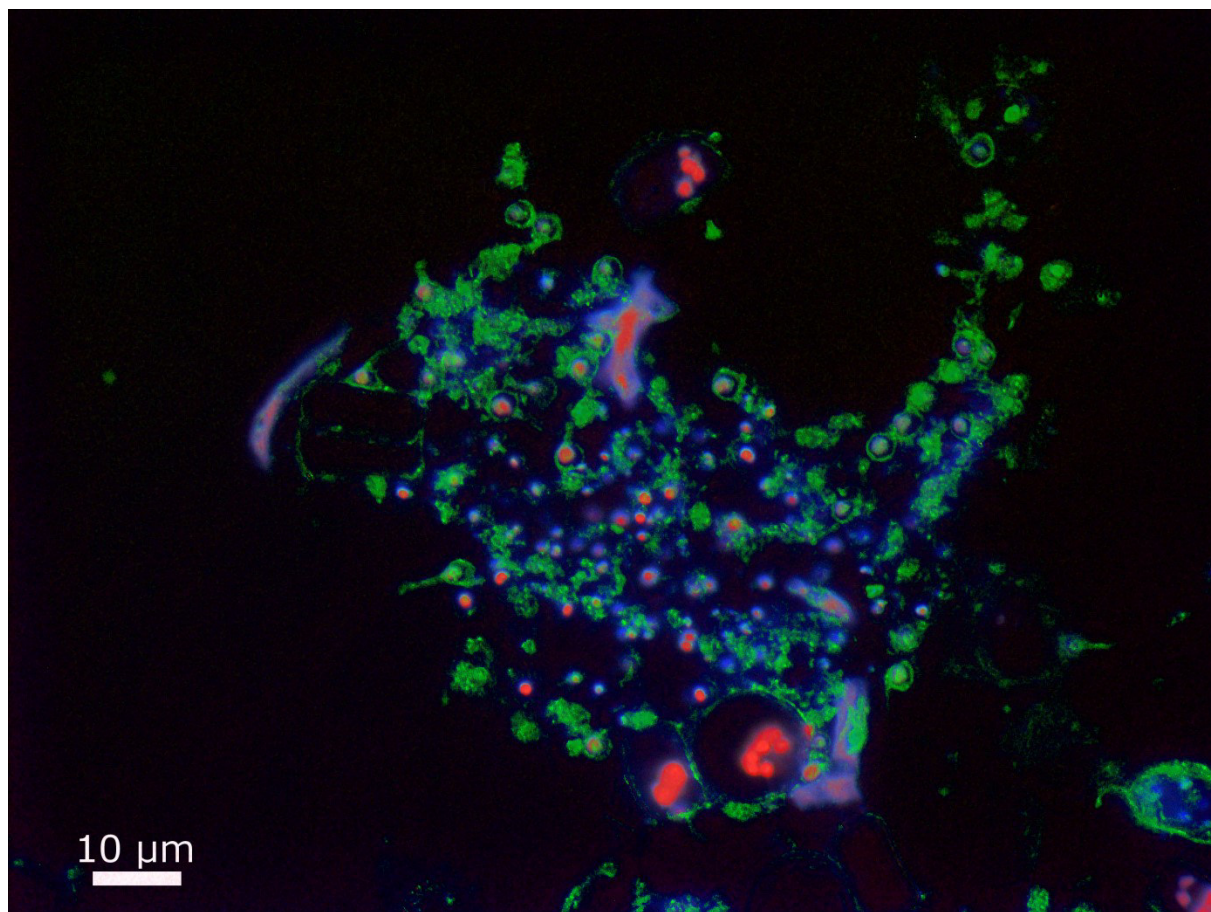
Zeder, M., Kohler, E., Zeder, L., and Pernthaler, J. (2011) A novel algorithm for the determination of bacterial cell volumes that is unbiased by cell morphology. Microsc Microanal 17: 799–809.

Supplementary Information

for

Paper III

1 **Supplementary Information**

10 μm

3 Fig. S1: Image overlap of TEP (green), Chlorophyll a autofluorescence (red) and nucleic acids

4 (blue) of methacrylate embedded aggregate sample acquired with a higher magnification using a

5 63x objective shows TEP exudates around algal cells with embedded prokaryotes.

6

7

8

9

10

11
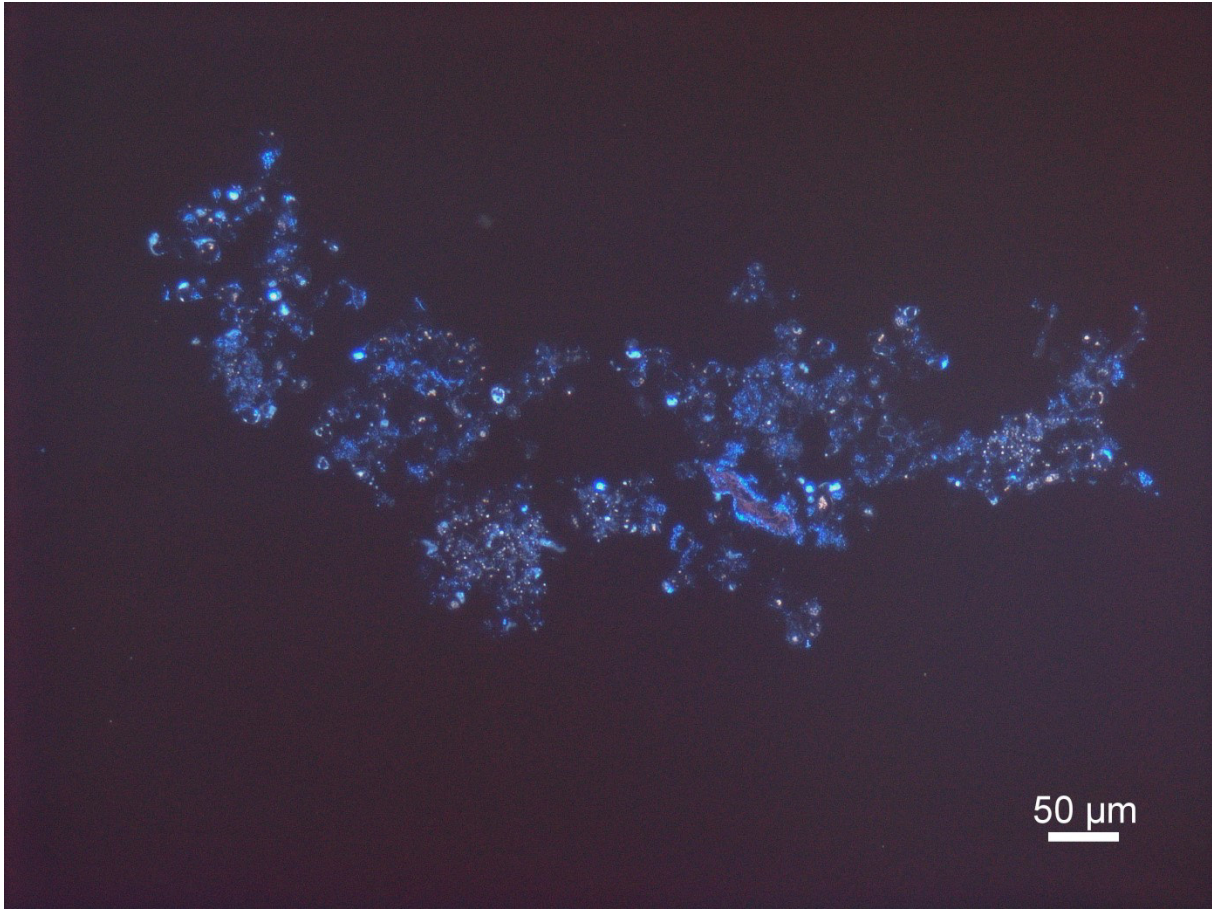
Fig. S2: Original micrograph of nucleic acids stained with DAPI of a methacrylate embedded

laboratory generated aggregate. Slice thickness: 2 μm.

14

Fig. S3: Original micrograph of chlorophyll a autofluorescence of methacrylate embedded laboratory generated aggregate. Slice thickness: 2 μm.
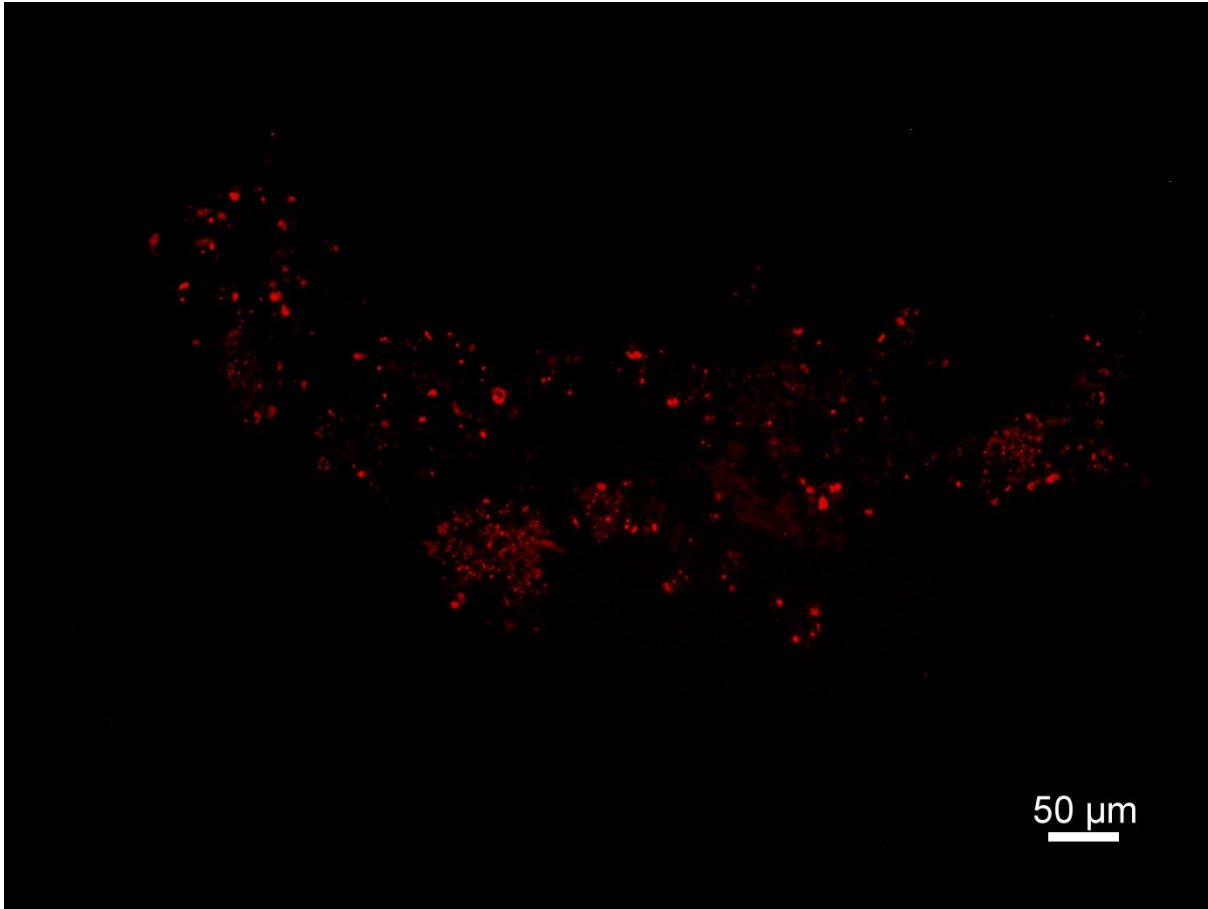
50 μm
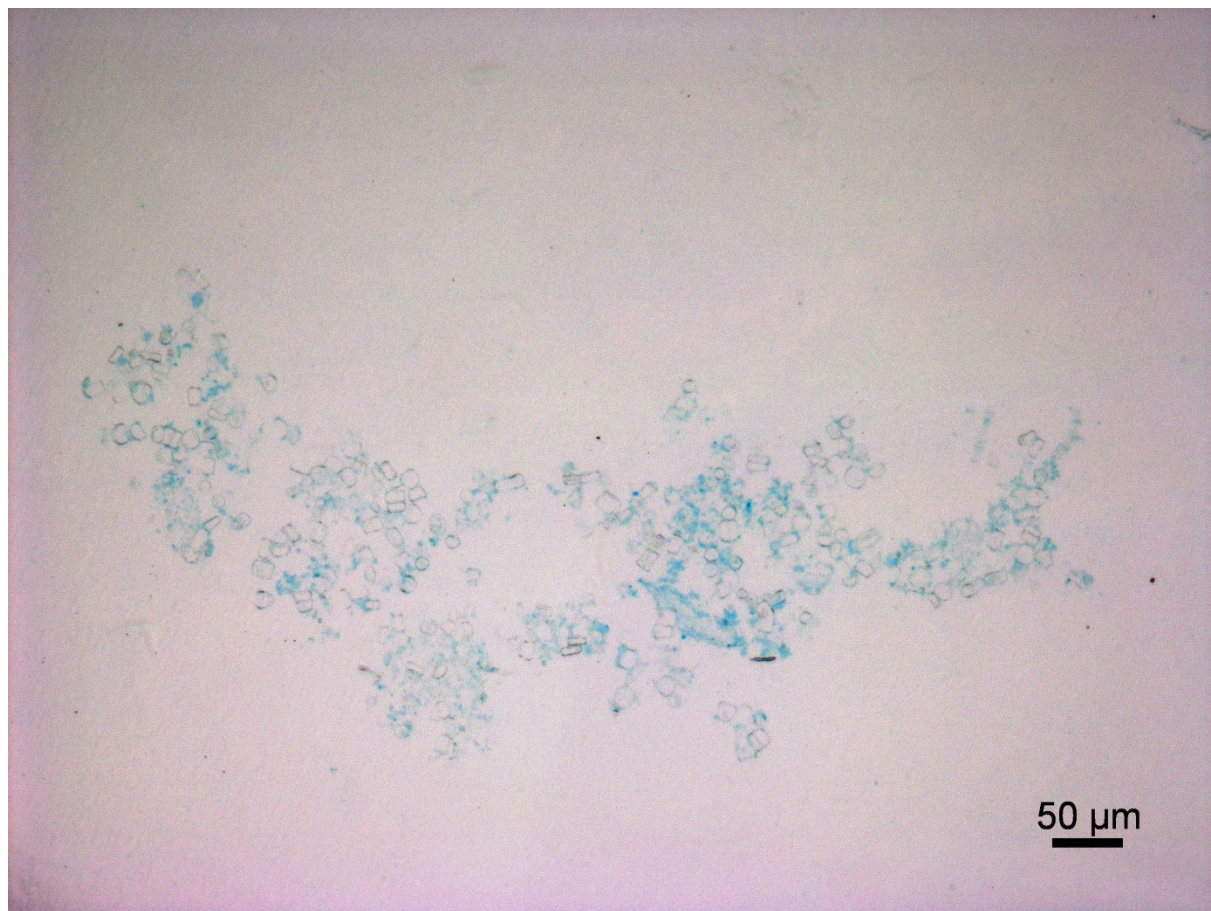
19

20   Fig. S4: Original micrograph of TEP compounds, stained with Alcian Blue of a methacrylate

21   embedded laboratory generated aggregate. Slice thickness: 2 μm.

22

23

24 Fig. S5: Original micrograph of eukaryotic cytoplasm, stained with eosinY / phloxine B of a

25 methacrylate embedded laboratory generated aggregate using bright field. Slice thickness: 2 µm.

26

Fig. S6: Original micrograph of eukaryotic cytoplasm, stained with eosinY / phloxine B of a methacrylate embedded laboratory generated aggregate using epifluorescence channel of chlorophyll a. Slice thickness: 2 μm.

30

31

Fig. S7: Original micrograph of CSP compounds, stained with Coomassie Brilliant Blue of a

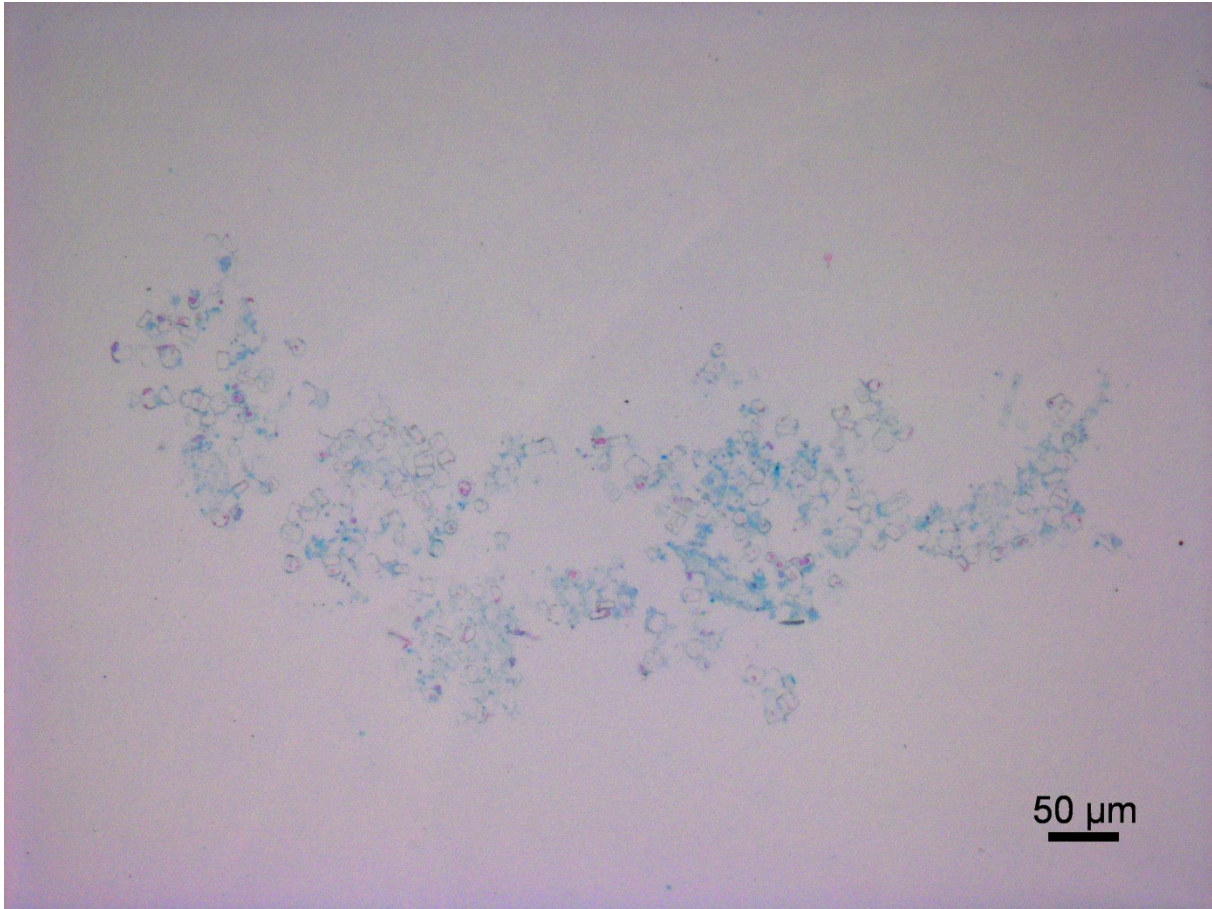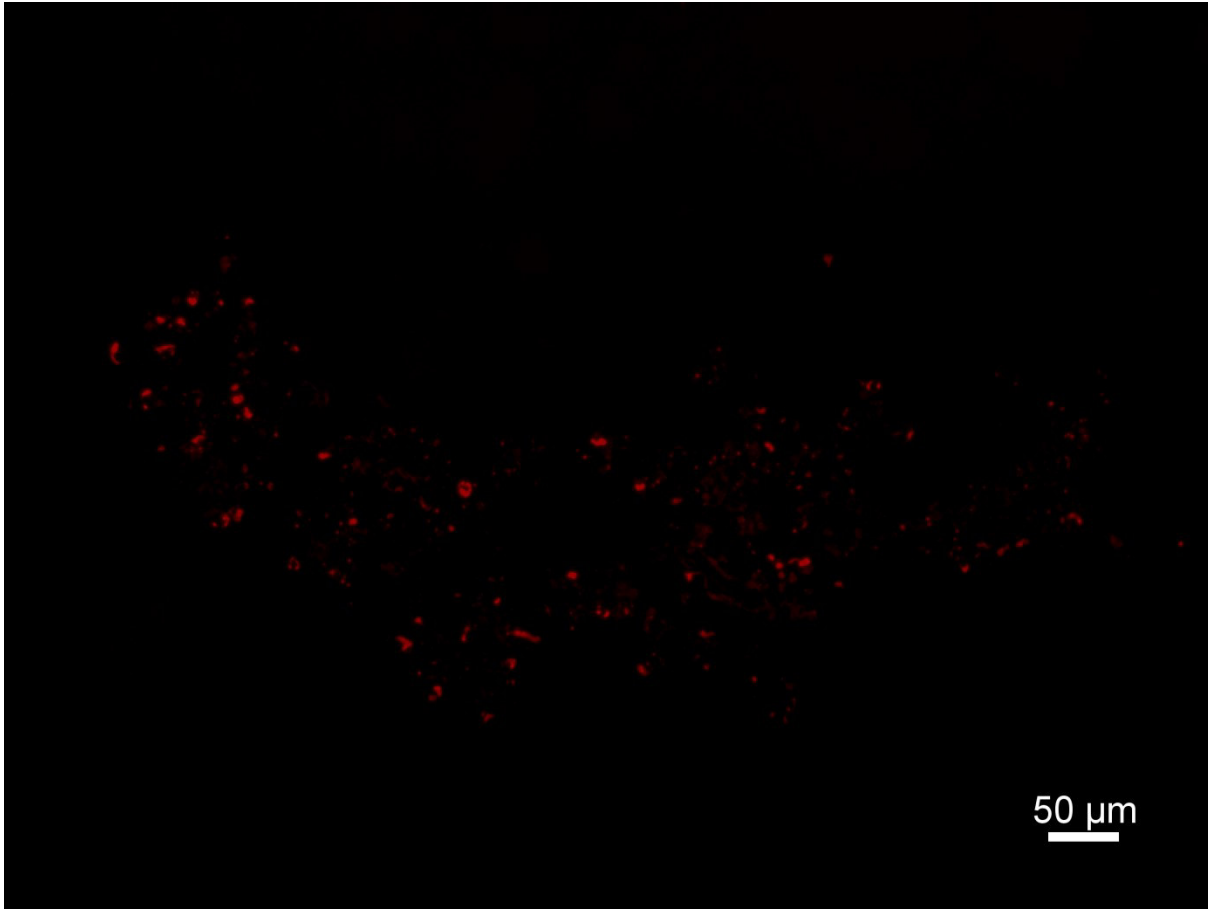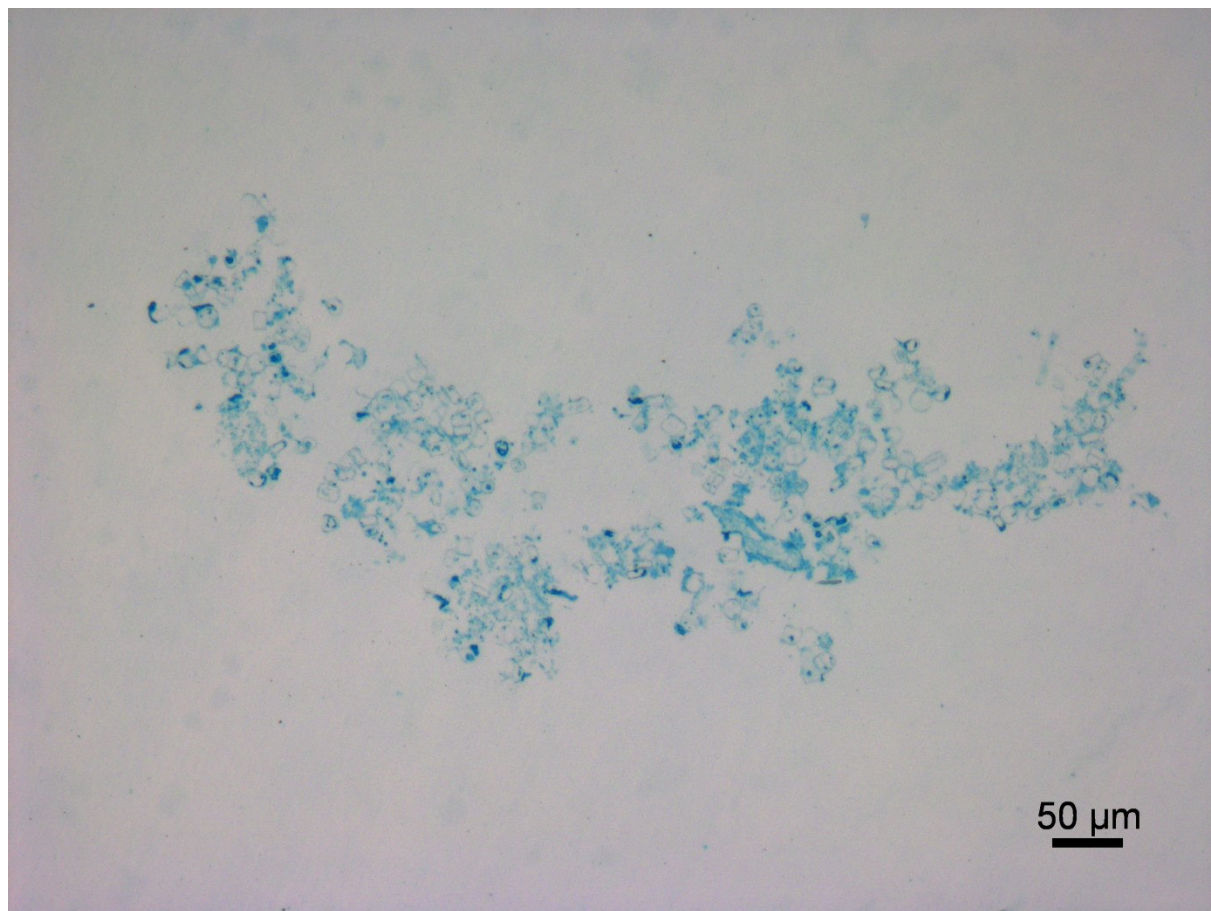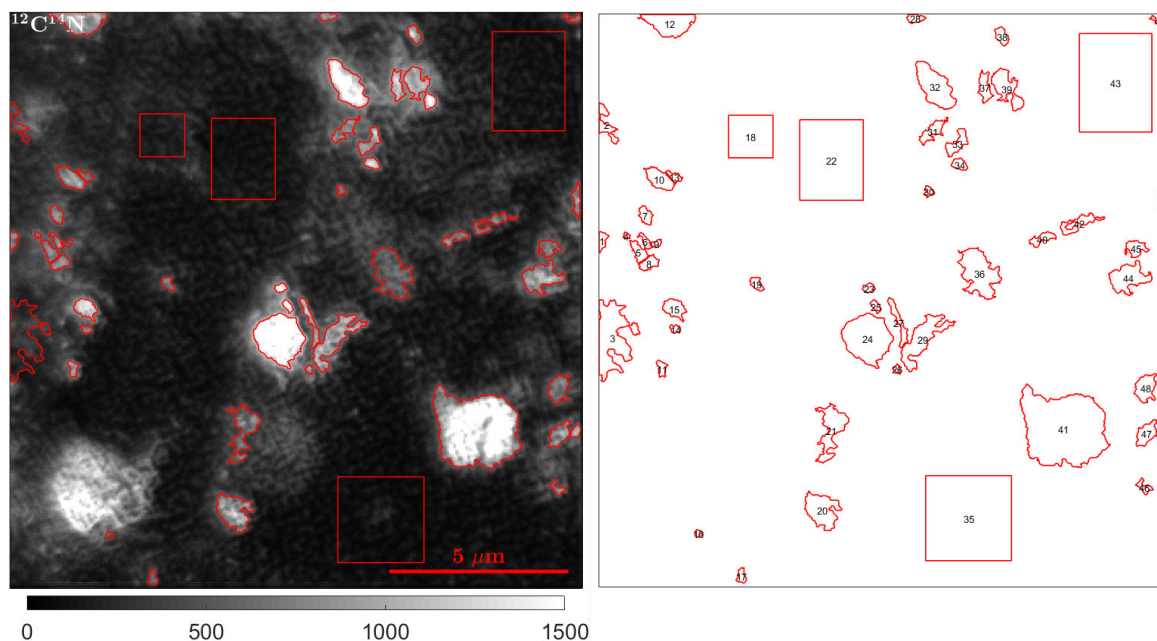methacrylate embedded laboratory generated aggregate. Slice thickness: 2 µm.

34

Fig. S8: ROI distribution of detail measurement #1 of labelled sample as shown in Fig. 8 as well as Fig. 7: 1: prokaryotic cell, 2: possibly sulfur particle, 3: possibly sulfur particle, 4: ignored due to insignificant ion counts, 5: prokaryotic cell, 6: prokaryotic cell, 7: prokaryotic cell, 8: prokaryotic cell, 9: prokaryotic cell, 10: prokaryotic cell, 11: prokaryotic cell, 12: prokaryotic cell, 13: prokaryotic cell, 14: prokaryotic cell, 15: prokaryotic cell, 16: ignored due to insignificant ion counts, 17: prokaryotic cell, 18: phytoplankton cytoplasm, 19: prokaryotic cell, 20: prokaryotic cell, 21: prokaryotic cell, 22: phytoplankton cytoplasm, 23: prokaryotic cell, 24: phytoplankton compartment, 25: prokaryotic cell, 26: prokaryotic cell, 27: prokaryotic cell, 28: prokaryotic cell, 29: prokaryotic cell, 30: prokaryotic cell, 31: prokaryotic cell, 32: prokaryotic cell, 33: prokaryotic cell, 34: prokaryotic cell, 35: resin matrix, 36: artefact, 37: phytoplankton compartment, 38: prokaryotic cell, 39: phytoplankton compartment, 40: prokaryotic cell, 41: phytoplankton compartment, 42: prokaryotic cell, 43: resin matrix, 44: phytoplankton compartment, 45: prokaryotic cell, 46: prokaryotic cell, 47: prokaryotic cell, 48: prokaryotic cell, 49: prokaryotic cell, 50: prokaryotic cell, 51: prokaryotic cell.
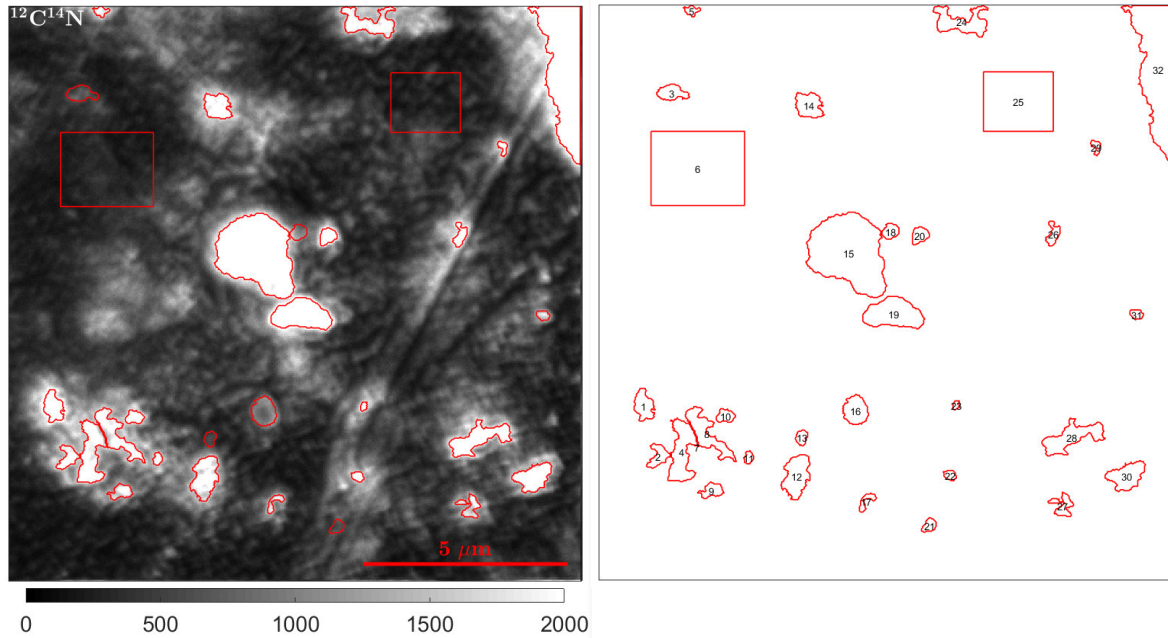
Fig. S9: ROI distribution of detail measurement #2 of labelled sample as shown in Fig. 8 as well as Fig. 7: 1: phytoplankton compartment, 2: phytoplankton compartment, 3: possibly sulfur particle, 4: phytoplankton compartment, 5: prokaryotic cell, 6: resin matrix, 7: ignored due to insignificant ion counts, 8: phytoplankton compartment, 9: prokaryotic cell, 10: prokaryotic cell, 11: prokaryotic cell, 12: prokaryotic cell, 13: possibly sulfur particle, 14: prokaryotic cell, 15: phytoplankton compartment, 16: possibly sulfur particle, 17: prokaryotic cell, 18: possibly sulfur particle, 19: prokaryotic cell, 20: prokaryotic cell, 21: possibly sulfur particle, 22: prokaryotic cell, 23: prokaryotic cell, 24: phytoplankton compartment, 25: resin matrix, 26: prokaryotic cell, 27: prokaryotic cell, 28: prokaryotic cell, 29: prokaryotic cell, 30: prokaryotic cell, 31: prokaryotic cell, 32: phytoplankton compartment.
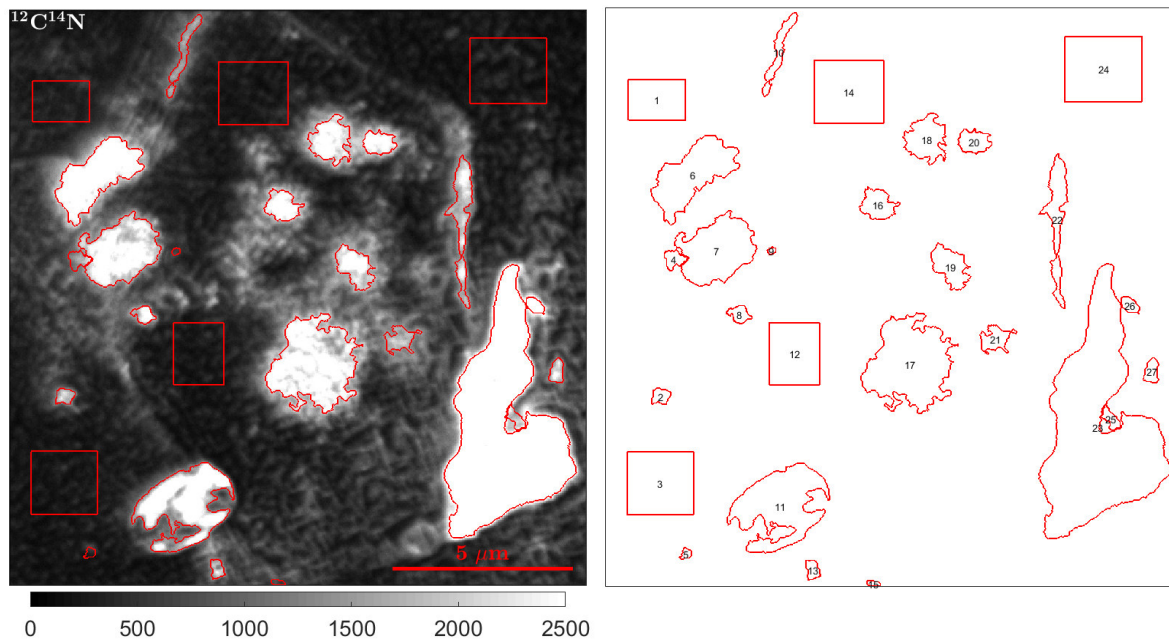
62

Fig. S10: ROI distribution of detail measurement #3 of labelled sample as shown in Fig. 8 as well

as Fig. 7: 1: resin matrix, 2: prokaryotic cell, 3: resin matrix, 4: possibly sulfur particle, 5: possibly

sulfur particle, 6: prokaryotic cell, 7: phytoplankton compartment, 8: phytoplankton compartment,

9: possibly sulfur particle, 10: phytoplankton frustule, 11: phytoplankton compartment, 12:

phytoplankton cytoplasm, 13: prokaryotic cell, 14: phytoplankton cytoplasm, 15: possibly sulfur

particle, 16: phytoplankton compartment, 17: phytoplankton compartment, 18: phytoplankton

compartment, 19: phytoplankton compartment, 20: phytoplankton compartment, 21:

phytoplankton compartment, 22: phytoplankton frustule, 23: artefact, 24: resin matrix, 25: possibly

sulfur particle, 26: prokaryotic cell, 27: prokaryotic cell.
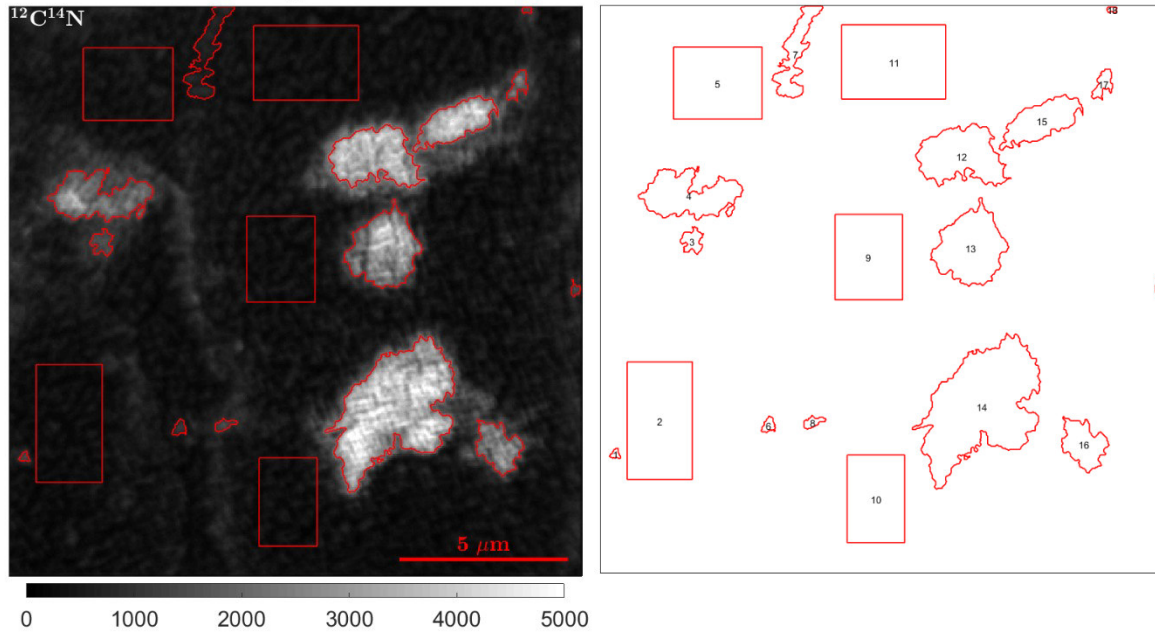
Fig. S11: ROI distribution of additional detail measurement #1 of labelled sample as shown in Fig. 8: ROI distribution of additional detail measurement #1 of labelled sample: 1: phytoplankton compartment, 2: phytoplankton cytoplasm, 3: phytoplankton compartment, 4: phytoplankton compartment, 5: resin matrix, 6: prokaryotic cell, 7: phytoplankton frustule, 8: prokaryotic cell, 9: phytoplankton cytoplasm, 10: phytoplankton cytoplasm, 11: phytoplankton cytoplasm, 12: phytoplankton compartment, 13: phytoplankton compartment, 14: phytoplankton compartment, 15: phytoplankton compartment, 16: phytoplankton compartment, 17: phytoplankton compartment, 18: prokaryotic cell, 19: prokaryotic cell.
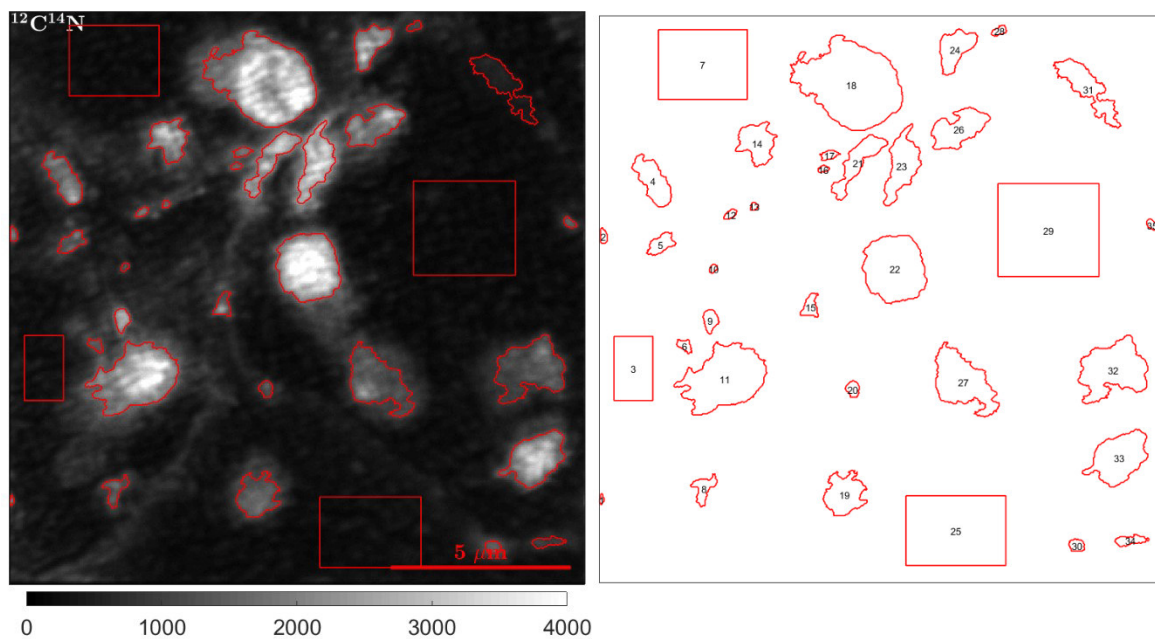
Fig. S12: ROI distribution of additional detail measurement #2 of labelled sample as shown in Fig. 8: 1: phytoplankton compartment, 2: prokaryotic cell, 3: phytoplankton cytoplasm, 4: prokaryotic cell, 5: prokaryotic cell, 6: phytoplankton compartment, 7: phytoplankton cytoplasm, 8: phytoplankton compartment, 9: phytoplankton compartment, 10: prokaryotic cell, 11: phytoplankton compartment, 12: prokaryotic cell, 13: prokaryotic cell, 14: phytoplankton compartment, 15: prokaryotic cell, 16: prokaryotic cell, 17: prokaryotic cell, 18: phytoplankton compartment, 19: prokaryotic cell, 20: prokaryotic cell, 21: prokaryotic cell, 22: phytoplankton compartment, 23: phytoplankton compartment, 24: prokaryotic cell, 25: resin matrix, 26: phytoplankton compartment, 27: phytoplankton compartment, 28: prokaryotic cell, 29: phytoplankton cytoplasm, 30: prokaryotic cell, 31: phytoplankton frustule, 32: phytoplankton compartment, 33: phytoplankton compartment, 34: phytoplankton frustule, 35: phytoplankton compartment.

94

Fig. S13: ROI distribution of additional detail measurement #1 of unlabelled control sample as shown in Fig. 8: 1: prokaryotic cell, 2: phytoplankton compartment, 3: prokaryotic cell, 4: phytoplankton compartment, 5: resin matrix, 6: phytoplankton compartment, 7: phytoplankton compartment, 8: phytoplankton compartment, 9: artefact, 10: prokaryotic cell, 11: prokaryotic cell, 12: phytoplankton compartment, 13: artefact, 14: resin matrix, 15: artefact, 16: artefact, 17: prokaryotic cell, 18: prokaryotic cell, 19: phytoplankto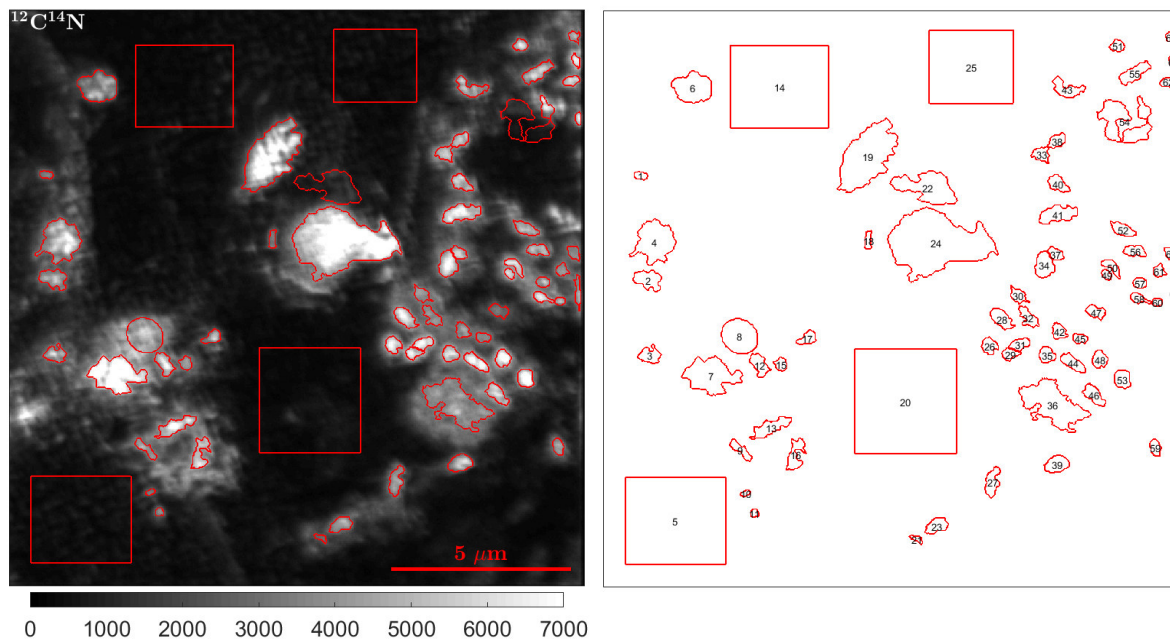n compartment, 20: resin matrix, 21: prokaryotic cell, 22: possibly sulfur particle, 23: prokaryotic cell, 24: phytoplankton compartment, 25: resin matrix, 26: prokaryotic cell, 27: prokaryotic cell, 28: prokaryotic cell, 29: prokaryotic cell, 30: prokaryotic cell, 31: prokaryotic cell, 32: prokaryotic cell, 33: prokaryotic cell, 34: prokaryotic cell, 35: prokaryotic cell, 36: phytoplankton compartment, 37: prokaryotic cell, 38: prokaryotic cell, 39: prokaryotic cell, 40: prokaryotic cell, 41: prokaryotic cell, 42: prokaryotic cell, 43: prokaryotic cell, 44: prokaryotic cell, 45: prokaryotic cell, 46: prokaryotic cell, 47: prokaryotic cell, 48: prokaryotic cell, 49: prokaryotic cell, 50: prokaryotic cell, 51: prokaryotic cell, 52: prokaryotic cell, 53: prokaryotic cell, 54: possibly sulfur particle, 55: prokaryotic cell, 56:

109   prokaryotic cell, 57: prokaryotic cell, 58: prokaryotic cell, 59: prokaryotic cell, 60: prokaryotic

110   cell, 61: prokaryotic cell, 62: prokaryotic cell, 63: prokaryotic cell, 64: prokaryotic cell, 65:

111   prokaryotic cell, 66: prokaryotic cell, 67: prokaryotic cell.

112
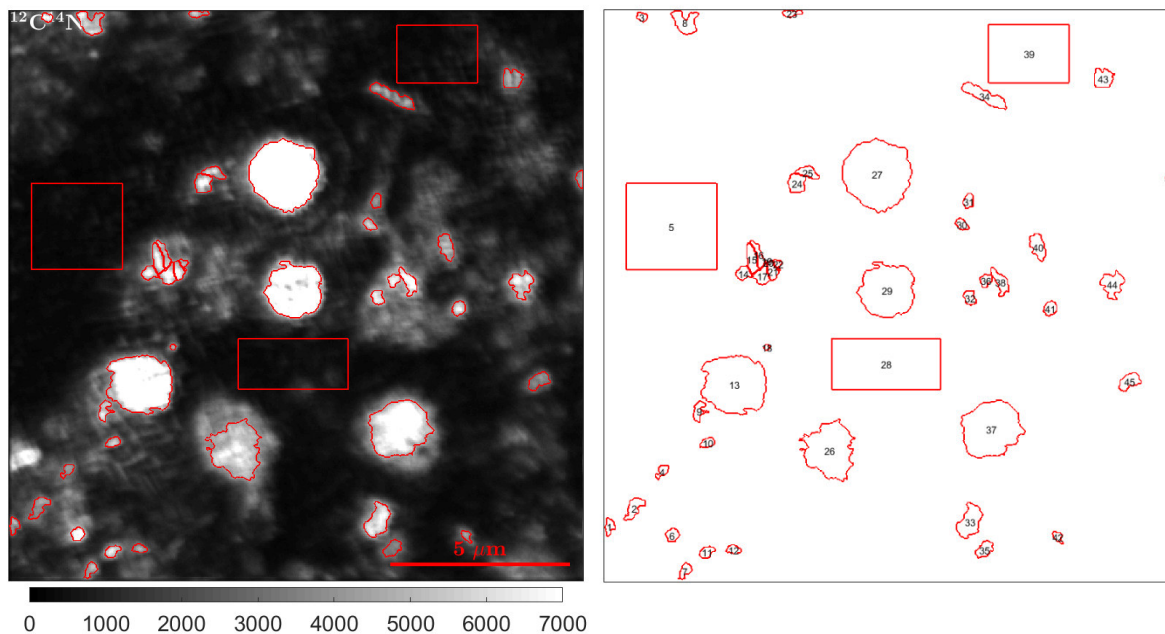
113

114   Fig. S14: ROI distribution of additional detail measurement #2 of unlabelled control sample as

115   shown in Fig. 8: 1: prokaryotic cell, 2: prokaryotic cell, 3: prokaryotic cell, 4: prokaryotic cell, 5:

116   resin matrix, 6: prokaryotic cell, 7: prokaryotic cell, 8: prokaryotic cell, 9: prokaryotic cell, 10:

117   prokaryotic cell, 11: prokaryotic cell, 12: prokaryotic cell, 13: phytoplankton compartment, 14:

118   prokaryotic cell, 15: prokaryotic cell, 16: prokaryotic cell, 17: prokaryotic cell, 18: prokaryotic

119   cell, 19: ignored due to insignificant ion counts, 20: ignored due to insignificant ion counts, 21:

120   prokaryotic cell, 22: prokaryotic cell, 23: prokaryotic cell, 24: prokaryotic cell, 25: prokaryotic

121   cell, 26: phytoplankton compartment, 27: phytoplankton compartment, 28: resin matrix, 29:

122   phytoplankton compartment, 30: prokaryotic cell, 31: prokaryotic cell, 32: prokaryotic cell, 33:

123   prokaryotic cell, 34: prokaryotic cell, 35: prokaryotic cell, 36: prokaryotic cell, 37: phytoplankton

14

124   compartment, 38: prokaryotic cell, 39: resin matrix, 40: prokaryotic cell, 41: prokaryotic cell, 42:

125   prokaryotic cell, 43: prokaryotic cell, 44: prokaryotic cell, 45: prokaryotic cell, 46: prokaryotic

126   cell.
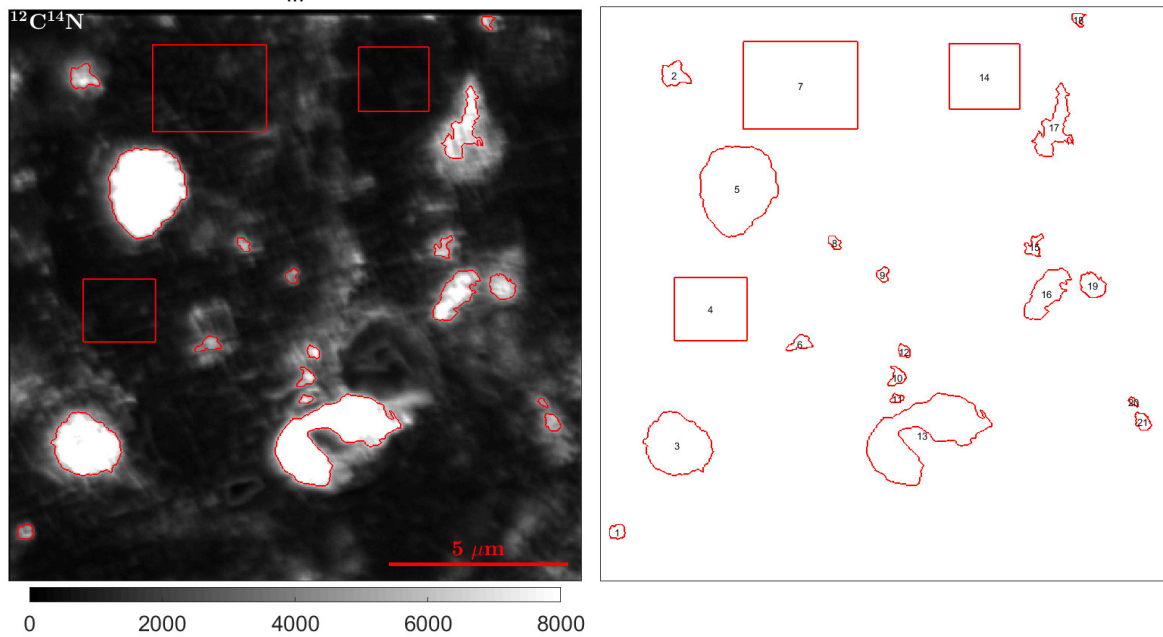
127

128   Fig. S15: ROI distribution of additional detail measurement #3 of unlabelled control sample as

129   shown in Fig. 8: 1: prokaryotic cell, 2: prokaryotic cell, 3: phytoplankton compartment, 4: resin

130   matrix, 5: phytoplankton compartment, 6: prokaryotic cell, 7: resin matrix, 8: prokaryotic cell, 9:

131   prokaryotic cell, 10: prokaryotic cell, 11: prokaryotic cell, 12: prokaryotic cell, 13: phytoplankton

132   compartment, 14: resin matrix, 15: prokaryotic cell, 16: prokaryotic cell, 17: prokaryotic cell, 18:

133   prokaryotic cell, 19: prokaryotic cell, 20: prokaryotic cell, 21: prokaryotic cell.
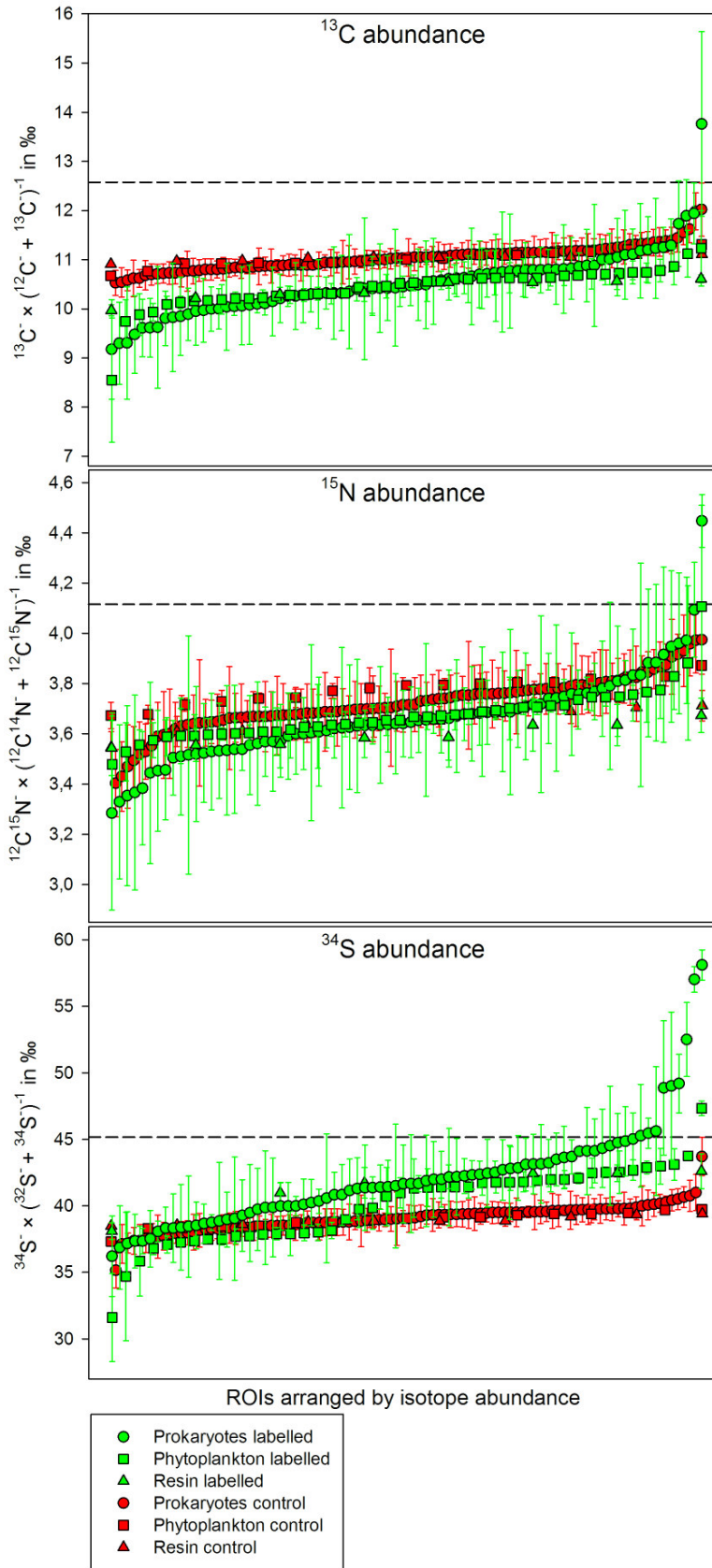
135   Fig. S16: Original, uncorrected isotope abundances in ‰, including Poisson Errors as error bars,

136   of all measured prokaryotic and phytoplankton cells as well as the resin itself without correction

137   using the internal standard. The dashed line indicates the enrichment threshold (maximum value

138   of the Poisson error of controls). Respective ROIs are shown in Suppl Fig. S8-S15.

139

Supplementary Chapter 1: Protocol and suggestions for CARDFISH procedure

141   Catalyzed reporter deposition fluorescence *in situ* hybridization (CARDFISH; Pernthaler et

142   al. 2002) enables the microscopical identification of specific microbial groups (FISH) with an

143   increased signal (CARD). Our procedure was based on an existing protocol for paraffin embedded

144   specimens on glass slides (Blazejak et al. 2005) with several modifications:

145   Methacrylate slices were encircled using a hydrophobic immunostaining pen (Daido Sangyo,

146   Japan). Endogenous peroxidase was inactivated by incubating with 0.01 M HCl for 10 min at room

147   temperature followed by a washing step in UW. Enzymatic digestion using Lysozyme as described

148   in the standard protocol (see above) for 1 hour at 37°C followed a washing step in PBST (0.01%

149   Triton X100 in 1 x PBS) and UW for 5 min, respectively. Hybridization buffer (HB) with 55%

150   formamide concentration was prepared according to standard protocols (see above). HB was

151   supplemented with 1% horseradish-peroxidase-labeled probe (final concentration 1pmol/µL) of the

152   control probes for eubacteria EUB338I (Amann et al. 1990), EUB338II and EUB338III (Daims et

153   al. 1999) as well as the nonsense probe as negative control, NonEUB (Wallner et al. 1993). The

154   samples were incubated with HB-probe mixture for 3 hours at 35°C in a humidity chamber (piece

155   of tissue supplemented with 2 – 3 mL of 55% Formamide and 45% UW in a 50 mL centrifugation

156   tube). HB was washed off twice in washing buffer (WB) for 5 min, followed by a washing step in

157   preheated WB for 30 min up to 1 hour at 37°C depending on background signal intensity. WB was

158   washed off in 1 x PBST for 15 min – 1 hour at 37°C. Immediately after this step CARD was carried

159   out to prevent the specimens running dry. Amplification buffer (AB), containing 0.0015% H_2O_2

160   and 0.005 – 0.05% fluorescently (carboxyfluorescein) labelled tyramide was added to the slices

161   and incubated for 20 min at 37°C in a humidity chamber (50 mL centrifugation tube including UW

162   soaked tissue) with UW. Afterwards AB was washed off in 1 x PBS twice at room temperature and

163   a third time in PBST for up to 1.5 hours at up to 60°C depending on background signal intensity.

164   After a short washing step in UW slides were air dried and counterstained with DAPI oil (see main

165   text). All washing steps were done under gentle shaking conditions to increase washing, but to

166   prevent slices from peeling off the glass slide.

167   Positive hybridization could be achieved, as well as negative results using the negative control

168   probe (Fig. S17). However, as the overlap with DAPI and Chl *a* autofluorescence (Fig. S18)

169   demonstrates, not all cells were hybridized. This may be due to non-optimal temperature or

170   formamide concentrations during hybridization or inhibited penetration of the probes into the resin.

171   Interestingly, the enzymatic digestion seemed not to be necessary, as treatments without digestion

172   resulted in comparable signals. The fact that FISH protocols could successfully be applied for

173   Technovit embedded benthic consortia by McGlynn et al. (2015) points potentially towards

174   inhibited penetration of tyramide conjugate through CARD amplification. The proof for that and

175   optimization requires further investigations.

176
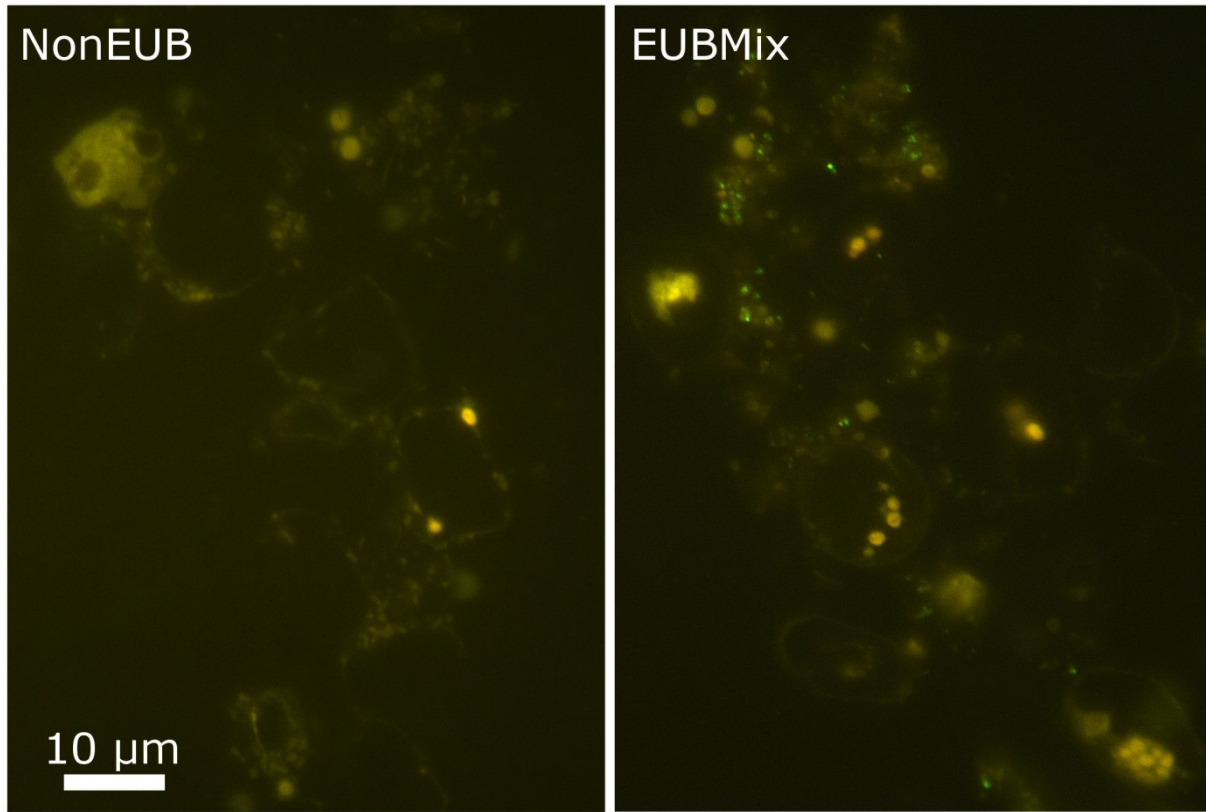
Fig. S17: Example for CARDFISH treatment: Fluorescence micrographs show the binding of the mixed EUBI - III (EUBMix) probe in green while the nonsense probe NonEUB shows no hybridization.
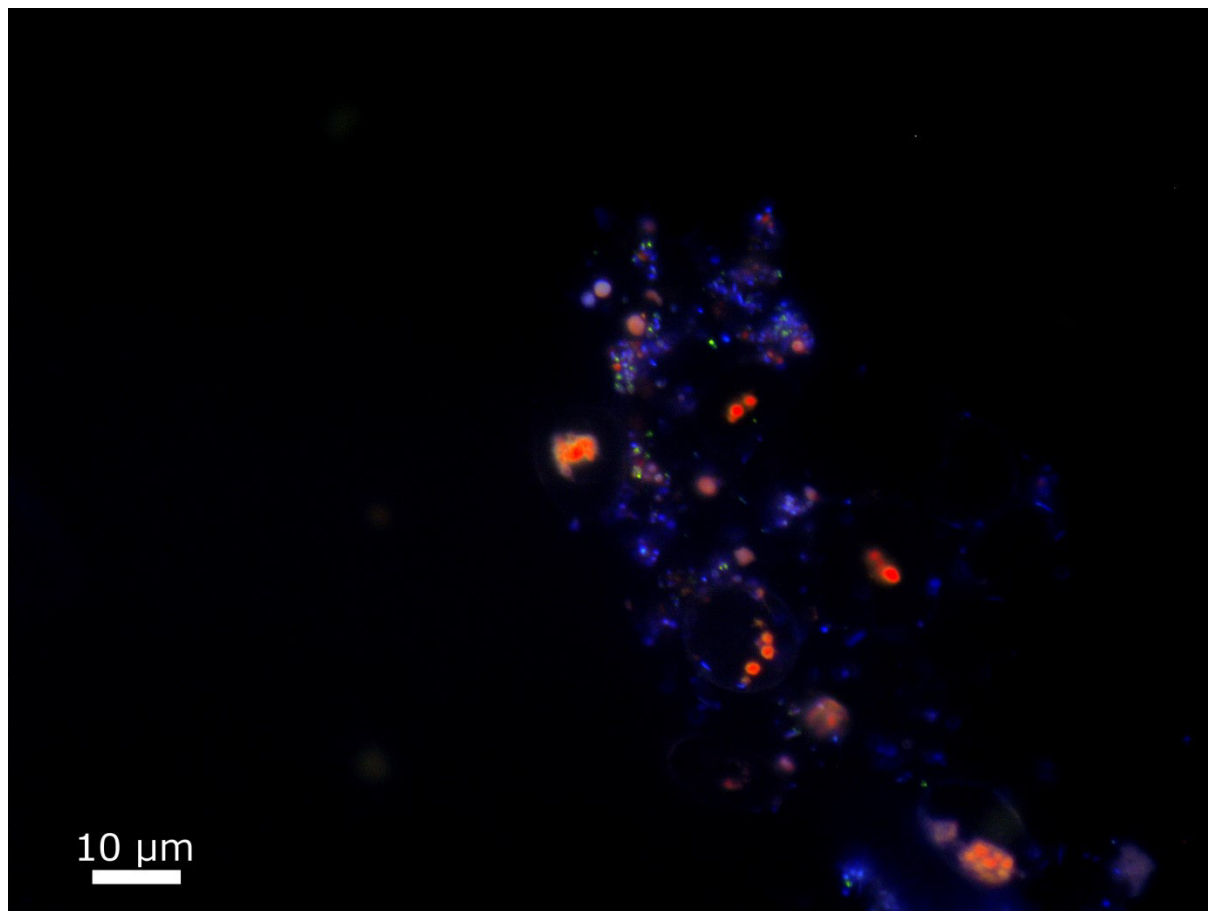
Fig. S18: Overlap image of DNA staining using DAPI using DAPI (blue), chlorophyll *a* auto-fluorescence (red) and CARDFISH of the EUBI-III probe (EUBMix; green) demonstrates positive signals but missing stringency.

Further protocol improvements, should consider that in our tests Biobond was ineffective as an adhesive during CARDFISH procedure. This is likely due to solvent effects associated with high formamide concentrations in the hybridization buffer. Here, the use of a mixture of $2-10\%$ acetone in UW as bedding between the slide and slice showed more promising results. The presence of acetone serves to soften the slice and increases bonding. Furthermore, careful handling during the CARDFISH process, i.e. reduction of shaking and increasing of washing time, notably improved successful binding.

191   Table S1: Comparison of embedding techniques between Flintrop et al. (in press), using cryogel

192   (Tissue-Tek® O.C.T.™ Compound; Sakura Fine Tek, Japan) and this study, using hard acrylic

193   and epoxy resins. Here we highlight a number of specific advantages of each method with regard

194   to handling time and convenience, and final analysis. See text and Flintrop et al. (in press) for

195   details.

	Cryogels (Flintrop et al. (in press))	**Hard and soft plastic resins: Methacrylate/ Araldite (Rogge et al.)**
Primary mode of Handling	Cryogel filled drifting sediment traps: passive handling From MSC[a] and lab-made aggregates: active handling	Active for lab-made aggregates and from MSC[a]
Active handling steps until immobilization	Gel traps: no active handling prior to sample mounting MSC[a]: min. 1 transfer from MSC to mold[b]	Gel traps: not tested MSC[a]: min. 2 transfers: pre-warming and pre-embedding[b]
Time required until sample is ready for sectioning[b]	Cryogel filled drifting sediment traps: 0 h (embedded in situ) MSC[a]: <5 min hands-on <1 h hands-off	~1 h hands-on ~74 h hands-off
Storage temperature of embedded samples	Below freezing point	Room temperature

Shelf life of embedded samples	Years to decades[c]	several decades
Slice thickness	5 – 100 μm	1 – 3 μm (methacrylate) 40 – 140 μm (araldite)
Storage temperature of sliced samples	-20°C or 4°C	Room temperature
Shelf life of sliced samples	Years to decades[c]	several decades
Successfully tested FISH protocols	monoFISH, MILFISH, CARDFISH	monoFISH[d]
Usability for NanoSIMS	No existing protocols	Yes: vacuum resistance, low dilution effects of N and S, no shrinking
Limitations when lithogenic compounds are included	Minimum slicing thickness 5μm; >5 μm no detectable rupture[e]	Leads to scratches or rupture with methacrylate / Araldite eliminates structural deformations
Treatment with organic solvents[b]	Polyvinyl alcohol (<11%)	Exchange of water with ethanol or acetone (100%)
Temperature treatment until sample is ready for sectioning	-20°C – room temperature[f]	4 – 50°C[g]

	Alcian Blue, Coomassie Brilliant Blue, Concanavalin A, Ruthenium Red, Periodic Acid Schiff-base stain, DAPI, FISH	Alcian Blue, Coomassie Brilliant Blue, eosin Y / phloxine B, DAPI, FISH
Tested stains	Alcian Blue, Coomassie Brilliant Blue, Concanavalin A, Ruthenium Red, Periodic Acid Schiff-base stain, DAPI, FISH	Alcian Blue, Coomassie Brilliant Blue, eosin Y / phloxine B, DAPI, FISH
Further possibilities	Variety of established staining protocols and cryogels	Variety of established staining protocols and resins

196

197 [a] MSC: Marine Snow Catcher; [b] excluding fixation or staining prior to embedding; [c] when stored

198 adequately in air-tight containers to prevent dehydration of cryogel during long-term storage; [d]

199 monoFISH was carried out elsewhere (McGlynn et al. 2015), whereas CARDFISH was tested in

200 this study but requires further development (see Supplementary chapter 1); [e] cannot be ruled out

201 due to pliable nature of cryogel; [f] processing at room temperature, storage at -20°C and slicing at

202 -25 to -30°C; [g] exothermic polymerization temperature does not exceed 50°C on cooling block

203

References

205 Amann, R. I., B. J. Binder, R. J. Olson, S. W. Chisholm, R. Devereux, D. A. Stahl. 1990.

206   Combination of 16S rRNA-targeted oligonucleotide probes with flow cytometry for

207   analyzing mixed microbial populations. Appl Environ Microbiol. 56: 1919–1925

208 Blazejak, A., C. Erseus, R. I. Amann, N. Dubilier. 2005. Coexistence of bacterial sulfide

209   oxidizers, sulfate reducers, and spirochetes in a gutless worm (Oligochaeta) from the Peru

210   margin. Appl. Environ. Microbiol. 71: 1553–1561, doi: 10.1128/AEM.71.3.1553-1561.2005

211   Daims, H., A. Brühl, R. Amann, K.-H. Schleifer, M. Wagner. 1999. The Domain-specific Probe

212   EUB338 is Insufficient for the Detection of all Bacteria. Syst Appl Microbiol. 22: 434–444,

213   doi: 10.1016/S0723-2020(99)80053-8

214   Flintrop, C., A. Rogge, S. Miksch, A. M. Waite, M. H. Iversen. in press. Embedding and slicing

215   of intact in situ collected marine snow. Limnol. Oceanogr.: Methods, doi:

216   10.1002/lom3.10251

217   McGlynn, S. E., G. L. Chadwick, C. P. Kempes, V. J. Orphan. 2015. Single cell activity reveals

218   direct electron transfer in methanotrophic consortia. Nature. 526: 531–535, doi:

219   10.1038/nature15512

220   Pernthaler, A., J. Pernthaler, R. I. Amann. 2002. Fluorescence In Situ Hybridization and

221   Catalyzed Reporter Deposition for the Identification of Marine Bacteria. Appl. Environ.

222   Microbiol. 68: 3094–3101, doi: 10.1128/AEM.68.6.3094-3101.2002

223   Wallner, G., R. Amann, W. Beisker. 1993. Optimizing fluorescent in situ hybridization with

224   rRNA-targeted oligonucleotide probes for flow cytometric identification of microorganisms.

225   Cytometry. 14: 136–143, doi: 10.1002/cyto.990140205

226

227

228

229

230

Supplementary Information

for

Paper IV

Supplementary Information for

Arctic sea ice enhances vertical connectivity of microbial communities through sinking particles

Eduard Fadeev, Morten H. Iversen, Claudia Wekerle, Ian Salter, Christina Bienhold, Andreas Rogge, Anya M. Waite, Laura Hehemann, Antje Boetius

Eduard Fadeev
Email: eduard.fadeev@awi.de

This PDF file includes:

SI Materials and Methods
Figs. S1 to S6
Table S1 to S2
SI reference citations

SI Materials and Methods

In situ measured marine particle size distribution. The in situ profiling of marine particles was carried out using Underwater Vision Profiler 5hd (UVP; Hydroptic, France) mounted to the water sampler rosette (1). The UVP5hd was operated in autonomous pressure mode (1), whereas acquisition was limited to the downcast. Maximum acquisition frequency was 20 Hz and the sampling volume was approximately 1L. The acquired images were analyzed using Zooprocess software (2) and Ecotaxa (3). The exported particle size distribution was based on 26 size classes of equivalent spherical diameter sorted in a logarithmic scale from 64 µm to 26.79 mm. For the purpose of this publication the particles were summed up into two size classes, small particles with equivalent spherical diameter 60-512 µm, and large particles 0.512-10.3 mm. The particles size is converted to volume assuming spherical structure. The total particle volumes are presented in ppm (particle volume / water volume).

On board characterization of marine particles and sinking velocity measurements. Using a marine snow catcher (MSC) we sampled intact aggregates of both ice-free and ice-covered regions, and measured on board their size, composition, and sinking velocities. The aggregates were individually transferred to a vertical flow chamber (4, 5) that was filled with GF/F filtered seawater collected from the same MSC and kept at in situ temperature. The x-, y-, and z-axis of each aggregate were measured in the vertical flow system using a horizontal dissection microscope and an ocular. The volume was thereafter calculated assuming an ellipsoid form, which was used to calculate the equivalent spherical diameter (ESD). The sinking velocity was measured by placing the aggregate in the middle of the flow chamber and increasing the upward flow until the aggregate was floating one diameter above the net. The sinking velocity was thereafter calculated by determining the flow speed three times, and dividing the average of these measurements by the area of the flow chamber. The composition of the aggregates was determined with an inverted light microscope using Utermöhl chambers (Fig. 2).

Modeled particles sinking trajectories. We use a Lagrangian particle tracking algorithm to track back particles from the sampling depth to the surface. It is based on the following equation:

$$\frac{d\,x}{dt} = \boldsymbol{u}(x, t),$$

Where x is the 3D particle position and u is the 3D velocity field at the particle position. If we knew the particle position at time n, the position at time n+1 will be:

$$x(t_{n+1}) = x(t_n) + \int_{t_n}^{t_{n+1}} u(x, t)\, dt.$$

The backward particle computation is done by reversing the flow field, i.e. particles are treated as if they were rising from the sampling depth to the surface with a negative sinking speed, being horizontally displaced with the reversed horizontal velocity. Particles were advected with daily averaged horizontal model velocities from the ocean general circulation model FESOM, whereas a constant sinking speed is used as vertical velocity. FESOM is an ocean-sea ice model based on unstructured meshes (6, 7). In this study, we use a FESOM configuration that was optimized for the Fram Strait, applying a mesh resolution of 1 km in this area (8). A more detailed description of the Lagrangian particle tracking approach, applied to study the catchment area of sediment traps deployed in the Fram Strait, is presented in the study by (9)

The backward trajectory calculation was performed for all three sampled regions (ice-free HG stations, and ice covered - EG and N), using the measured on board sinking velocities (Table 1). The duration of trajectories released at ~2600 m depth (the seafloor) were thus ~40 days. Trajectories were computed once per day during the time period March – July 2016. A time step of 1 hour was used for the trajectory calculation, and thus hourly positions and corresponding temperature and salinity values were stored. To quantify the vertical distribution of particles, particle positions are binned into a grid with bin size of 25 m depth x 0.05° Longitude/Latitude and then divided by the total number of particles to determine the fraction of particles originating from each grid box (Fig. 2). The daily concentrations were of sea ice were retrieved from Centre d'Exploitation et de Recherche SATellitaire (CERSAT; http://cersat.ifremer.fr/).

Water sampling and metadata collection. The sampling was carried out with 12 L Niskin bottles mounted on a CTD rosette (Sea-Bird Electronics Inc. SBE 911 plus probe) equipped with double temperature and conductivity sensors, a pressure sensor, altimeter, chlorophyll a fluorometer, and transmissometer. Hydrographic data of the seawater including temperature and salinity were retrieved at PANGAEA (10), as well as chlorophyll a concentrations in the water column (11). The integrated chlorophyll a over the depth of the euphotic zone was calculated according to Boss and Behrenfeld 2010 (12). The mean monthly sea-ice

concentrations were retrieved from http://data.seaiceportal.de (13). Sea surface temperature was obtained from NOAA NCEP real-time analysis (http://polar.ncep.noaa.gov/sst/rtg_high_res/).

At all stations water samples were collected from surface at 10 - 30 m, 100 m, 1000 m and ~50 m above the seafloor (Table S1). For assessing archaeal and bacterial community composition 4L in epipelagic (<100 m) and 8-12L in meso- and bathypelagic waters were filtered with a peristaltic pump (Masterflex; Cole Parmer) through successive membrane filters of 5 µm (Whatman Nucleopore, 47 mm polycarbonate), and 0.22 µm (Millipore Sterivex filters). All samples were collected in duplicates and stored at -20°C until DNA isolation.

DNA isolation and 16S rRNA amplicon sequencing. Genomic bacterial and archaeal DNA was isolated from the 5 µm- and the 0.22 µm- filter membranes to analyze the particle-associated (PA) and the free-living (FL) community. The isolation was conducted by a combined chemical and mechanical procedure using the PowerWater DNA Isolation Kit (MO BIO Laboratories, Inc., Carlsbad, CA, USA). Prior to DNA isolation the Sterivex cartridges of the 0.22 µm membranes were cracked open in order to place the filters in the kit-supplied bead beating tubes. The isolation was continued according to the manufacturer's instructions, and DNA was stored at - 20°C. Library preparation was performed according to the standard instructions of the 16S Metagenomic Sequencing Library Preparation protocol (Illumina, Inc., San Diego, CA, USA). The hyper variable V4–V5 region of the 16S rRNA gene was amplified using bacterial primers 515F-Y (5`-GTGYCAGCMGCCGCGGTAA-3`) and 926R (5`-CCGYCAATTYMTTTRAGTTT-3`)(14). Sequences were obtained on the Illumina MiSeq platform in a 2 × 300 bp paired-end run (CeBiTec Bielefeld, Germany), following the standard instructions of the 16S Metagenomic Sequencing Library Preparation protocol (Illumina, Inc., San Diego, CA, USA).

Bioinformatics and statistical analyses. The raw paired-end reads were primer-trimmed using cutadapt (15), quality trimmed using trimmomatic with sliding window of 4 bases and a minimum average quality of 15 v0.32 (16) and merged using PEAR v0.9.5 (17). Clustering into OTU was done with Swarm algorithm using default parameters v2.0 (18). One representative sequence per OTU was taxonomically classified using SINA v1.2.11 (19) against Silva reference database release 132 (20) at a minimum alignment similarity of 0.9,

and a last common ancestor consensus of 0.7. The OTUs which were not taxonomically assigned to Bacteria/Archaea (based on the data set) or occurred with only a single sequence in the whole data set were excluded from further analysis. Furthermore, all OTUs which were taxonomically assigned to mitochondria and chloroplast were removed from the dataset.

All the statistical analyses were conducted using R v3.4.1 (http://www.Rproject.org/) in RStudio v1.0.153 (21). Sample data matrices were managed using the R package 'phyloseq' v1.20.0 (22) and plots were generated using R package 'ggplot2' v2.2.1 (23). The samples rarefaction analysis and alpha diversity calculations were conducted using R package 'iNEXT' v2.0.12 (24). The rarefaction curves for each sample were generated based on 40 equally spaced rarefied sample sizes with 100 iterations.

A prevalence threshold (i.e., in how many samples did a taxon appear at least once) of 5% was applied to the OTU table prior to downstream analysis following (25). Principal component analysis (PCA) and dissimilarity comparisons between FL and PA communities were conducted on variance stabilized OTUs abundance matrix (26). The significance of the clustering was tested using 'ADONIS' (Permutational Multivariate Analysis of Variance Using Distance Matrices) function in R package 'vegan' v2.5-2 (27). The fold-change in abundance of each OTU between the water layers was calculated using the R package 'DEseq2' v1.16.1 (28). The method applies a generalized exact binomial test on variance stabilized OTU abundance.

Microbial source tracking. A Bayesian MST algorithm 'SourceTracker' v1.0 (29) was applied to estimate potential colonization of marine particles by free-living microbes, and their export from surface water to the deep ocean. The algorithm performance was validated using 'leave-one-out' approach, in which each 'source' (i.e., FL) community was hidden, in turn, from the training datatset, and its origin was predicted based on the rest of the source samples in the dataset. The entire analysis was conducted under default conditions: burn-in period – 100, restarts - 10, dirichlet hyperparameters (α, β) - 0.001. All samples were randomly sub-sampled to 4000 reads.
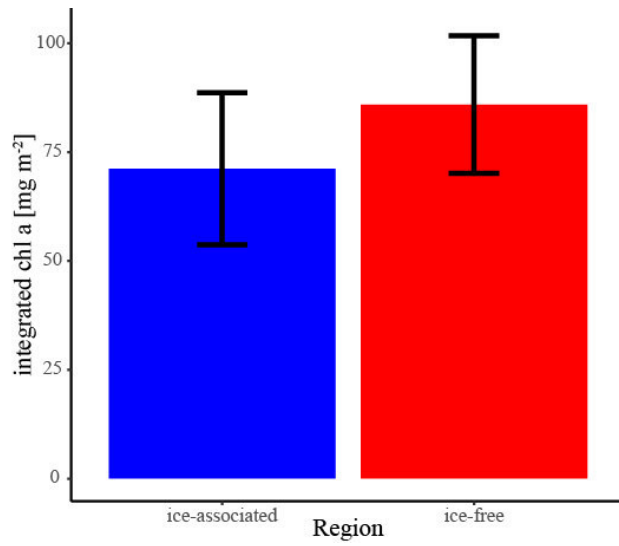
Fig. S1: Mean chlorophyll a concentration integrated over the depth of the euphotic zone in ice-covered (4 stations) and ice-free (5 stations) regions of the Fram Strait.
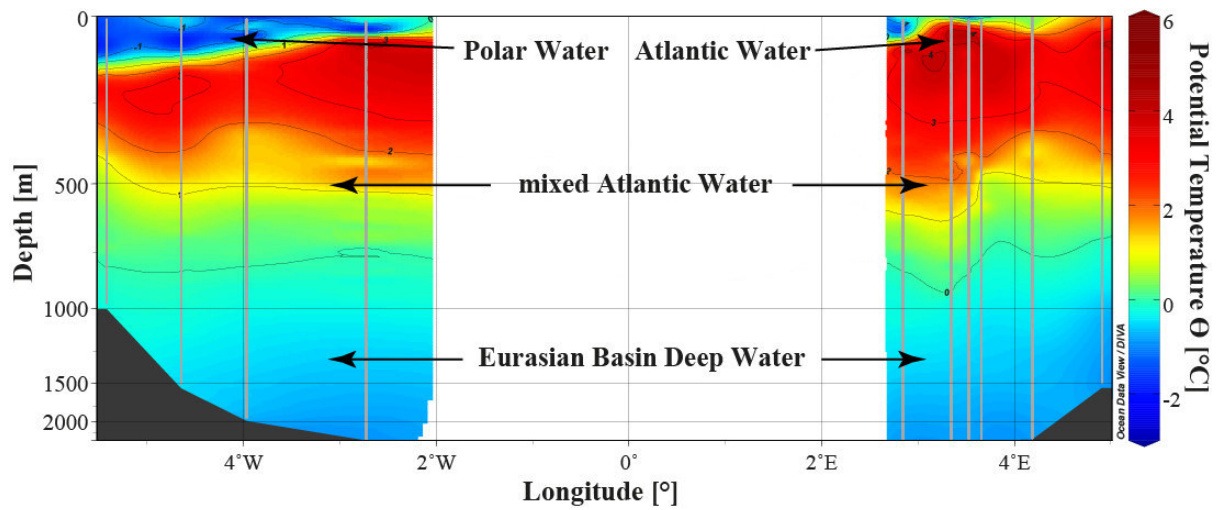
Fig. S2: Potential temperature (θ) of the water column along the 79°N latitude in the Fram Strait. The gray lines represent the location of the measurement, conducted using a CTD (Conductivity-Temperature-Depth) sensor. The values were plotted using Ocean Data View v5.0.0 (30) and spatially extrapolated using DIVA algorithm in Ocean Data View.
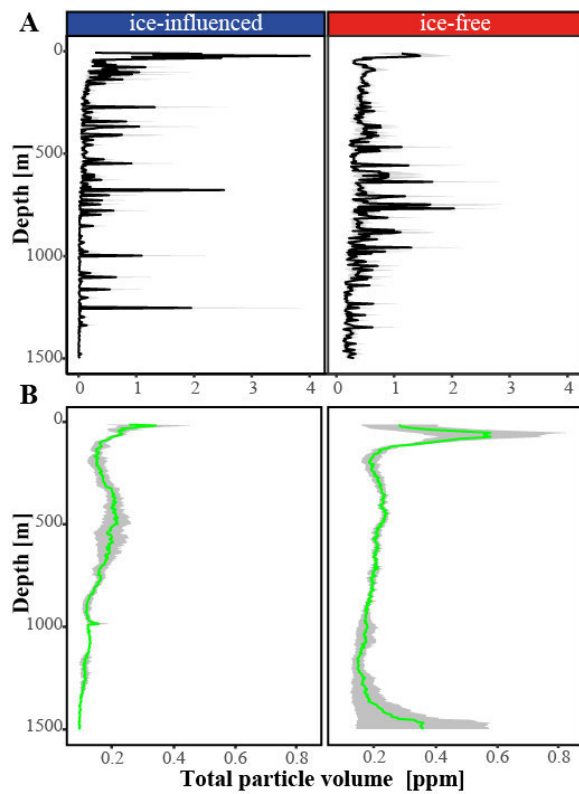
Fig. S3: Mean vertical distribution profiles of particles in ice-covered and ice-free regions. (A) The total volume of large particles (0.512-10.3 mm). (B) The total volume of small particles (64-512 µm). The total volume of particles was calculated assuming spherical structure of the particles. The gray area represents the standard error between the stations in each region.
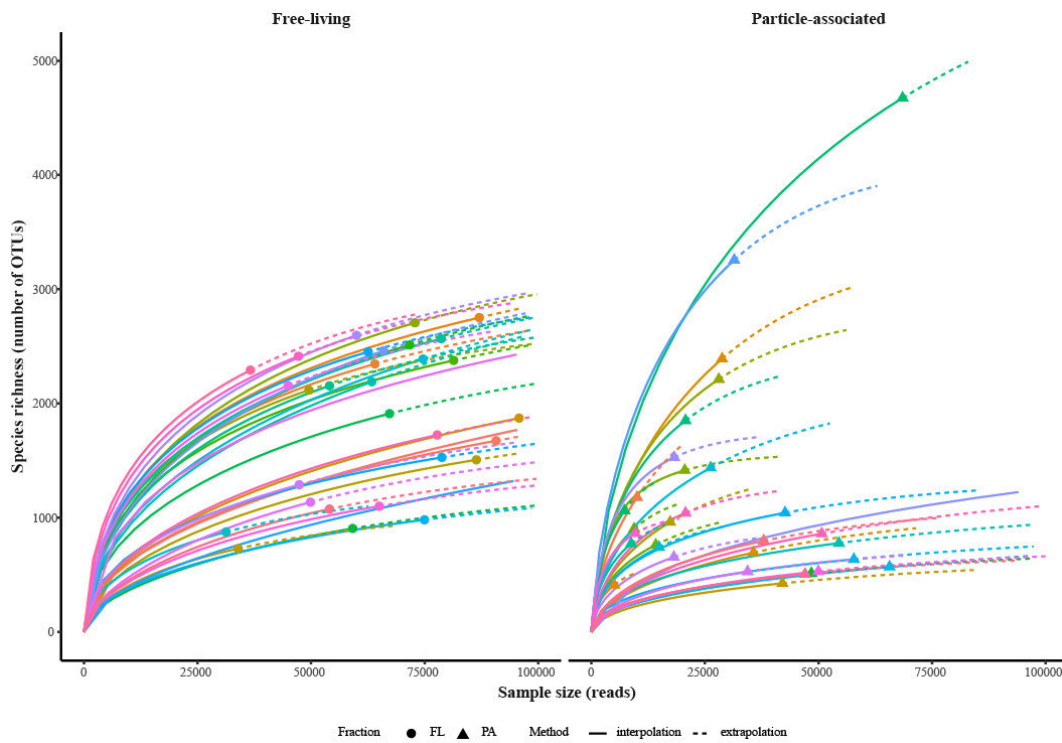
Fig. S4: Rarefaction analysis of 16S rRNA gene analysis of bacterial and archaeal communities. The solid lines represent the observed accumulation with the number of reads sampled, and the dashed lines represent the extrapolated accumulation up to the double amount of reads. The observed values for each community are denoted by solid shapes. Sample-size-based rarefaction curves generated with the R-package "iNEXT", based on the Hill number of order q = 0.
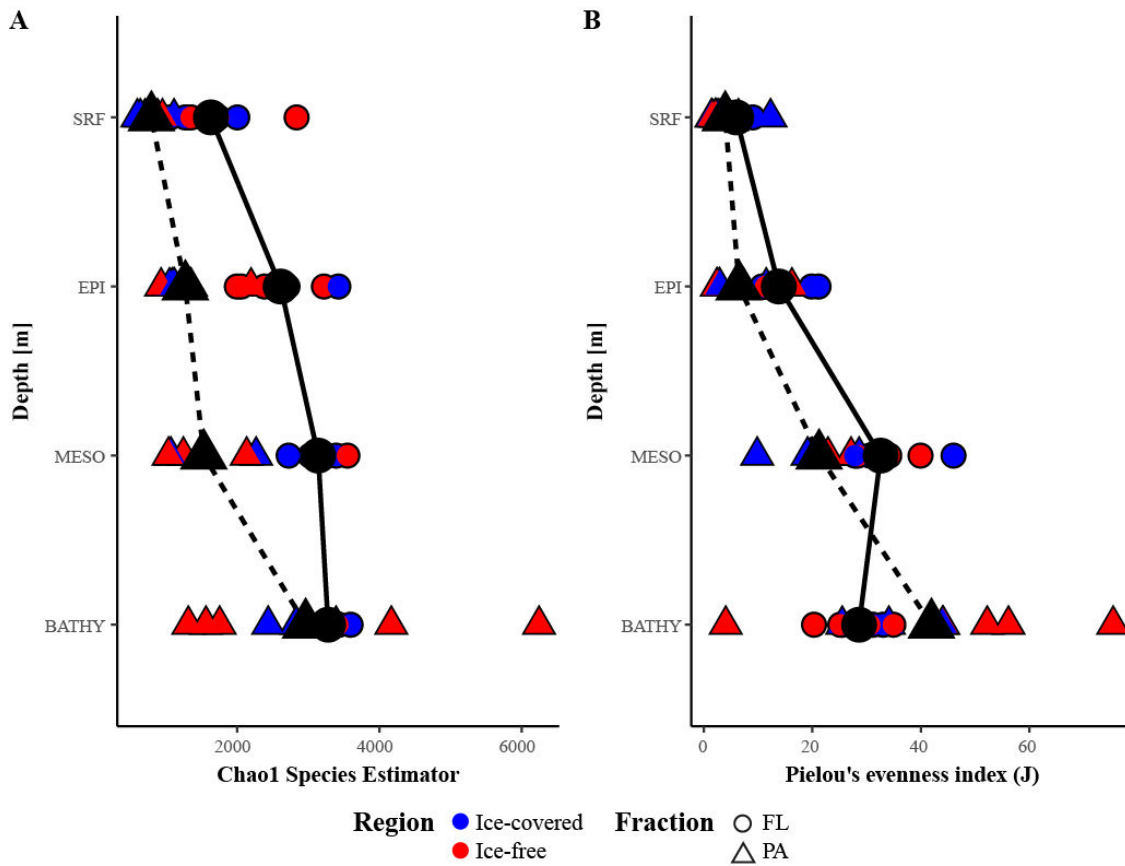
Fig. S5: Alpha diversity of microbial communities by depth. (A) Chao1 species estimator. (B) Pielou's evenness index (*J'*). Black points connected with a line represent the mean values for each fraction at each depth ('SRF' ~20m, 'EPI' – 100m, 'MESO' – 1000m, 'BATHY' >1200m), and the colored points represent individual samples and their geographic origin. The calculation of the alpha diversity indices was conducted using the R-package "iNEXT".
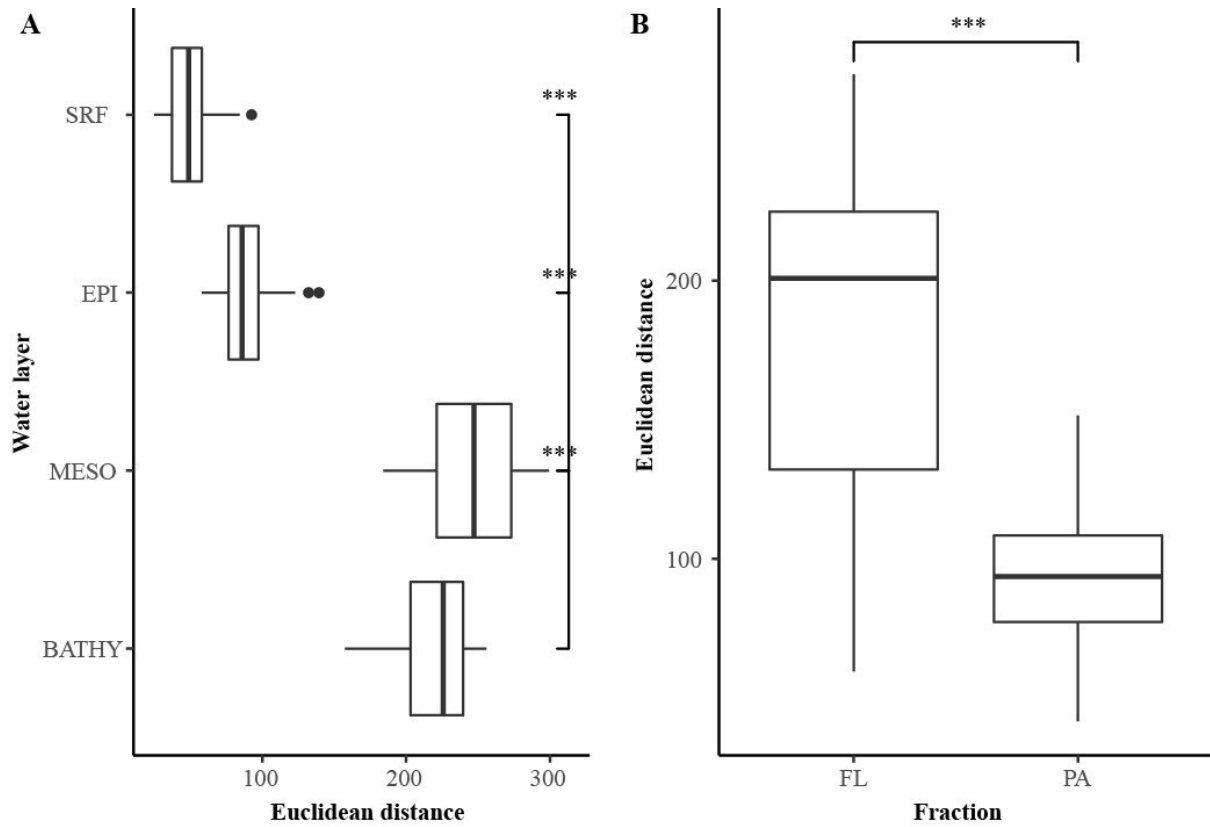
Fig. S6: Dissimilarity distribution between microbial communities. (A) Box-plots of distances between FL and PA communities, at each depth ('SRF' ~20m, 'EPI' – 100m, 'MESO' – 1000m, 'BATHY' >1200m). (B) Dissimilarities within FL and PA fractions throughout the entire water column. The asterisks represent the statistical significance of Mann-Whitney-Wilcoxon test between the different depths (p value <0.001).

Table S1: Overview of microbial samples collected during RV Polarstern expedition PS99.2.

The table consists of sampling information for each station, number of sequences and alpha

diversity estimations, conducted using the R package 'iNEXT'.

PANGAEA StationID	Station Name	Long (°E)	Lat (°N)	Ice covered ?	Layer	Depth (m)	Fraction	No of sequences	No of OTUs	Chao1 richness	Richness coverage (%)	Shannon diversity index (H)	Simpsons diversity Index	Pielou's evenness index (J)	Good's completeness estimator (%)
PS99/051-1	EG1	-5.418	78.990	Yes	SRF	13	FL	86382	1507	2003	75	49.6	11.5	6.8	99
PS99/051-1	EG1	-5.418	78.990	Yes	SRF	13	PA	5038	412	597	69	74.0	22.0	12.3	97
PS99/051-1	EG1	-5.418	78.990	Yes	EPI	100	FL	67267	1911	2609	73	150.0	39.5	19.9	99
PS99/051-1	EG1	-5.418	78.990	Yes	EPI	100	PA	14181	762	1113	68	76.4	23.9	11.5	98
PS99/051-1	EG1	-5.418	78.990	Yes	MESO	971	FL	36646	2292	3118	74	356.0	65.7	46.0	98
PS99/051-1	EG1	-5.418	78.990	Yes	MESO	971	PA	7301	1062	1484	72	133.2	11.6	19.1	94
PS99/048-11	EG4	-2.729	78.816	Yes	SRF	24	FL	31292	876	1270	69	61.2	16.1	9.0	99
PS99/048-11	EG4	-2.729	78.816	Yes	SRF	24	PA	54502	778	1113	70	15.9	4.6	2.4	99
PS99/048-11	EG4	-2.729	78.816	Yes	EPI	100	FL	74645	2389	3423	70	164.5	44.5	21.1	99
PS99/048-11	EG4	-2.729	78.816	Yes	EPI	100	PA	14909	742	1050	71	48.4	13.2	7.3	98
PS99/048-1	EG4	-2.729	78.816	Yes	MESO	1000	FL	78634	2567	3392	76	218.5	52.6	27.8	99
PS99/048-1	EG4	-2.729	78.816	Yes	MESO	1000	PA	8769	773	1069	72	137.8	40.9	20.7	97
PS99/048-1	EG4	-2.729	78.816	Yes	BATHY	2527	FL	54056	2155	2899	74	196.1	59.9	25.6	99
PS99/048-1	EG4	-2.729	78.816	Yes	BATHY	2527	PA	20737	1851	2437	76	331.0	81.7	44.0	97
PS99/055-1	N4	4.508	79.739	Yes	SRF	22	FL	54053	1076	1548	69	42.5	16.6	6.1	99
PS99/055-1	N4	4.508	79.739	Yes	SRF	22	PA	47046	507	707	72	17.2	7.0	2.8	100
PS99/055-1	N4	4.508	79.739	Yes	EPI	100	FL	90722	1674	2489	67	79.7	26.3	10.7	99

PS99/055-1	N4	4.508	79.739	Yes	EPI	100	PA	37949	798	1118	71	19.6	7.4	2.9	99
PS99/055-7	N4	4.508	79.739	Yes	MESO	1000	FL	64043	2346	3030	77	250.6	65.5	32.3	99
PS99/055-7	N4	4.508	79.739	Yes	MESO	1000	PA	10060	1178	2267	52	202.5	56.5	28.6	94
PS99/055-7	N4	4.508	79.739	Yes	BATHY	2500	FL	87025	2752	3595	77	261.8	84.7	33.1	99
PS99/055-7	N4	4.508	79.739	Yes	BATHY	2500	PA	28778	2391	3391	71	198.4	40.7	25.5	97
PS99/053-2	N5	3.062	79.921	Yes	SRF	19	FL	33960	730	1061	69	22.9	7.5	3.5	99
PS99/053-2	N5	3.062	79.921	Yes	SRF	19	PA	42075	426	640	67	8.5	3.3	1.4	100
PS99/053-2	N5	3.062	79.921	Yes	EPI	100	FL	95782	1872	2708	69	82.4	25.6	10.9	99
PS99/053-2	N5	3.062	79.921	Yes	EPI	100	PA	35708	695	1088	64	18.7	7.2	2.9	99
PS99/053-2	N5	3.062	79.921	Yes	MESO	1000	FL	49521	2117	2725	78	234.5	62.8	30.6	99
PS99/053-2	N5	3.062	79.921	Yes	MESO	1000	PA	17343	962	1485	65	67.6	18.2	9.8	98
PS99/053-2	N5	3.062	79.921	Yes	BATHY	2427	FL	72863	2706	3428	79	246.4	79.1	31.2	99
PS99/053-2	N5	3.062	79.921	Yes	BATHY	2427	PA	28063	2212	2832	78	262.7	60.1	34.1	97
PS99/066-05	HG1	6.088	79.138	No	SRF	17	FL	74929	982	1352	73	47.3	15.0	6.9	99
PS99/066-05	HG1	6.088	79.138	No	SRF	17	PA	57785	636	883	72	41.3	16.8	6.4	100
PS99/066-05	HG1	6.088	79.138	No	EPI	100	FL	78775	1528	2058	74	88.1	24.6	12.0	99
PS99/066-05	HG1	6.088	79.138	No	EPI	100	PA	42644	1043	1351	77	112.9	34.7	16.2	99
PS99/066-05	HG1	6.088	79.138	No	MESO	500	FL	62547	2452	3072	80	266.7	61.1	34.2	99
PS99/066-05	HG1	6.088	79.138	No	MESO	500	PA	26258	1437	2134	67	166.4	48.0	22.9	98
PS99/066-05	HG1	6.088	79.138	No	BATHY	1253	FL	65940	2461	3323	74	196.3	55.9	25.1	99
PS99/066-05	HG1	6.088	79.138	No	BATHY	1253	PA	31445	3255	4168	78	610.1	168.0	75.4	96
PS99/056-1	HG2	4.907	79.134	No	SRF	22	FL	106357	1406	2836	50	42.7	18.0	5.9	99

PS99/056-1	HG2	4.907	79.134	No	SRF	22	PA	65637	570	950	60	13.9	6.3	2.2	100
PS99/056-1	HG2	4.907	79.134	No	EPI	100	FL	114402	1922	3219	60	86.0	29.2	11.4	99
PS99/056-1	HG2	4.907	79.134	No	EPI	100	PA	169192	1530	2196	70	18.4	7.1	2.5	100
PS99/056-1	HG2	4.907	79.134	No	MESO	1000	FL	122433	2630	3550	74	168.8	49.6	21.4	99
PS99/056-1	HG2	4.907	79.134	No	BATHY	1500	FL	63364	2190	3417	64	156.2	51.9	20.3	99
PS99/056-1	HG2	4.907	79.134	No	BATHY	1500	PA	68506	4674	6244	75	474.4	97.3	56.1	98
PS99/042-11	HG4	4.185	79.065	No	SRF	28	FL	49852	1136	1737	65	42.1	16.2	6.0	99
PS99/042-11	HG4	4.185	79.065	No	SRF	28	PA	34397	529	772	69	13.1	5.4	2.1	99
PS99/042-11	HG4	4.185	79.065	No	EPI	100	FL	47394	1289	1996	65	92.3	28.9	12.9	99
PS99/042-11	HG4	4.185	79.065	No	EPI	100	PA	18161	655	931	70	40.5	12.8	6.3	99
PS99/042-01	HG4	4.185	79.065	No	BATHY	2462	FL	59986	2596	3347	78	274.6	75.2	34.9	99
PS99/042-01	HG4	4.185	79.065	No	BATHY	2462	PA	18246	1528	1755	87	382.9	115.8	52.2	98
PS99/059-2	HG9	2.841	79.134	No	SRF	24	FL	65026	1101	1547	71	25.5	7.0	3.6	99
PS99/059-2	HG9	2.841	79.134	No	SRF	24	PA	49964	530	755	70	9.7	3.6	1.6	100
PS99/059-2	HG9	2.841	79.134	No	EPI	100	FL	77765	1724	2384	72	86.8	28.3	11.6	99
PS99/059-2	HG9	2.841	79.134	No	EPI	100	PA	50728	860	1329	65	16.2	5.9	2.4	99
PS99/059-2	HG9	2.841	79.134	No	MESO	1000	FL	47208	2413	3147	77	311.1	70.7	39.9	98
PS99/059-2	HG9	2.841	79.134	No	MESO	1000	PA	9670	863	1037	83	137.9	17.7	20.4	98
PS99/059-2	HG9	2.841	79.134	No	BATHY	2499	FL	44936	2156	2935	73	234.8	68.4	30.6	98
PS99/059-2	HG9	2.841	79.134	No	BATHY	2499	PA	20740	1041	1314	79	28.1	4.3	4.0	98
PS99/041-5	S3	5.047	78.607	No	SRF	28	FL	59153	906	1325	68	41.9	17.4	6.1	99
PS99/041-5	S3	5.047	78.607	No	SRF	28	PA	48430	513	740	69	28.1	13.0	4.5	100

PS99/041-1	S3	5.047	78.607	No	MESO	1000	FL	81377	2377	3085	77	220.5	54.7	28.4	99
PS99/041-1	S3	5.047	78.607	No	MESO	1000	PA	9428	902	1244	73	184.6	39.2	27.1	96
PS99/041-1	S3	5.047	78.607	No	BATHY	2338	FL	71696	2512	3291	76	220.3	66.8	28.1	99
PS99/041-1	S3	5.047	78.607	No	BATHY	2338	PA	20579	1415	1563	91	320.1	66.8	44.1	99

Table S2: Estimated sources contribution to PA communities by 'SourceTracker'. The values represent the mean estimated contribution of different FL microbes to the PA communities along the water column ('SRF' ~20m, 'EPI' – 100m, 'MESO' – 1000m, 'BATHY' >1200m).

Station Name	Ice covered?	Type	Epipelagic AW	Epipelagic PW	Mesopelagic	Bathypelagic	Unknown
EG1	Yes	SRF	0 ± 0	0.81 ± 0	0 ± 0	0 ± 0	0.17 ± 0
EG1	Yes	EPI	0 ± 0	0.72 ± 0.01	0.1 ± 0.01	0.03 ± 0	0.13 ± 0.01
EG1	Yes	MESO	0 ± 0	0.05 ± 0	0.01 ± 0	0.01 ± 0	0.91 ± 0
EG4	Yes	SRF	0.01 ± 0	0.97 ± 0	0 ± 0	0 ± 0	0.01 ± 0
EG4	Yes	EPI	0.01 ± 0	0.9 ± 0	0.01 ± 0	0 ± 0	0.06 ± 0
EG4	Yes	MESO	0 ± 0	0.39 ± 0	0.08 ± 0	0 ± 0	0.5 ± 0.01
EG4	Yes	BATHY	0.01 ± 0	0.02 ± 0	0 ± 0	0.16 ± 0	0.79 ± 0
N4	Yes	SRF	0.95 ± 0	0.01 ± 0	0 ± 0	0 ± 0	0.02 ± 0
N4	Yes	EPI	0.33 ± 0.01	0.04 ± 0.01	0 ± 0	0 ± 0	0.61 ± 0
N4	Yes	MESO	0.01 ± 0	0.14 ± 0	0.01 ± 0	0 ± 0	0.82 ± 0
N4	Yes	BATHY	0.02 ± 0	0.11 ± 0	0.01 ± 0	0.46 ± 0	0.38 ± 0
N5	Yes	SRF	0.12 ± 0.02	0.86 ± 0.02	0 ± 0	0 ± 0	0 ± 0
N5	Yes	EPI	0.26 ± 0.03	0.7 ± 0.03	0 ± 0	0 ± 0	0.02 ± 0
N5	Yes	MESO	0.02 ± 0	0.17 ± 0	0 ± 0	0.41 ± 0	0.38 ± 0
N5	Yes	BATHY	0.01 ± 0	0.97 ± 0	0 ± 0	0 ± 0	0 ± 0
HG1	No	SRF	0.09 ± 0.01	0.83 ± 0.01	0 ± 0	0 ± 0	0.06 ± 0
HG1	No	EPI	0.05 ± 0.01	0.09 ± 0.01	0 ± 0	0.09 ± 0	0.74 ± 0
HG1	No	MESO	0.01 ± 0	0.98 ± 0	0 ± 0	0 ± 0	0 ± 0

HG1	**No**	**BATHY**	0.45 ± 0.03	0.52 ± 0.03	0 ± 0	0 ± 0	0.01 ± 0
HG2	**No**	**SRF**	0.01 ± 0	0.11 ± 0	0.03 ± 0	0 ± 0	0.83 ± 0
HG2	**No**	**EPI**	0.01 ± 0	0.1 ± 0	0 ± 0	0.02 ± 0	0.85 ± 0
HG2	**No**	**BATHY**	0.08 ± 0.01	0.9 ± 0.01	0 ± 0	0 ± 0	0 ± 0
HG4	**No**	**SRF**	0.08 ± 0.01	0.88 ± 0.01	0 ± 0	0 ± 0	0.02 ± 0
HG4	**No**	**EPI**	0.01 ± 0	0.39 ± 0	0.08 ± 0.01	0.04 ± 0.01	0.45 ± 0.01
HG4	**No**	**BATHY**	0.01 ± 0	0.41 ± 0	0 ± 0	0.22 ± 0	0.34 ± 0
HG9	**No**	**SRF**	0.01 ± 0	0.98 ± 0	0 ± 0	0 ± 0	0 ± 0
HG9	**No**	**EPI**	0.16 ± 0.01	0.8 ± 0.01	0 ± 0	0 ± 0	0.02 ± 0
HG9	**No**	**MESO**	0.02 ± 0	0.51 ± 0	0.03 ± 0	0.01 ± 0	0.41 ± 0
HG9	**No**	**BATHY**	0.01 ± 0	0.29 ± 0	0 ± 0	0.24 ± 0.01	0.44 ± 0.01
S3	**No**	**SRF**	0.96 ± 0	0.02 ± 0	0 ± 0	0 ± 0	0 ± 0
S3	**No**	**MESO**	0 ± 0	0.01 ± 0	0.07 ± 0	0 ± 0	0.9 ± 0
S3	**No**	**BATHY**	0 ± 0	0 ± 0	0 ± 0	0.11 ± 0	0.87 ± 0

SI reference citations

1.   Picheral M, et al. (2010) The Underwater Vision Profiler 5: An advanced instrument for high spatial resolution studies of particle size spectra and zooplankton. *Limnol Oceanogr Methods* 8(9):462–473.

2.   Picheral M (2008) Zooprocess Manual Version 5.08.

3.   Picheral M, Colin S, Irisson JO (2015) EcoTaxa, a tool for the taxonomic classification of images.

4.   Ploug H, Jørgensen BB (1999) A net-jet flow system for mass transfer and micro electrode studies in sinking aggregates. *Mar Ecol Prog Ser* 176(1987):279.

5.   Ploug H, Terbrüggen A, Kaufmann A, Wolf-Gladrow D, Passow U (2010) A novel method to measure particle sinking velocity in vitro, and its comparison to three other in vitro methods. *Limnol Oceanogr Methods* 8(8):386–393.

6.   Danilov S, et al. (2015) Finite-Element Sea Ice Model (FESIM), version 2. *Geosci Model Dev* 8(6):1747–1761.

7.   Wang Q, et al. (2014) The Finite Element Sea Ice-Ocean Model (FESOM) v.1.4: formulation of an ocean general circulation model. *Geosci Model Dev* 7(2):663–693.

8.   Wekerle C, et al. (2017) Eddy-Resolving Simulation of the Atlantic Water Circulation in the Fram Strait With Focus on the Seasonal Cycle. *J Geophys Res Ocean* 122(11):8385–8405.

9.   Wekerle C, Krumpen T, Dinter T, Iversen M, Salter I (2018) Origin and properties of sediment trap catchment areas in Fram Strait : results from Lagrangian modelling and remote sensing. *Front Mar Sci*:1–26.

10.   Tippenhauer S, et al. (2017) *Physical oceanography measured on water bottle samples during POLARSTERN cruise PS99.2 (ARK-XXX/1.2)* doi:10.1594/PANGAEA.871952.

11.   Nöthig E-M, Knüppel N, Lorenzen C (2018) *Chlorophyll a measured on water bottle samples during POLARSTERN cruise PS99.2 (ARK-XXX/1.2)* doi:10.1594/PANGAEA.887855.

12.   Boss E, Behrenfeld M (2010) In situ evaluation of the initiation of the North Atlantic phytoplankton bloom. *Geophys Res Lett* 37(18):1–5.

13.   Grosfeld K, et al. (2016) Online sea-ice knowledge and data platform. *Polarforschung* 85(2):143–155.

14.   Parada AE, Needham DM, Fuhrman JA (2016) Every base matters: assessing small subunit rRNA primers for marine microbiomes with mock communities, time series and global field samples. *Environ Microbiol* 18(5):1403–1414.

15. Martin M (2011) Cutadapt removes adapter sequences from high-throughput sequencing reads. *EMBnet.journal* 17(1):10.

16. Bolger AM, Lohse M, Usadel B (2014) Trimmomatic: a flexible trimmer for Illumina sequence data. *Bioinformatics* 30(15):2114–2120.

17. Zhang J, Kobert K, Flouri T, Stamatakis A (2014) PEAR: a fast and accurate Illumina Paired-End reAd mergeR. *Bioinformatics* 30(5):614–620.

18. Mahé F, Rognes T, Quince C, de Vargas C, Dunthorn M (2015) Swarm v2: highly-scalable and high-resolution amplicon clustering. *PeerJ* 3:e1420.

19. Pruesse E, Peplies J, Glöckner FO (2012) SINA: Accurate high-throughput multiple sequence alignment of ribosomal RNA genes. *Bioinformatics* 28(14):1823–1829.

20. Quast C, et al. (2013) The SILVA ribosomal RNA gene database project : improved data processing and web-based tools. 41(November 2012):590–596.

21. RStudio Team (2015) RStudio: Integrated Development Environment for R. Available at: http://www.rstudio.com/.

22. McMurdie PJ, Holmes S (2013) phyloseq: An R Package for Reproducible Interactive Analysis and Graphics of Microbiome Census Data. *PLoS One* 8(4):e61217.

23. Gómez-Rubio V (2017) ggplot2 - Elegant Graphics for Data Analysis (2nd Edition). *J Stat Softw* 77(Book Review 2). doi:10.18637/jss.v077.b02.

24. Hsieh TC, Ma KH, Chao A (2018) iNEXT: Interpolation and Extrapolation for Species Diversity. Available at: http://chao.stat.nthu.edu.tw/blog/software-download/.

25. Callahan BJ, Sankaran K, Fukuyama JA, McMurdie PJ, Holmes SP (2016) Bioconductor Workflow for Microbiome Data Analysis: from raw reads to community analyses. *F1000Research* 5(3):1492.

26. McMurdie PJ, Holmes S (2014) Waste Not, Want Not: Why Rarefying Microbiome Data Is Inadmissible. *PLoS Comput Biol* 10(4). doi:10.1371/journal.pcbi.1003531.

27. Oksanen J (2016) vegan: Community Ecology Package. R package version 2.4-2.

28. Love MI, Huber W, Anders S (2014) Moderated estimation of fold change and dispersion for RNA-seq data with DESeq2. *Genome Biol* 15(12):550.

29. Knights D, et al. (2011) Bayesian community-wide culture-independent microbial source tracking. *Nat Methods* 8(9):761–763.

30. Schlitzer R (2015) Ocean Data View. Available at: http://odv.awi.de.

Supplementary Information

for

Paper V

Supplementary Information

(Italicized points represent incomplete descriptions)

Methods

Cruise description and sensor setup

Data was collected during the GO-SHIP cruise MSM060 between January 4th and February 1st 2017 on board RV Maria S. Merian. The ship was equipped with a shipboard Acoustic Doppler Current Profiler (sADCP) *(model, company, frequency)*. A water sampler rosette *(custom)* was equipped with a SBE 911 plus conductivity, temperature and density sensor (CTD; Seabird scientific, USA) as well as a lowered Acoustic Doppler Current Profiler (lADCP; *modell, company, frequency*) and an Underwater Vision Profiler 5hd (Hydroptic, France). This allowed simultaneous data acquisition of the physical parameters conductivity, temperature and pressure as well as deep current velocities and particle data during casts. The UVP 5hd was operated in autonomous pressure mode as described elsewhere[1], whereas acquisition was limited to the lowering part of every cast. Maximum acquisition frequency was 20 Hz and the sampling volume was approximately 1L.

Nutrient analyses

Water samples for nutrient analyses were filtered through 0.2 µm syringe GF/F (material?) filters (company) and subsequently stored at -20 °C until analyses using standard methods [2] and a QuAAtro39 microfluidic system (SEAL Analytical, USA). Ocean Data View v5.1.5 [3] was used to create section plots of nitrate concentrations. The global bathymetry dataset ETOPO1 (6x6 min) was used to define bathymetry polygon. Data interpolation was achieved using DIVA gridding[4] with defined correlation length scales (161 ‰ horizontally, 141 ‰ vertically).

Cyclone identification using remote sensing

The hourly mean sea surface height above geoid was used to identify the investigated cyclonic eddy. Data of the product GLOBAL_ANALYSIS_FORECAST_PHY_001_024 from marine.copernicus.eu was used to plot the sea surface anomaly for 03:30 GMT on January 7th 2017, the time at which the ship was inside the eddy.

sADCP and lADCP data processing

Calculation of vorticity and horizontal shear

Underwater Vision Profiling and image sorting

After post-processing of the large particle matter (LPM) data and vignettes using the ImageJ based software Zooprocess v7.14 [5], a deep learning prediction was carried out according to[6]. Validated images out of this classification were used to create a learning set for the following random forest classifications in Ecotaxa[7] followed again by manual validation. Living organisms and fecal pellet were sorted following the tree of live taxonomy in Ecotaxa. Detritus was separated visually into four different classes to improve the scoring of the following random forest prediction. Special detritus classes were defined as follows: larger dark detritus: >50% dark, rather fluffy, relatively large; larger grey detritus: <50 % dark, fluffy, relatively large; smaller dark detritus: >50 % dark, rather circular, fluffy; smaller grey detritus: < 50 % dark, rather circular, compact (See plotted values of size, grey value and porosity in Figures S3 – S5). Detritus classes were subsequently summed up and further termed 'large identified detritus'. Section plots of zooplankton and particle data were

generated analogously to nitrate section plots but with less smoothing during the DIVA data interpolation due to higher resolution of data points (21 ‰ horizontally, 1 ‰ vertically).

Calculation of particle volume depth distribution and carbon flux

Carbon export was calculated as reported elsewhere[8] based on globally distributed carbon measurements and modelled sinking velocities. Total volume of LPM size classes up to minimum vignette acquisition size of 1020 µm as well as fecal pellets and identified large detritus were summed up for each station and depth. Section plots of total particle volume and carbon flux were generated analogously to particle abundance and zooplankton section plots. Median values for total particle volume were calculated for defined depth intervals (every 100 m in upper 1000 m and every 500 m below 1000m) and every single particle class (including visually distinguished detritus classes) and plotted cumulatively using Sigmaplot 12 (Systat Software GmbH, Germany). Calculation of depth interval averaged carbon fluxes and standard deviations were performed using the box averaging tool in Ocean Data View.

Calculation of carbon-specific degradation

Data availability

Cruise data is available at XXXX

Numerical results of particle and Zooplankton processing are available at https://www.pangaea.de *(doi:XXXX).* UVP images and validations can be reviewed at *https://ecotaxa.obs-vlfr.fr/ (project: uvp5_MSM60; for detailed questions please contact A.R.)*
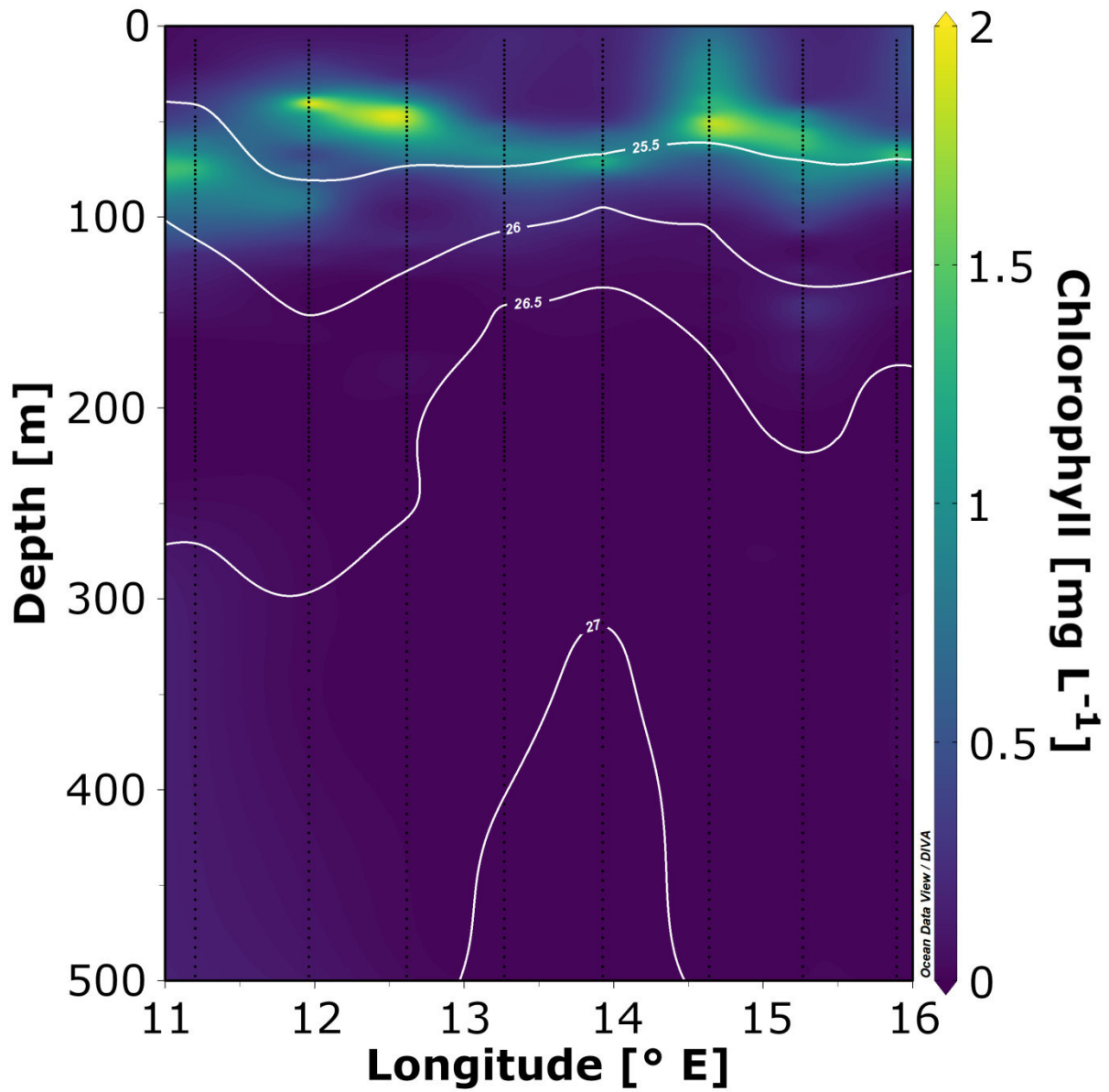
Supplementary Figures

Fig. S1: Chlorophyll concentrations in the upper 500 m as measured by fluorometer sensor attached to CTD.
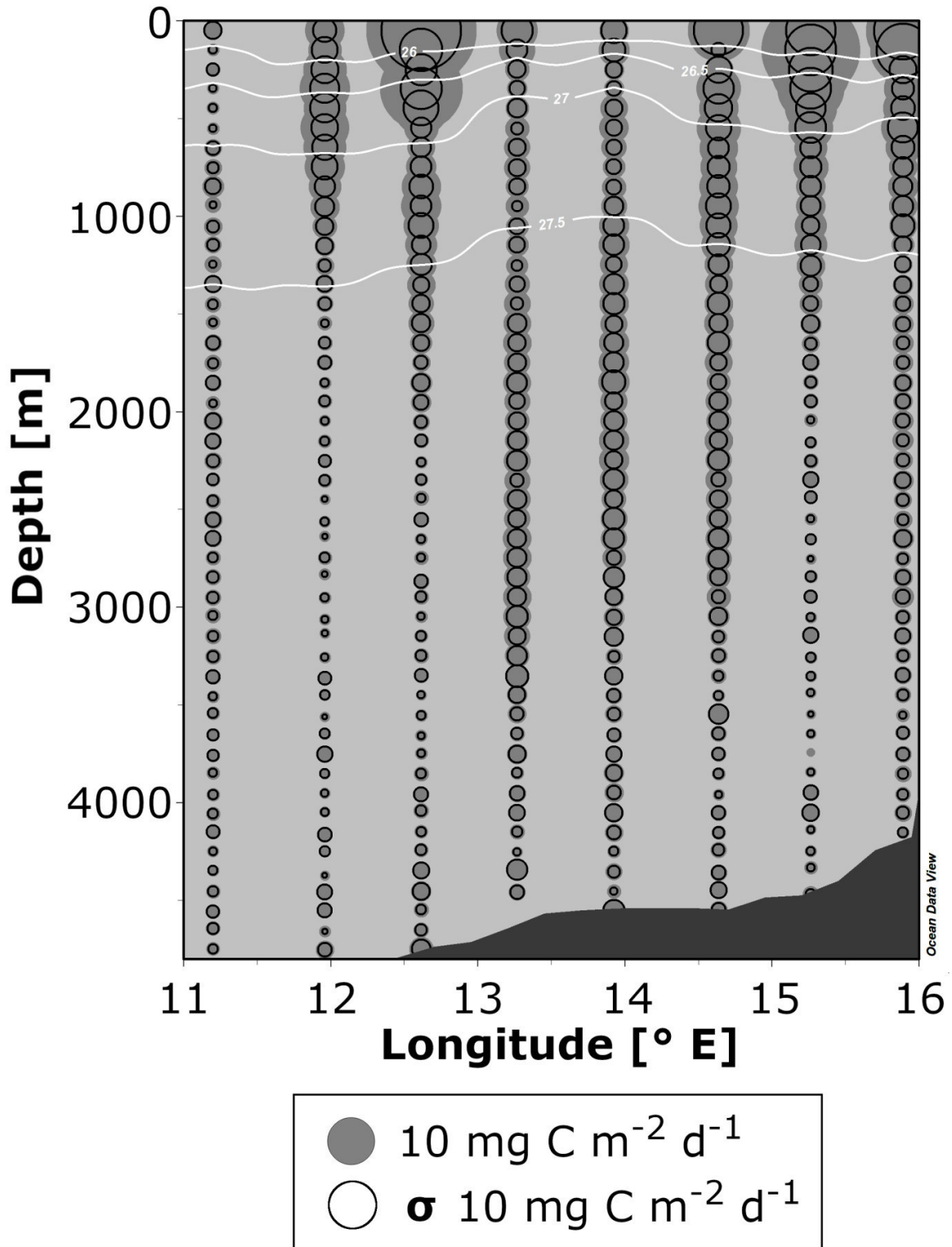
Fig. S2: Dot size plot of carbon flux averaged over 100 m depth intervals. Size of grey filled circles indicate average carbon flux in mg C m-2 d-1. Size of black circles indicate standard deviation of the respective depth bin in mg C m-2 d-1. White lines indicate isopycnals in kg m⁻³ (ρ – 1000 kg m³).
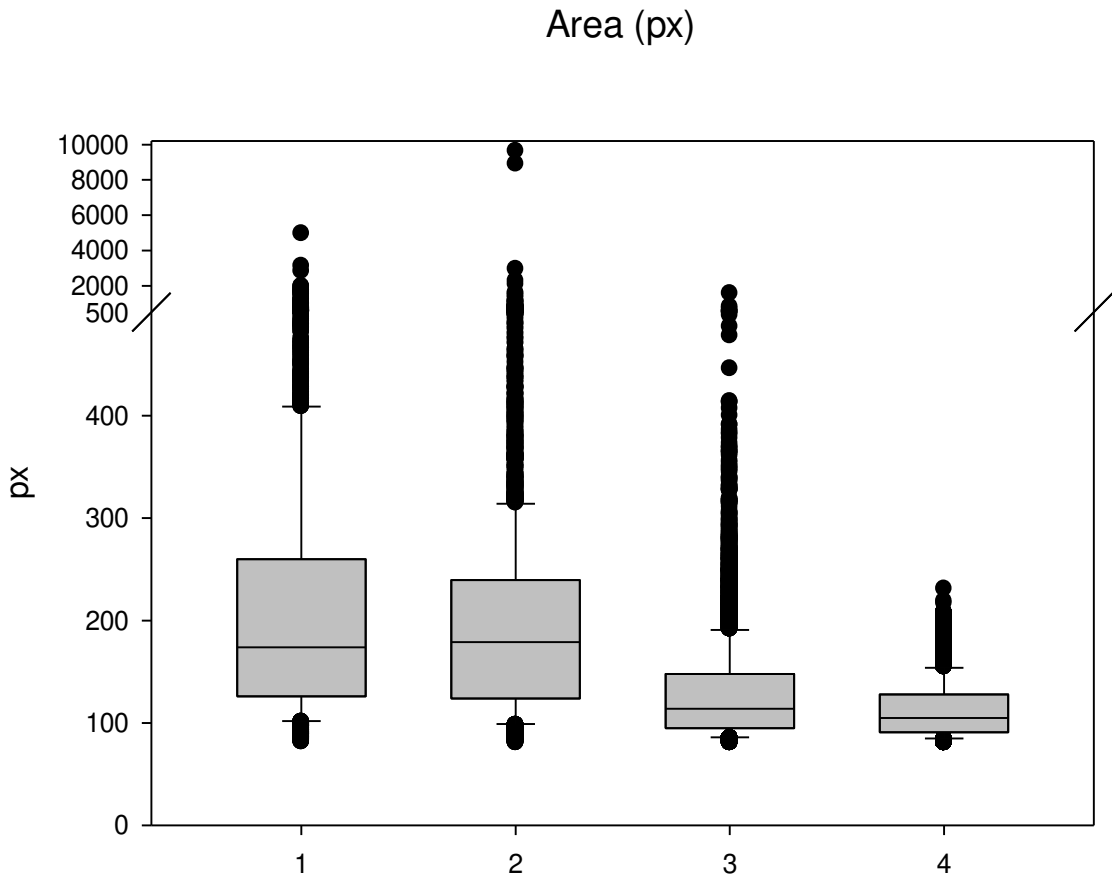
Area (px)

Fig. S3: Area in pixels of 1: larger grey detritus, 2: larger dark detritus, 3: smaller grey detritus, 4 smaller dark detritus.
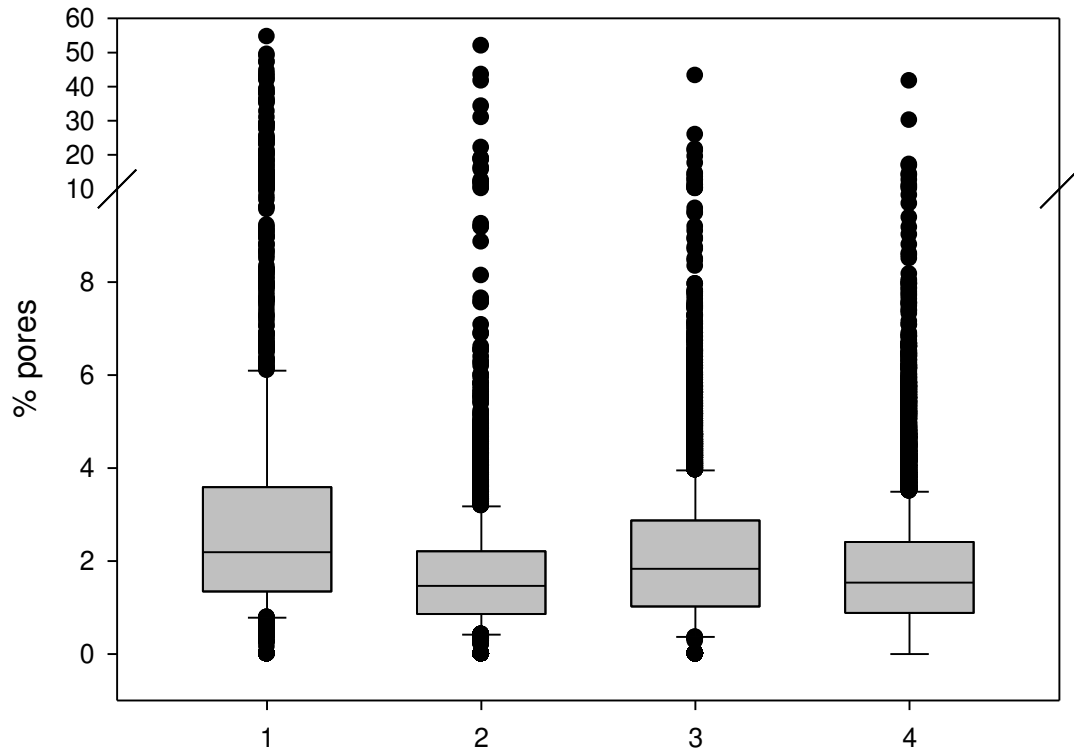
Fig. S4: Percentage of holes/pores of 1: larger grey detritus, 2: larger dark detritus, 3: smaller grey detritus, 4 smaller dark detritus.

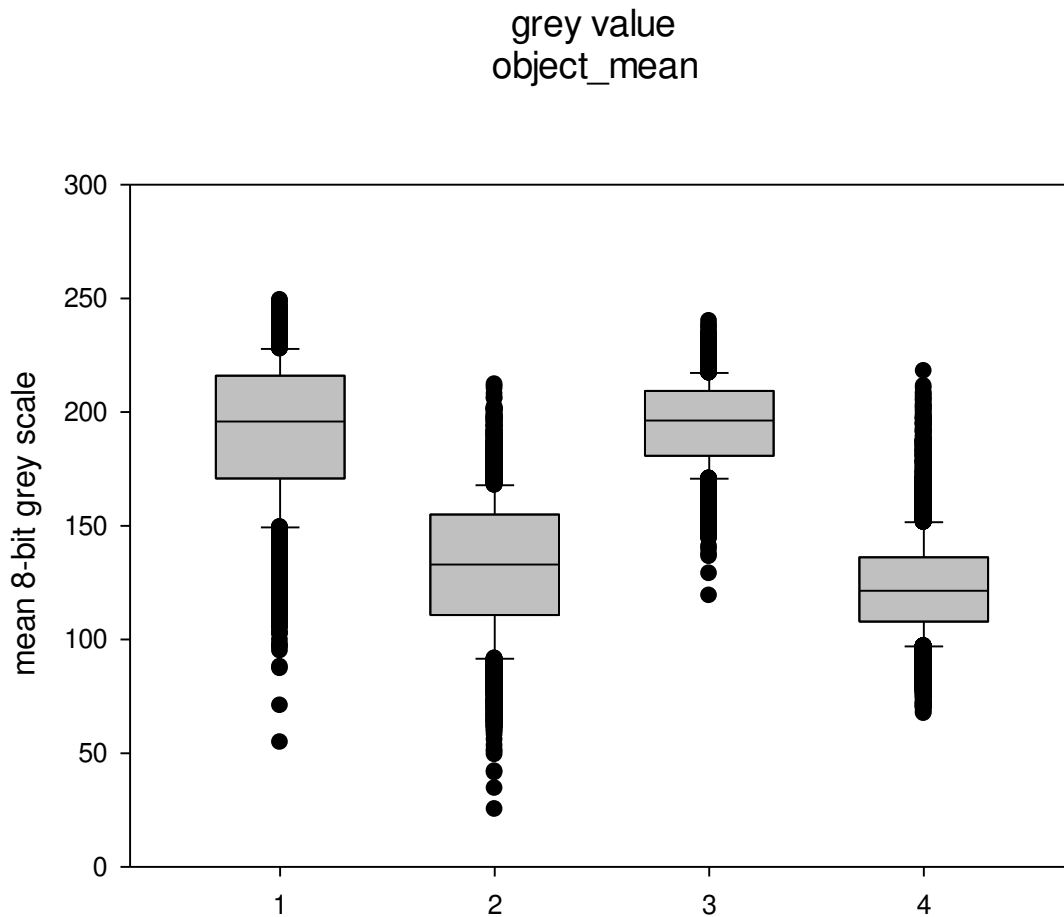Fig. S5: Individual mean 8 bit grey scale of 1: larger grey detritus, 2: larger dark detritus, 3: smaller grey detritus, 4 smaller dark detritus.

References

1. Picheral, M. *et al.* The Underwater Vision Profiler 5. An advanced instrument for high spatial resolution studies of particle size spectra and zooplankton. *Limnol. Oceanogr.: Methods* **8,** 462–473; 10.4319/lom.2010.8.462 (2010).

2. Grasshoff, K., Kremling, K. & Ehrhardt, M. *Methods of Seawater Analysis* (Wiley-VCH Verlag GmbH, Weinheim, Germany, 1999).

3. Schlitzer, R. Ocean Data View. *https://odv.awi.de* (2018).

4. Troupin, C. *et al.* Generation of analysis and consistent error fields using the Data Interpolating Variational Analysis (DIVA). *Ocean Modelling* **52-53,** 90–101; 10.1016/j.ocemod.2012.05.002 (2012).

5. Gorsky, G. *et al.* Digital zooplankton image analysis using the ZooScan integrated system. *Journal of Plankton Research* **32,** 285–303; 10.1093/plankt/fbp124 (2010).

6. Christiansen, S. *et al.* Particulate matter flux interception in oceanic mesoscale eddies by the polychaete Poeobius sp. *Limnol. Oceanogr.* (2018).

7. Picheral, M., Colin, S. & Irisson, J.-O. EcoTaxa, a tool for the taxonomic classification of images. *http://ecotaxa.obs-vlfr.fr* (2017).

8. Guidi, L. *et al.* Relationship between particle size distribution and flux in the mesopelagic zone. *Deep Sea Res., Part I* **55,** 1364–1374; 10.1016/j.dsr.2008.05.014 (2008).